УДК 533,9+536,46

This book of contributed papers includes the original abstracts of lectures and reports presented at the International Workshop "Noncquilibrium Processes in Combustion and Plasma Based Technologies» (Minsk, August 23-28, 2008).

Данный сборник трудов содержит оригинальные тексты лекций и докладов, представленных на международную научную конференцию "Неравновесные процессы в горении и плазменных технологиях" (Минск, 23-28 августа 2008 г.).

Институт тепло- и массообмена им. А. В. Лыкова НАН Беларуси, 2008

In Memory of Mikhail Nikolaevich ROLIN

Mikhail Nikolaevich ROLIN was born in 1946. His youth, student days, and the beginning of his scientific work coincided with the best period in the history of the Soviet Union, when such notions as the collectivism and unselfishness were the reality of everyday life, the prestige of education was high, and many of the young people pursued the only object in life - SCIENCE that paved the way to outer space and where every working day promised meeting with the unknown. At that time of romanticism, talented young people selected the professions of physicists, chemists, mathematicians, biologists; half the century lay in wait till the dominance of financiers and managers.

In 1969 Mikhail graduated from the V. I. Lenin Byelorussian State University in Minsk, Department of Atomic Physics, and went to work at the Heat and Mass Transfer Institute of the Academy of Sciences of the BSSR. His subsequent 39 years of work were devoted to the Heat and Mass Transfer Institute. His passion for the science and striving for cognition were the main traits of his character; he was entirely devoid of the pangs of vanity and craving for quick promotion. The difficulties of the years of "perestroika" (ideological reorientation) have not shaken Mikhail Nikolaevich - he kept being true to himself, to his principles, country, and the science.

From the start of his working life Mikhail Nikolaevich has set a very high level of demands on the studies carried out. Any new topic was studied extensively and thoroughly and only then the methods and direction of search were outlined. His reports were thoroughly worked out with a clearly cut physical picture of the process studied. His replies to the questions posed were delightedly noteworthy for exactness and laconism, which is only possible in the case of the deepest mastery of the topic. There were changes in the trends of investigations and laboratories, where Mikhail Nikolaevich was on the staff, but unaltered remained the thoroughness of his studies, the elegance of the proposed models, and the effectiveness of the computational programs created by him.

The list of his publications numbers 62 scientific works, plus 3 being in press. The range of his scientific interests was broad enough: various areas of nonequilibrium processes of the physics of plasma, the properties of heat shielding materials, gas dynamics, radiation of high-enthalpy gas flows, chemical kinetics, tomography, etc. In recent year Mikhail Nikolaevich has been engaged in research of the physicochemical processes occurring in various discharge facilities. He has become utterly engrossed in the creation of models to describe the barrier and microwave

discharges. His self-consistent model of atmospheric pressure microwave discharge in inert gases ranks among scientific novelties of the worldwide level.

Mikhail Nikolaevich has made a great contribution to the scientific activities of the Heat and Mass Transfer Institute by his works and his influence on the colleagues by pre- assigning the high level of discussions, sharing his knowledge and results of research with his colleagues. We have lost a very talented scientist, a specialist with encyclopedic knowledge in various areas of physics, engineering, and culture. Fond memories of this kind and pure person who personified the best traits of the Soviet scientist will long live in our hearts.

Friends and colleagues

1. ELEMENTARY PROCESSES IN PLASMA AND COMBUSTION PHENOMENA

ELECTRONIC ENERGY-EXCHANGE PROCESSES IN HIGH-TEMPERATURE AIR

S.A. LOSEV, V.N. JARYGINA

Institute of Mechanics, M.V. Lomonosov Moscow State University, Moscow, Russia

The electronic states as electronic terms are the system of complicated energetic surfaces that differs from the notation of vibrational states in the form of separate energy-levels. The electronic state variation is the result of electronic energy-exchange at atoms/molecules collisions. These processes are accompanied by transition between various electronic potential surfaces as nonadiabatic transitions. The nonadiabatic transitions happen with high probability if potential surface come close or intersect.

The electronic energy-exchange processes are connected with chemical processes, this suggests to consider electronic-chemical reactions. The goal function of processes under study is the coefficients in kinetic equations as the rate constants of electronic-chemical reactions.

The analysis of kinetic processes with excited electronic states of atoms and molecules in high-temperature air is performed. 12 excited states with metastable levels of molecular and atomic oxygen, nitrogen and nitrogen oxide lower than energy of dissociation are considered. The formation of the excited electronic states in atoms and molecules is the result of recombination process, electronic energy-exchange by particles collisions, and chemical exchange reaction. The most rapid processes of the excited electronic states formation are taking place in atoms recombination and isoenergetic transfer of vibrational energy to electronic one from high-excited vibrational levels. The quenching of metastable particles is due to dissociation and to particles collisions.

The excited electronic atoms and molecules are treated as separate components in gas mixtures with corresponding complexes of vibrational levels.

The theoretical examination of rate constant values in electronic-chemical reactions is performed with the method of transient state for potential surface of collisional complex. The results of dynamic equation solution is the rate constants of these reactions. These values are cited only in two articles (Gonzalezet al [1], Tully [2]) under consideration of high- temperature air.

The main values of rate constants of electronic-chemical reactions in high-temperature gas are received using experimental investigation results. These data are based on the analysis of research results in shock tubes, discharge flows, and other facilities. The analysis of experimental investigations has been given in six reviews, as well as in seven individual articles.

The prepared complex of rate constants of electronic-chemical reactions in high- temperature air composes the corresponding database for temperatures above one to several thousands Kelvin degrees. This database includes the data on:

formation of the excited electronic states as the results of atoms recombination (5 reactions), and particles collisions (9 reactions);

electronic energy-exchange due to particles collisions (17 reactions), and atoms recombination (4 reactions);

quenching of the excited electronic states of atoms and molecules due to particles collisions (13 reactions), and molecules dissociation (5 reactions).

The rate constants are represented as parameters in Arrhenious formula. The procedure of model extension for dissociation (Kustova et al [3]), and chemical exchange reaction (Starik et al [4]) is supported to describe these processes involving molecules in the excited electronic states. The calculation leads to the conclusion that the values of rate constants for dissociation of oxygen molecules in accordance with Marrone-Treanor model differ by some orders for various electronic states.

The excitation of electronic states leads to intensive radiation of atoms and molecules as a results of radiation of atoms and molecules as a result of different radiative transitions. The nonequiiibrium radiation essentially affects population of electronic states of atoms and molecules, so there is a need to take into account when solving physical and chemical kinetic problems.

The created database on rate constants of electronic-chemical reactions in high- temperature air promotes the solution of kinetics problems.

The absence of considering of excited electronic states in thermally nonequiiibrium processes leads to appreciable errors in gas parameters behind shock wave front. The comprehensive account of processes with the participation of atoms and molecules in excited electronic states along with consideration of vibrational excitation of molecules make the modeling of relaxational and reacting gas at high temperature more approximated to reality.

References

Gonzalez M., Miquel I, Sayos R. VTST kinetics study of the $N(^2D)+0_2(X)\rightarrow 0(^3P,^1D)$ reactions based on CASSCF and CASPT2 ab initio calculations including excited potential energy surfaces // *Chem. Phys. Letters.* 2001. Vol. 335. Pp. 339-347.

Tully J.C. Collision complex model for spin forbidden reactions: Quenching of $O(^1D)$ by N_2 // *J. Chem. Phys.* 1974. Vol. 61. No. 1. Pp. 61-67.

Kustova E.V., Aliat A., Chikhaoui A. State-to-state dissociation rate coefficients in electronically excited diatomic gases // *Chem. Phys. Letters.* 2004. Vol. 390. Pp. 370-375.

Starik A.M., Titova N.S. Initiation of combustion and detonation in burning mixtures by exciting of molecular oxygen to $O_2(a)$ state // *Chem. Phys. Reports.* 2001. Vol. 20, No. 5. Pp. 17-25.

VIBRATIONAL NONEQUILIBRIUM OF $H0_2$ RADICAL IN THE REACTION OF HYDROGEN WITH OXYGEN; 1000 < T < 1200 K

O.V. SKREBKOV, S.P. KARKACH

Institute of Problems of Chemical Physics RAS, Chernogolovka, Russia

Introduction

At present, the mechanism of the reaction of hydrogen with oxygen is considered as the most studied one (in contrast, for example, to hydrocarbon oxidation). However, all the kinetic calculations executed for interpretation of experiments was based on use of the assumption about an availability of equilibrium on the internal and external degrees of freedom of molecules and radicals. Comparative (from the practical standpoint) successes of kinetic descriptions in terms of the equilibrium approach have been achieved owing to considerable variations of the rate coefficients of important processes. Thus, the rate coefficient of the most important chain branching reaction $H+O_2 \rightarrow O+OH$ obtained by different authors (see [1]) considerably differ depending on experimental conditions, about half obtained values are over the theoretical upper bound estimate (see [2]).

A series of experimental facts and results of quantitative comparison of theory with experiment (for more detail see [2]) suggest a necessity of not only making the kinetic scheme more precise and detail but also a revision of itself kinetic concept which is based on the assumption about an availability of equilibrium on the internal (vibrational) degrees of freedom.

In accordance with conclusions of the work [2], it relates first of all to the reactions with participation of vibrationally excited radical $H0_2(v)$ which forms in result of bimolecular recombination $H+0_2 \rightarrow H0_2(v)$ and the following (fast for high vibrational excitations) redistribution of H--0_2 bond energy between vibrational degrees of freedom (modes) of $H0_2$. They are the following main (in conventional chain branching mechanism of hydrogen oxidation) reactions: the above reaction $H+0_2 \rightarrow O+0H$ and the inhibiting reaction $H+0_2+M \rightarrow H0_2+M$. In terms of existing kinetic concept, these (and other less important for considered conditions) overal reactions interpret as the elementary ones depending only on the gas temperature, T.

An impossibility to explain in this terms the formation (already during the most early steps of combustion process) of the electronically excited radical $OH(^2\Sigma^+)$ is a significant example of insufficiency of this traditional equilibrium kinetic concept. As the only quantitatively acceptable

variant can be the reaction $H+0_2+H_2 \rightarrow OH(^2\Sigma^+)+H_20$ suggested in [3]. This overal reaction we suppose now proceeds by two following steps: $H+0_2 \rightarrow H0_2(v)$ and $H0_2(v)+H_2 \rightarrow OH(^2\Sigma^+)+H_20$, i.e., via forming the vibrationally excited $H0_2(v)$ radical.

The subject of this research is the creation and approbation of theoretical model based on consistent account of the vibrational nonequiiibrium of $H0_2$ radical that is assumed to act as a key intermediate in the process of chain branching and in a generation of electronically excited species [2]. In terms of the proposed model, the chain branching $H+0_2 \rightarrow O+0H$ and inhibiting $H+0_2+M \rightarrow H0_2+M$ reactions are considered as a general multichannel process of forming, intramolecular energy redistribution between modes, relaxation, and unimolecular decay of the long-lived (see [2]) intermediate or vibrationally excited $H0_2(v)$ radical which is capable moreover to react with another components of a mixture. The latter means a revision of all the chemical mechanism in the hydrogen-oxygen system.

Theoretical backgrounds

Equations of chemical and vibrational kinetics for general case of reacting multi- component gas mixture in the frames of macroscopic (or hydrodynamic) description (i.e., in the form of equations for the average energies of vibrational modes, ε_κ, and concentrations of mixture components, n_i) were first published in [4]. According to the model [4] (see also [5]), chemical and vibrational kinetics of HO_2 radical and another molecules is described by the equations for n_i, as well as ε_κ for given gas temperature, T, and pressure, p.

The vibrational nonequiiibrium manifests itself via the dependence of corresponding rate constants on the vibrational temperatures T_κ (or averaged energies, ε_κ) of modes:

$$k_r(T,T_k)=\kappa_r(T,T_k)k_r^0(T),\ \kappa_r(T,T_k)=\exp\left[E_r\left(\frac{1}{T}-\frac{\sum_i \beta_{ri}^2}{\sum_i \beta_{ri}^2 T_i}\right)\right],\ T_k=\frac{\theta_k}{\ln[(1+\varepsilon_k)/\varepsilon_k]}.$$

Here, k_r^0 is the rate constant of rth reaction provided the thermodynamic equilibrium; E_r is the portion of the activation energy of rth reaction refered to the vibrational degrees of freedom; θ_k is the characteristic temperature of kth vibration; $\sum_i \beta_{ri}^2 = 1$, $\beta_{r1}=\beta_{r2}=\ldots.$

The effect of the chemical reactions on the process of vibrational relaxation is expressed through the terms in the right parts of vibrational kinetics equations for ε_k:

$$\left(\frac{d\varepsilon_k}{dt}\right)_{chem}=(\rho n_j)^{-1}\sum_r(\nu'_{jr}-\nu_{jr})[(\chi_{rk}-\varepsilon_k)(R_r-R'_r)].$$

Here, χ_{rk} is the average numbers of vibrational quanta obtained by kth mode in one act of formation of the j-type molecule in rth reaction; $\sum_i \beta_{ri}^2=1$, $\beta_{r'1}=\beta_{r'2}=\ldots.$ The total set of χ_{rk} values characterizes an energy distribution between modes of the rth reaction products.

For description of the initiation and development of chain reaction in the $H_2 + O_2 + Ar$ system for temperatures $1000 < T < 1200$ K and pressures $0.9 < p < 2.0$ atm, we have used the kinetic scheme, which takes into account chemical reactions with participation H_2, O_2, H_2O, HO_2, H, O, OH, H_2O_2, O_3 in the ground electronic state as well as $O_2(^1\Delta)$, $O(^1D)$, $OH(^2\Sigma^+)$, and relaxation channels of the vibrational modes H_2, O_2, $O_2(^1\Delta)$, $HO_2(\nu_1) \equiv HO_2(100)$, $HO_2(\nu_2) \equiv HO_2(010)$, and $HO_2(\nu_3) \equiv HO_2(001)$; in all the details, see [6].

The behaviour of intermediate HO_2 radicals are described by the following elementary processes:

$H+O_2 \rightarrow HO_2(100)$ (formation as a result of bimolecular recombination); (1)

$HO_2(3E\ 0\ 0) \rightarrow HO_2(EEE)$, $3E \approx D_{H\text{-}O2}$, (intramolecular redistribution of H-O_2 bond energy); (2)

$HO_2 + (M) \rightarrow H+O_2 + (M)$ (dissociation along H-O_2 bond); (3)

$HO_2 + (M) \rightarrow O+OH + (M)$ (dissociation along O-O bond, i.e. chain branching); (4)

$HO_2(100)+X(0) \leftrightarrow HO_2(000)+X(1)$, X = H_2, O_2 (VV′-exchange); (5)

$HO_2(010)+X(0) \leftrightarrow HO_2(000)+X(1)$, X = H_2, O_2 (VV′-exchange); (6)

$HO_2(001)+M \leftrightarrow HO_2(000)+M$, M = H_2, O_2, H_2O, Ar (VT- exchange); (7)

$HO_2+Y_i \leftrightarrow Y_j+Y_k$, $i, j, k = 1,2,\ldots,N$ (chemical reactions). (8)

The main difference on traditional schemes is the absence of $H+O_2 \rightarrow O+OH$ reaction as the elementary one. According to suggested model, the process of the formation of the $H0_2(v)$ radical has been presented by the fast bimolecular recombination reaction (1). The reactivity of $H0_2(v)$ and its subsequent evolution are determined by the processes of energy redistribution between modes (2), relaxation (5)-(7), and unimolecular decay (3), (4), as well as the reactions with its participation (8).

Results and discussion

Results of the calculations are called to illustrate the efficiency of suggested approach from standpoint of both elucidating a physically adequate mechanism of the high-temperature oxidation of hydrogen and quantitative interpreting experimental data.

At present research, the results [7, 8] was chosen for comparison with our kinetic (isothermal) calculations. These results can be used for direct comparison with isothermal kinetic calculations since their authors specially saw to that an influence of such a "non- kinetic" factor as self warming-up (when gas-dynamical and thermal phenomena are brought to the foreground) was minimal.

Comparison of the results of simulative kinetic calculations in terms of single kinetic scheme *with* the corresponding *experimental results* [7, 8] is illustrated by Table 1. Describing the results of the comparison on the whole, we establish a qualitative and quantitative agreement of calculated results with experimental ones (at the worst case, No. 4, the difference is 24%).

Table 1. Measured [7 [a], 8 [b]] and calculated in terms of the single kinetic scheme [c] the values t_{50} [d] and t* [e]

No.	T, K	p, atm	Experiment		Calculation	
			t*, μs [8]	t_{50}, μs [7]	t*, μs	t_{50}, μs
1	1050	1.9	945÷1120	–	1102	
2	1225	1.5	600	–	603	
3	1052	2.2	–	618		525
4	1074	0.935	–	1005		1241
5	1086	0.94	–	985		1130
6	1102	1.2	–	836		911
7	1115	2.248	–	393		404

[a] reflected shock wave, reach mixture (4% H_2+1% O_2+95% Ar), monitoring absorption of OH; [b] incident shock wave, stoichiometric mixture (0.93% H_2+0.46% O_2+98.61% Ar), monitoring emission of OH*; [c] see [6] 1; [d] the time between a front and the point in time at which the light absorption OH→OH* reached a half of its maximum value (in the calculations, the point in time at which a half-maximum concentration of OH radicals was reached); [e] the time between a front and the point in time at which the emission at $\lambda \approx 306$ nm reached a maximum (at the calculations, it was identified with the point in time at which a maximum concentration of OH* was reached).

Being extracted from calculation, the apparent ***rate constant*** of the $H+O_2 \rightarrow O+OH$ overall process is $k^{eff}_{H+O_2 \rightarrow O+OH} = R_3/[H][O_2]$; its ***dependence on experimental conditions*** is illustrated by Fig. 1. The values of $k^{eff}_{H+O_2 \rightarrow O+OH}$ as functions of t are obtained in the calculations corresponding the cases for practically the same temperatures $T \cong 1050$ K.

The pronounced dependence, on pressure and time, of the apparent rate constant of the most important overall reaction determining the rate of full process on the whole is a consequence of its nonequiiibrium character and a change of the role of different elementary reactions and vibrational relaxation channels during different stages. Especially nonequiiibrium character of

the hydrogen oxidation process is illustrated by Fig. 2 in which the typical (for considered conditions) time profiles for vibrational temperatures, T_k, are given.

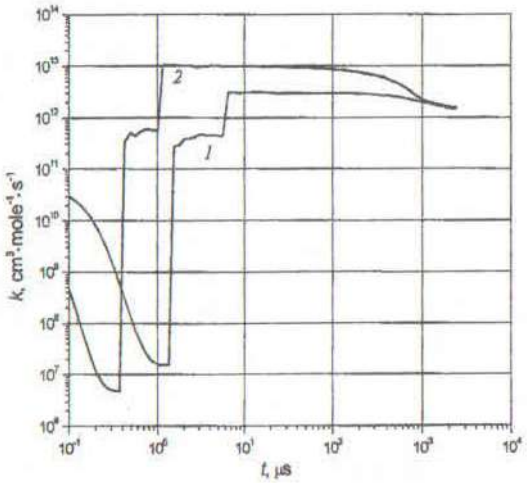

Fig. 1. Dependences on time of value $k^{eff}_{H+O_2\rightarrow O+OH} = R_3/[H][O_2]$ (apparent rate of the overall process $H+O_2 \rightarrow O+OH$) for two variants of the calculation: *1* – No. 1 of Table 1; *2* – No. 3 of Table 1. For calculations, the coordinate system was attached to the flow behind the shock wave (the gas rests, $T = const$, $p = const$, $t = 0$ when the shock front is passing)

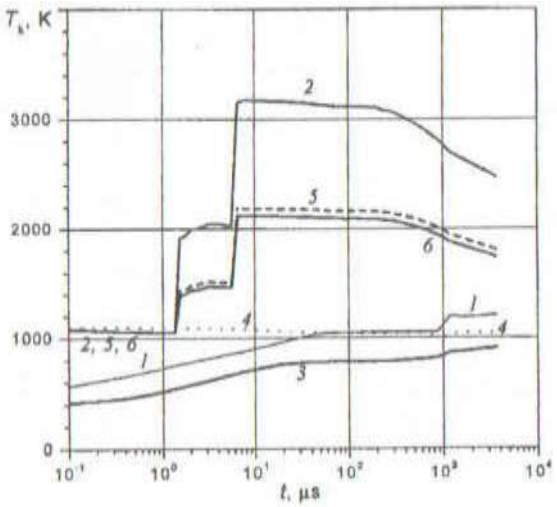

Fig. 2. Typical, for considered conditions, the time profiles of vibrational temperatures, T_k. The curves are numbered by order of decreasing characteristic temperatures of vibrational modes, θ_k, namely: *1* – H_2, *2* is $HO_2(\nu_1)$, *3* – O_2, *4* – O_2*, *5* – $HO_2(\nu_2)$, and *6* – $HO_2(\nu_3)$. Here, the calculated variant No. 1 of Table 1 is illustrated

The reaction rate constants depend on vibrational temperatures of reagents, and these dependencies are described by multipliers $\kappa_r\ (T_i\ ,\{T_k\})$ of several orders of magnitude. So considerable difference of nonequilibrium factors, κ_t, from 1 means that *the nature of*

hydrogen-oxygen reaction is especially nonequilibrium, and the vibrational nonequilibrium of HO_2 radical is the essence of hydrogen oxidation process.

Typical, for considered conditions, behaviour of species concentrations in reacting $H_2 + 0_2 + Ar$ mixture behind shock wave are illustrated by Fig. 3.

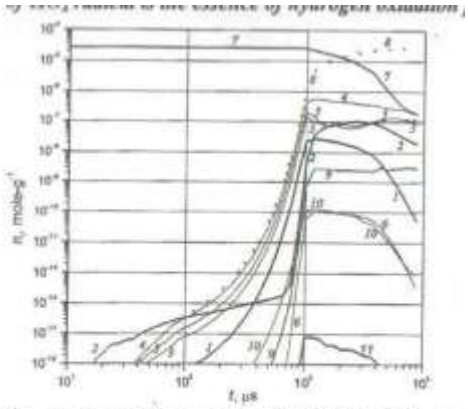

Fig. 3. The time profiles of concentrations, n_i (mole/g), of HO_2 (*1*), $O_2(^1\Delta)$ (*2*), OH (*3*), H (*4*), O (*5*), $O(^1D)$ (*6*), H_2 (*7*), H_2O (*8*), H_2O_2 (*9*), O_3 (*10*), and $OH(^2\Sigma^+)$ (*11*). Here, the calculated variant No. 1 of Table 1 is illustrated

While commenting Fig. 3 we note first of all the considerable quantities of singlet molecular oxygen, O_2 ($^1\Delta$), already in the earliest stages of the process. As reaction proceeds, the O_2 ($^1\Delta$) concentrations reach values which mean that *the singlet molecular oxygen is one of the most important intermediates* like HO_2, H, O, or OH[1].

We grateful to DSc A.N. Ivanova and Mrs. S.S. Kostenko for programming and helping when calculating. This work was supported by RFBR (Grant No. 080300785).

References

Mallard W.G., Westley F., Herron J.T., Hampson R.F. NIST Chemical Kinetics Database - Ver. 6.0, NIST Standard Reference Data. Gaithersburg, MD, 1994.

Skrebkov O.V., Karkach S.P. // *Kinetics and Catalysis.* 2007. Vol. 48. P. 367.

Belles F.E., Lauver M.R. *// J. Chem. Phys.* 1964. Vol. 40. P. 415.

Vasil'ev V.M., Kulikov S.V., Skrebkov O.V. // *Prikl. Mekh. Tekhn. Fiz.* 1977. Vol. 4. P. 13.

Skrebkov O.V., Kulikov S.V. // *Chem. Phys.* 1998. Vol. 227. P. 349.

Skrebkov O.V., Karkach S.P., Kostenko S.S., Ivanova A.N. // *Physical and Chemical Kinetics in Gas Dynamics.* 2008. Vol. 6. http://www.chemphys.edu.ru

Ryu S.-O., Hwang S.M., Rabinovitz M.J. *// J. Phys. Chem.* 1995. Vol. 99. P. 13984.

[1] In the current calculation practice, the singlet molecular oxygen and reactions with its participation as a rule are not taken into account if the question is not an artificial introduction of this species to calculation when one attempts to simulate an effect of discharge or radiation.

Skrebkov O.V., Karkach S.P., Vasil'ev V.M., Smirnov A.L. // *Chem. Phys. Lett.* 2003. Vol. 375. P. 413.

FORMATION AND EXCITATION OF CN MOLECULES IN GAS DISCHARGE PLASMAS

G. M. GRIGORIAN

V.A. Fock Institute of Physics, St. Petersburg University, St. Petersburg, 198504, Russia

The carbonated radicals occur in a wide variety of man-made and natural environments. They play an important role in interstellar and comets chemistry, in the combustion process, in shock tubes and MHD experiments, in plasma-based technologies and many other fields. In particularly, the CN radical is a very plausible candidate for the dominant growth precursor in plasma deposition experiments dedicated to the production of a new super hard material - carbon nitride.

Emission by electronically excited CN molecules is prominent in the spectrum of active nitrogen containing traces of carbonaceous species. A large amount of experimental work has been devoted to the investigation of CN emission. However up to day the plasma chemistry of CN radicals and processes lead to the excitation of CN electronic states are still poorly understood.

In this work we focus our attention to the kinetic of CN radicals in the gas discharge plasmas in He-CO-N_2 and He-CO_2-N_2 mixtures.

Our apparatus and the experimental and analytical procedures used in the measurements have been described in detail elsewhere [1, 2]. We used molybdenum glass discharge tubes of diameter 15-22 mm that were cooled by running water or liquid nitrogen. The discharge was operated in DC mode. The length of the discharge region was 40-50 cm. Different electrode materials were used (Ta, Cu, graphite) in experiments. Studies were carried out in the He-CO-N_2 and He-CO_2-N_2 mixtures. The concentration of CO and CO_2 molecules in the mixtures were 4+16 %, the concentration of N2 - 1+16 %. The total gas pressure in the discharge tube was varied from 5 to 15 torr and the discharge current was 20+100 mA. The set up can work in sealed-off regime (operating without gas circulation through the discharge tube) as well as in gas-flow regime. The gas mixtures used in experiments were preliminary carefully purified by using a system of traps with silica gel and zeolite.

The emission from the axial region of the positive column of the discharge and from the regions near the electrodes surface in the spectral range of 200-3000 nm was recorded with a

spectrometer. The analysis of the emission spectra allowed us to determine the populations of the vibrational levels of CO($X^t\Sigma^+$) molecules, the gas temperature and the concentrations of the electronically excited particles in the gas discharge plasma.

Concentrations of CN* molecules appeared in the discharge plasma due to plasma chemical reactions have been measured in the wide range of experimental conditions. For monitoring concentrations of CN molecules in $B^2\Sigma^+$and $A^2\Pi$ states violet ($B^2\Sigma^+ \rightarrow X^2\Sigma^+$) and red ($A^2\Pi \rightarrow X^2\Sigma^+$) band systems were used. The vibrational distribution of CO molecules in the ground electronic state was determined from the spectra of IR molecular emission at the first and second overtones. The influence of the lasing oscillation in the CO ($X\ ^t\Sigma^+$) vibrational levels on the concentration of CN($B^2\ \Sigma^+$) and CN($A^2\Pi$) molecules has been examined.

The electric field in the discharge was determined by measuring the voltage drops across the discharge gap and the electrode sheaths. The electrode sheath voltages were found from the voltage measurements in experiments with different discharge lengths.

Experimental concentrations of CN molecules in the ground state and in electronically excited states $B^2\ \Sigma^+$ and $A^2\Pi$ were compared with theoretical ones.

The electron drift velocity and the rate constants for the processes in the discharge plasmas with the participation of electrons were obtained by numerically solving the kinetic Boltzmann equation for the electron energy distribution function (EEDF). The energy distribution ftmctions for electrons (EEDF) were calculated for our conditions by I.V. Kochetov and coworkers by using the method described in [1,3]. The cross sections for the electron excitation of electronic states CN* were calculated in the Born approximation formulas from [4]. Transition probabilities for violet and red systems were adopted from [5].

The study of populations of excited states CN* molecules and their dependence on discharge current, pressure and gas mixture in gas-flow and sealed-off regimes have been carried out. Investigation of the behavior of CN(($B^2\ \Sigma^+$) and CN($A^2\Pi$) concentrations in the axial region of the discharge tube and comparisons of experimental concentrations of CN* and calculations showed that good agreement between experiment and theory may be obtain if we proposed the following scheme for processes governed the concentrations of CN molecules.

1. Formation of $CN(A^2\Pi)$:

$$CN(X^2\Sigma^+) + e \rightarrow CN(A^2\Pi) + e, \quad (1)$$

$$N_2(A^3\Sigma) + CO(X^1\Sigma^+, v\geq 6) \rightarrow CN(A^2\Pi); \quad (2)$$

2. Formation of $CN(B^2\Sigma^+)$:

$$CN(X^2\Sigma^+) + e \rightarrow CN(B^2\Sigma^+) + e; \quad (3)$$

3. Formation of $CN(X^2\Sigma^+)$:

$$CO(X^1\Sigma,) + N_2(A^3\Sigma^+, v\geq 2) \rightarrow CN(X^2\Sigma^+) + NO(X^2\Pi), \quad (4)$$

$$CN(A^2\Pi) \rightarrow CN(X^2\Sigma^+) + h\nu. \quad (5)$$

Rate constants $K_2 = 1\cdot10^{-11}$ cm^3/s and $K_4 = 2.6\cdot10^{-12}$ cm^3/s have been estimated in [6].

The main channels of $CN(X^2\Sigma)$ molecules decomposition in our conditions were diffusion and plasma chemical reactions:

$$CN(X^2\Sigma^+) + N \rightarrow C + N_2, \quad (6)$$

$$CN(X^2\Sigma^+) + O \rightarrow CO + N, \quad (7)$$

$$CN(X^2\Sigma^+) + O_2 \rightarrow \text{products}. \quad (8)$$

The excited states $A^2\Pi$ and $B^2\Sigma^+$ of the CN molecule were deactivated via radiative transitions and collisional quenching.

In CO-N_2-He mixtures concentration of oxygen (appeared in the discharge due to processes of dissociation of CO molecules) was very low and reactions (7) and (8) were not important, the dominant $CN(X^2\Sigma^+)$ decomposition process was reaction (6). In CO_2-N_2-He mixtures processes (7) and (8) must be taken into account.

Measured concentrations of $[CN(A^2\Pi)]$ and $[CN(B^2\Sigma^+)]$ in He-C0_2-N_2 mixtures in our experimental conditions were ~ 10^{10} / 10^{11} cm^{-3} and ~10^7/10^9 cm^{-3} respectively.

The measurements of CN ground-state density in the axial region of the discharge tube through absorption spectroscopy have been performed. The concentration of $[CN(X^2\Sigma^+]$ was estimated as ~ 10^{12}+10^{13} cm^{-3}. In He-C0_2-N_2 mixtures concentrations of CN molecules in the ground slate as well as in the exited states were much less (in 10/30 times) than in He-CO- N_2 mixtures.

Rotational temperatures of $CN(B^2\Sigma^+)$ - $T_r^{CN(B)}$ obtained from the shape of the violet bands in the axial region of the discharge tube was closed to the gas temperature (determined from the rotational spectrum of CO) - 150-250 K for liquid nitrogen cooling and 350-500 for water cooling, vibrational temperature - $T_V^{CN(B)}$ did not exceed 500-1000 K.

Spectra of violet system and red system of CN recorded in positions closed to the surface of the graphite cathode showed a number of peculiarities, in particularly, rotational and vibrational temperatures of $CN(B^2\Sigma^+)$ differed essentially from the temperatures in the axial

region of the discharge. Rotational and vibrational temperatures measured in this region were $T_r^{CN(B)}$ =1000÷3000 K, $T_v^{CN(B)}$=7000÷10000 K.

The behavior of CN($B^2\Sigma^+$) and CN($A^2\Pi$) concentrations in the cathode region differed essentially from ones in the axial region of the discharge tube. This phenomenon may be caused by heterogeneous processes. It is reasonable to suggest that near the cathode CN molecules are primarily formed in surface reactions between any nitrogen species and the graphite surface.

This study was partially supported under grant No. 07-02-01114a of Russian Foundation for Basic Research.

References

1. Grigorian G.M., Kochetov I.V., Dyatko N.A. New mechanism for the influence of Xe on the concentration of CO2 molecules in self-sustained CO-laser discharge // *Plasma Phys. Reports.* 2003. Vol. 29. No. 8. Pp. 709-714.

2. Grigorian G.M., Kochetov I.V. Balance of CO molecules in the plasma of a sealed-off CO laser // *Plasma Phys. Reports.* 2004. Vol. 30. No. 9. Pp. 788 -796.

3. Konev Yu.B., Kochetov I.V., Pevgov V.G., Sharkov V.F. // Preprint LAE-2821. Moscow, 1977 (in Russian).

4. Vainshtein L.A., Sobel'man 1.1., and Yukov E.A. Cross Sections for the Excitation of Atoms and Ions by Electrons. Moscow: Nauka, 1973. P. 141.

5. Knowles P.J., Werner H.J., Hay P.J., Cartwright D.C. The $A^2\Pi$-$X^2£^+$ red and B^2I^+-X^2I^+ violet systems of the CN radical: Accurate multireference configuration interaction calculations of the radiative transition probabilities // *J. Chem. Phys.* 1988. Vol. 89. Pp. 7334-7343.

6. Grigorian G.M., Ionikh Yu.Z. Proceedings of the 22nd Meetnig on the Spectroscopy. Zvenigorod. Part 1,2001. P.109.

INFORMATION SUPPORT OF MATHEMATICAL MODELING IN THERMOCHEMICAL NONEQUILIBRIUM GASES (FROM AVOGADRO DATABASES TO CATALOGUE OF MODELS)

A. SERGIEVSKAYA, S. LOSEV

Institute of Mechanics, M.V. Lomonosov Moscow State University, Moscow, Russia

Introduction

Knowledge of the mechanism and characteristics of various physical and chemical elementary processes in gases and plasmas is necessary for simulation of heat fluxes during hypersonic spacecraft flows in Earth, Mars and other planets atmosphere, high-power shock waves, laser technology, etc.

The traditional practice of preparing of the solution of a gas dynamics problem includes retrieval, analysis and accumulation of the thermodynamic data about components of medium, about dynamic and kinetic parameters of physical and chemical processes. It is known the thermodynamic information on medium components is matched enough and is authentic. But it is impossible any prior estimation of veracity and conformity of the data on process characteristics chosen from the different references or from various databases.

The information support of modeling is meant to provide a user with recommended data, formulas and relationships including specific numbers for coefficients and parameters. The set of the functional, information and graphic tools, intended for maintenance of versatile researches of models of elastic molecular collisions, vibrational energy exchange, thermal nonequilibrum reactions of dissociation, decay of polyatomic molecules and bimolecular reactions are accessible for user.

AVOGADRO databases

The main problem of modeling in physical and chemical gasdynamics is the values of coefficients in kinetics equations such as rate coefficients of processes.

The purpose of AVOGADRO Project at Moscow State University was to ensure information support for mathematical modeling of physical and chemical processes in gases and plasmas with recommended value of kinetics characteristics as the results of expert analysis of prominent carried out by Russian specialists. The works on creation, filling and commissioning of research information system of the Automated proVisiOn for Gas Dynamics with Recommendations using expert evaluation (AVOGADRO system) concerns to 1985 [1].

The basis of the system concept is the integration of information fund (data bases) with research software system. Such integration of information, logical and algorithmic funds develops into the scientific expert system which in addition to diagnostics and recommendations provides users with new possibilities: performance of computer experiments, investigation of substances and processes properties, as well as prediction of substances behavior under given conditions on the basis of data, logical relations, and algorithms included in the system. Such use of the system indicate that it is a great computer system, functionally adequate to the expert system supported with knowledge base.

The first appreciable results on a way of creation of AVOGADRO system were databases [2, 3]. AVOGADRO database holds recommended values of the coefficients of analytic models

for rate coefficients of physical and chemical processes for different ranges of K»N temperature with the indication of data uncertainty and expert comments. The only one data set, which was obtained as a result of expert review of all data set, is related to one process. This data set has attribute of degree of reliability, expert comment with recommendation on rules of use and restrictions. Recommended data have various level of recommendation.

Now reorganization of AVOGADRO databases for maintenance of an easy accesses to them from the Internet is carried out. For these purposes Web-interface is developed.

Base of mathematical models of physical and chemical processes

In the case when there is no information necessary to user in database, user is accorded the possibility to use the other part of AVOGADRO Project which is the base of models, and to carry out the calculation or to obtain an estimate for the values of probabilities, cross- section or rate coefficients for processes in question. The base of models consists of two sections: textual representation of models and collection of computational modules.

The textual representation of models base includes: expert judgment of each physical model, short indication of the modeling method, physical assumptions and restrictions, mathematical formulas and relations, description of coefficients and parameters, examples of model realization, adequacy and accuracy estimation of the model, comments and references. The base of models is attended with subject reviews and an expended presentation of expert substantiation and bibliography summary. The textual representation in the form of Handbook was published in Russian and English [4, 5].

More than 100 models of collision processes are accumulated in this base, including models for elastic collisions, models for rotational and vibrational energy exchange and chemical and plasmachemical reactions.

The collection of modules is a computer implementation of the models and is essentially the logical and algorithmic representation of physical models. The library of modules is intended to perform calculations of cross-sections for elastic and inelastic collisions, and probabilities, rate coefficients for energy exchange processes and reactions within the wide range of arguments, i.e. collision energy, gas temperature, etc., with the estimated accuracy. Computer version of the Handbook was realized on CD. It is distributed together with the book.

Application for examination of processes models for nonequilibrium flows

The absence of equilibrium between vibrational and translational degrees of freedom of molecules is the important of the present-day gasdynamics. Studies of chemical reactions in systems where various degrees of freedom are not equilibrated have started in the 60 s. Such

studies are still under way, because of great variety of nonequilibrium phenomena, because of difficulties in developing general quantitative models of nonequilibrium reactions, and because of practical applications. Arguably the most common type of nonequilibrium is that between translational and vibrational modes of molecular motion: it is present in high-altitude hypersonic flight and other shock flows, in fast expansion nozzle flows, in low-temperature electric discharges such as those used in lasers, etc.

The creation of the thermal nonequilibrium processes models collection is very urgent problem for modem chemical kinetics. The urgency is determined by absence of experimental data on nonequiiibrium rate coefficients and absence of enough the consistent and complete description of models of processes.

The Catalogue of recommended models of physical and chemical processes in thermally nonequiiibrium gas represents the association of the algorithms realizing these models [6]. Catalogue is self-sufficient tool, allowing to run through all stages of computational experiment, from data input to calculation results analysis. The Catalogue realised by Internet technologies. Advantages of location of the such application in the Internet are availability of actual, checked up by the expert, on a regular basis filled up information, use of the removed computing capacities and independence from the user hardware platform and operational system (http://chemphvs.edu.ru/kintvt).

The set of processes models included in Catalogue was composed the basis of previous KINTVT code [7]. Some models of elastic scattering and vibrational energy exchange are added because it is necessary for solving some gasdynamics problems. Classification of the processes included in the Catalogue of models is below submitted.

1.	**Chapter T**. Elastic collisions of neutral particles [X]+[Y] → X+Y
2.	**Chapter V.** Vibrational energy exchange
2.1.	VT models for transition 1→0 levels; process subclass VT
2.2.	Generalized models of VT-transitions
2.3.	Models of VV-transitions
3.	Chemical reactions
3.1.	**Chapter C.** Thermally equilibrium reactions in one-temperature description
3.2.	**Chapter CV**. Thermally nonequilibrium chemical reactions in two-temperature (T, T_v) description and three-temperature description
3.3.	**Chapter CL**. Thermally nonequilibrium chemical reactions in level description (T,m)

The Catalogue allows to carry out the independent all-round analysis of computing characteristics of each model. The user can investigate a range of applicability, a deviation of obtained results from author's estimations and available experimental data, accuracy of received values of criterion function, effectiveness of model in sense of volume of a required input data set, convenience to inclusion of model in applied gas dynamics task.

The main problem in modeling the two-temperature kinetics of dissociation and exchange reactions is obtaining rate coefficients as functions of T and T_v: $k(T, T_v)$. The better way to reveal the nonequilibrium nature of the reaction is to use a dimensionless nonequilibrium factor

$$Z(T,T_v) = k(T,T_v) / k^\circ(T).$$

Here $k^\circ(T)$ is the rate coefficient at $T_v=T$, commonly called the equilibrium rate constant. Perhaps the most important aspect in examining models of two-temperature dissociation is a possible compare various models on wide range of temperature with taking into account the restrictions of each model. The Catalogue allows carry out such experiment.

The graphic module of the Catalogue provides the exposition on one plot results of calculation $Z(T_v, T)$ on various models in a wide temperature range, especially at very high temperatures. Such temperatures are typical for hypersonic flight in the upper atmosphere (Fig.l). But not all model can calculate nonequilibrium factor for such temperature. And Catalogue show only possible calculation results. For example, Losev model (β-model) has restriction on temperature (T< 17000 K). It is demonstrated on this figure.

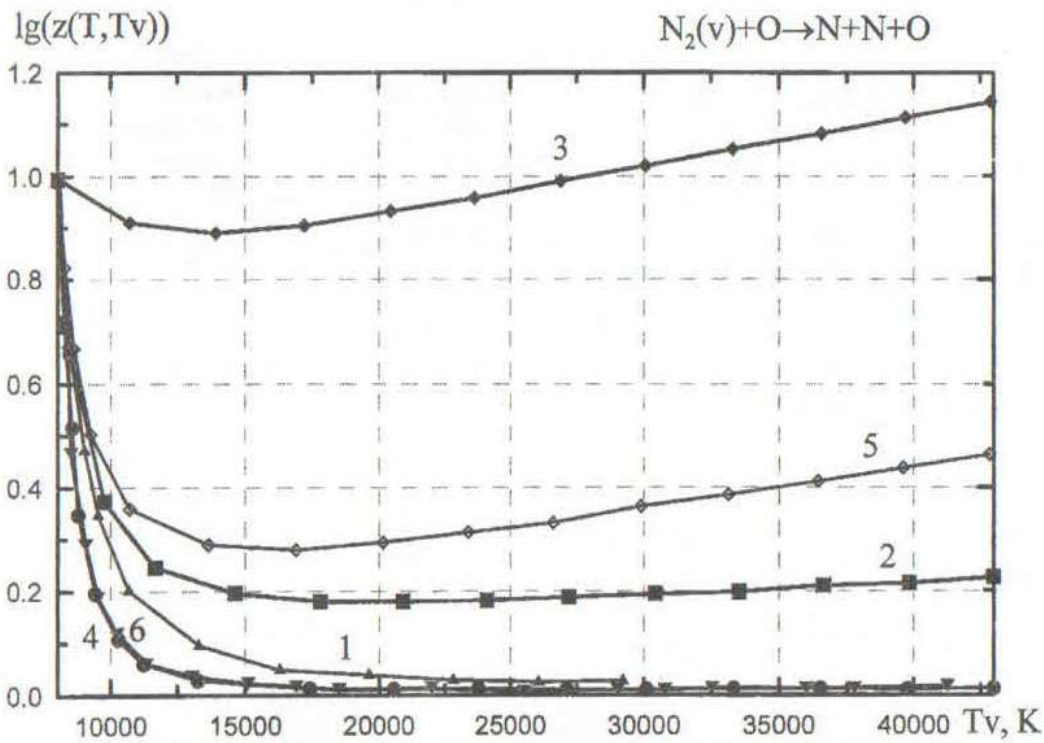

Fig. 1. Nonequilibrium factor for nitrogen dissociation calculated with different models: 1 – Kuznetsov model, 2 – adiabatic Smechov model, 3 – Park model, 4 – Marrone-Treanor model, 5 – Hammerling model, 6 – β-model (Losev model)

In the same figure the intuitive Park model which is very popularity among experts because of the simplicity and a minimality of requirements to a supply with information is shown also. Values of the nonequilibrium factor, calculated with different models, strongly differ at greater degrees of nonequilibrium, i.e. at appreciable deviations of ratio T_v/T.

The greatest interest here represents an opportunity of comparison of behaviour of the nonequilibrium factor in different conditions of modeling. At research of each empirical model with parameter in the Catalogue can vary not only ranges of gas or vibrational temperatures, but also value of empirical parameters of models.

Such various picture of behaviour of models helps the researcher to realize opportunities of these models and their real restrictions, and to be prepared for their modification by means of selection of parameters in comparison with more complex models.

There are following components of the Catalogue: tree of processes models, executable modules for realization of process models, the module for graphic representation of the calculated data, module for generation of reports .

The **tree of models** is the set of service programs which control the interfaces for a choice of model, selection the according information and a transfer of the data to calculating modules. The structure of the tree of models coincides with the qualifier structure.

Executable module select data from database and send the obtained results in a standard job output stream (STDOUT). Realization of executable modules is made in programming language C ++, with use only standard libraries that allows to compile and execute them under the control of various operational systems. Module for generation of reports allow generate the reports in ASCII, HTML and PDF formats.

Conclusion

The modern information support of modeling of physical and chemical processes is favorable to solve the applied gasdynamics problems with most effectiveness. The method of investigation is mathematical and information modeling of physical and chemical processes which is built on integration of base of mathematical models and databases on relevant information with special software system. These computer systems was realized at Moscow State University for purposes of examination of models for diverse, often unattainable in the laboratory, conditions and selection the most suitable for practical problems.

Acknowledgments

Authors would like to acknowledge helpful discussion and computer experiments to E.A. Kovach, E.G. Kolesnichenko.

References

1. Kovach E.A., Kotlarova., Losev S.A. at al. Creation System and Information Support for AVOGADRO System. In Informatika v physico-chemicheskoi gasodynamike. Moscow: Moscow Univ. Publish., 1992. Pp. 55-64.

2. Kovach E.A., Losev S.A., Sergievskaya A.L. Experience of Building of Information System for Scientific Investigations in Gas Dynamic // *Doklady Ros. Akad. Nauk, Metals,* 1993, No. 4.

3. Kovach E.A., Sergievskaya A.L. Realisation of "PROCESS" database // Report of Institute of Mechanics, Moscow State University, 1991, N4120.

4. Physical and Chemical Processes in Gas Dynamics: Computerized Handbook / Ed. by G.G. Chernyi and S.A. Losev. Vol. 1. Physical and Chemical Processes in Dynamics. Moscow Univ. Press. Moscow, 1995 (In Russian).

5. Physical and Chemical Processes in Gas Dynamics: Cross Sections and Rate Constants for Physical and Chemical Processes. Vol. I / Ed. by G.G. Chernyi, S.A. Losev, S.O. Macheret, and B.V. Potapkin. Progress in Astronautics and Aeronautics. 2002. Vol. 196.

6. Sergievskaya A.L., Kovach E.A., Spichkov A.B., Sergievsky N.I. Creation of scientific environment for modeling of physical and chemical processes based on Internet technologies // XXXII Conf. "New Inform. Technologies for Sciene, Education and Economy", Ukraina, Krimea, October 1-10. 2005. Open Education, No. 10. Appendix, 2005. Pp. 91-93.

7. Kovach E.A.,Losev S.A., and Sergievskaya A.L. Two-Temperature Kinetic Miodels for Dissociation of Molecules in Strong Shock Waves // *Chem. Phys. Repts.* 1995. Vol. 14(9). Pp.1353-1387.

KINETIC MODELING OF ELECTRONIC-VIBRATIONAL COUPLING IN THE OXYGEN REACTIVE FLOW

B.I. LOUKHOVITSKI[1], S.A. LOSEV[2], A.M. STARIK [1]

[1]P. I. Baranov Central Institute of Aviation Motors, Scientific Research Center "Raduga", Russia, star@ciam.ru

[2]Institute of Mechanics, M.V. Lomonosov Moscow State University, Moscow, Russia

Introduction

During last years the state-to-state vibrational chemical kinetics has been extensively studied for the high temperature gas behind shock waves and in the expanding nozzle flows [1-5]. However, in the variable nonequilibrium phenomena, besides vibrational-chemistry coupling, there observed strong interaction between vibrational and electronic energy exchange. Recent experimental and theoretical studies of the nonequilibrium kinetics of O_2 molecules at the atmospheric conditions [6-8], in the electrical discharge [9-11], and at the laser- or plasma-induced combustion [12, 13] exhibit a strong coupling between the vibrational relaxation, electronic kinetics, and chemical reactions.

This paper is focused on the analysis of nonequilibrium processes in the molecular oxygen reactive flow and on the role of vibrational-electronic coupling in the evolution of species concentrations and flow parameters behind the strong shock wave. The analysis was made using two different thermally nonequilibrium kinetic models: model of vibrational temperatures and state-to-state kinetics for chemically reacting gas.

Model description

Let us assume that translational and rotational degrees of freedom of molecules are in a thermodynamic equilibrium with corresponding Maxvell-Boltzmann energy distribution.

For O_2 dissociating gas, the following species were involved in the kinetic model: $O_2(X^3\Sigma_g^-,V)$, $O_2(a^1\Delta_g,V)$, $O_2(b^1\Sigma_g^+,V)$, $O(^3P)$, $O(^1D)$, $O_3(^1A_1)$. For oxygen molecules, the vibrational level kinetics took into account 41 vibrational levels for the O_2 molecule in the ground electronic state $X^3\Sigma_g^-$, 37 vibrational levels for the $a^1\Delta_g$ electronic state, and 32 vibrational levels for the $b^1\Sigma_g^+$ electronic state. The vibrations of O_3 molecule were modeled by three harmonic oscillators with corresponding frequencies ν_1, ν_2 and ν_3 (symmetric, deformation, and asymmetric modes, respectively). The energy of vibrational levels for $O_2(X^3\Sigma_g^-)$, $O_2(a^1\Delta_g)$, and $O_2(b^1\Sigma_g^+)$ molecules were estimated using the polynomial dependencies which approximate with high accuracy the data reported in [14, 15].

The kinetic model involves the processes of intramode and intermode vibrational-vibrational (*V-V)* exchange, vibrational-translational *(V-T)* relaxation, electronic-electronic (E-E) exchange, electronic-translational (E-T) relaxation, and reversible chemical reactions with excited and non-excited atoms and molecules. The rate constants for these processes were taken mostly in according to the recommendations [16-21].

The model used for calculations of the fluid dynamics is based on the one-dimensional steady-state Euler equations for reactive thermally nonequilibrium gas and may be writhen in following form

$$\frac{d(\rho u)}{dx}=0,\ u\frac{du}{dx}+\frac{1}{\rho}\frac{dP}{dx}=0,\ \frac{dH}{dx}+\sum_{i=1}^{M}\frac{de_v^i}{dx}+u\frac{du}{dx}=0,$$

$$u\frac{d\varepsilon_\xi}{dx}=q_\xi^{VT}+q_\xi^{VV'}+q_\xi^{ch},$$

$$u\frac{dN_i}{dx}=Q_i^{ch},\ i=1,2,6,\ \ u\frac{dN_{e,V}}{dt}=Q_{e,V}^{VT}+Q_{e,V}^{VV}+Q_{e,V}^{VV'}+Q_{e,V}^{ET}+Q_{e,V}^{EE}+Q_{e,V}^{ch},$$

$$e_v^i=\begin{cases}0,\ i=1..2\\ \dfrac{R}{\mu N}\sum_V E_{e,V}N_{e,V},\ i=3..5, e=i-2,\\ \gamma_i\dfrac{R}{\mu}\sum_{\xi=1}^{3}\Theta_\xi\varepsilon_\xi,\ i=6,\end{cases}$$

$$\varepsilon_\xi=\frac{g_\xi y_\xi}{1-y_\xi},\ y_\xi=\exp\left(-\frac{\Theta_\xi}{T_\xi}\right),\ H=\frac{1}{\mu}\sum_{i=1}^{M}h_{0i}\gamma_i+\left(\frac{5}{2}+C_R\right)\frac{R}{\mu}T,$$

$$\mu=\sum_{i=1}^{M}\mu_i\gamma_i,\ C_R=\sum_{i=1}^{L}\gamma_i+\frac{3}{2}\sum_{i=L+1}^{S}\gamma_i\ \ \gamma_i=\frac{N_i}{N},\ N_{i=e+2}=\sum_{V=0}^{V^{max}}N_{e,V},\ N=\frac{P}{kT}.$$

Ierein ρ, P, T, and u are

Herein ρ, P, T, and u are, respectively, the density, pressure, translational temperature, and velocity of the gas; N_i is the number density of molecules of the ith sort ($i = 1, 2, 3, 4, 5, 6$ are related to the following mixture components $O(^3P)$, $O(^1D)$, $O_2(X^3\Sigma_g^-)$, $O_2(a^1\Delta_g)$, $O_2(b^1\Sigma_g^+)$, O_3); M is the number of molecular and atomic components in the mixture; $N_{e,V}$ is the number density of O_2 molecules in the electronic state e ($e = X^3\Sigma_g^-, a^1\Delta_g, b^1\Sigma_g^+$) with the vibrational quantum number V; $E_{e,V}$ is the vibrational energy of oxygen molecule in this state; Θ_ξ, T_ξ, and g_ξ are the characteristic temperature, local vibrational temperature, and degeneracy multiplicity of ξth mode of ozone molecule, respectively; h_{0i} and μ_i are the enthalpy of formation at $T = 298$ K and molar mass of the ith component; L is the number of components consisting of linear molecules; S is the total number of molecular components; R is the universal gas constant; k is the Boltzmann constant.

The terms q_ξ^{VT}, $q_\xi^{VV'}$, and q_ξ^{ch} specify the rate of the gain or loss of the vibrational quanta by ξ mode of O_3 molecule due to V–T relaxation, intermode V–V' exchange, and via formation (or destruction) of O_3 molecule in the course of chemical reactions. The terms Q_{eV}^{VT}, Q_{eV}^{VV}, $Q_{eV}^{VV'}$, Q_{eV}^{ET}, Q_{eV}^{EE}, Q_{eV}^{ch} denote, respectively, the intensity of sources of electronically and vibrationally excited O_2 molecules in the electronic state e with vibrational quantum number V due to V–T relaxation, intramode V–V exchange, intermode V–V' exchange, electronic-translational E–T relaxation, electronic-electronic E–E exchange, and via chemical reactions.

Results and discussion

The developed model makes it possible to describe the thermally nonequilibrium processes behind the strong shock wave, upon the laser induced excitation of vibrational and electronic states of 0_2 molecules and at the initiation of combustion in O_3-O_2 mixture due to vibrational excitation of O_3 molecules by resonance laser radiation. Sure, any novel extended kinetic model should be validated against a number of experimental data obtained for thermally nonequilibrium conditions. Such experiments have been conducted by different research groups for past years [6, 7, 22].

The novel precise measurements of the variation of vibrational temperature behind the iiu ident shock wave propagating in the pure molecular oxygen was reported recently in [22]. Fig. 1 shows the predicted and measured temporal evolution of translational and vibrational temperature of molecules in the post shock region. The vibrational temperature in [22] was determined using the comparison of the measured and calculated absorption coefficient for Shuman-Runge bands. As is seen there observe two typical modes in the behavior of gas temperature. A strong decrease of Γ value at the first stage is due to excitation of vibrations of O_2 molecules caused by the fast V-T exchange (the mode of the developed vibrational- translational exchange). At the final stage of this mode the vibrational temperature $O_2(X^3\Sigma_g)$ molecules is equilibrated with translational temperature, i.e. $T_v(O_2(X^3\Sigma_g^-)) = T$. The second mode that follows just after this time instant is associated generally with the stage of chemical

transformation. The gas temperature drops at this stage mostly due to O_2 molecule dissociation. At parameters considered, the total decrease of T value achieves 2100 K, and the time duration of these modes is approximately 600 ps. It is worth to note that the model makes it possible to describe properly both this modes and prediction using this model is consistent quite well with experiment.

It should be noted, the state-to-state thermally nonequilibrium kinetic model predicts the much faster appearance of oxygen atoms and O_3 molecules downstream the shock front as compared to the predictions of the model using the mode approximation for molecular vibrations. It is clearly seen from the plots of $\gamma_i(x)$ shown in Fig. 2. for theses two cases.

Nevertheless, both the state-to-state kinetic model and the model using the mode approximation predict the same evolution of gasdynamic parameters (temperature, pressure, gas density, and velocity) downstream the shock front (see Fig 1.)

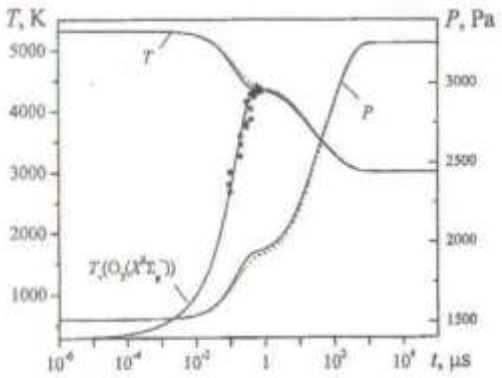

Fig. 1. Variation of the translational temperature, vibrational temperature of the $O_2(X^3\Sigma_g^-)$ molecules and pressure behind the incident shock wave front versus time at P_0 = 2 torr and shock wave velocity of 3.07 km/s. Points present the experimental data [22], solid and dotted lines depict the predicted temporal profile $T(t)$ and $T_v(O_2(X^3\Sigma_g^-))(t)$ using the state-to-state and mode kinetics

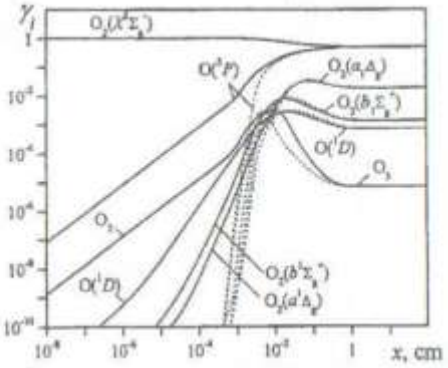

Fig. 2. Variation of species mole fractions versus the distance from the incident shock wave front at T_0 = 300 K, $P_0 = 10^3$ Pa, and M_0 = 13. Solid lines are predictions using the state-to-state model, and dotted lines are predictions using the mode approximation

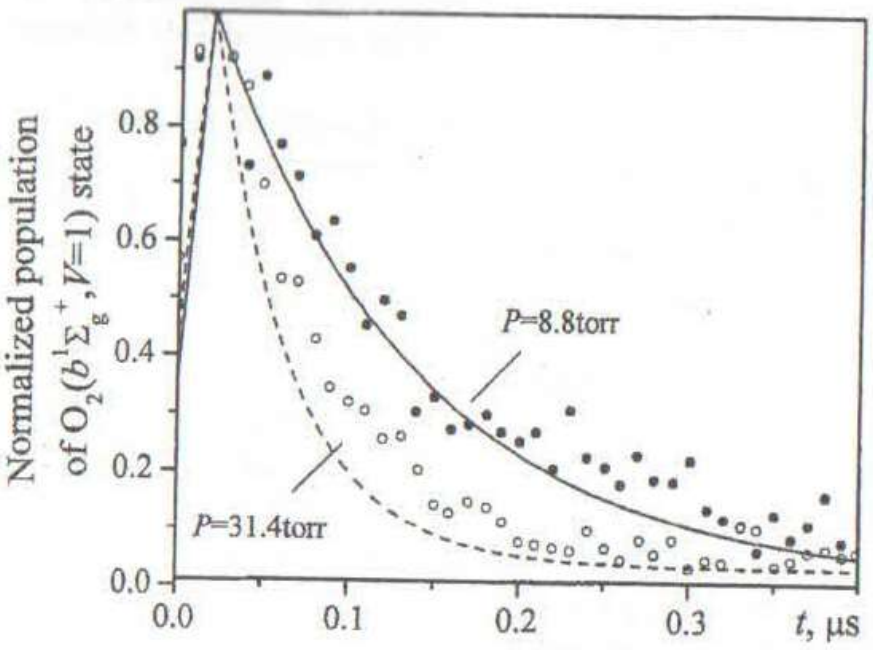

Fig. 3. Normalized population of $O_2(b^1\Sigma_g^+, V=1)$ state as a function of the delay time between laser pulses at 580 K for pressures of 31.4 and 8.8 torr. Points are experimental data [7]; lines are the calculations of the present work

One can conclude that in order to estimate the evolution of the macroscopic flow parameters in the post shock front region: temperature, pressure, density, Mach number it is sufficient to use the thermally nonequilibrium chemical kinetic model with mode approximation, however, to calculate the spatial profiles of species concentrations at the early stage of 0_2 molecule dissociation it is need to use the model based on the state- to-state kinetics.

It is worth noting that the developed state-to-state kinetic model makes it possible to predict properly the temporal relaxation of the

population of the $O_2(b^1\Sigma_g^+, V=1)$ state measured by Pejakovic et al. in [7]. In that study the collisional removal of $O_2(b^1\Sigma_g^+, V=1)$ by O_2 was investigated at low temperature using a two laser technique, in which the visible output of the first laser directly excites ground-state oxygen molecules to the $V=1$ level of the $b^1\Sigma_g^+$ state and the ultraviolet output of the second laser probes the $O_2(b^1\Sigma_g^+, V=1)$ population by resonantly enhanced multiphoton ionization via the $V=4$ level of the $d^1\Pi_g$ Rydberg state. Fig. 3 shows the comparison of the temporal evolution of the predicted and detected evolution of the normalized population of $O_2(b^1\Sigma_g^+, V=1)$ state between two laser pulses. The population of excited state of molecular oxygen in experiment was about 0.1%. In numerical calculations the laser intensity was chosen in that way to provide the same value of $O_2(b^1\Sigma_g^+, V=1)$ concentration as that in the experiment. The simulation reveals that the main process affecting the deactivation of $O_2(b^1\Sigma_g^+, V=1)$ state is E–E exchange $O_2(b^1\Sigma_g^+, V=1)+O_2(X^3\Sigma_g^-, V=0) \rightarrow O_2(b^1\Sigma_g^+, V=0)+O_2(X^3\Sigma_g^-, V=1)$.

Conclusions

The detailed thermally nonequilibrium state-to-state kinetic model for $O(^3P) - O(^1D) - O_2(X^3\Sigma_g^-) - O_2(a^1\Delta_g) - O_2(b^1\Sigma_g^+) - O_3$ atomic-molecular system was build. The model involves the processes of *V-T* relaxation, *V-V* and *V-V'* exchange, *E-T* relaxation, E-E exchange, and chemical reactions The model was validated against recently published experimental data on the variation of vibrational temperature behind the strong shock wave and the temporal profile of the normalized population of $O_2(b^1\Sigma_g^+, V=1)$ state.

The modeling of the dissociation of oxygen molecule behind the shock wave front was conducted using two different thermally nonequilibrium kinetic models: model of vibrational temperatures and state-to-state model for chemically reacting gas. Calculations demonstrated that in order to predict properly the spatial profiles of the species concentrations downstream the shock front it is needed to use the state-to-state kinetic model taking into account the excitation of vibrations of O_2 molecule both in the ground electronic state $X^3\Sigma_g^-$ and in the low exeitcd electronic states $a^1\Delta_g$ and $b^1\Sigma_g^+$. However, in order to predict the evolution of macroscopic parameters downstream the shock front it is sufficient to use the simpler model of vibrational temperatures at the conditions considered.

Acknowledgements

This work was supported by Russian Foundation for Basic Research (grants 08-01-1)0808 and 08-08-0765).

References

1. Esposito F., Capitelli M., and Corse C. // *Chem. Phys.* 2000. Vol. 257. Pp. 193-202.

2. Kustova E.V. and Chikhaoni A. // *Chem. Phys.* 2000. Vol. 255. Pp. 59-71.

3. *Y* TranorC.E., Adamovich I.V., Williams M.J., and Rich J.W. // *J. Thermophys. Heat Transfer.* 1998. Vol. 10. No. 2. Pp. 193-199.

4. Kustova E.V., Aliant A. and Chikhaoni A. // *Chem. Phys.* 2001. Vol. 76. Pp. 638-646.

5. Colonna G. and Capitelli M. *// J. Phys. D.: Appl. Phys.* 2001. Vol. 34. Pp. 1812-1818.

6. Slanger T.G. and Copeland R.A. *// Chem. Rev.* 2003. Vol. 103. Pp. 4731-4765.

7. Pcjakovic D.A., WoutersE.R., Phillips K.E. et al. // *J. Geophys. Res.* 2007. Vol. 110. A03308.

8. Pejakoviz D.A., Copeland R.A., Cosby Ph.C., and Slanger T.G. // *J. Geophys. Res.* 2007. Vol. 112. A10307.

9. Stafford S.D. and Kushner M.J. *// J. Appl. Phys.* 2004, Vol. 96. Pp. 2451-2465.

10. lonin A.A., Kochetov I.V., Napartovich A.P., and Yuryshev N.N. // *J. Phys. D.: Appl. Phys.* 2007. Vol. 40. Pp. 25-61.

11. Gordiets B.F., Ferreira C.M., Guerra V.L. et al. *// IEEE Transactions on plasma science.* 1995. Vol. 23. Pp. 750-768.

12. Starik A.M. and Lukhovitski. B.I. *// Doklady Physics.* 2005. Vol. 50. No. 5. Pp. 252-257.

13. Starik A.M., Lukhovitski B.I., NaumovV.V., and TitovaN.S. *// Techn. Phys.* 2007. Vol. 52, No. 10. Pp. 1281-1290.

14. Slanger T.G. and Cosby P.C. *// J. Phys. Chem.* 1988. Vol. 92. No. 2. Pp. 267-282.

15. Dayou F., Hernandez M.I., Campos-Martinez J. and Hernandez-Lamoneda R. // *J. Chem. Phys.* 2007. Vol. 126. Pp. 194309-194321.

16. Adamovich I.V., Macheret S.O., Rich W.J., and TreanorC.E. // *J. Thermophys. Heat Transfer.* 1998. Vol. 12. No. 1. Pp. 57-65.

17. Stafford D.S. and Kushner M.J. *// J. Appl. Phys.* 2004. Vol. 96, No. 5. Pp. 2451-2465.

18. *Kulagin Yu.A., Shelepin L.A., and Yargina V.I. //* Transactions of the P.N. Lebedev Physical Institute of the Russian Academy of Sciences. *1994. Vol. 228. Pp. 166-227.*

19. Atkinson R., Baulch D.L., Cox R.A. et al. // *J. Phys. Chem. Ref. Data.* (Suppl. 4.) 1992. Vol. 21. No. 6. Pp. 1125-1568.

20. Starik A.M. and Titova N. S. *// Kinetics and Catalysis.* 2003. Vol. 44. No. 1. Pp. 28-39.

21. Yankovsky V.A. and Manuilova R. O. *// Ann. Geophys.* 2006. Vol. 24. Pp. 2823-2839.

22. Ibraguimova L.B., BykovaN.G., Zabelinskii I.E. et al. // West-East High Speed Flow Field Conference. Moscow, 2007. (CD).

2. NONEQUILIBRIUM PROCESSES IN PLASMA

REPETITIVELY PULSED NONEQUILIBRIUM PLASMAS FOR PLASMA ASSISTED COMBUSTION, FLOW CONTROL, AND MOLECULAR LASERS

I.V. ADAMOVICH, W.R. LEMPERT, J.W. RICH

Dept. of Mechanical Engineering, The Ohio State University, Columbus, OH 43210, USA

The lecture discusses results of recent experimental studies of high voltage (15-20 kV), short pulse duration (20-30 ns), high repetition rate (up to 50 kHz) discharge plasmas for engineering applications. High reduced electric field during the pulse (E/N-500- 1000 Td) allows efficient ionization and molecular dissociation. Between the pulses, additional energy can be coupled to the decaying plasma using a DC field set below the breakdown threshold. While the DC sustainer discharge adds 90-95 % of all the power to the flow, it does not produce any additional ionization. The pulser and the sustainer discharges are fully overlapped in space. Low duty cycle of the pulsed ionizer, -1/1000, greatly improves plasma stability and allows sustaining diffuse and uniform pulser-sustainer plasmas at high pressures and power loadings.

The first experiment is using the pulsed discharge for ignition of premixed hydrocarbon-air flows. In this case, the sustainer discharge was not used. In the experiments, two different operation regimes have been identified, (i) oxidation, with relatively low fuel fractions oxidized in the absence of visible flame, and (ii) ignition, with large fuel fraction burned, large amounts of CO and CO_2 generated, and flame detected in the reactor. Ignition occurred at air flow temperatures as low as 300 °C (before adding fuel). In both regimes, significant plasma temperature rise is detected in air-fuel flows, up to $\Delta T = 300$ °C. Comparing these results with temperatures and dissociated fuel fractions in nitrogen-fuel flows demonstrates that the temperature rise in air-fuel flows is due to exothermic plasma chemical fuel oxidation process, which results in ignition when the flow temperature approaches autoignition temperature. This conclusion was confirmed by kinetic modeling calculations, which also demonstrated that ignition delay time is significantly reduced by the presence of radicals in the flow. The kinetic model has been validated using time-resolved measurements of O atom concentration in single-pulse nanosecond discharges in air, methane-air, and ethylene-air mixtires. Calculations showed that the model correctly predicts oxidized fuel fractions and resultant temperature rise in the plasma in the oxidation regime but significantly overpredicts bumed fuel fractions in the ignition regime. Transition from the oxidation to the ignition regime predicted by the model is consistent with the experiment.

The second experiment using the pulser-sustainer discharge is Lorentz force acceleration of externally ionized, low-temperature (T-100 K), supersonic flows. In this case, the pulsed discharge was used to generate electrical conductivity in M = 4 nitrogen flows, while the DC sustainer discharge produced transverse (Faraday) current in the presence of transverse magnetic field of B = 1.5 T. Accelerating or retarding Lorentz force was generated by changing DC field and/or magnet polarity. MHD effect on the supesonic flow was detected from the static pressure measurements. Retarding Lorentz force applied to the flow produced a static pressure increase of up to 20 %, while accelerating force of the same magnitude resulted in static pressure rise of up to 10 %, i.e. a factor of two smaller. The fraction of the discharge power going into Joule heat inferred from these experiments is low, -0.1-0.2, because most of the input discharge power remains frozen in the vibrational energy mode of nitrogen. The measured static pressure changes are in good agreement both with quasi-l-D MUD flow model and with a 3-D compressible Navier-Stokes MHD flow code. The results show that the retarding Lorentz force increases the static pressure rise produced by Joule heating alone, while the accelerating Lorentz force reduces it. This result provides first direct evidence of cold supersonic flow acceleration by Lorentz force.

The third experiment is singlet oxygen generation in a high-pressure pulser-sustainer discharge. The key advantage of this approach is the ability to independelty vary E/N of the sustainer discharge, to maximize the sustainer energy input into electron impact excitation of $O_2(a^1\Delta)$. The results demonstrate operation of a stable and diffuse crossed discharge in O_2-He mixtures at P = 60-120 torr, T = 330-430 K, m = 1.5-3.0 g/s, discharge powers of up to 1.6- 2.2 kW, and E/N = 6-12 Td. $O_2(a^1\Delta)$ yield at these conditions, up to 6 %, was inferred from the integrated intensity of $O_2(a^1\Delta \rightarrow X^3\Sigma)$ infrared emission spectra calibrated using a blackbody source. Static pressure and temperature measurements in the supersonic laser cavity located downstream of the discharge section show that a steady-state M = 3 flow in the cavity, at temperatures of T= 100-110 K, can be sustained for up to -10 seconds. At these How conditions, the measured $O_2(a^1\Delta)$ yield considerably exceeds the laser threshold yield. This makes possible achieving positive gain and lasing in the transverse laser cavity. The highest gain and laser power measured so far are 0.08 %/cm and 1.5 W.

MODELING OF PLASMA-ASSISTED CONVERSION OF LIQUID ETHANOL INTO HYDROGEN ENRICHED SYNGAS IN THE NONEQUILIBRIUM ELECTRIC DISCHARGE PLASMA-LIQUID SYSTEM

D.S. LEVKO[1], A.I. SHCHEDRIN[1], V.V. NAUMOV[1,2], V.YA. CHERNYAK[3], V.V. YUKHYMENKO[3],1.V. PRYSIAZHNEVYCH[3], S.V. OLSZEWSKI[3]

[1]Institute of Physics, Ukrainian Academy of Sciences, Kiev, Ukraine,
ashched@iop.kiev.ua

[2]Institute of Fundamental Problems for High Technology, Kiev, Ukraine,
naumov@ifpht.kiev.ua

[3]Radiophysical Faculty, Kiev National T. Shevchenko University, Kiev, Ukraine,
chern@univ.kiev.ua

Introduction

Today, there is a great interest in biofuels as an alternative to traditional fossil fuels and natural gas. Bio-ethanol can be a good candidate since it can be obtained in sufficient amounts from agricultural biomass. However, pure ethanol (ethyl alcohol C2H5OH) has a set of physicochemical limitations including a relatively low heat of combustion and low speed of ignition. One possible way is to use plasma-chemical conversion of ethanol into hydrogen-enriched synthesis gas (syngas) improving fuel combustibility and reducing pollution exhaust. There are various methods of plasma fuel conversion using thermal and non-thermal plasma. Thermal plasma, which is thermodynamically equilibrium, has characteristics of high ionization and higher energetic density that has merits of fast decomposition but demerits of poor selectivity of chemical transformations and high expenditure of power (> 1 kW). Nonthermal plasma, which is kinetically non-equilibrium, has characteristics of low ionization but benefits of high reactivity and selectivity of transformations, providing high enough productivity at relatively low power consumption (< 1 kW) that can be obtained by a high voltage discharging in a flow at atmospheric pressure. Applying non-thermal plasma, different electric discharge techniques were used e.g. corona, spark, MW, RF, DBD, gliding arc and various hybrids. In fact, all systems have their merits and demerits depending on the use [1]. Among possible types, one specific case is of our current research interest in Kiev [2-6]. It is a dynamic plasma-liquid system (PLS) using nonequilibrium plasma of the electric discharge in a gas channel with liquid wall (DGCLW). It can provide simultaneously a high level of nonequilibrium and high density of reacting species. Its main features are: (i) well-developed plasma-liquid interface and large surface-to-volume ratio; (ii) wide possibilities of control of plasma-created gas- and liquid-phase components during the processing; (iii) possibility to work in the cw regime using both dc and ac modes. The main idea is that the DGCLW can be burning within liquid fuel without preliminary gasification. In this work we report recent results of our experimental and theoretical studies related to plasma conversion of ethanol into syngas in the DGCLW PLS using available diagnostics and numerical modeling.

Experiments and modeling

Experiments were done in the PLS reactor of the DGCLW type [5] using atmospheric air injected in the ethanol-water solution in the gap between the electrodes, so the discharge was burned in the gaseous cavity in the mixture of air and ethanol-water vapors. Fig. 1 shows a schematic of the DGCLW for two different schemes of electrodes: (a) solid electrode + liquid under positive (+) or negative (-) potential, and (b) two solid electrodes (coaxial cooper rods) immersed in liquid when a gas channel formed by the counter-flow air streams between the electrodes. In all cases the discharge worked in the continuous regime powered by the high voltage dc supply. Fig. 2 shows typical current-voltage characteristics of the DGCLW in the ethanol-water solution 5:1 for three different modes: (1) solid electrode + liquid cathode, (2) solid electrode + liquid anode, and (3) two solid electrodes. The dropping character of *I-V* curves at currents from 50 to 300 mA indicates the transition regime from the abnormal glow to the arc discharge. The enhanced voltage up to 3.5 kV in case of liquid electrodes is aassociated with the additional potential drop across a liquid and weaker secondary ion- electron emission as compared to metal electrodes.

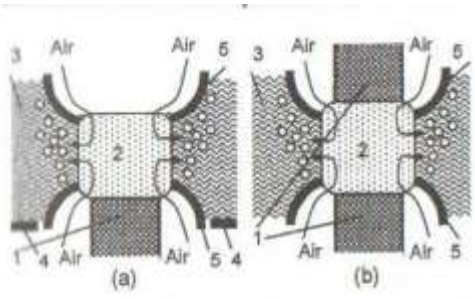

Fig. 1. Basic schemes of the DGCLW: 1 – copper rod electrodes, 2 – discharge plasma, 3 – liquid ethanol, 4 – metallic flange, 5 – quarts tubes

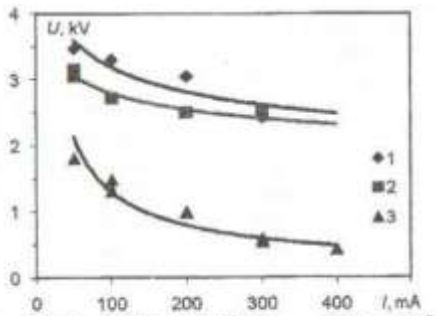

Fig. 2. Current-voltage curves of DGCLW: 1 – liquid cathode; 2 – liquid anode; 3 – two solid electrodes. $C_2H_5OH:H_2O = 5:1$

In experiments, the gap between electrodes, discharge currents, air flow rates, ethanol-water mixing ratios and processing time were varied to optimize the process. In nominal regimes, the discharge power did not exceed 100-300 W. The temperature of the work solution in the reactor was measured by the immersed thermocouple. It was found that the time of the temperature stabilization depended on the composition of the solution: in case of pure ethanol it needs 1-1.5 min, in case of pure water in needs 6-8 min.

The plasma conditions in the discharge during the processing were diagnosed by optical emission spectroscopy [5] using a high-speed CCD-based UV-NIR diffraction spectrometer Solar SL40-3648. The measurements have shown that the DGCLW spectra are multi-

component and contains molecular bands of OH UV-system ($A^2\Sigma^+$-$X^2\Pi$: (0-0) 306.4-308.9 nm), N_2 2^+-system ($C^3\Pi_u$-$B^3\Pi_g$: (0-0) 337.1, (0-1) 357.7, (0-2) 380.5, (1-4) 399.8 nm), CN ($B^2\Sigma^+$-$X^2\Sigma^+$: (0-0) 388.3 nm), C_2 Swan band ($d^3\Pi_g$-$a^3\Pi_u$: (0-0) 516.5 nm, (1-1) 512.9 nm, etc); and atomic lines of HI (656.3, 486.1 nm), OI (777.1, 844.6, 926.6 nm), and CuI (324.7, 327.4, 465.1, 510.5, 515.3, 521.8 nm) which identify a nonequilibrium nature of the DGCLW plasma. The H Balmer series emission indicates the vaporization and dissociation of ethanol and water molecules and production of hydrogen, the C_2 emission relates to the carbon formation, the N_2 and CN emissions relate to the dissociating air. The OES simulations of selected spectral lines (Cu, O, H) and bands (N_2, OH, CN) give the character electronic and vibrational temperatures in the range of 0.5 eV (T_e) and 0.35 eV (T_v).

The component content of the output synthesis gas products after the processing was analyzed by mass-spectrometry using a monopole mass-spectrometer MX 7301 and by gas chromatography using a gas chromatograph 6890 N Agilent [5]. The measurements have shown that gas-chromatography and mass-spectrometry data correlate well, and that H_2 and CO are the main components of synthesis gas produced from ethanol in the DGCLW. The fractional amount of H_2 and CO in the syngas reaches -87-89 % that is many times higher than for all hydrocarbons including CH_4, C_2H_2, C_2H_4, and C_2H_6 (the total syngas amount in the output gas products is about 30 % by volume). With increasing discharge power and with water dilution, the H_2 yield slightly increases whereas the O_2 content slightly decreases, and the N_2 content changes non-monotonically. The maximal yield of H_2 is revealed if ethanol and water in the mixture are in equal amounts.

Numerical modeling of the process in the DGCLW PLS was made using the system of kinetic equations for kinetically valuable components in air-ethanol-water vapor plasma and the Boltzmann electron energy distribution function similarly to the fluid (volume averaged) model used in [6, 7]. In the model statement it is supposed that (i) discharge is burning in the cavity with a radius that equals to the radius of the electrode tubes and with a length that equals to the gap between the electrodes; (ii) electric field in the discharge does not vary in space and time; (iii) after the pass of the gas through the discharge into the liquid its content in the discharge is totally refreshed and its flow rate in the reactor is the same as in the discharge. In calculations, the complete time of the discharge operation is divided into the equal time intervals which duration is determined by the cavity filling time. In the given case, this time is determined only by the time of the gas flowing that equals to the ratio of the cavity volume to the gas flow rate. This allows doing plasma-chemical calculations in the discharge during the one time interval only as the concentrations of components in the every time interval come to the same values, and the previous periods did not influence on the subsequent periods. According to the model, reactive plasma is characterized by two temperatures: the electron temperature T_e is determined by the applied electric field E/N and calculated EEDF; the gas temperature T is determined by the temperature conditions of surrounding gas-liquid medium. The full kinetic mechanism

includes 65 species (C_2H_5OH, H_20, N_2, 0_2, H_2, CO, $C0_2$, etc.), 76 electron-impact processes, and 364 chemical reactions (details are available at http://wvvw.iop.kiev.ua/~pla5macherngroup).

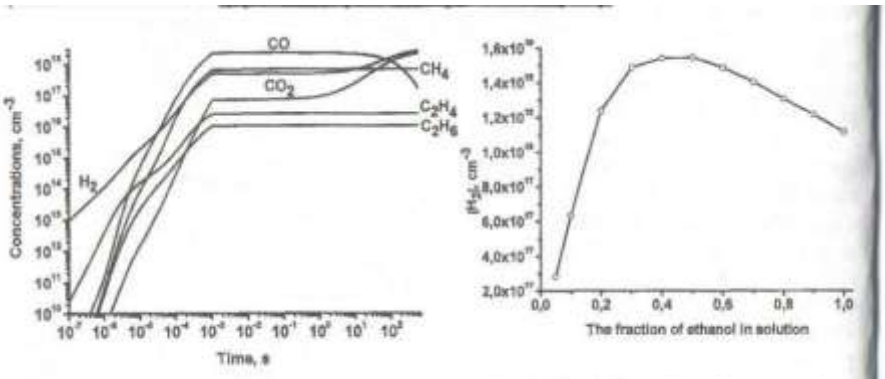

Fig. 3. Formation of synthesis gas components

Fig. 4. H_2 yield vs. ethanol-water ratio

Fig. 3 shows results of modeling of dynamics of formation of basic components of synthesis gas during the processing of ethanol in the DGCLW PLS (calculated for C_2H_50H:H_20= 1:1, 1 = 200 mA, G = 55cm^3/s, 7=323 K). It is seen that during the discharge time up to ~$10'^3$s, the concentrations of H_2, CO and other species steeply grow with the residence time. Outside the discharge, during the time period from 10^{-3} to -10 s (the time of the gas output from the reactor) they have no dramatic changes. The final transformation of CO and CO_2 at the end of the process is related to the water-gas shift (WGS) reaction

$$H_2O + CO \rightarrow CO_2 + H_2 \ (\Delta H = -41 \text{ kJ/mol}). \quad (1)$$

Fig. 4 depicts the H_2 output depending on the ethanol-water ratio. As seen it reaches maximum at equal amounts of ethanol and water. This is explained by concurrent reactions of the hydrogen generation and e-impact dissociation of ethanol and water molecules:

$$C_2H_5OH + H \rightarrow CH_3CH_2O + H_2, \quad (2)$$

$$C_2H_5OH + e \rightarrow CH_3CH_2O + H + e, \quad (3)$$

$$H_2O + e \rightarrow OH + H + e. \quad (4)$$

Fig. 5 presents results of calculations of the component content of the synthesis gas at the outlet of the DGCLW performed for two values of medium temperature, $T=$ 323 K and 155 K, in comparison with experimental data at different discharge currents I = 200, 300 and 400 mA. Despite the scatter of the data, one can see that in the case of $T =$ 323 K (as measured by the thermocouple) the calculated concentrations of the main syngas components, H_2 and CO, are close to experimental values, whereas in the case of T- 355 K (as assumed for the boiling 50 %-ethanol-water solution) the concentrations of syngas components differ. At that, the content of H_2 does not vary very much, because, on one side, the water vapor content that plays a dominant role in the H_2 production outside the electric discharge in the volume increases leading to

increasing of the H_2 yield; on the other side, the time of the air (lowing through the volume decreases, therefore, the H_2 yield decreases too. Under the influence of complementary factors, the H_2 content keeps at the same level.

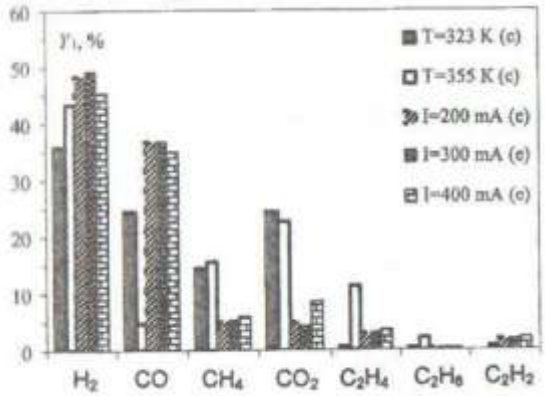

Fig. 5. Component content of synthesis gas products

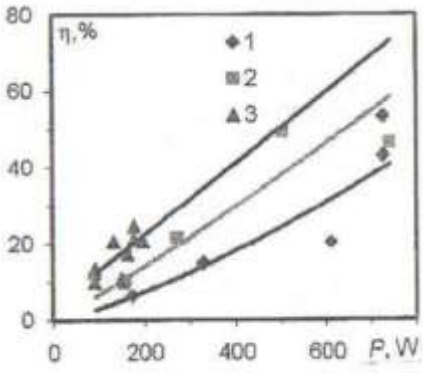

Fig. 6. Efficiency of ethanol conversion

The efficiency of the conversion of ethanol into syngas by the DGCLW was estimated on the basis of thermochemical calculations using criteria: (a) energy cost of 1 m^3 syngas, (b) productivity of conversion, and (c) specific heat of 1 m^3 syngas combustion, utilizing the parameter of efficiency from Fulcheri [1]:

$$\eta = \frac{(Y_{H2} + Y_{CO}) \times LHV\,(H_2)}{IPE + Y_{HC} \times LHV\,(HC)} \quad (5)$$

Here, IPE is the input plasma energy; Y and LHV are the molar fraction and lower heating value of syngas components; HC means the hydrocarbon fuel (ethanol). The formula (5) assumes that CO can be totally transformed into H_2 by the WGS process (1) with zero energy cost. Fig. 6 demonstrated results of estimations of the conversion efficiency of the DGCLW in ethanol-water solution 5:1 for three different modes with (1) liquid cathode, (2) liquid anode, and (3) two solid electrodes. One can see that the energy efficiency of the proposed method grows with the electric power up to ~50-55%. These numbers correlate with out earlier results [4, 5] and comparable with the best known plasma-aided ethanol reforming processes [1].

Conclusions

- A dynamic PLS with the DGCLW is quite efficient in plasma conversion of ethanol into syngas. The most effective is the DGCLW with impact air jets between the electrodes.
- The main components of syngas produced from ethanol in the DGCLW are and CO which relative yield is many times higher than for other hydrocarbons CH_4, C_2H_2, C_2H_4, and C_2H_6. The net yield of H_2 increases with increasing electric discharge power and reaches maximum if ethanol and water in the solution are in equal amounts.

- The numerical plasma-chemical kinetic modeling in air-water-ethanol vapors is in a fairly good agreement with experimental data for the main components of plasma and syngas.
- The minimal value of the electric power consumption in the investigated discharge regimes is ~2 kWh/Nm^3 whereas the obtained syngas power is ~4 kWh/Nm^3.

Although there is a lot of research needed before such technology can be made technically viable, this non-thermal plasma-fuel reforming process looks very promising.

Acknowledgements

The work was supported in part by the Ukrainian Ministry of Education and Science, by the Academy of Sciences of Ukraine and by the Science & Technology Center in Ukraine.

References

1. Petitpas G., Rollier J.-D., Darmon A., Gonzalez-Aguilar J., Metkemeijer R., Fulcheri L. A comparative study of non-thermal plasma assisted reforming technologies // *Intern. J. Hydrogen Energy.* 2007. Vol. 32. Pp. 284&-2867.
2. Chernyak V.Ya., Naumov V.V., Yukhymenko V.V., Veremii Yu.P., Prysiazhnevych I.V., Slyusarenko Yu.I. Plasma reforming of hydrocarbons in plasma-liquid systems with secondary discharges // Intern. Workshop "Nonequilibrium Processes in Combustion and Plasma Based Technologies". Minsk, HMTI, 2006. Pp. 171-173.
3. Yukhymenko V.V., Chernyak V.Ya., Naumov V.V., Veremii Iu.P., Zrazhevskij V.A. Combustion of ethanol+air mixture supported by transverse arc plasma *// Problems Atomic Sci. Technol., Series: Plasma Physics.* 2007. Vol. 13, No. 1. Pp. 142-144.
4. Chernyak V.Ya., Yukhymenko V.V., Slyusarenko Yu.L, Solomenko E., Olzhewskij S.V., Prysiazhnevych I.V., Naumov V.V., Lukyanchikov V., Demchina V.P., Kudryavtsev V.S. Plasma conversion of ethanol *Hind. Heat Eng.* 2007. Vol. 29, No. 7. Pp. 165-169.
5. Yukhymenko V.V., Chernyak V.Ya., Olshevskii S.V., Prisyazhnevich I.V., Naumov V.V., Zrazhevskii V.A., Verovchuk M.O., Solomenko O.V., Skalny J.D., Matejcik J.D., Demchina V.P., Kudryavtsev V.S., Naumov V.V. Plasma conversion of ethanol-water mixture to synthesis gas // *Ukr. J. Phys.* 2008. Vol. 53, No. 5. Pp. 409-413.
6. Shchedrin A.I., Levko D.S., Chernyak V.Ya., Yukhymenko V.V., Naumov V.V. // *JETP Letters.* 2008. Vol. 88, No. 2. Pp. 107-110.

7. Kalyuzhna A.G., Levko D.S., Schedrin A.I. Comparison of varions methods of calculation of plasma kinetics in barrier discharge *// J. Tech. Phys.* 2008. Vol. 78, No. 6. Pp. 122-126.

PLASMA ASSISTED COMBUSTION OF HETEROGENEOUS FUEL

A. KLIMOV, V. BITYURIN, A. GRIGORENKO, V. KUTLALIEV, I. MORALEV, B. TOLKUNOV

Joint Institute of High Temperature RAS, Izhorskaya 13/19, Moscow, 127415, Russia

There are many works devoted to study of plasma-assisted combustion (PAC) of different hydrocarbon- airflow gaseous mixtures today [1-14]. But there is insufficient number of works devoted to PAC study of heterogeneous fuel-airflow mixtures (liquid aerosol fuel, dusty particles, cluster particles and others). This problem is connected with a real jet engine operation, industrial explosions, multi-initiation detonation and low combustion completeness of metal powders.

This work is devoted to PAC study of a heterogeneous fuel. Ignition and combustion of tiny metal dusty particles and liquid aerosol particles assisted by capacity HF discharge is studied in this work. It is revealed that PAC completeness of these dusty particles is increased considerably.

It is obtained that multi-ignition and multi-initiation detonation of a heterogeneous fuel is possible at HF plasma assistance. Plasma-assisted detonation of aluminum- water vapor mixtures is studied in normal condition.

PAC gas dynamics and PAC electrodynamics are studied in this work also. Gas flow around longitudinal plasmoid is studied by optic interferometer namely. It is revealed that advanced mixing of fuel in high-speed airflow is realized by this plasmoid.

It is obtained that there is high electric positive potential (up to 7000 V) on plasmoid's surface created by HF discharge in Al powder - water aerosol mixture. The electric conductivity of this plasma-chemical formation is very high also. There is considerable attenuation of probe MW radiation by this plasmoid.

Nomenclature

PAC - plasma-assisted combustion

PCF - plasma-chemical formation

HF - high frequency

PG - plasma generator

I_{HF} - electric HF discharge current

M - Mach number

N_{HF} - HF power input in plasma

P_{st} - static pressure

T_g - gas temperature

T_R - rotation temperature

T_v - vibration temperature

Heterogeneous PAC of aluminium powder in water vapour

Using of low-cost aluminium in electric energy production is discussed in [15]. This method is named as aluminium-hydrogen energy production. The operation of power generator is based on the following reaction:

$2Al + 3H_20 = Al_2O_3 + 3H_2 + Q$, where Q~20 MJ/кG Al.

It is well-known that aluminium powder is used in explosives and rocket engine also [14]. However fuel combustion completeness is not high in this case. There is a real problem to increase this value for high-effective explosives by plasma assistance.

So, it is interesting to study PAC of aluminium powder in airflow and water vapour flow in detail. This task was studied in our work [15]. This study is continued in this work.

Plasma-chemical reactor used in PAC experiment is shown in Fig. 2. HF electric discharge is created in this reactor. This HF discharge is created between two electrodes] (1, 2). Typical distance between electrodes is about 50-100mm. Down electrode is covered by I water layer. This water is evaporated by HF electric discharge. Reactor wall is manufactured from quartz glass. Aluminium powder is injected from the top electrode (2). Vortex argon flow is created in this reactor by swirl generator (3). This reactor design is optimal one for separation of hydrogen and Al_20_3 by inertial body force. Hydrogen is evacuated from reactor by thin quartz tube (chemical probe) arranged near axis. Ball "hot" electrode is connected with Tesla's coil. This electrode is connected with metal cylindrical electrode (6) also. There is capacity connection between the cylindrical electrode (6) and down conical electrode (2).

HF plasma generator has the followings output parameters:

- Output voltage ~30 kV
- HF power 0.1-1 kW
- HF frequency 0.5 MHz
- Operation regime continuous

It is revealed that cylindrical plasma formation is created in region near reactor's axis, Fig. 1. Typical optical spectrum consists of exited argon and Al optical lines, OH and AlO

molecular bands. This spectrum is changed at Al powder injection, Fig. 3. One can see the optical lines of exited hydrogen and OH molecular band.

Hydrogen is evacuated from this reactor by chemical probe. This gas sample is analyzed by chromatograph. The maximal H_2 concentration measured in this experiment is about 50 %. Low air component (N_2 and 0_2) concentrations arc measured in this experiment due to residuum air in chemical probe tube.

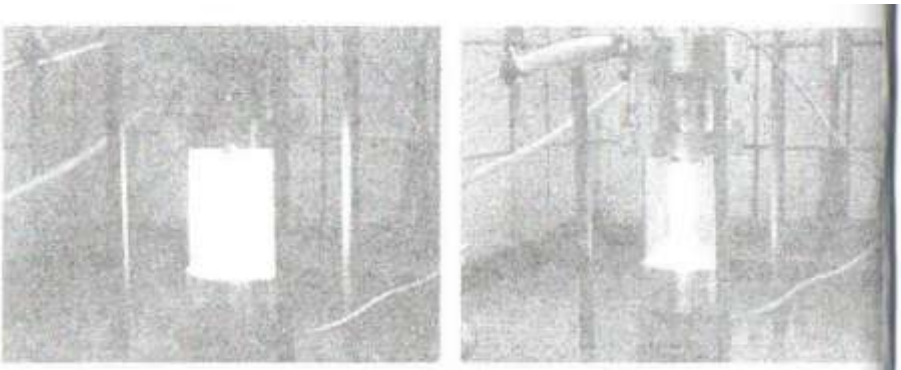

Fig. 1. Operation regime of Al–H_2O reactor at plasma on and Al-powder injection off (left) and on (right). Mass argon flow rate ~ 10 G/s, N_{HF} ~ 1 kW, mass Al-powder flow rate ~ 1 G/s

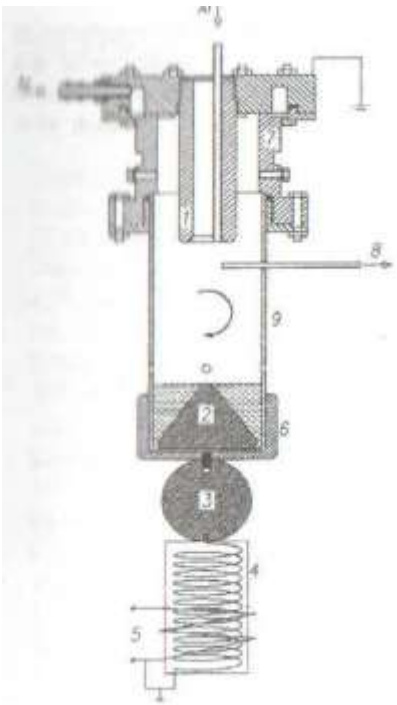

Fig. 2. Scheme of Al-water plasma-chemical reactor: 1 – top grounded electrode (Al), 2 – down conical electrode (Al) , 3 – ball "hot" electrode, 4 – Tesla's coil, 5 – inductor, 6 – down cylindrical electrode (container), 7 – swirl generator, 8 – chemical probe, 9 – quartz wall

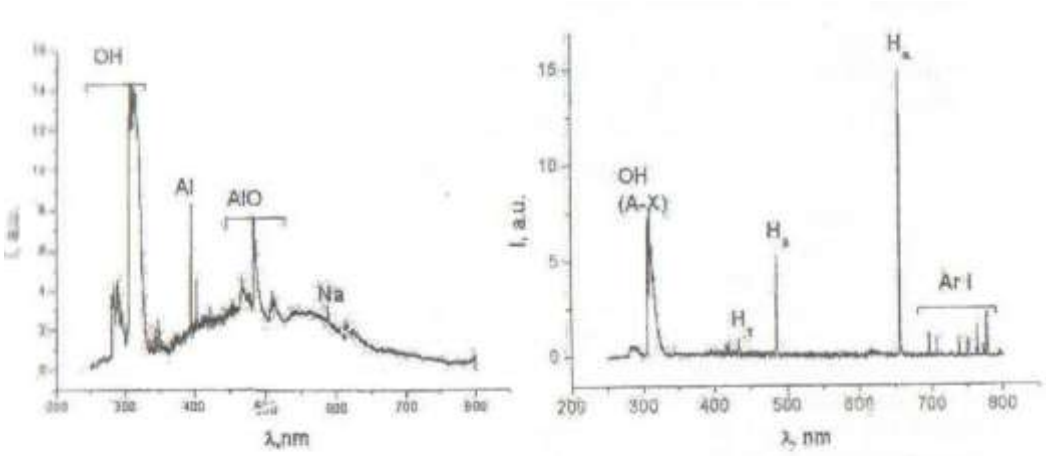

Fig. 3. Optical spectra obtained in Al–H_2O reactor at HF plasma on and Argon injection on (right) and off (left)

Note that the typical time of Al powder- hot water chemical reaction is about 24 hours at plasma off. The typical chemical reaction time of Al powder in water is about 1 sec at plasma on. So, plasma accelerates this chemical reaction considerably.

Heterogeneous plasma-assisted detonation of aluminium powder in water Aerosol

We succeeded in realization of plasma-assisted detonation in Al powder-water aerosol mixture. Scheme of this experiment is shown in Fig. 4. One can see that there is explosion of Al powder water acrosol mixture at plasma assistance. It is measured that PAC completeness is about 100 % in this experiment. The final species of plasma assisted detonation of this mixture arc analyzed by different diagnostic methods (X-ray analyser, secondary electron emission method, ion mass-spectroscopy). Al_2O_3 powder is created in test section after experiment only.

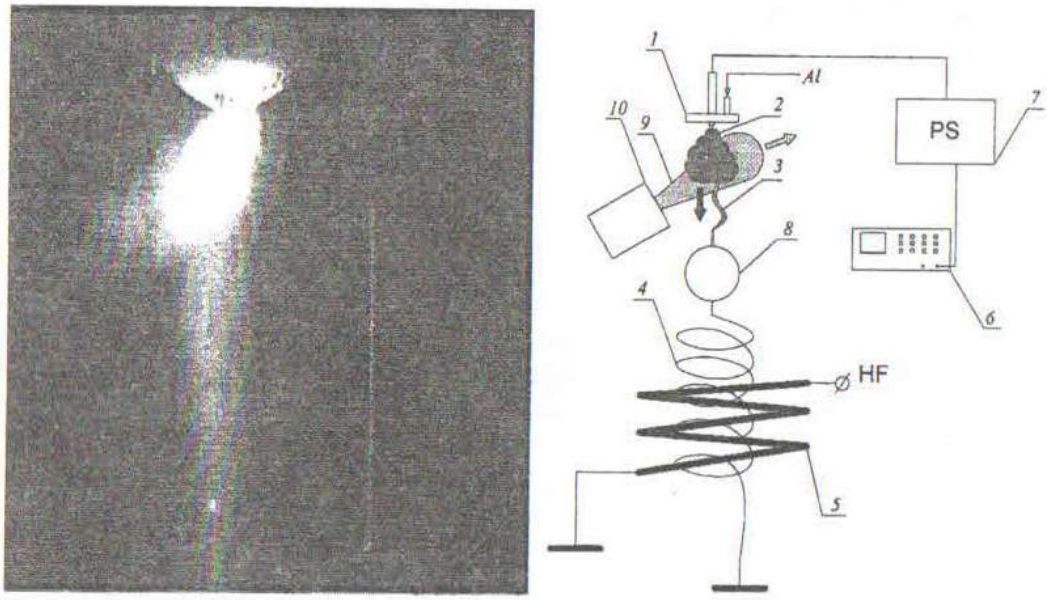

Fig. 4. Plasma-assisted detonation of Al-powder and water aerosol mixture in air (right). HF discharge. Scheme of experimental set up (left). 1 – PG, 2 – Al powder injection; 3, 4 – Tesla's coil, 5 – inductor, 6 – oscilloscope, 7 – power supply, 8 – ball HF electrode, 9 – water aerosol injection, 10 – aerosol generator

PAC electrodynamics

It is revealed that plasma-chemical formation shown in Fig. 4 has a very high electric positive potential. Its value is about 1000-7000 V. Note that there is charge separation inside this formation also. Negative charge is concentrated in a head part of this plasma formation. Positive charge is arranged in a down (main) part of this plasmoid. So, high-voltage charged PAC formation is created in this experiment. It is revealed that there is strong interaction between a charged plasmoid and a metal plate due to induced electric forces. In a result of this interaction the charged plasmoid is deflected by metal plate and then it touches this plate. It is revealed that electric conductivity of this plasma-chemical formation is very high. The value of electron concentration Ne of this PAC plasmoid is about 1014 cm^{-3} and higher. This value is estimated by measured conductivity and probe MW radiation decay. Note that there is considerable attenuation of probing MW radiation by this plasma-chemical formation.

Conclusion

1. Al-H_2O chemical reaction assisted by HF plasma is studied in this work. Considerable acceleration of this chemical reaction is obtained in this experiment.
2. Plasma-assisted detonation of Al-water aerosol mixture is obtained in air at normal conditions. High combustion completeness is measured in this experiment.
3. PAC electrodynamics is studied in this work also. It is revealed that charged (non- neutral) plasma-chemical formation is created at propane PAC and Al-powder injection. The typical value ofplasmoid's electric potential is about several kV.

Acknowledgments

I In N Work was supported in part by the European Office of Research and development (FOARD) under Contract Work 37947P and Program RAS P-09.

References

1. Salamandra E. Photo Recording of High- Speed Gas Dynamic Processes. Moscow: Nauka, 1974. Pp. 1-199.
2. Klimov A., Bityurin V., Kuznetsov A., Tolkunov B., Vystavkin N., Vasiliev M., I sternal and Internal Plasma- Assisted Combustion, AIAA Paper 2004-1014 // Proc. 42ed AIAA Aerospace Sciences Meeting & Exhibit, 4-8 January 2004, Reno, NV. Pp.1-10.
3. Klimov A., Bityurin V., VanWie D., et al. Plasma Assisted Combustion. AIAA Paper 2002-0493 // Proc. 40th AIAA Aerospace Sciences Meeting & Exhibit, 14-17 January]002, Reno, NV. Pp. 1-9.
4. Klimov A., Byturin V., Kuznetsov A., Sukovatkin N., Vystavkin N, Van Wie D.M. // 33id AIAA Plasma dynamics and Lasers Conference, 11-14 June 2002, Maui, Hawaii. Pp. IV 1-10.
5. Klimov A., Byturin V, Brovkin V., Kuznetsov A., Sukovatkin N.. Vystavkin N, VanWie D. Optimization of Plasma Assisted Combustion // Proc. 4 Workshop on MPA, Moscow 23-25 April, 2002, IVTAN. Pp. 1-31.
6. Klimov A., Bityurin V., Kuznetsov A., Tolkunov B., Vystavkin N., Sukovatkin N., Nerov Yu., Savischenko N., Yuriev A. External and Internal Plasma- Assisted Combustion AIAA Paper 2003-6240 // Proc. 41st AIAA Aerospace Sciences Meeting & Exhibit, 6-9 January 2003, Reno, NV. Pp. 1-9.
7. 7 Klimov A., Byturin V., Brovkin V., Kuznetsov A., Sukovatkin N., Vystavkin N., Plasma-Assisted Ignition and Combustion in Airflow // Proc. 5th Workshop on MPA, Moscow 23- 25 April, 2003, IVTAN. Pp. 1-31.
8. Klimov A., Bityurin V., Kuznetsov A., Vystavkin N., Vasiliev M. External and Combined Discharge Plasma in Supersonic Airflow, Paper 2004-0670 // Proc. 42nd AIAA Aerospace Sciences Meeting & Exhibit, 4-8 January 2004, Reno, NV. Pp. 33-38.
9. Kolesnichenko Yu., Flow Control by MW Energy Deposition // Proc. 5lh Workshop on MPA, Moscow 23-25 April, 2003, IVTAN. Pp. 15-29. 10.
10. *Ball Lightning in Laboratory*, edited by R.F. Avramenko, V.L. Bychkov, A.I. Klimov, O.A. Sinkevich, Moscow, Khimia publishers (in Russian), 1994. Pp. 1-291.

11. Klimov A., Bityurin V., Chinnov V. Non-Premixed Plasma-Assisted Combustion of Hydrocarbon Fuel in High-Speed Airflow, Paper 2006-0670 // Proc. 44nd AIAA Aerospace Sciences Meeting & Exhibit, 9-13 January 2006, Reno, NV. Pp. 1-10.
12. Potapkin B., Rusanov V. Plasma Catalysis, Low Temperature Plasma // Encyclopedia. M. RAS, 2006. Pp. 4-36.
13. Combustion Laws, 2006, Moscow, RAS IVTAN. Pp. 352-360.
14. Klimov A., Moralev I., et al. Non-Premixed Plasma-Assisted Combustion, AIAA Paper // Proc. 45th AIAA Conf. Reno NV, 7-11 Jan. 2007. Pp. 1-11.
15. Sheindlin A.E., Zhuk A.Z., et al. Using of Low-Coast Aluminium in Electric Energy production // *J. Power Sources.* 2006. Pp. 121-132.

FORMATION OF CONE STRUCTURES DURING CARBON NANOWHISKER GROWTH IN GLOW DISCHARGE PLASMA

F. N. BOROVIK, S. P. FISENKO

A.V. Luikov Heat and Mass Transfer Institute of NAS of Belarus, Minsk, Belarus,

fsp@hmti.ac.by

Introduction

The new experimental data about the formation of carbon cone structure during in glow discharge plasma have been discussed in [1]. Cone structures attract considerable interest [2 and references therein] as they can be used in optoelectronics as emitters.

The physical idea on the nature of cone structure and experimental evidence has been put forward in [1]. In fact, the main idea is that the carbon cones have the internal structure. Carbon vapor, which formed during the process of hydrocarbon plasma decomposition, deposits onto the fresh grown carbon nanowhisker and makes a cone.

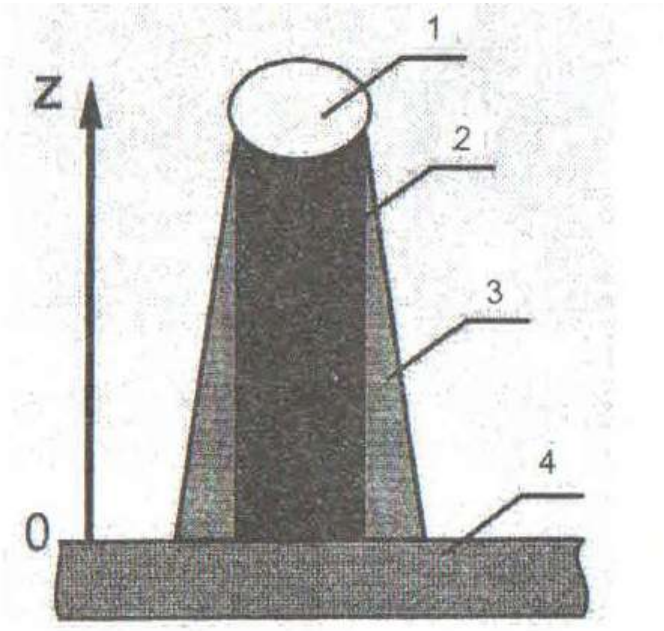

Fig. 1. The structure of a cone object on a nanowhisker. 1 – a catalytic nanodroplet, 2 – a carbon nanowhisker, 3 – amorphous carbon, 4 – a substrate

In this work we present the theoretical description of this process using the mathematical model of carbon nanowhisker growth via the complex mechanism 'vapor - liquid - solid' developed in [3]. The physical

picture of formation and growth of cone structure is shown in Fig. 1. The growth of a cone structure is due to carbon atoms, which a glow discharge generates in the gas phase. Carbon atoms in the nanowhisker are generated by the catalytic decomposition reaction of gas phase molecules bombarding the surface of the catalytic nanodroplet.

Mathematical model

The growth rate of the nanowhisker length L is governed by the equation [3]

$$\frac{dL}{dt} = D(T)\frac{Sn_1}{Rn_s}, \qquad (1)$$

where D(T) is the carbon diffusion coefficient in a catalytic particle material of radius R and substrate temperature T, $n_1(J)$ is a numerical density of carbon molecules corresponding to the carbon equilibrium solubility in the catalyst material, n_s, is a carbon numerical deputy in a nanowhisker, $S = n/n_i$ is the average supersaturation in the catalytic nanodroplet, n is a carbon numerical density in the nanodroplet. For tubular nanowhisker the expression of the growth rate has been obtained also in [3].

И should be noted that nanodroplets of Ni or Fe (or of their alloys) are usually used as catalytic particles. If the specific flow J of molecules carrying carbon from gas phase (plasma) to nanodroplet surface exceeds the value $D(T)Sn_1/R$ then the covering of the nanodroplet surface by amorphous carbon takes place. The composition of the J depends on the plasma composition and the discharge conditions [4]. Also, we assume that the nanowhisker temperature is equal to the substrate temperature [5].

Even for experiments at the atmospheric pressure the process of carbon atom deposition onto the nanowhisker occurs in the free molecular regime as the nanowhisker diameter nearly coincides with the catalytic nanodroplet diameter [3]. Thus even for the atmospheric pressure discharge [4] the Knudsen number $Kn = \lambda/R \gg 1$, where λ is the mean free path of carbon atoms.

According to [1] a cone forms due to depositing of plasma carbon onto the nanowhisker surface. It can be easily shown that in the free molecular regime the equation for the change of the cone radius R(z) at a height z is of the form

$$\frac{dR(z)}{dt} = \begin{cases} 0, \text{if } z > L \\ \dfrac{P_c}{n_a\sqrt{2\pi mkT_p}}, \text{if } z < L, \end{cases} \qquad (2)$$

Where n_s is a numerical density of carbon atoms in the amorphous layer, m is the carbon atom mass, κ is Boltzman's constant, T_p is a plasma temperature; P_c is a partial pressure of carbon atoms in the discharge, for determination of this value special calculations or measurements has to be done. From equations (1), (2) it follows that for the given height z the cone radius grows linearly in time. It should be noted that in the equation (2) we ignored the carbon evaporation from the nanowhisker because the nanowhisker temperature is equal to about 600-800 °C and it is determined by the substrate temperature. For such temperatures the carbon saturated vapor pressure is extremely small.

The angle αgenerated by the element of the cone and its height is defined by an equiation which is obtained on the base of simple geometric considerations

$$\tan(\alpha) = \frac{R\left(P_c n_s - 1\right)}{n_a D(T) S n_i(T)\sqrt{2\pi m k T_p}}. \qquad (3)$$

It follows from equation (3) that the larger the nanodroplet radius the larger the cone angle Meliorated by amorphous carbon around the nanowhisker. At a constant carbon partial pressure the cone angle much decreases in increasing the substrate temperature as the diffusion coefficient D(T) and the solubility $n_i(T)$ exponentially increase when elevating temperature. It is possible that due to this fact the experimental observations of cone structures are quite seldom. It is obvious from (1) that carbon cone structures should be observes at low enough temperatures [1, 2, 4]. When elevating the carbon partial pressure the substrate temperature should increase to observe the invariable angle of the cone.

Results

The experimental values of the angle α are in the range of 5 - 15 degree [1, 6]. The numerical estimation according to (3) shows that for a nickel nanodroplet of $R =$ 10 nm at the temperature T = 700 °C such angles take place if the pure carbon partial pressure is 0.2 Pa. As already noted above the pure carbon partial pressure depends on the total pressure, the gas phase composition and plasma source power. The use of atom hydrogen generated by injecting hydrogen molecules or ammonia ones into the plasma allows working at higher pressure of carbon. In this process a part of carbon is removed by hydrogen from the nanowhisker surface [1] i.e. the cone angle decreases.

If during the course of the experiment a set of nanowhiskers closely located formed then the cone angle will change in moving from the center of cone structure massive to the periphery by reason of encumbering effects

At high partial pressure of carbon vapor the cone radius will rapidly increase about up to the value equal to the free path after which the growth rate decrease sharply in the diffusion regime as it is common knowledge. As a result the nanowhisker near the substrate is covered with a practically cylindrical layer of amorphous carbon. The cone part will be observed only near the catalytic nanodroplet. The experimental observation of this transition to a cylindrical.) layer is given in [7].

References

1. Klein K.L., Melechko A.V., McKnight T.E., et al. Surface characterization and functionalization of carbon nanofibers *// J. of Appl. Physics.* 2008. Vol. 103. (061301).
2. Ostrikov K. and Murphy A.B. Plasma-aided nanofabrication: where is the cutting edge? / *J. of Physics D: Applied Phys.* 2007. Vol. 40. Pp. 2223-2241.
3. Borovik F.N., Fisenko S. P. Kinetics of nanowhisker growth via the vapor-liquid-solic mechanism // *Technical Physics Letters.* 2007. Vol. 33. No. 2. Pp. 151-153.
4. Zhdanok S. A., Gorbatov S. V., Michajlov A. A. *et al.* Low temperature synthesis of car bon nanotubes... // *J. Engineering Physics and Thermophysics.* 2008. Vol. 81. No. 2. Pp. 203-205.
5. Borovik F. N., Fisenko S. P., and Kas'kova S. I. Thermodynamics and transfer processe in nanowhisker formation on a substrate // Physics, Chemistry and Application of Nanos tructures, 2007 / V.E. Borisenko, S.V. Gaponenko, V.S. Gurin, Singapore, World Scien tffic. 2007. Pp. 451-454.
6. Merkulov V.I., Melechko A.V., Guillorn M. A. et al. Sharpening of carbon nanocone tips during plasma- enhanced chemical vapor growth *// Chem. Phys. Lett.* 2001. Vol. 350. Pp. 381-385.
7. Kiselev N.A., Krestinin A.V., Hatchinson J.L. *et al.* Extreme length carbon nanofilamen with single-walled nanotube cores grown by pyrolysis of methane or acetylene // *Carbon* 2006. Vol. 44. Pp. 2289-2300.

PARAMETERS OF NONEQUILIBRIUM PLASMA AND STRUCTURE OF NORMAL ATMOSPHERIC PRESSURE GLOW DISCHARGE IN HELIUM AT DISCHARGE RANGE OF 0.1mA - 10A

V.I. ARK.HIPENKO, A.A. KIRILLOV, YA.A. SAFRONAU, L.V. SIMONCHIK, S.M. ZGIROUSKI

И I Mopitnov Institute of Physics NAS of Belarus, Minsk,Belarus, kirillov@imaph.bas-net.by

Introduction

The rapidly increasing interest in Atmospheric Pressure Glow Discharges (APGD) is because of the possibility for reducing the expense of vacuum systems in a wide spectrum of industrial applications. Potentially new processes and methods for plasma technologies or improvements in existing plasma based technologies will certainly follow from investigations of APGD plasmas and their applications. Despite all obvious experimental facts and theoretical estimations it is still relevant to ask as done in [1] if APGD in helium is a normal glow discharge or a stabilized arc. On the other hand, why it did say in [1, 2] about an instability and a glow-to-arc transition on a milliampere level yet? At the same time a high-current normal dc APGD operates stably at current up to about 10 A according to [3]. At what conditions the diffusive and contracted discharge forms are observed? What is the nonequllibrium degree of APGD in helium at discharge current differed in orders of magnitude? We will try to answer these and other questions.

Experimental setup

Glow discharge was created in air-locked chamber 1 with quartz glass windows used for discharge observation. Discharge was ignited between two electrodes: weakly rounded tungsten anode (6 mm in dia) and flat cooled cathode, made from copper and steel (36 mm in dia). Cathode has a form of cylindrical barrel. An external surface of the barrel bottom serves mi a working cathode surface. The barrel was closed hermetically with cover in which were soldered tubes for supply and taking aside cooling water.

Interelectrode gap varied from 0.5 mm to 10 mm. Working gas flow about 1 1/min at atmospheric pressure was produced through a discharge chamber. In this experiment was used gas helium. An impurity concentration (H2, N2, 0_2, Ar, CO2, CO, Ne, H_2O) in helium didn't exceed 0.02%. Discharge was fed by a dc unstabilized power supply. Depending on the experimental situation two power supplies were used. These were typical rectifiers with step-up transformer and capacitive filter. Voltage variation was performed by an autotransformer. The power supply with output voltage under 3 kV and ballast R of several tens kΩ was used HI low discharge currents (less than 100 mA); the other source with output voltage up to 600 V and ballast R of about 100 Q was used at high discharge currents (more than 100 mA). Posiitive terminal of power supply was connected to anode through a ballast R, negative one wax connected to cathode which was grounded.

The scanning 0.5 m high resolution monochromator (two gratings with 1800 grooves/mm) was used for a photoelectric registration of the APGD emission spectra. Inverse linear dispersion was ~ 0.5 nm/mm. Halfwidth of a Gaussian instrumental profile was equal to $\Delta\lambda_a \cong 0.01$ nm. The photoelectric multiplier FEU-171 was used as a converter of light Intensity to electric signal. Two times enlarged discharge image was focused onto the entrance slit of monochromator with help of optical system consisted of two achromatic lenses. Experimental data were collected and processed using a personal computer.

Results and discussion

Images of the discharge at different discharge currents and the same interelectrode gap of 1 cm are shown in Fig. 1. As one can see, the APGD has the following structure: thin layer (less than 0.5 mm in thickness) of negative glow (ng) is situated above cathode surface; positive column (pc) extends to anode. There is Faraday dark space (fds) between these two luminous regions. Anode end is covered by glowing layer of anode region (ar).

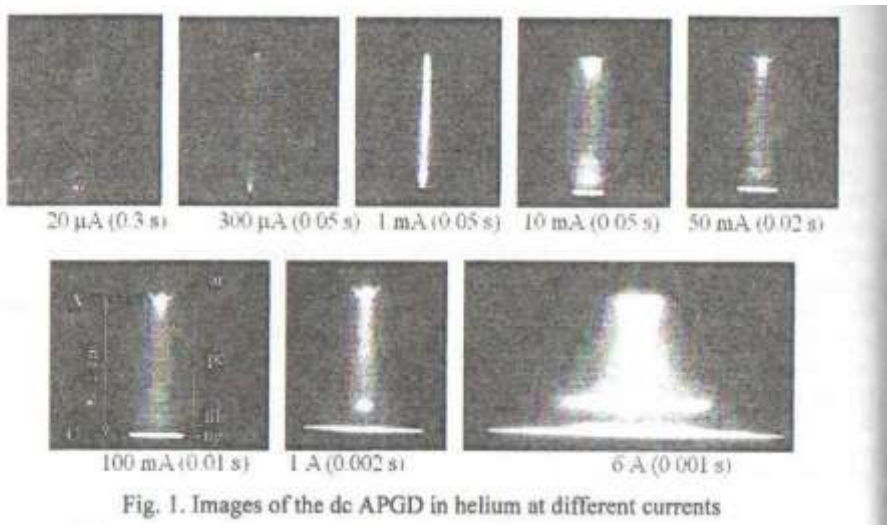

Fig. 1. Images of the dc APGD in helium at different currents

At discharge current more than 50 mA diameter of positive column is less than a negative glow one. The discharge has a contracted form. At discharge current less than 10 mA positive column is more extensive than negative glow. The diffusive discharge form is observed. As one can see (Fig. 1, photos at 300 μA and 1 mA), in this case positive column develops from a negative glow in a form of divergent luminous cone. Colour of the positive column glow is reddish at current more than 100 mA, and this one has much blue colour at current less than 100 mA. The discharge becomes stratified in axial direction at the current range from 10 to 100 mA.

The voltage-current (V-I) characteristics (dependence of the interelectrode gap voltage on discharge current) of the APGD at two interelectrode gaps (0.1 and 1 cm) are shown in Fig. 2. As it follows from Fig. 2, the V-I characteristic is relatively "flat" for small gap (1 mm). Positive column at such gap is practically absent. Voltage increase is observed at current less than 10 mA.

Normal cathode fall for normal helium APGD is 145 V [4]. An exceeding of this value is due to other regions of discharge (negative glow, Faraday dark space, anode region). Electric power in the range 0.05 - 2500 W corresponds to the current range of this V-I characteristic. When the interelectrode gap is large (1 cm) the largest discharge part is formed by positive column (Fig. 1). The V-I characteristic for this case is shown in Fig. 2. Electric power which corresponds to this characteristic current range is in the range I = 2500 W.

Electric field strength $E(x)$ in the cathode fall in APGD was determined by a spectropolarized method [4]. For this purpose an effect of Stark broadening of hydrogen levels in external electric field was used. The profiles of the H_β (486.1 nm) lines were registered in cathode fall. Experiments were performed at discharge current of 1 A. The maximal field strength value at discharge axis and close to the cathode surface in the helium APGD with copper cathode is about 62 kV/cm. Electric field strength is practically constant in radial direction up to the edge of cathode fall region. The cathode fall thickness is in the range of 0.06-0.07 mm. Electric field strength in positive column was determined using wire tungsten probe (wire diameter - 0.05 mm, length of uninsulated part is 5 mm). It was determined that when the current is increased the electric field strength decreases from the value of 1 kV/cm at current less than 1 mA to the value of 50 V/cm in case of several amperes.

Gas temperature $T_g(x)$ in the APGD was determined by the resolved rotational bands of both a nitrogen ion and hydroxyl [4]. Significant decrease of temperature is observed in cathode region due to water cooling of cathode. Temperature in cathode region is changed slightly and its value agrees closely with a room temperature (Fig. *3b).* It is evident since the cathode parameters are practically constant in wide current range.

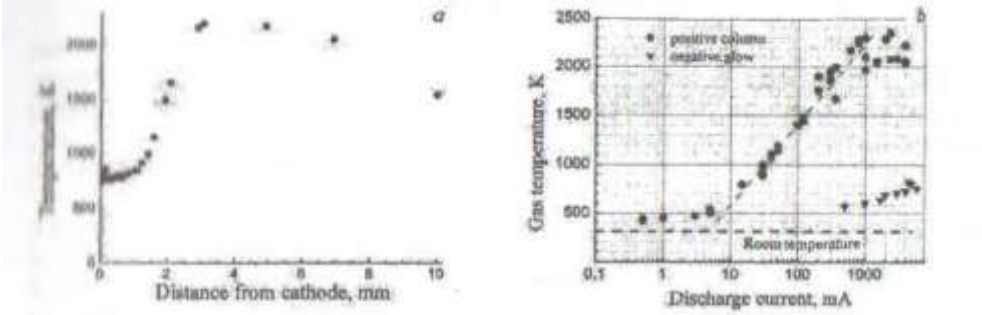

Fig. 3. Axial distribution of gas temperature (gap is 10 mm at discharge current of 1 A) (*a*) and gas temperature vs discharge current in both the positive column and negative glow (*b*)

On the contrary, gas temperature in positive column is varied significantly. At small eurrent (10 mA) one can assert that gas temperature within the limits of errors exceeds on l00+200 K an ambient temperature. At current increase from 10 mA to 1 A temperature increases in 5 times and reaches the value about 2300 K. At further increase of discharge curient it is remaining practically constant. The temperature values the same as other parameters of the positive column plasma were obtained at the middle part of the discharge gap.

The electron density was determined by the Stark emission spectroscopy technique. I lie hydrogen H_β line was used. Experimental profile of this line was fitted by convolution of different profiles, namely, instrumental, Doppler, Van-der-Waals and Stark ones. Resonance broadening did not take into account, because the concentration of the hydrogen atoms presenting in discharge chamber is small.

Axial distribution of electron density in the APGD at discharge current of 1 A is shown in Fig. 4a. As it is seen electron density is maximal in negative glow and is about $2*10^{14}$ cm^{-3}. Electron density in positive column is less in a few times at the same discharge current of 1 A and its value depends on discharge current (Fig. *4b).* This dependence is practically linear at discharge currents less than 0.8 A. At currents larger than 0.8 A the current changes don't occur. At high current at the same time significant broadening of positive column is observed (Fig. 1, images at 1 A and 6 A). Thus plasma of the dc APGD in helium is weakly ionized. A degree of its ionization is a few thousandths of percent.

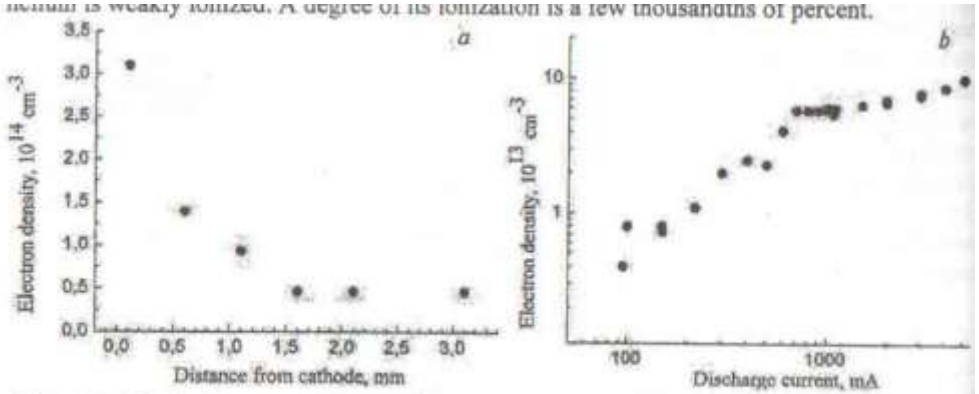

Fig. 4. Axial distribution of electron density in cathode region (*a*) at current of 1 A and electron density in positive column vs discharge current (*b*)

Current density in different APGD cross sections was determined as ratio of discharge current value to a cross section area through which current flows. A transverse distribution of integral plasma emission intensity in visible region was used for an estimation of a current region dimension in chosen cross section.

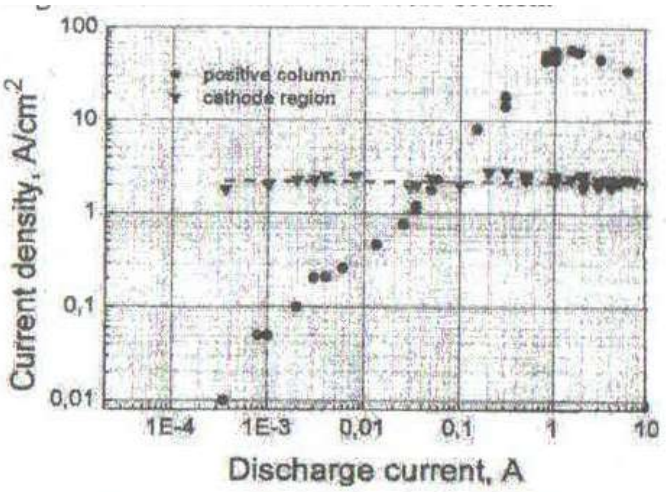

Fig. 5. Current density in the helium APGD vs a discharge current

It is seen in Fig. 5, that current density in cathode region stays constant in wide current range of 10^{-4}-10A (about five orders of magnitude) and equal to the value of about 2.3 A/cm^2. It doesn't depend on the length of discharge gap. This data points out the fact that the APGD in helium is a normal glow discharge.

In positive column current density has a strong dependence on the discharge current values. At current of about 1 A current density is maximal and is about 30-40 A/cm^2. When decreasing current less then 1 A its density in positive column decreases droningly. At current of about 50 mA current densities in cathode region and positive column become equal. At current less than 50 mA positive column can be considered as diffusive one since current density in it is less than in cathode area. And on the contrary, at discharge current more than 50 mA positive column is contracted.

Taking into account dependences of both the electric field strength and the gas temperature on discharge current one can obtain values of reduced electric field strength against discharge current in positive column. The reduced electric field strength values are 4.5 - 6 Td at discharge current less than 0.1 A. Reduced electric field decreases at the discharge current growth and it is about 1.5 Td at discharge current of a few Amperes. In positive column the average electron energy in plasma is defined only by the value of reduced electric field E/N. The average electron energy is about 3-4 eV at low current (<0.1 A). It becomes less than 1 eV at discharge currents of 3-4 A.

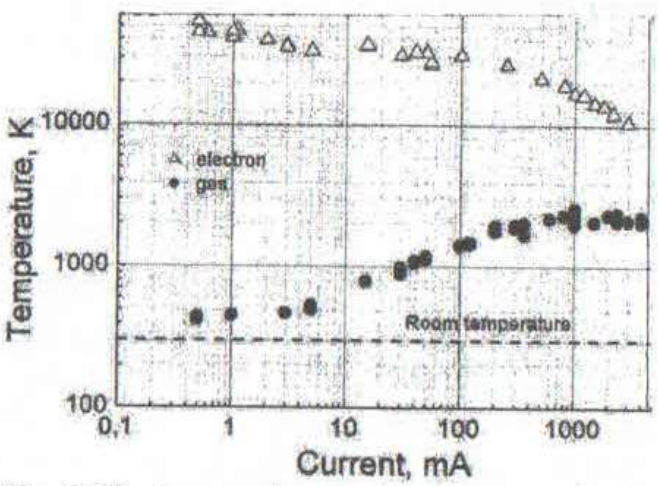

Fig. 6. Electron and gas temperatures in the APGD

It is known that atomic gas plasma is non-equilibrium if its electron temperature exceeds gas one ($T_e \gg T_g$). It is seen in Fig. 6, that a nonequilibrium degree of positive column plasma depends on discharge current values. The electron and gas temperatures are differed on two

orders of magnitude at discharge currents less than 10 mA. This means that plasma is strongly non-equilibrium. At the same time the difference is only 4-5 times at discharge current more than 1 A. Therefore, plasma non-equilibrium degree decreases with a current increase.

Conclusions

We present the self-sustained normal dc APGD in helium operating in large current Millie from hundred microamperes to ten amperes. The discharge appearance essentially depends on the current value. At discharge current less than 10 mA the positive column is tin не extensive than the negative glow - the discharge is diffusive, at current more than 50 mA the positive column is tighter than the negative glow - the discharge is contracted. The V-I characteristic is "flat" only at a gap less than 1 mm. At larger gaps (≥10 mm) the characteristic is dropping at current increase. The APGD plasma is weakly ionized (a few thousandths percent). Parameters of cathode region are constant within the whole current range of the normal APGD mode. The non-equilibrium degree of positive column plasma depends on discharge current. Electron temperature is two orders of magnitude higher than the gas one at low current (<10 mA). The difference of these temperatures is only about 4-5 times at discharge current more than 1 A.

References

1. Andrade F.J., Wetzel W.C., Chan G. C.-Y. et al. A new, versatile, direct-current helium utmospheric-pressure glow discharge *// J. Anal. At. Spectrom.* 2006. Vol. 21. Pp. 1175-IIK4.
2. Staack D., Farouk B., Gutsol A.F. and Fridman A.A. Characterization of a dc atmospheric pressure normal glow discharge // *Plasma Sources Sci. Technol.* 2005. Vol. 14. Pp. 700- 711.
3. Arkhipenko V.I., Zgirovskii S.M., KJrillov A.A. and Simonchik L.V. Cathode Fall Parameters of a Self-Sustained Normal Glow Discharge in Atmospheric-Pressure Helium *// Plasma Phys. Rep.* 2002. Vol. 28. Pp. 858-865.
4. Arkhipenko V.I, Kirillov A.A., Simonchik L.V. and Zgirouski S.M. Self-sustained normal de atmospheric pressure glow discharge // *Spectroscopy of plasma and nature objects* / I il by V.I. Arkhipenko, V.S. Burakov and A.F. Chemiavski. Minsk: Belaruskaya nauka, 2007. Pp. 10-65 (in Russian).

EFFECT OF SURFACE HIGH-FREQUENCY BARRIER DISCHARGE ON A FLAT PLATE DRAG REDUCTION

P. KHRAMTSOV, O. PENYAZKOV, M. CHERNIK, I. SHATAN, I. SHIKH

'A.V. Luikov Heat and Mass Transfer Institute of NAS of Belarus, Minsk, Belarus,

shatan@omut.biz

Introduction

Application of discharge plasma for drag reduction of aircraft is a wide and active developing research field, which is carried out all over the world [1-6]. Method of high-frequency barrier discharge is a very perspective way to generate surface plasma at one atmosphere and has an effect on aerodynamic drag. The purpose of this work is an experimental investigation of dependence between total aerodynamic drag of flat plate, the velocity of incident flow and electrical parameters of discharge.

Experimental equipment

As a prototype system was used a flat caprolon plate with total dimensions 10x180x120 mm. Needle electrodes system was placed on the front peaked edge. The electrodes were arranged with 3 mm step parallel to the upper and lower surfaces at a height of 3 mm on both sides of the plate. The second electrode was a segment of copper wire, covered by fluoroplastic isolation. It was built-in in the plate parallel to the front edge at 40 mm distance from the needle electrodes ends.

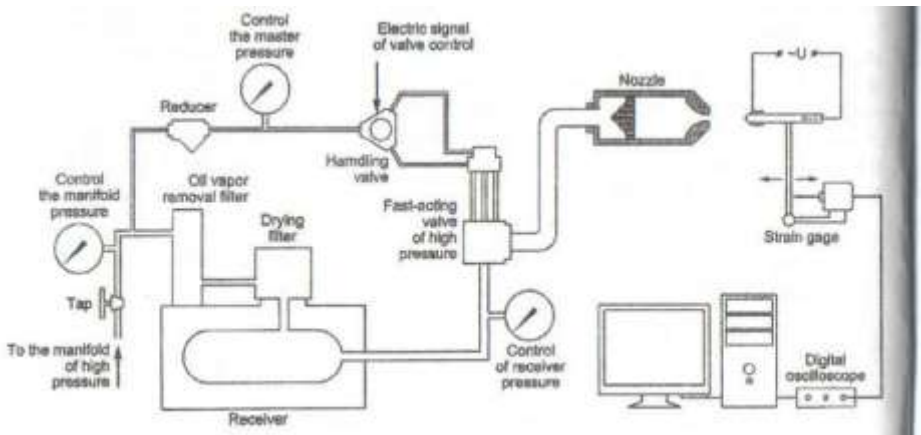

Fig. 1. Experimental equipment for measurement aerodynamic drag

High-voltage electrical pulses with duration 200 microseconds, amplitude 70 kV and frequency 1 kHz were supplied on the electrodes and generated high-frequency barrier discharge on the flat plate. In the result of interaction between charged particles and electrodynamics mass forces, the gas flow appeared (its velocity was about 5-10 m/s) and turbulent boundary layers were formed on the surfaces [7]. The blow of the plate was produced by two-dimensional air stream that flowed through a nozzle with exit section 15*200mm. The scheme of experimental facility for drag measuring is shown on Fig. 1. Compressed air from high pressure manifold

stored in the receiver with enclosed volume it m l he pressure in the receiver was set depending on the required flow velocity.

The plate was placed across the flow axes at 120 mm distance from the nozzle section and was fixed on the hinge. The force from the plate was transmitted to the strain gauge. Ensor's electric signal was registered by the digital oscilloscope. The flow velocity was measured by Pitot-Prandtl tube. The shadow pattern of blow on the flat plate with barrier discharge is shown on Fig. 2. The flow velocity near the front edge of the plate was μ=60 m/s. As follows from the shadow patterns, barrier discharge causes boundary layer constriction to the surface.

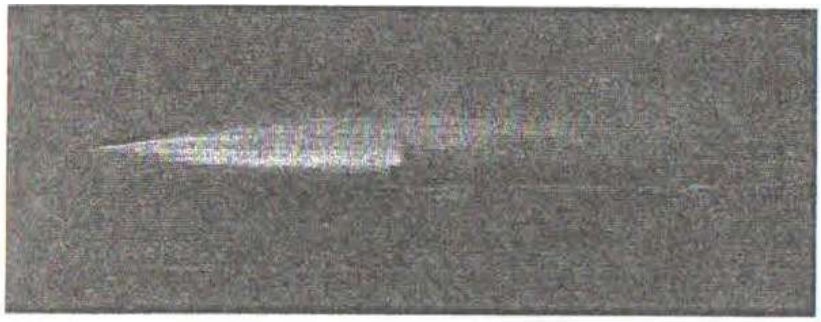

Fig. 2. Shadow pattern of blow on the flat plate by two-dimensional air stream

Results and discussion

I he photography of the plasma light with air flow and without it was used for the estimation of the flow effect on the barrier discharge structure. As shown on the Fig. 3, the Mow presence leads to the elongation of the discharge lightning area. The elongation was «bout 15 % with the flow velocity 60 m/s.

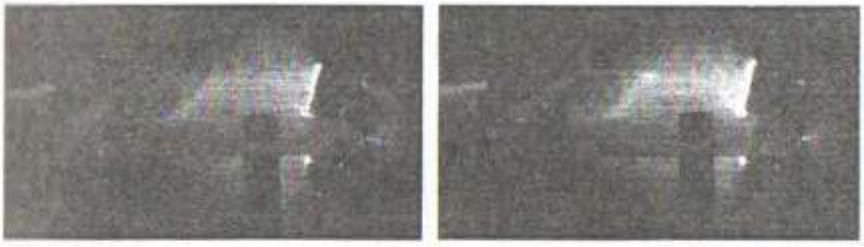

Fig. 3. The photos of the plasma light without air flow (left) and with air flow u = 60 m/s (right)

Total aerodynamic drag of the plate was measured by electromechanical strain gauge. I he blow on the plate was produced with a discharge and without it in turn. The velocity of the incident flow was reducing while the pressure in the receiver was decreasing. The total plate drag dependence from time with a discharge and without it is shown on Fig. 4.

The profile drag coefficient of the flat plate was calculated by formula [8, 9]

$$c_W = \frac{F}{\rho u^2 bh},$$

where b - plate width; c_w - profile drag coefficient of the plate; h - plate thickness; u - velocity of the incident flow; F- profile aerodynamic drag; ρ - air density.

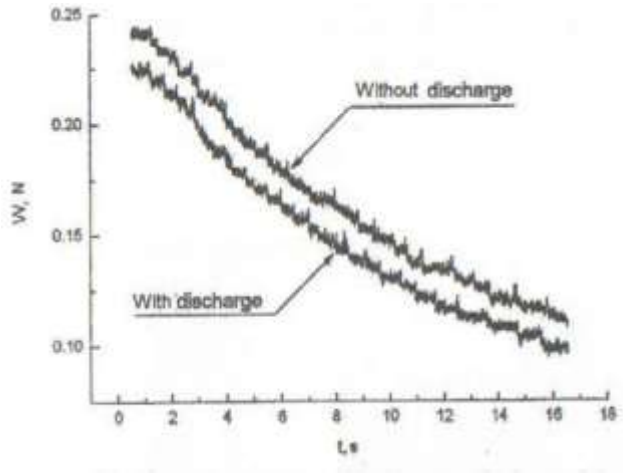

Fig. 4. The total plate drag dependence from time with a discharge and without it

The dependence of profile drag coefficient of the plate on Reynolds number with and without barrier discharge is shown on the Fig. 5. The presence of high-frequency barrier discharge on the surface of the plate leads to the profile drag coefficient decrease on 3-7 %. It should be mentioned that in the investigated range of Reynolds number profile drag is the sum of two comparable components: friction drag and pressure drag.

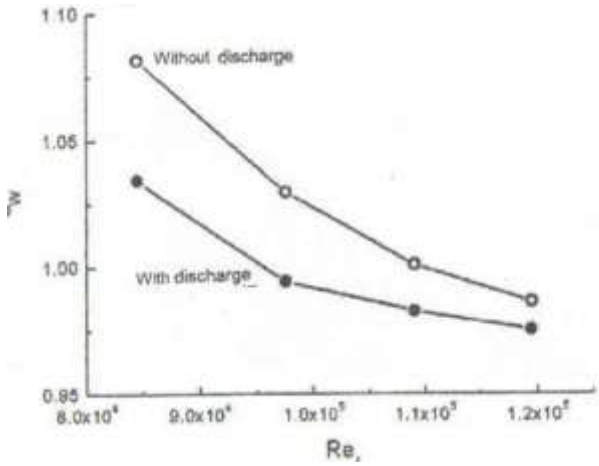

Fig. 5. The dependence of profile drag coefficient of the plate on Reynolds number with and without barrier discharge

To define optimal discharge condition for greater influence on aerodynamic drag the dependence investigation of profile drag coefficient on electric power of discharge was carried out. The result is shown on Fig. 6. While increasing electric power, the efficiency of barrier discharge influence on the plate drag increases until some critical point. Its value of specific surface density power input P_k = 9.5 kW/m^2. The further growth of electric power leads to total aerodynamic drag of the plate increase. It is connected with discharge contraction processes in its own magnetic field and formation of filamentary structures. Filamentary plasma structures shunt discharge gap because of its high electroconductivity. In such conditions electrical power of the discharge is spent mainly on heating, and a part of energy used for ion wind generation decreases.

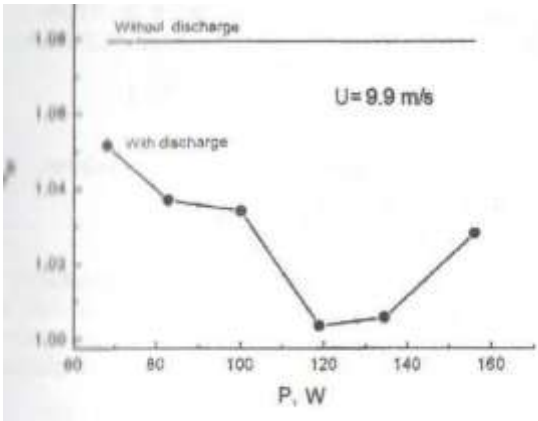

Fig. 6. Dependence of profile drag coefficient on electric power of discharge

Conclusions

In the result of the experiments was established that the use of high frequency surface harrler discharge allows achieving profile drag coefficient decrease on 3-7 %. The discharge is bound inflexibly to the electrodes and almost isn't blown out by incident flow. The critical value of specific surface density power input Pit, which has maximal efficiency of barrier discharge influence on the plate drag, is quite high to use it in engineering design of aircrafts in wide range of electrical parameters.

References

1. Koth J. R. Plasma Processing Applications of a One Atmosphere Uniform Glow Discharge Plasma // Int. Symp. Plasma 2001. Warsaw, Poland, September 19-21, 2001.
2. Fadeev V. M., Jusupaliev U., Shyteev S. A. Barrier discharge in the modern technologies [Internet resource] //Access mode: http://www.optics.phis.spbu.ru/
3. Boubnov E., Udovenko D., Sharshembiev K., Borombaev M.K. VoItage-charge characteristic of barrier discharge on duplex wire // The materials of the first republican science workshop of students physicist and young scientists. Kharakol, 2001. Pp. 92-101.
4. Samoilovich V.T., Gibalov V.I., Kozlov K.V. Physical chemistry of barrier discharge // Moscow, MSU, 1989. P. 176.
5. Philipov U.V., Emelyanov U.M. About active power of ozonizers // *Journal of Chemical Physics*. 1959. Vol. 33, No. 5. Pp. 1042-1046.
6. Uniform barrier discharge [Internet resource] // Access mode: http://www.optics.phis.spbu.ru/
7. P. Khramtsov, O. Penyazkov, M.Chernik, I. Shikh, Shadow method of measuring of average electron concentration in ionized gas flow induced by high-frequency barrier discharge // *J. of Engineering Physics and Thermophysics,* in print.
8. Hantly G. Dimensional analysis. Moscow: Mir, 1970.

9. Schlichting G. The theory of boundary layer Moscow: Nayka, 1969.

AVERAGED TEMPERATURE AND CONCENTRATION DISTRIBUTION OF ELECTRONS IN HIGH FREQUENCY BARRIER DISCHARGE PLASMA

P. KHRAMTSOV, 0. PENYAZKOV, M. CHERNIK, I. SHIKH

A.V. Luikov Heat and Mass Transfer Institute ofNAS of Belarus, Minsk, Belarus,

emerald_@tut.by

Introduction

Optical method was employed to measure distribution of electrons concentration in ionized airflow induced by high frequency barrier discharge. It was shown that ion acceleration take place mostly near minimum of electrons concentration and extremum of electrons temperature distribution are in antiphase to respective extremum of electrons concentration.

Experimental setup

As an experimental model flat plate made from caprolone (10x180x120 mm) was used. On the sharpened front surface on both sides of plate 2 rows of joint needles was installed (needle spacing was 3 mm, needles rows was placed 3 mm over plate) as first electrode. Second electrode was an isolated copper wire installed inside of plate. Electrodes were 40 mm apart. When high voltage impulse applied on electrodes high frequency barrier discharge appears. Electrical network for power supply is shown on Fig. 1.

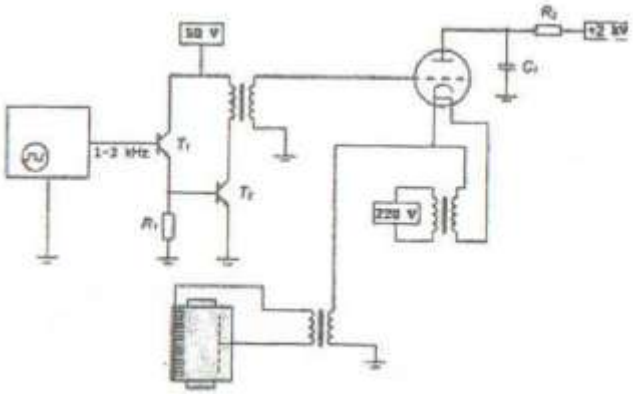

Fig. 1. Electrical network for power supply

Rectangular impulse 5 micros long with frequency 1-2 kHz was putted on input of thyratron supply network. Peak voltage is in between 70-140 kV. The typical oscillogram of voltage impulse on electrodes is shown on Fig. 2.

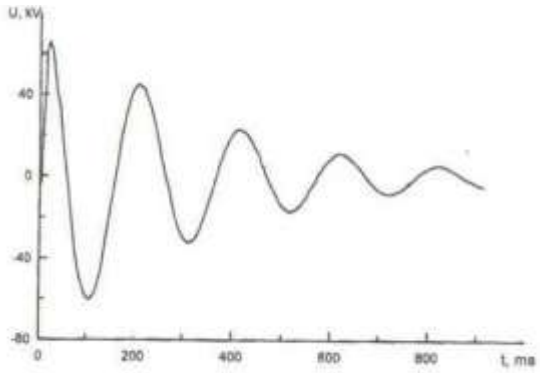

Fig. 2. Typical oscillogram of voltage impulse on electrodes

This discharge induces ionized airflow with speed range 5-10 m/s and the flow forms turbulent boundary layer over flat plate (Fig. 3).

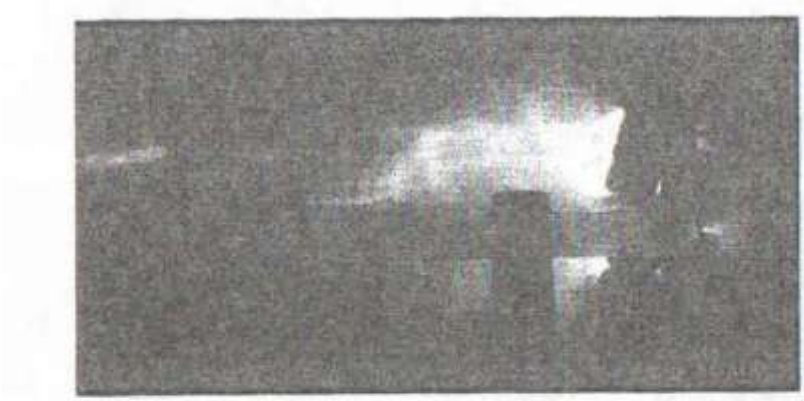

Fig. 3. Optical photograph of dielectric barrier discharge on flat plate

To measure distribution of electrons concentration in ionized airflow induced by high frequency barrier discharge, Tepler photograph photometric measurements were performed. [1]. Installation diagram for speed measurements and optical visualization is shown on Fig. 4.

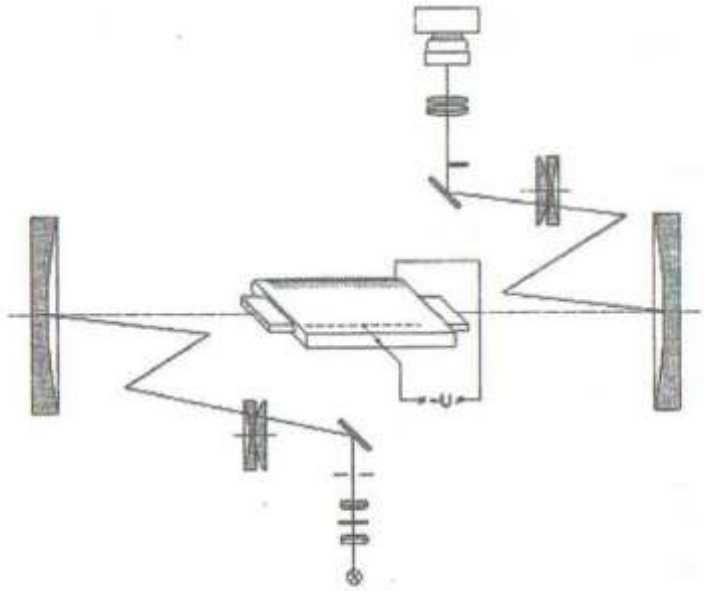

Fig. 4. Installation diagram for speed measurements and optical visualization

Focus of objective lens was F- 3213.5 mm. Diameter of observed field was 800 mm. Slit diaphragm (Δx = 0.1 mm wide) was installed parallel to the flat plate. To average turbulent fluctuations in the airflow photograph exposition was Δt = 2 s. In the illuminating part of device blue and red color filters with transparency maximum λ_b = 420 nm and λ_r = 640 nm respectively were installed alternately (Fig. 5).

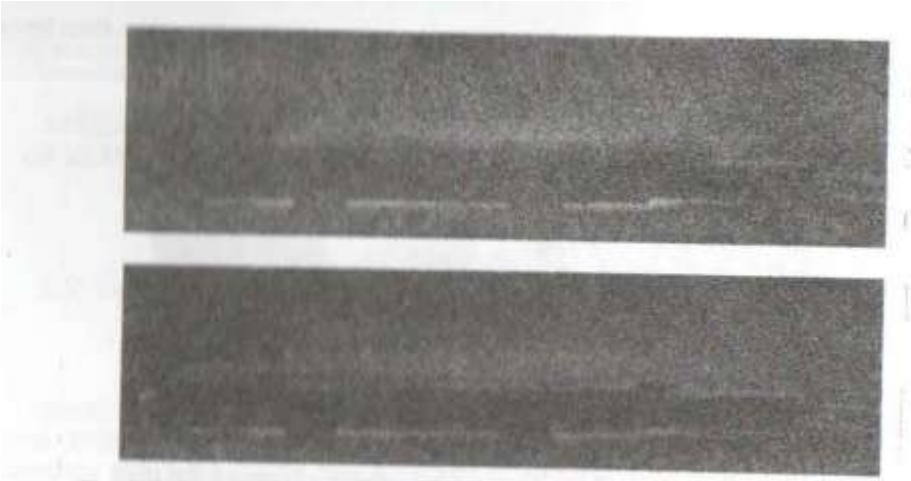

Fig. 5. Tepler snap-shot of boundary layer over flat plate for two wavelengths

Results and discussion

In case of little deviation angles in tested optical inhomogeneity, Euler equation can be used in simplified form [1].

$$tg\varepsilon_x \approx \int_{z_1}^{z_2} \frac{d\{\ln[n(x,y,z)]\}dz}{dx}; \qquad tg\varepsilon_y \approx \int_{z_1}^{z_2} \frac{d\{\ln[n(x,y,z)]\}dz}{dy}. \tag{1}$$

In investigated situation $\frac{\partial n}{\partial x}$ — is not dependent function from coordinate z and $\frac{\partial n}{\partial y}$ — is negligible quantity. So, the set of equations (1) modifies to equation

$$\varepsilon_x = \frac{1}{n_0}\frac{\partial n}{\partial x}(z_2 - z_1). \tag{2}$$

The value of ε_x can be determined from photometric measurements of Tepler photographs

$$\frac{\Delta I}{I_0} = \frac{\varepsilon_x F}{\Delta x}, \tag{3}$$

where I_0 is a background light intensity.

Absolute value of index of refraction in turbulent boundary layer can be found by using following equation

$$n(x,y) = n(x_0,y) - \int_{x_0}^{x} \frac{\partial n}{\partial x}(x,y)\,dx. \tag{4}$$

Index of refraction of plasma can be found from equation [2]

$$n - 1 = k\rho(1 + \beta T) - K\lambda^2 N_e, \tag{5}$$

$$\text{where } K = \frac{\pi e^2}{2 m_e c^2}.$$

Solving the set of equations (5) for λ_r = 650 nm and λb = 420 nm end employing dispersion formula for air index of refraction [3]

$$n - 1 = \frac{1}{10^6}\left[64.328 + \frac{29498.1}{146 - 10^6/\lambda^2} + \frac{255.4}{41 - 10^6/\lambda^2}\right]. \quad (6)$$

We will obtain temperature and concentration of electrons [4].

Two-dimensional distribution of averaged values of temperatures and concentrations of electrons in boundary layer are shown on Fig. 6.

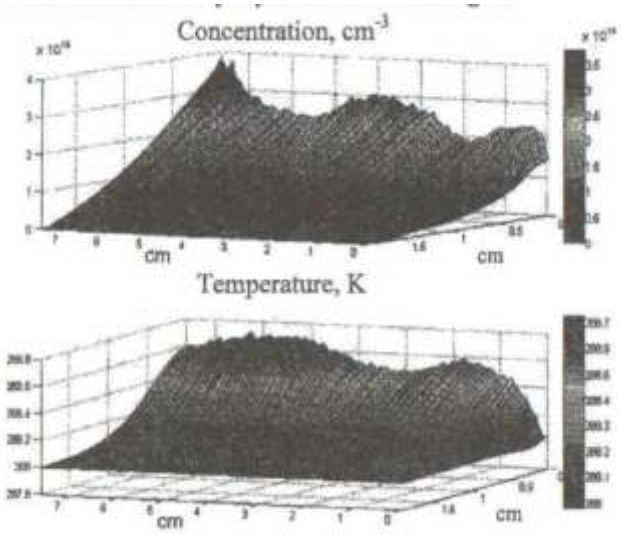

Fig. 6. Two-dimensional distribution of averaged values of temperatures and concentrations of electrons in boundary layer

On Fig. 7 distribution of averaged values of temperatures and concentrations of electrons along the flow on distance 10 mm, 6 mm and 3 mm from the plate surface is shown.

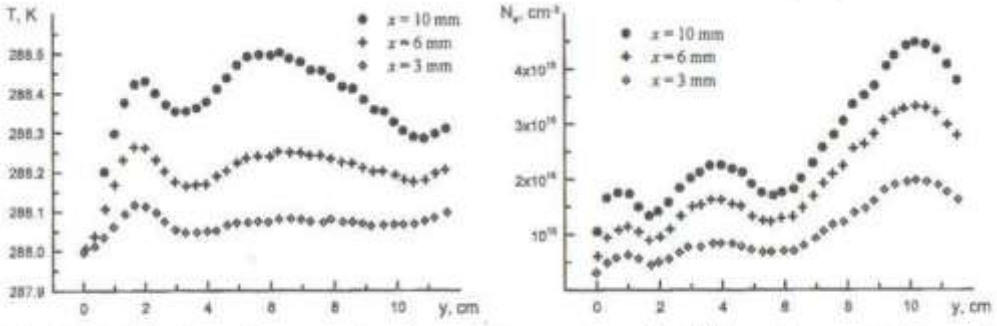

Fig. 7. Distribution of averaged values of temperatures (at left) and concentrations of electrons (at right) along the flow

Conclusions

Obtained concentration of electrons values is comparable to the relevant values for glow discharge. Wave-like behavior of concentration of electrons distribution along the flow is due to

volume charges generation, leading to potential redistribution. It can be seen from the non uniform temperature distribution. This effect is similar to Faraday dark space and cathode space forming in glow discharge. Ion acceleration in induced flow takes place mostly near minimum of electrons concentration distribution. Extremum of electrons temperature distribution are in antiphase to respective extremum of electrons concentration. So, in investigated discharge few interlaced spaces appear: near minimum of concentration distribution dominance of heating of flow appears and near maximum ion acceleration take place.

References

1. Vasil'ev L.A. Shadow methods. M.: Science, 1968.
2. Haddlstoun R. and Lenard M. Plasma diagnostic. M.: Peace. 1967.
3. Kikoin I.K. Tables of physical constants. M.: Atomizdat. 1976.
4. Gonsales R., Woods R., Eddins S. Digital image processing in MATLAB. M.: Technosphere, 2006. Pp. 206-253.

3. THERMALY NONEQUILIBRIUM PROCESSES

ROLE OF GAS MOTION IN FILTRATION COMBUSTION IN HIGH-VELOCITY REGIME

V.S. BABKIN

Institute of Chemical Kinetics and Combustion of SB RAS, Novosibirsk, Russia

Filtration gas combustion is a novel actively developing combustion field, which is theoretical and applied interest. This field includes a number of steady -state regimes with a wide range of velocities of thermal wave's propagation and reaction transmission mechanisms. Many aspects of filtration gas combustion are studied in details [1,2] and results of basic research were applied for solving practical problems of fire and explosion safety, power engineering, ecology, chemical and building engineering.

On the other hand, many principal aspects of filtration gas combustion are unexplained and unclear. Effects of forced filtration flows in high-velocity regime (HVR) are some of these problems. Really, all known studies of HVR deals with natural gas flow, i.e. caused by combustion process. In this case velocity of filtration is a function of the process and as key parameter is absent. Therefore, known formulas for the wave velocity under critical conditions do not include velocity of filtration [3]. This fact derived a viewpoint that main interphase interaction is a force one (flow turbulization), whereas thermal interaction does not influence on chemical transformation. However, the theory of filtration gas combustion [4] and analysis reveal that in principle in HVR thermal interphase interaction in chemical reaction zone is

possible if values of filtration velocity and burning rate are close. The goal of the present study is to clarify this problem.

A comprehensive investigation of influence unburnt gases flow on behavior, velocity, structural and critical characteristics of wave of filtration gas combustion in HVR was performed [5, 6]. A number of novel results were obtained by studying combustion of CH_4/air and C_3H_8/air mixtures in inert porous medium and individual narrow channels that model these processes in porous medium. A counterflow of combustible mixture was shown to reduce the linear burning rate up to complete stopping of the combustion wave at flow value equal to normal burning velocity of laminar flame. Here HVR changes into low-velocity regime (LVR) continuously in theory and in fact step-wise. The ratio of flame velocities in these regimes is of order of magnitude of 10^4. Though this phenomenon may be termed as "quasi-stabilization under HVR-conditions". Then, porous medium or wall of the tube is heated as a result of slow propagation of the flame in the location of combustion zone. In consequence of this, heat recovery takes place that results in rise of burning rate. Therefore, a further heating of porous medium and rise of burning rate is observed. .As the results of this positive feedback combustion wave reaches unsteady stabilization under LVR-conditions and then propagates in cocurrent coflow regime.

In some cases when diameter of channels is more than the critical one, a flameout is observed. The flameout is stipulated by the increase of the flow. At high gas flows, thermokinetic vibrations are observed under LVR conditions. Acoustic vibrations are also excited. Favorable conditions for formation of acoustic waves are large pores and combustible mixtures inclined to formation of cellular flames. At low velocity of propagation instability of the flame front that is caused by free convection is observed. The above phenomena were studied and their role in the mechanism of flame front propagation was determined.

Thus, the filtration flow in HVR was shown to appreciably influence on behavior of flame, its velocity and structural characteristics and determines a possibility of HVR-LVR transition, can result in instability and flame extinguishing, excite vibration processes.

Acknowledgements

This work was partly supported by grants: Program "Energy-saving SB RAS-2008", RFBR (grant No.06-03-32524).

References

1. Babkin V.S. Filtrational combustion of gases. Present state of affairs and prospects // *Pure and Applied Chemistry.* 1993. Vol. 65. Pp. 335-344.
2. Dobrego K.V., Zdnnok S.A. Phisics of filtration gas combustion, A.V. Luikov heat and mass transfer institute, Minsk, 2002. 203 p.

3. Bubltin V.S.. Korzhavin A.A., Buncv V.A. Propagation of premixed explosion flames in porous media // *Combustion and Flame.* 1991. Vol. 87. Pp. 182-190.
4. Laevsky Yu.M., Babkin V.S., Filtration gas combustion // Thermal wave propagation heterogenous media / Ed. by Yu. Matros, Novosibirsk: Nauke, 1988. Pp. 108-145.
5. Babkin V.S., Korzhavin A.A., Namyatov I.G., Drobyshevich V.I., Laevsky Yu.M. Filtration gas combustion under high velocities // 8-th, Asia-Pacific International Symposium on Combustion and Energy Utilization , Sochi, October 10-12, 2006.
6. Zamashchikov V.V., Kozlov Ya.V., Korzhavin A.A. Babkin V.S. Gas combustion in narrow individual channels // Submitted To Combustion , Explosion, and Shock Waves.

GROWTH RATE OF CARBON FILAMENTS IN METHANE PYROLYSIS ON AN IRON CATALYST AND ITS INTERPRETATION USING A KINETIC-THERMODYNAMIC APPROACH

A.V. KRESTININ, A.V. RAEVSKII, M.B. KISLOV

Institute of Problems of Chemical Physics, Russian Academy of Sciences,

Chernogolovka, Moscow Region, 142432, Russia

Among carbon filaments and nanoparticles of different types, single-wall carbon nanotubes (SWCNTs) and multi-wall carbon nanotubes (MWCNTs) are most promising in commercial application. Specific structure of carbon nanotubes combined with their "molecular" perfection provides this type of nanofilaments with a unique combination of chemical and physical properties. Unfortunately, wide application of SWCNTs and MWCNTs nowadays is strongly restricted by their high price, which was hundreds of USA dollars per 1 g of purified product for the last years.

Advances in developing efficient technologies of SWCNT and MWCNT production in catalytic hydrocarbon conversion could be more prominent if based on knowledge of mechanisms of nanotube nucleation and growth. Nowadays there are only fragmentary data on kinetics and growth mechanism of carbon nanotubes. Since kinetic model of a process is usually based on kinetic data, in this report we observed available kinetic data on carbon filament growth and presented some additional results in this field.

Kinetic studies of carbon filament growth were first reported more than 30 years ago by Baker et al. [1]. Initially a special technique of controlled atmosphere electron microscopy (CAEM) was developed [2] to directly observe the formation of carbon filaments on metal catalysts. In this case carbon filaments were grown in situ inside a specimen chamber of a transmission electron microscope (TEM) modified for this purpose. Consequently recorded

images of a growing filament allowed one to build a growth rate curve for the filament produced from a particular catalyst particle under given conditions.

A typical kinetic curve of carbon filament growth (Fig. 1) can be characterized by three scalar parameters, namely, induction time of filament nucleation, x, a linear growth rate in steady state, wfil, and the upper limit of filaments grown under given conditions, l_{max}. It was found that these values depend on the type of catalyst, temperature, gas phase chemical composition, and catalyst particle size.

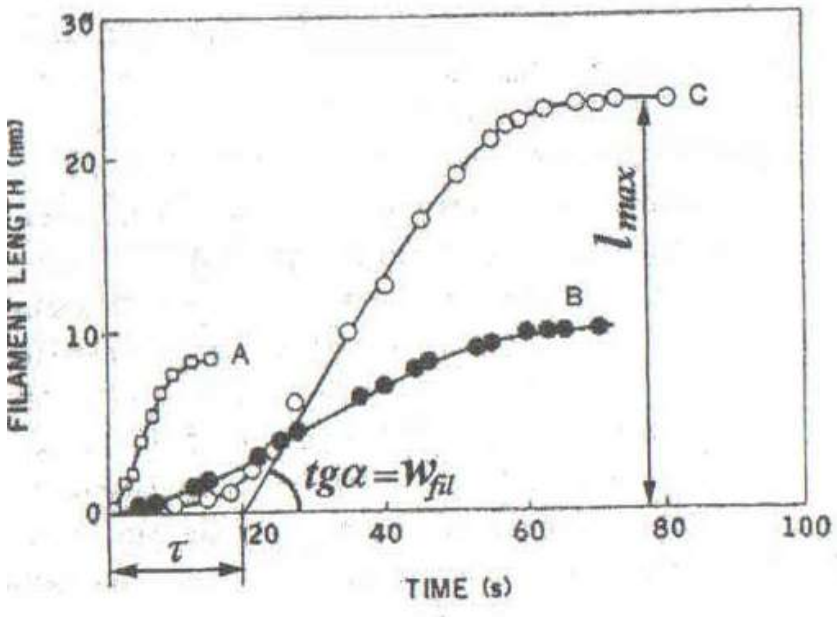

Fig. 1. Kinetic curves for filament growth (reproduced from Baker [3]). The main scalar parameters of a typical curve are: (i) the induction time of filament nucleation, τ, (ii) the linear growth rate at a quasi-steady state, w_{fil}, (iii) the maximal length of filaments grown in given conditions, l_{max}

To determine the filament groqth rate at steady state of the process we used a simple linear approximation of a corresponding part of a kinetic curve (Fig. 1) based on three measurements of the filament lengths depending on growth time. Lengths of filaments grown in different time points were measured with an optic microscope. Optical microscopy allows such measurements for carbon filaments ~ 100 nm and more in diameter. Detailed description of the measurement technique was given in [4].

Experimental measurements of the filament growth rate

Growth rate measurements were performed in HCH_4/H_2 mixtures at 950-1050 °C on an iron catalyst. The dependence of filament growth rate on methane concentration in the feeding flow is shown for three temperatures in Fig. 2.

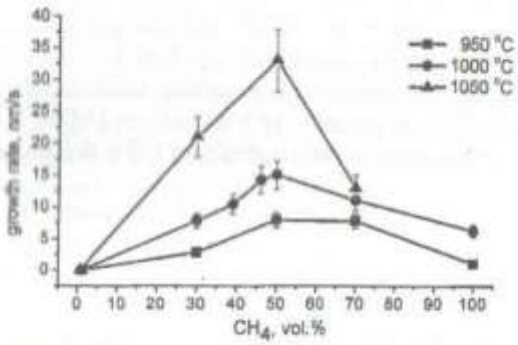

Fig. 2. Filament growth rate *versus* methane concentration in feeding CH_4/H_2 mixture at different temperatures. The feeding flow rate, v_{flow} = 0.6 l/min

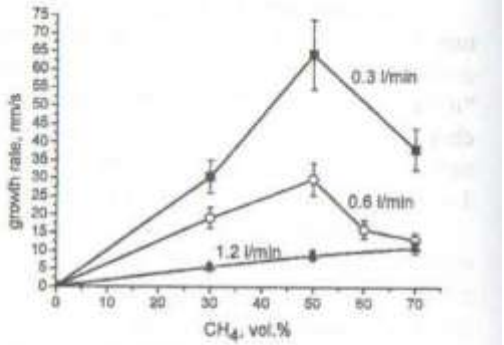

Fig. 3. Filament growth rate *versus* methane concentration in CH_4/H_2 feeding mixture at 1050 °C for different feeding gas flow rates

Further investigations revealed that methane concentration in the feeding flow could not be the only parameter, which enabled one to characterize fully gas phase activity in filament growth at elevated temperatures. It is seen from Fig. 3 that the lower was the rate of gas flow, i.e. the larger was the average residence time of gas in the hot zone of the reactor, the higher became the growth rate of carbon filaments. Thus, gas phase reactions affect the gas chemical composition and the growth rate. Detailed analysis of experimental data, which demonstrate the effect of methane pyrolysis products on kinetics of carbon filament growth was reported in [4].

Different modes of filament growth mechanism

The contribution of methane pyrolysis products to the filament growth rate near its maximal value is more than 10 times higher than the methane contribution (see Fig. 3, 50 % of methane, v_{flow} = 0.3 l/min). One can suppose that, providing continuously lowering gas flow rate, the maximal value of the filament growth rate increases to that characteristic of filament growth in acetylene atmosphere. As it was measured by others, the growth rate in 2 torr acetylene is ~ 400 nm/s for filaments of ~ 20 nm in diameter and ~ 1-2 pm/s for SWCNTs. The question arises: "What does this transition from one mode of the growth process to the other look like? Is it continuous in dependence on the gas flow rate or has a disruption of continuity?"

We were unable to perform experiments at very low gas feeding rates because of some restrictions of our set-up. However, to achieve higher concentrations of methane pyrolysis products one can subsequently increase methane concentration in the feeding gas flow. The results presented in Fig. 4 show that initially the growth rate lowers with increasing methane content in the feeding gas up to -60-70 % and then sharply rises up to ~ 200-400 nm/s when methane concentration increases in the range of 70-80 %. The latter values of the growth rate correspond to the filament growth rate in acetylene atmosphere measured by Baker.

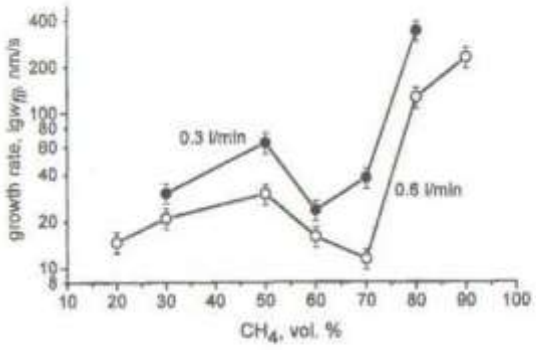

Fig. 4. Filament growth rate (lg w_{fil}) *versus* methane concentration in the feeding gas flow. T = 1050 °C

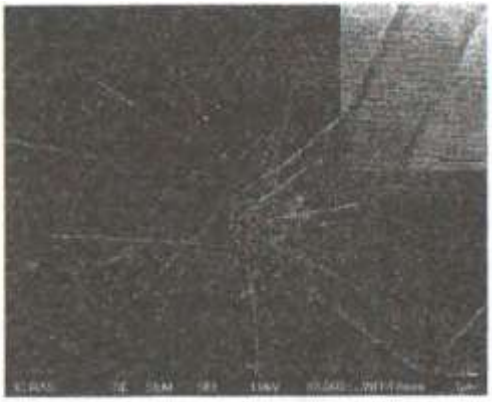

Fig. 5. Carbon filament grown in methane enriched mixtures at high growth rates, 1050 °C

In terms of non-equilibrium thermodynamics the result can be interpreted as follows. After the concentration of pyrolysis products reaches a critical value, the transformation occurs from one stable non-equilibrium state of a catalyst particle to another. The first state can be due to the filament growth from methane, the second state can be associated with the filament growth from acetylene. Possibly, such transition of the mechanism from one mode to another is accompanied by a disruption of continuity due to critical phenomena in the catalytic process. It is evident that such transition of a catalyst particle should entail some changes in the filament structure and/or morphology. Indeed, carbon filaments grown at high methane concentrations (T = 1050 °C) demonstrated another structural features (Fig. 5).

Application of joint kinetic-thermodynamic approach to kinetics of carbon filament growth

The catalytic filament growth in hydrocarbon environment is considered in existing models to consist of several consequent stages, which can be written as follows (Fig. 6). To analyze this phenomenon we used the joint kinetic-thermodynamic approach [5], which allows one to discuss any chemical kinetic phenomena in terms of chemical potentials of the reagents rather than in terms of their concentrations. As a starting point of this approach, a conventional representation of an elementary chemical reaction rate known in the theory of absolute rates of chemical reactions is used. After simple rearrangements the reaction rate can be written in the form where thermodynamic and kinetic parameters are well separated from each other. See for details [5].

A. Kinetic scheme of the mechanism of carbon filament growth in quasi-steady state:

(A1) $(1/n)C_nH_m + Cat \leftrightarrow C(surf.\ ads) + (m/2n)H_2 + Cat,$

(A2) C(surf. ads) ↔ C(surf. face),
(A3) C(surf. face) → C(surf. rear),
(A4) C(surf. rear) ↔ C(fil).

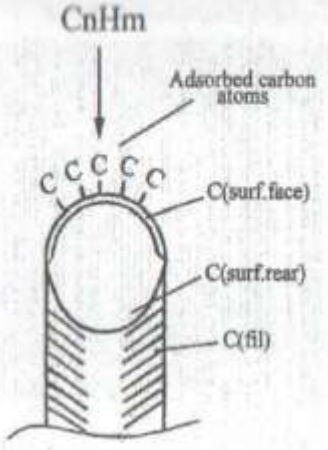

Fig. 6. Kinetic scheme of carbon filament formation

Provided that at steady state of filament growth process the rates of the consequent processes are equal, the filament growth rate, w_{ftl} can be presented as follows [6]:

$$w_{fil} = A(T, H_2)(a_{CnHm} - a_{C(surf.face)}),$$
$$a_{C(sur.face)} = \frac{d_{Cat}^{\delta}}{D_C} w_{fil} + a_{C(fil)}, \quad (1)$$
$$A(T, H_2) = \varepsilon_1 \exp\left(\frac{(m/2n)\mu_{H2} + \mu^0_{C(gr)} + \mu^0_{Cat}}{RT}\right).$$

Here a_{CnHm}, $a_{C(surf face)}$, $a_{C(fil)}$ are carbon activities of different carbon forms as denoted in Fig. 6; d_{cat} is a diameter of a catalyst particle; D_C is a diffusion coefficient of carbon dissolved in catalyst; ε_1 is permeability of a potential barrier of the catalytic reaction, μ_{H2}, $\mu^0_{C(gr)}$, μ^0_{Cat} are actual chemical potential of hydrogen, standard chemical potentials of graphite and catalyst, respectively.

Simple analysis showed [6] that the filament growth rate is linearly proportional to the difference between absolute activities of initial reagents and final reaction products that is linearly proportional to $(a_{CnHm} - a_{C(fil)})$. This theoretical prediction contradicts with experimental observations (Figs. 2, 3).

To overcome this contradiction we assumed that catalytic activity depends on carbon concentration in the monoatomic surface layer of a particle. A correction for the rate of the catalytic reaction was chosen as a linear term like that, which accounts for dissolved carbon in the chemical potential of a metal-carbon (ideal) solution. Thus, we obtained the following

expression for the rate of filament growth, W_{ftl}, considering the effect of "catalyst carbonization" on catalytic activity [6]:

$$w_{fil} = A(T, H_2)\exp(-\beta a_{C(surf.face)} / RT)(a_{CnHm} - a_{C(surf.face)}),$$
$$a_{C(surf.face)} = \frac{d_{Cat}^{\delta}}{D_C c^0 Me} w_{fil} + a_{C(fil)}. \quad (2)$$

Here β is a coefficient, which accounts for the increase in potential barrier of the catalytic reaction due to dissolved carbon in the surface layer of a catalyst. Detailed analysis of this model of the filament growth rate is given in [6].

Conclusion

The joint kinetic-thermodynamic approach in its canonic form cannot properly describe the observed experimental kinetic features of carbon filament growth. A correct description becomes possible after considering a negative effect of dissolved carbon on catalytic activity. The analysis of the proposed model showed that in conditions of high carbon activity in gas phase, when dissolved carbon affects strongly the catalytic reaction (inequality $\frac{\beta(a_{C(surf.face)} - a_{C(fil)})}{RT} >> 1$ in Eq. (2) holds), the filament growth rate depends on temperature and particle size precisely as if diffusion was a rate limiting step of filament growth. This explains kinetic data obtained by Baker and other authors in pure acetylene atmosphere. On the contrary, at low carbon activities in gas phase (before maximum of the growth rate in Figs. 2, 3) the catalytic reaction remains a rate limiting step of filament growth. In this case the growth rate does not depend on diffusion parameters.

A decrease of the filament growth rate when the latter passes its maximum can be explained by two effects acting simultaneously: a) a strong negative influence of dissolved carbon on catalytic activity, which makes the filament growth rate controlled by diffusion parameters, and b) a decrease of carbon diffusion in metal at high concentrations of dissolved carbon.

A jump in the filament growth rate at high carbon activities of gas phase was revealed (Fig. 4), which can be explained by a change in the quasi-steady state of a catalyst particle caused by changes in its physical state.

Acknowledgment

This work was supported by Russian Foundation for Basic Research, Grant # 05-03-33119, #08-03-00149.

References

1. Baker R.T.K., Barber M.A., Harris P.S., Feates F.S., Waite R.J. *// J. Catal.* 1972. Vol. 26. Pp. 51-62.

2. Baker R.T.K., Harris P.S. // *J. Physics E.* 1972. Vol. 5(8). Pp. 793-797.

3. Baker R.T.K., Chludzinski J.J., Dudash N. S., Simoens A.J. // *Carbon.* 1983. Vol. 21. Pp. 463-468.

4. Krestinin A.V., Raevskii A.V., Kislov M.B., Zvereva G.I., Kolesova 0.1. // *Kinetics and Catalysis.* 2008. Vol. 49(1). Pp. 74-84.

5. Parmon V.N. // *Catalysis Today.* 1999. Vol. 51. Pp. 435-456.

6. Krestinin A.V., Raevskii A.V., Kislov M.V. // *Carbon*, in press.

EXPERIMENTAL AND THEORETICAL STUDY OF SINGLE WALL QUENCHING OF LAMINAR FLAME AT HIGH PRESSURES

M. BELLENOUE[1], B. BOUST[1], S.I. FUTKO[2], S. LABUDA[1], J. SOTTON[1]

[1]Laboratoire de Combustion et de D6tonique, ENSMA, Futuroscope, France [2]A.V.' Luikov Heat and Mass Transfer Institute ofNAS of Belarus, Minsk, Belarus,

labuda@lcd.ensma.fr

Introduction

It is well known that flame stops propagating towards the wall because heat losses are large enough to slow down chemical reactions and flame is thus quenched. Flame quenching is accompanied by the peak of heat flux to the wall of high amplitude. Due to this circumstance the heat losses during flame quenching must be taken into account for optimization of total energetic balance of combustion or ignition device [1]. Moreover, information on combustion obtained with diagnostic gauge inserted in combustion chamber is typically affected by the flame quenching in vicinity of this gauge [2]. Thus, correct interpretation of gauge signal needs detailed knowledge on flame quenching phenomenon.

Implementation of new combustion technologies, further thermal and environmental improvement of internal combustion (1C) engines and development of new combustion diagnostics need information on the heat exchange processes during wall flame quenching at elevated pressures. For some pressure ranges (some tens of bar), this information is very poor. Moreover, 1C engines also require data compatible with non-stationary, single-shot combustion; such data cannot be predicted by stationary correlations, as previously demonstrated in [3, 4]. Because at high pressures the carrying out of flame quenching experiments would be difficult an

adequate model of flame-wall interaction is needed to predict and connect the main quenching parameters, such as quenching distance and wall heat flux, in a wide pressure range. The development of model of flame/wall interaction taking into account the gasdynamics flow structure near the wall and flame stretching, without the use of any empirical coefficient, is a key of importance, first of all for engineering application. Correct modelling of flame quenching at high pressures also helps to understand detailed mechanism of transient flame wall quenching at these conditions.

In this paper the results of experimental and numerical study of single wall flame quenching in the pressure range 0.1-2.5 MPa are compared and numerical prediction for evolution of quenching parameters (wall heat flux and quenching distance) for the pressure up to 5 MPa has been made.

Theoretical model

A numerical ID code taking into account flame hydrodynamics, viscosity force, heat transfer, species diffusion and chemical kinetics of methane oxidation has been developed and used for the modelling of flame-wall interaction. Software application package GASBURN characterised by very stable and fast algorithms with controllable numerical (artificial) viscosity was intended for this purpose. Verification of the molecular transport model as far as the chemical and thermal structure of the flame has been made using the CHEMKIN database.

A comprehensive model describing phenomena of flame quenching includes the governing set of the equations describing non-steady gas dynamics of chemically reacting gas.

This set includes the Navier-Stokes equations of gas mass continuity, mass conservation equations for gas components and corresponding equation of energy conservation:

$$\frac{d\rho}{dt} = -\rho\nabla\mathbf{u}, \tag{1}$$

$$\rho\frac{d\mathbf{u}}{dt} = -\nabla p + \nabla\boldsymbol{\sigma}', \tag{2}$$

$$\rho\frac{dc_i}{dt} = \dot{\rho}_i + \nabla\cdot(\rho D\nabla c_i),\ i = \overline{1,N}. \tag{3}$$

Here p_i - i-th component mass generating rate due to chemical reactions, $\sum_i \dot{\rho}_i = 0$; D - diffusivity. Energy conservation equation is written in form of enthalpy conservation with regard to diffusion and heat conductivity processes:

$$\rho\frac{dH}{dt} = \frac{dP_0}{dt} + \nabla\cdot\left(\rho\sum_i h_i D\nabla c_i + \lambda\nabla T\right), \tag{4}$$

where h_i - mass enthalpy of i-th gaseous component, λ - heat conductivity coefficient. State of gas is defined by pressure P, temperature T, gas velocity u, gas components concentrations C_i

(molar) or c (mass) together with gas state equations $\rho = \frac{PM}{RT}$ ***and*** $H(T, c_1, ..., c_N) = \sum_i^N c_i h_i(T)$. Initial gas temperature was varied from T_0 =300 K up to 450 K, according to the experimental conditions. Combustion ignition is simulated by setting temperature step function (floor temperature - T_0, top temperature - T_{ol}). During flame propagation pressure remains constant and equal to P. Impermeability and no-slip conditions for gas are implied at the wall:

$$(\mathbf{n} \cdot \nabla) p = 0; \quad \mathbf{u} = 0 \text{ at } z = 0 \text{ or } r = R. \tag{5}$$

Conditions of impermeability are implied on gas components concentrations at tube's walls, i.e. $(\mathbf{n} \cdot \nabla) c_i = 0.$ At the wall, the temperature boundary conditions are $T_w = T_{gas} = T_0$, where T_0 - initial (ambient) gas temperature, T_{gas} - gas temperature in vicinity of the wall, T_w - wall temperature. These conditions mean that all heat transported through the gas to the wall is totally absorbing by the wall having infinite thermal conductivity. Developed numerical code allows reconstruction of the temporal and spatial evolutions of all quenching parameters including the energy release across the flame front, gas temperature profiles, maximal wall heat flux and spatial distributions of chemical species. Simplified and detailed chemical kinetics of methane oxidation has been used in calculations. For verification of physical model used for calculations, the results of modelling have been compared with experimental data obtained.

Experimental

Experiments were carried out with a constant volume chamber of 70x75x120 mm^3. Methane-air mixtures were ignited by spark electrodes. For each shot, the time evolution of pressure was recorded by a piezoelectric transducer Kistler 601 A. Simultaneous measurements of quenching distance and wall heat flux were used to characterize flame/wall interaction. The chamber was fitted with lateral glass windows in order to measure quenching distance by direct visualization. Quenching distance was determined as the distance between emission zone of flame front and wall, through the processing of images [3] obtained with a 16-bit intensified camera (Princeton Instruments PI-MAX:IK) running in single-shot mode and synchronized with ignition event. For a frame size 1024x1024 pxl^2, the resolution was 14μm/plxel. Heat losses to the obstacle were recorded by a heat flux gauge CFTM, provided by CRMT. The gauge of

diameter 4 mm comprises two J-type thermocouples formed by the junction of constantan wires with the steel body; one is placed at the surface of the gauge, the other one is 6 mm deep in the body. Their time response is of the order of 1 μs, according to the manufacturer.

In head-on quenching (HOQ) configuration the heat flux gauge was flush-mounted in the chamber wall. Spark electrodes ignited the mixture at the centre of the chamber, just in front of the heat flux gauge. As the flame front reached the wall, its curvature was weak enough to ensure that the interaction was in head-on configuration. In side-wall quenching (SWQ) configuration, spark electrodes were shifted relatively to symmetry axis of heat flux gauge. As a result, the flame front propagated and quenched continuously along the wall where gauge was placed, allowing sidewall interaction.

Results and discussion

Results of quenching distance and maximal wall heat flux measurements are shown in Figs. 1-2. For each pressure, quenching distance was determined as the minimum value obtained in 10 shots. Simultaneous measurements of quenching distance and heat flux were made with methane-air mixtures at equivalence ratio ϕ = 0.7 and ϕ = 1.0, in HOQ and SWQ configurations, for initial pressure ranging in 0.05-0.25 MPa. In Fig. 1 and Fig. 2 P_q indicates the pressure during quenching.

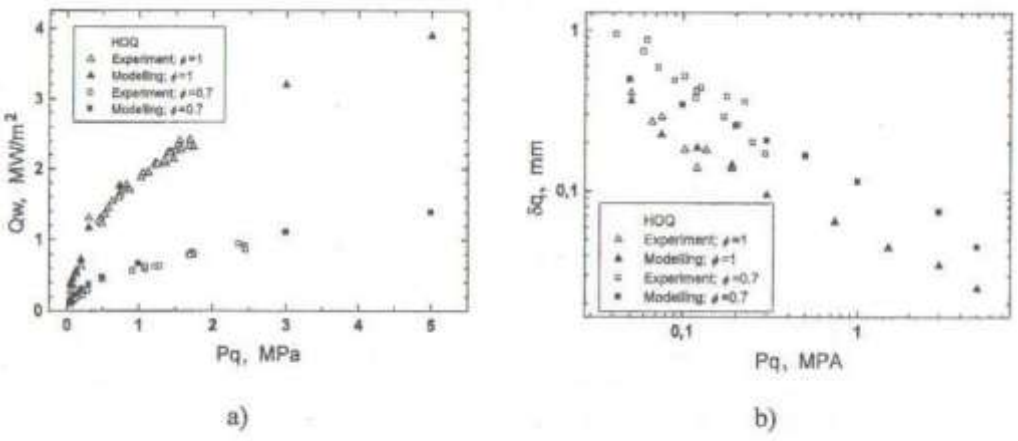

Fig. 1. Pressure evolution of wall heat flux (a) and quenching distance (b) for stoichiometric and lean fuel (ϕ = 0.7) mixtures for HOQ

During flame-wall interaction, heat flux reaches its maximum value, Q_w, as the flame-wall distance, δ_q, reaches its minimum. Heat flux results show that wall heat flux is higher in HOQ than in SWQ configuration. In SWQ configuration, flame front is naturally stretched, so flame quenching can occur due to smaller heat losses. This is also the reason why quenching distance is higher in SWQ configuration. The tendency of wall heat flux variation versus pressure or versus equivalence ratio is the same in HOQ and SWQ configurations. Similarly, the evolution of quenching distance versus pressure or equivalence ratio is also the same for HOQ

and SWQ. Thus, both types of flame-wall interactions do not differ in the tendency of quenching parameters but in their magnitude. For HOQ pressure evolution of maximal wall heat flux has been studied experimentally in increased pressure range for P_q - up to 2.7 MPa. Results obtained show that Q_w continues to grow monotonically with pressure rise, also for the range of high pressures (see Fig. la).

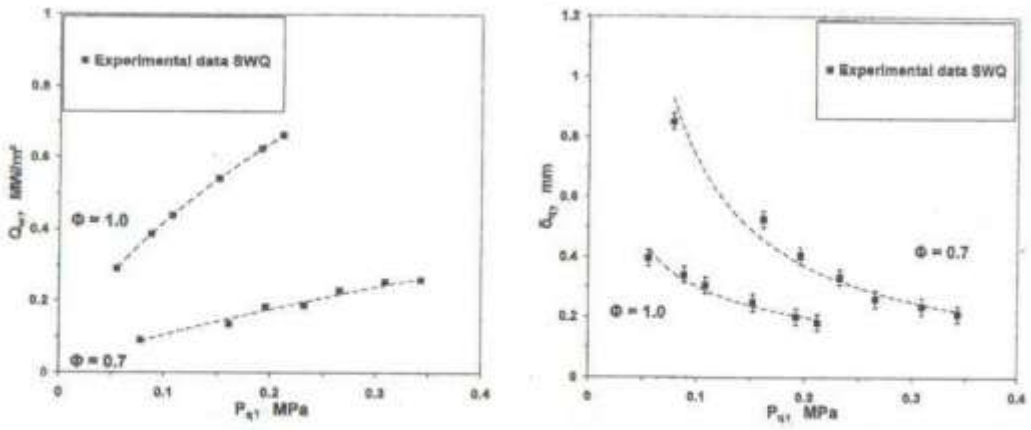

a) b)

Fig. 2. Pressure evolution of wall heat flux (a) and quenching distance (b) for stoichiometric and lean fuel ($\phi = 0.7$) mixtures for SWQ

With stoichiometric and lean fuel mixture used, quenching distance became too thin for pressure P_q superior 0.2-0.25 MPa, and could not be optically measured. As expected, 5_q is thinner in HOQ than in SWQ configuration (see Fig.lb and 2b), and decreases with increasing of pressure P_q. In addition, 5_q is approximately 2-3 times thinner for ϕ = 1.0 than for ϕ = 0.7. This confirms that the flame gets closer to the wall as the flame power grows due to pressure or equivalence ratio.

Comparison of theoretical and experimental results

Developed theoretical model of flame quenching on a single wall was tested against the experimental data in a pressure range 0.05-1.8 MPa for stoichiometric and 0.7-2.5 MPa for lean (ϕ=0.7) CH_4/air mixtures. Experimental and calculated temporal profiles of wall heat flux showed good correlation for both mixtures used. As one sees in Fig. la, calculated values of maximal wall heat flux during HOQ for stoichiometric and lean fuel mixtures correlates well with its experimental data obtained in the pressure range up to 2.7 MPa. It is worth noting that calculations have been carried out for extended pressure range, up to 5 MPa, where experimental measurements are difficult to carry out with our experimental set-up. Numerical results predict the following increasing of Q_w with pressure rise, also for increased pressures. It is worth noting that simplified kinetic model used for calculations needs to be verified for the pressure range superior 4-5 MPa as well as for very low pressures (less than 0.1 MPa).

The same comparison between experimental and numerical data has been carried out for pressure evolution of quenching distance. Correlations between experimental and modelling results are presented in Fig. lb. It is evident that both curves correlate well. As for maximal wall heat flux, numerical code allows prediction of the pressure evolution of 6_q for high pressures in the range 1-5 MPa (Fig. lb). It is worth noting that behavior of 6_q obtained in our calculations correlates well with data predicted from other flame quenching formulation [1].

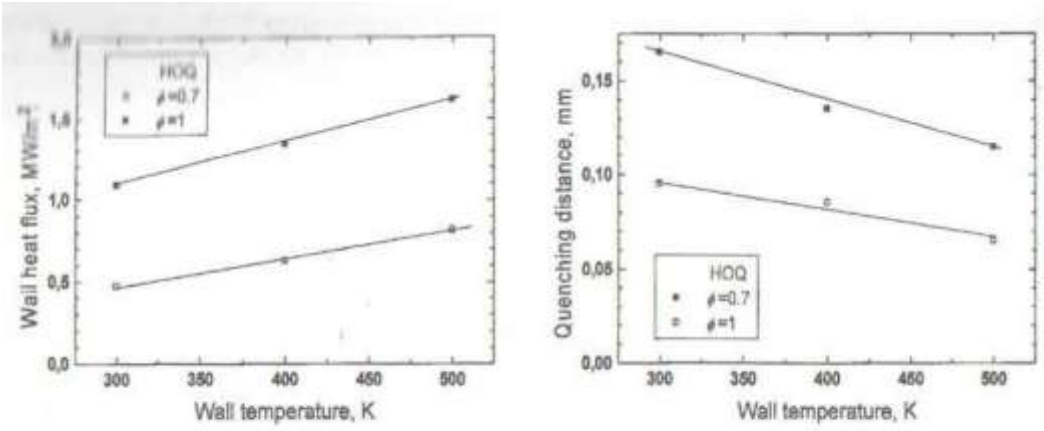

a) b)

Fig. 3. Dependence of calculated maximal wall heat flux (a) and quenching distance (b) on the wall temperature for stoichiometric and lean fuel ($\phi = 0.7$) mixtures. $P_q = 0.5$ MPa

Because the wall temperature can significantly modify the flame quenching, we have numerically analyzed the dependence of quenching characteristics on wall temperature. Results of calculations, presented in the Fig. 3, confirm expected from [5] increasing of wall heat flux and the decreasing of quenching distance with the rise of wall temperature. Both dependencies can be attributed to closer position of the flame to the wall at quenching for higher wall temperatures.

Conclusions

Experimental study of laminar flame quenching on a single wall has been carried out. Experimental results obtained were used for validation of theoretical model describing the thermal flame quenching on a single wall. It was shown that results of numerical modelling of HOQ using both simplified and detailed kinetic mechanism of methane oxidation correlate well with experimental data in all range of pressure variation during experiment. Coincidence of experimental and theoretical results in the pressure range 0.05-2 MPa allowed prediction of quenching parameters (quenching distance and maximal wall heat flux) on the pressure variation for increased pressure range, up to 5 MPa, where experimental data are difficult to obtain. Numerical and experimental results obtained are important for the improvement of numerical models of ignition at elevated pressures, optimization of near wall combustion and its diagnostics.

The work was conducted as part of the joint project #20166 CNRS-FRFRB.

References

1. Sher E., Heywood J.B., Hacoben J. // *Combustion Science and Technology.* 1992. Vol. 83. Pp. 323-325.
2. Bellenoue M., Karrer M., Labuda S., Makarov M., Sotton J. The use of Langmuir probe for diagnostics of flame quenching //21st ICDERS, Poitiers, ID156.
3. Sotton J., Boust B., Labuda S.A., Bellenoue M.// *Combustion Science and Technology.* 2005. Vol. 177. Pp. 1305-1322.
4. Boust B., Sotton J., Labuda S.A., Bellenoue M. // *Combust. Flame.* 2007. Vol. 149. Pp. 286-294.
5. Popp P., Baum M. // *Combust. Flame.* 1997. Vol. 108. Pp. 327-348.

MODELING OF COATING MODIFICATION USING CONDENSED PHASE SYNTHESIS

S.N. SOROKOVA[1], A.G. KNYAZEVA[2]

[1]Tomsk Polytechnic University, Tomsk, Russia, s_sorokova@tpu.ru [2]Institute of strength physics and materials science SB RAS, Tomsk, Russia

Introduction

Solid phase synthesis, including self-propagating high-temperature synthesis, provides wide possibilities for producing a variety of materials. The use of the energy of the electron beam has proved effective in many fields, including thermal treatment and plating. The combined technique of electron-beam treatment [1, 2] of a precoated material, during which the coating synthesis is performed, allows realizing the advantages of electron beam treatment and solid phase transformations to obtain the coatings with required properties.

A mathematical model of the electron-beam-heating-assisted synthesis of a $TiNi_3$+Ti coating on an iron substrate with solid phase transformations is proposed and studied below. We note that the joining formation or transient regions between the materials are rarely formed during the synthesis of a coating on a substrate [3]. To form the transient region, additional heat treatment is required. However, the substrate that removes heat from the heating region may considerably affect the regimes of reaction initiation and layer-by-layer propagation in the solid phase, similar to the effect of inert inclusions [4], inert rods [5], or the materials being joined [6] on the transformation regimes in such systems.

Now we discuss the features which appear in the synthesis regimes when the stresses and strains are taken into consideration.

The mathematical model

Let assume that the $TiNi_3$+Ti - coating of h_c thickness is deposited on thin plate from iron of h_b thickness. To a first approximation the elements re-allocation on plate thickness with coating can not considered. We can neglect elements redistribution along the plate thickness assuming that this slow process happens after coating synthesis that is during cooling stage. The plate is free from external forces action. According to [7], one can believe, that the conditions correspond to plane stressed state. Let consider that external source moving along the coating surface with the rate V, heats the surface in the axis direction perpendicular to motion direction uniformly. Described conditions realize when the scanning electron beam flared-out into line is used and scanning thickness exceeds the specimen thickness. Under action of external energy source, the chemical reactions initiate in the coating. The coating and substrate are thermally thin, that allows integrating all equations along the specimen thickness. As a result we come to one dimensional problem formulation which is analogous to [8] and includes thermal conductivity equation coupling with the stresses,

$$c_{eff}\frac{\partial T}{\partial t}=\frac{\partial}{\partial x_1}\left(\lambda_{T,b}\left(\delta\left(k_{\lambda,T}-1\right)+1\right)\frac{\partial T}{\partial x_1}\right)-D\left(A-3B\right)\frac{\partial \sigma_{22}}{\partial t}-$$
$$-\sigma_0\varepsilon_{eff}\frac{\left(T^4-T_0^4\right)}{h_c+h_b}+\frac{q_s\left(t,x_1\right)}{h_c+h_b}+W_{eff};$$

the kinetic equation system for $TiNi_3$+Ti [9]

$$\frac{\partial y_1}{\partial t}=-y_1\varphi_1,\ \frac{\partial y_2}{\partial t}=-y_2y_3\varphi_2-y_2y_4\varphi_3,\ \frac{\partial y_3}{\partial t}=2y_1\varphi_1-y_2y_3\varphi_2,$$
$$\frac{\partial y_4}{\partial t}=y_1\varphi_1-y_2y_4\varphi_3,\ \frac{\partial y_5}{\partial t}=y_2y_4\varphi_3 \qquad (2)$$

and equations for determination of the stress and strain tensor components succeeding basic equation [10]

$$\sigma_{22}=\left(-\tilde{\varepsilon}^T+\left(\frac{4}{L_x}-\frac{6x_1}{L_x^2}\right)I_1+\left(\frac{12x_1}{L_x^3}-\frac{6}{L_x^2}\right)I_3\right)\left(A-B\right)^{-1}+$$
$$+\left(-\tilde{\varepsilon}^{(i)}+\left(\frac{4}{L_x}-\frac{6x_1}{L_x^2}\right)I_2+\left(\frac{12x_1}{L_x^3}-\frac{6}{L_x^2}\right)I_4\right)\left(A-B\right)^{-1}, \qquad (3)$$

$$\varepsilon_{11}=-B\sigma_{22}+\tilde{\varepsilon}^T+\tilde{\varepsilon}^{(i)},$$
$$\varepsilon_{22}=\left(A-B\right)\sigma_{22}+\tilde{\varepsilon}^T+\tilde{\varepsilon}^{(i)}, \qquad (4)$$
$$\varepsilon_{33}=-B\sigma_{22}+\tilde{\varepsilon}^T+\tilde{\varepsilon}^{(i)},$$

where T is the temperature; $y_1=[TiNi_3]$, $y_2=[Ti]$; $y_3=[Ni]$, $y_4=[TiNi]$, $y_5=[Ti_2Ni]$ are the molar concentrations of reagents and reaction products; $\delta=h_c/(h_c+h_b)$; $c_{eff}=c_b\rho_b(\delta(k_c-1)+1)+3D\alpha_{T,b}[\delta(k_\alpha-1)+1]$; $\tilde{\varepsilon}^T=\alpha_{T,b}(T-T_0)[\delta(k_\alpha-1)+1]$ – total thermal strain; $\tilde{\varepsilon}^{(l)}=\delta\sum_{l=1}^{5}\alpha_l(y_l-y_{l,0})$ – total concentration strain; $D=3\alpha_{T,b}K_b(\delta(k_V k_\alpha-1)+1)T$;

$A=\frac{1}{2\mu_b}\left(\delta\left(\frac{1}{k_\mu}-1\right)+1\right)$; $B=\frac{\lambda_b}{6\mu_b K_b}\left(\delta\left(\frac{k_\lambda}{k_\mu k_V}-1\right)+1\right)$; $k_{\lambda,T}=\lambda_{T,c}/\lambda_{T,b}$; $k_c=c_c\rho_c/c_b\rho_b$;

$k_V=K_c/K_b$; $k_\alpha=\alpha_{T,b}/\alpha_{T,c}$; $k_\lambda=\lambda_c/\lambda_b$; $k_\mu=\mu_c/\mu_b$; $k_\rho=\rho_c/\rho_b$; $c_b,\rho_b,\lambda_{T,b}$ – specific heat, mass density and heat conduction of substrate; $c_c,\rho_c,\lambda_{T,c}$ – specific heat, mass density and heat conduction of coating; K_b,K_c – effective bulk modulus of substrate and coating; $\lambda_c,\mu_c,\lambda_b,\mu_b$ are effective Lame coefficients in substrate and coating; subscripts "c" – correspond to the effective properties of the coating; subscripts "b" – correspond to the effective properties of the base, (in the general case all properties depend on temperature); α_l – is the concentration expansion coefficients [11], $l=1...5$; $\alpha_{T,b},\alpha_{T,c}$ – is the linear heat expansion coefficients for the base and coating; L_x – sample length.

The functions φ_v takes the form:

$$\varphi_v=k_v\exp\left(-\frac{E_{av}}{RT}\right)\exp(-m_v y)y^{-n_v},\ v=1,2,3,$$

where k_v and E_{av} are the preexponents and activation energies of the reactions; $y=y_4+y_5$ is the concentration of the total reaction product; m_v,n_v are the deceleration parameters [8].

The total heat source from the chemical reactions of W_{eff} in the heat conduction equation is

$$W_{eff}=\delta W_1-3\delta DW_2=\delta\rho_c\sum_{l=1}^{5}\frac{h_l}{m_l}\frac{dy_l}{dt}-3\delta D\sum_{l=1}^{5}\alpha_l\frac{\partial y_l}{\partial t},$$

or, taking into account the kinetic equations,

$$W_{eff}=(\delta Q_1-3\delta D\Delta Q_1)y_1\varphi_1+(\delta Q_2-3\delta D\Delta Q_2)y_2y_3\varphi_2+(\delta Q_3-3\delta D\Delta Q_3)y_2y_4\varphi_3,$$

where $Q_{1,2,3}$ are the heats of the chemical reactions:

$$Q_1=\frac{\rho_c}{m}(-h_1+2h_3+h_4);\ Q_2=\frac{\rho_c}{m}(-h_2+h_4-h_3);\ Q_3=\frac{\rho_c}{m}(-h_2-h_4+h_5);$$

h_l is the partial molar enthalpies of the materials. Quantities $\Delta Q_{1,2,3}$ are calculated with the help of the formulae

$$\Delta Q_1=-\alpha_{l,1}+2\alpha_{l,3}+\alpha_{l,4};\ \Delta Q_2=-\alpha_{l,2}+\alpha_{l,4}-\alpha_{l,3};\ \Delta Q_3=-\alpha_{l,2}-\alpha_{l,4}+\alpha_{l,5}.$$

At the initial time, we have the conditions

$$t=0:\ T(x,0)=T_0,\ y_1=y_{10},\ y_2=y_{20},\ y_3=y_4=y_5=0,\ \sigma_{22}=0,\ \varepsilon_{11}=\varepsilon_{22}=\varepsilon_{33}=0.$$

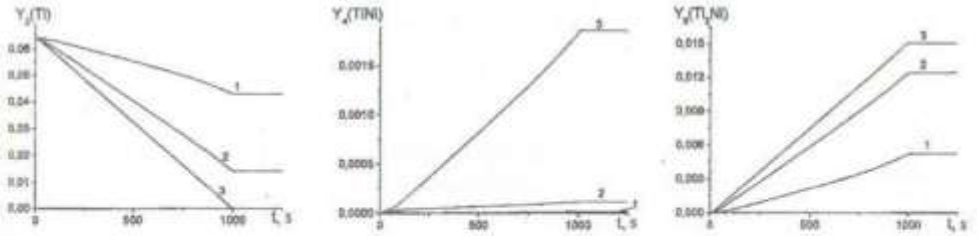

Fig. 1. Of total concentrations for coupled problem definition as a function of the source power density: $1-q_0=1000$ W/cm^2, $2-q_0=2000$ W/cm^2, $3-q_0=3000$ W/cm^2

The thermodynamic and physical properties are known from the experimental date or are calculated of special shape [8, 11]. The problem was solved numerically using an implicit difference scheme that is second-order accurate in space and first-order accurate in time with linear sweep.

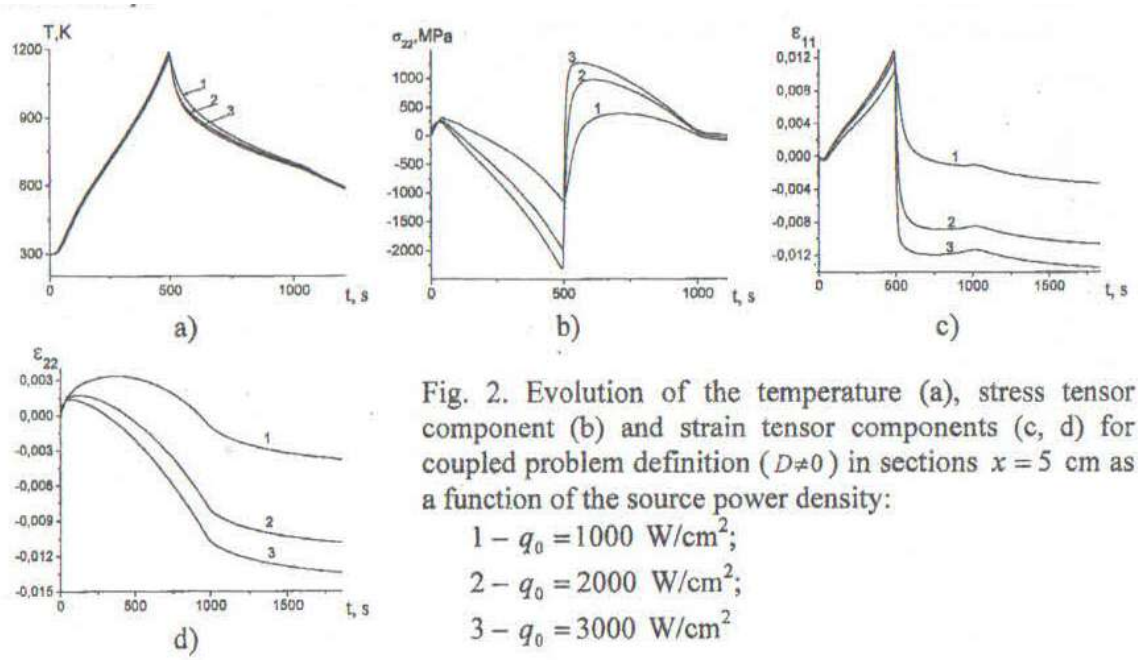

Fig. 2. Evolution of the temperature (a), stress tensor component (b) and strain tensor components (c, d) for coupled problem definition ($D\neq0$) in sections $x=5$ cm as a function of the source power density:

$1-q_0=1000$ W/cm^2;

$2-q_0=2000$ W/cm^2;

$3-q_0=3000$ W/cm^2

Analysis of results

In addition to spatial distribution of temperature and concentrations for various time moments, the dynamics of coating synthesis on a substrate can be characterized by the integral curves

$$Y_l(t)=\frac{1}{L_x}\int_0^{L_x} y_l(x,t)dx\,,\ l=1,...,5\,.$$

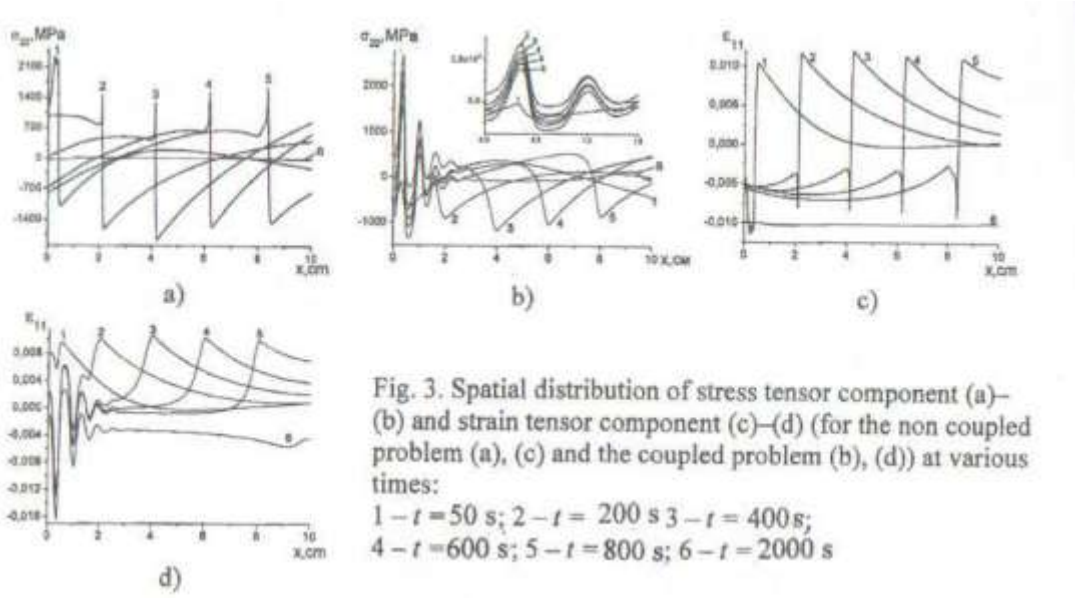

Fig. 3. Spatial distribution of stress tensor component (a)–(b) and strain tensor component (c)–(d) (for the non coupled problem (a), (c) and the coupled problem (b), (d)) at various times:
$1 - t = 50$ s; $2 - t = 200$ s $3 - t = 400$ s;
$4 - t = 600$ s; $5 - t = 800$ s; $6 - t = 2000$ s

The change of integral concentrations in time for different values of the power density are shown in Fig. 1 for Ti, TiNi and Ti_2Ni. As evident that TiNi and Ti_2Ni phase emission increases when power density of the source rises. The increasing of power density effect weakly on the temperature curve maximum, bat it leads to the increasing of stress in sections (Fig. 2 b) and implies the compressing strains appearance (Fig. 2, c, d).

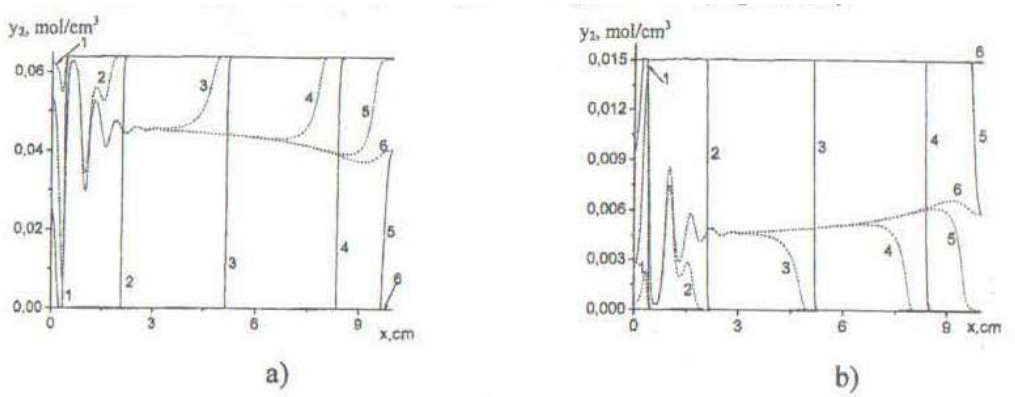

Fig. 4. Spatial distribution of Ti (a) and Ti_2Ni (b) concentrations at various times $1 - t = 50$ s; $2 - t = 200$ s; $3 - t = 400$ s; $4 - t = 600$ s; $5 - t = 800$ s; $6 - t = 2000$ s (solid lines is non coupled problem; dashed lines is coupled problem)

The results of the numerical investigation has shown that the coupled character of the heat transfer and deformation processes is principal because allows to discover new qualitative effects. If stresses and strains influence on the process synthesis are not into account in the model, the resulting stress and strain fields in the synthesis finish will practically homogeneous. The coupled character of various processes leads to essential no homogeneous residual stresses and strains and not uniform structure in the specimen region close to start of the source motion. For $x \to 0$, the stresses are zero obviously. Similar effects have been found in experimental researches also. The Figs. 3, 4 illustrate that. So, the distributions of phases Ti and Ti_2Ni

concentrations along the plate are presented in Fig. 4 for the problem when $D = 0$ (solid lines) and $D \neq 0$ (dashed lines).

The result was depended on the selecting chemical system, the synthesis conditions and the geometric parameter.

The work was supported by the Russian Science Foundation, grant № 08-08-90008-Bel_a.

References

1. Knyazeva A.G. and Pobol I.L. Composition Coating Formation on the Base of Intermetallide Phase Using Electron-Beam Treatment // *Trans, of 8th Int. Conf. On Modification of Materials with Particle Beams and Plasma Flows.* Tomsk, 2006. P. 396.
2. *Knyazeva A.G. and Pobol I.L. Formirovanie pokrytiya s ispoPzovaniem sinteza v kondensirovannoi faze i elektronno - luchevoi obrabotki* II Trudy II Mezhdunarodnoi nauchno-tekhnicheskoi konferentsii ".Mashinostroenie i tekhnosfera XXI veka" (Proc. II Int. Sci-Tech. Conf. on Mechanical Engineering and Technosphere of the 21st Century), *Sevastopol. 2005. Vol. 4. P. 195.*
3. Pobol I.L. Nauchnye i tekhnologicheskie osnovy obrabotki konstruktsionnykh i instrumental'nykh materialov i polucheniya izdelii s ispoPzovaniem elektronnoluchevogo vozdeistviya (Scientific and Technological Foundations of Constructional and Tool Material Treatment and Article Production Using the Effect of Electron Beams), Doctoral (Eng.) Dissertation, Minsk: Physicotechnical Institute, National Academy of Sciences of Belarus, 2007.
4. Prokof'ev V.G. and Smolyakov V.K. Impact of Structural Factors on Unsteady Combustion Modes of Gasless Systems // *Combust. Explos. Shock Waves.* 2003. Vol. 39, No. 2. P. 167.
5. Ivleva T.P. and Merzhanov A.G. Mathematical Simulation of Three-Dimensional Spin Regimes of Gasless Combustion // *Combust. Explos. Shock Waves.* 2002. Vol. 38, No. 1. P. 41.

6. Knyazeva A.G. and Chashchina A.A. Numerical Study of the Problem of Thermal Ignition in a Thick-Walled Container // *Combust. Explos. Shock Waves.* 2004. Vol. 40, No. 4. P. 432.
7. Sedov L.I. Continuum mechanics, 1994.
8. Sorokova S.N., Knyazeva A.G. Simulation of coating phase structure formation in solid phase synthesis assisted by electron-beam treatment *// Theoretical Foundations of Chemical Engineering.* 2008. Vol. 42, No. 4. Pp. 443-451.
9. Hansen M.A. and Anderko K.P. Constitution of Binary Alloys, New York: McGraw-Hill, 1957.
10. Boley B., Weiner J. Theory of thermal stresses, 1964.
11. *Sorokova S.N., Knyazeva A.G. //* The materials of X international conferences of"Physics - chemical processes in inorganic materials". *2007. Vol. 2. Pp. 167-170.*

PERFECTION OF PHENOMENOLOGICAL MODEL OF DEFLAGRATION EXPLOSION UNDER NON-SELF-SIMILAR CONDITIONS

S.I. SHABUNYA[1], V.V. MARTYNENKO[1], A.S. MIKANOVICH[2]

[1]A.V. Luikov Heat and Mass Transfer Institute ofNAS of Belarus, Minsk, Belarus, stas@itmo.by

[2] Command-engineering institute" of the Ministry on extraordinary situations of the Republic of Belarus, Minsk, Belarus

Introduction

Computer modeling of deflagration explosions on industrial sites faces serious difficulties which are already emphasized in [1, 2]. The parameters of physical processes describing this type of explosions are well-known enough and far from extreme. All difficulties of modeling are generated by the contradiction between typical scales of studied physical phenomena and dimension of computational grid acceptable at a modern level of computer equipment. The gap in these scales is so great, what even modern rates of computer power growth do not allow to expect fast resolving of this contradiction. Such situation naturally generates the attempts to use phenomenological models in order to describe deflagration processes using accessible grids.

Model description

Adequate description on burning is one problem of this modeling. Thickness of flame front is too small, and within the framework of accessible grids it has no thickness. Therefore it is possible (it follows) to speak about a surface of burning, and about its motion at deflagration explosion. At such approach chemical kinetics of mixture burning is not simulated, and there are only average parameters describing burning of studied mixture, for example: expansion rate (at isobaric combustion), maximum pressure (at isochoric combustion) and velocity of laminar flame propagation. If to combine these characteristics with empirical information on coupling of velocities of laminar and turbulent burning, and also an assumption about propagation of burning normally to burning surface which is not contradicting to common sense, it is possible to construct enough simple algorithm calculating motion of flame front. The example of such algorithm is discussed in [2], where the examples of calculations are resulted, both for simple areas, and for more complex two- dimensional situations. At calculation of flame front propagation it is possible to use the conditions of gasdynamic incompressibility and flow potentiality that allows calculating velocity field based on solution of Poisson equation.

Such way of modeling is merely kinematic, and does not provide calculation of pressure field. As level overpressure is necessary to estimate the scales of destruction, the model of flame front propagation should be supplemented by model calculating overpressure. In one-dimensional situations admitting formulation of the problem, the overpressure is easily estimated by classical solution of piston movement [1-3]. However deviation from automodeling conditions demands other algorithm of overpressure assessment.

One of variants estimating overpressure has been used to simulate deflagration explosions in open ended tube filled by methane-air mixture ignited at closed end face [4]. At a simultaneous ignition over whole cross-section of a tube the propagation of a flame can be described by automodeling solution of flat piston motion. Such approach is applicable only up to time instant when the shock wave leaves a tube; after that it is necessary to take into account conditions of gas mixture outflow from open end of tube. Flow pattern (and overpressure) can even more considerably affected due to variation (evolution) of the shape of burning surface which can be initiated by influence of boundary layer or ignition inhomogeneity resulting in nonplanar shape of flame front. It is well-known, that in long tubes (instead of classical solution with constant flame front velocity) the mode with acceleration up to detonation (in long tubes, where tube length exceeds 60 calibres) is realized. Such acceleration is basically caused by increase in burning surface and only at latest stage of transition to a detonation the heating of gas mixture by shock wave propagating in front of burning plays essential, and then the determining role. Intensive shock waves and detonation processes cannot be described within the framework

of approach of incompressible flow, but initial stages of front acceleration and overpressure growth can be detected.

Overpressure behind flame front is connected with a necessity to accelerate some amount of gas by expanding products of combustion. It is possible to formulate the following phenomenological ratio to estimate overpressure:

$$\Delta P \int_{S_f} ds = \int_V \rho a dv = \int_V \rho \frac{du}{dt} dv .$$

In this expression ΔP is overpressure, S_f is a surface which is shifted by overpressure, V is volume of gas moving by effect of deflagration explosion, ρ and $a \equiv \frac{du}{dt}$ are density and acceleration of unit volume correspondingly. In this ratio ΔP depends only on time, and has no spatial dependence. To higher extent this value corresponds to pressure behind flame front, and only in flat one-dimensional case the area of the raised pressure occupies whole space up to a shock wave.

The ratio (1) should be used taking into account the geometrical specificity of each problem under consideration, also there should be an understanding of restrictions incorporated in the model calculating velocity field. Thus in case of open areas the volume V should be limited by surface of sound perturbation S_{Jound}. Though formally the velocity field found from solution of Poisson equation can distribute indefinitely, integration procedure must be applied only up to S_{Jound}. It is easy to check up, that in one-dimensional flat case of flame front moving with velocity u_f (1) results in a classical assessment of overpressure $\Delta P = P_0 \gamma \frac{u_f}{c}$ [5], where γ, c, P_0 are adiabatic exponent, speed of sound and pressure of initial gas mixture respectively.

At consideration of confined areas (buildings) with vented orifices the condition coupling ΔP with velocity of gas outflow from orifices should be set to avoid solution of "external" problem. The integration (1) over whole such area results in zero value immediately in one-dimensional flat case (the small correction providing outflow is artificially made). In this case tracking of surface S_{Jound} position allows calculating the initial stage of deflagration explosion

with $\Delta P = P_0 \gamma \frac{u_f}{c}$ which exists up to time instant, when formed shock wave reaches vented orifice. Propagation of underpressure waves and formation of corresponding pressure fields is not described by ratio (1). Without consideration of transient processes with characteristic time interval corresponding to time of sound propagation from flame front to vented orifice, using (1) it is possible to estimate overpressure arising at acceleration of flame front. At the end of acceleration such calculation will instantly result on zero value of ΔP.

The variant of taking into account relaxation in case of simple situation open ended tube is resulted below. However such approach is still not developed in case of objects with more complex (more general) geometry. Nevertheless, this variant of estimation has allowed making some conclusions about the reasons of acceleration of flame front in a tube.

It is accepted, that overpressure (behind flame front) is determined by two processes - acceleration of front and relaxation:

$$\frac{d\tilde{P}}{dt} = F_{acceleration} - F_{relaxation}, \qquad (2)$$

where $\tilde{P} \equiv \frac{\Delta P}{P_0}$. The expressions (3) and (4) define $F_{acceleration}$ and $F_{relaxation}$ which have obvious physical sense: the first expression provides the classical solution $\tilde{P} = \gamma \frac{u_f}{c}$, and the second one is classical relaxation ratio with characteristic time of sound perturbation propagation. ^F

$$F_{acceleration} = \begin{cases} 0, & \frac{du_f}{dt} \le 0, \\ \frac{\gamma}{c}\frac{du_f}{dt}, & \frac{du_f}{dt} > 0, \end{cases} \qquad F_{relaxation} = \begin{cases} 0, & t - \tau \le 0, \\ \frac{\tilde{P} - \tilde{P}_{out}\left(u_{out}(t-\tau/2)\right)}{\tau}, & t - \tau > 0, \end{cases} \qquad (3)$$

$$\tilde{P}_{out} = \frac{\gamma}{2}\left(\frac{u_{out}}{c}\right)^2, \qquad \tau = 2\frac{X_{end} - x}{c - u_f}. \qquad (4)$$

Using such model the experimental results [6] on propagation of flame front in pipe (see Fig. 1) are analyzed. The experiments are carried out in different configurations (an arrangement of diaphragms in tube and variation of their sizes). However in article there are the indications of pressure sensors only for variants with the high overpressure (several bars). Such intensive modes lay beyond the framework of applicability of used approach of gasdynamic incompressibility. At the same time the maximal overpressure equal to 0.12 bar measured in the experiment without diaphragms is resulted as a reference point in [6].

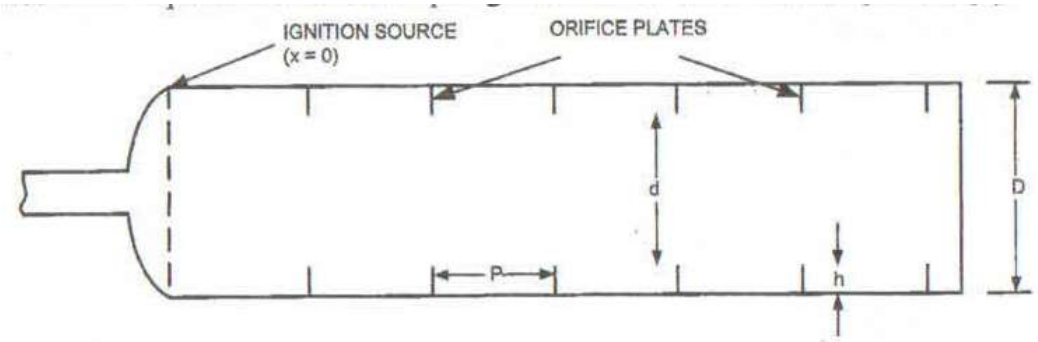

Fig. 1. Sketch of experimental bench [6]

Estimated of overpressure equal 0.04 bar calculated by flame front velocity in case of methane-air mixture burning in one-dimensional flat front is three times less, than the value observed in the experiment. As it was already spoken above, the reason of overpressure growth is front acceleration which in turn caused by a curvature (increase) in a surface of burning.

The series of calculations have been carried out to estimate the probable reasons of nonplanar shape of flame front. The computational algorithm is the following. At first the problem of flame front movement (Poisson equation) is solved and calculated function $u_f(t)$ is stored. Then the equation (2) is solved, when $u_f(t)$ is used to calculate function $P(t)$.

Firstly the effect of viscosity is examined. As viscosity is not taken into account in our model, artificial braking of gas flow close to surface is modeled. Such calculations have shown, that the required increase in overpressure demands unreasonably thick "boundary layer", about 10 cm. Other two calculations simulate a situation of non-uniform ignition. In one case gas mixture is ignited in the central part (delay of ignition close to cylindrical surface), in the second case to the contrary - there is no ignition in the central area. The simulation results of these two variants are shown in Fig. 2,3. As calculations demonstrate, the situation with localization of ignition area in the central part enables to explain observable value of overpressure.

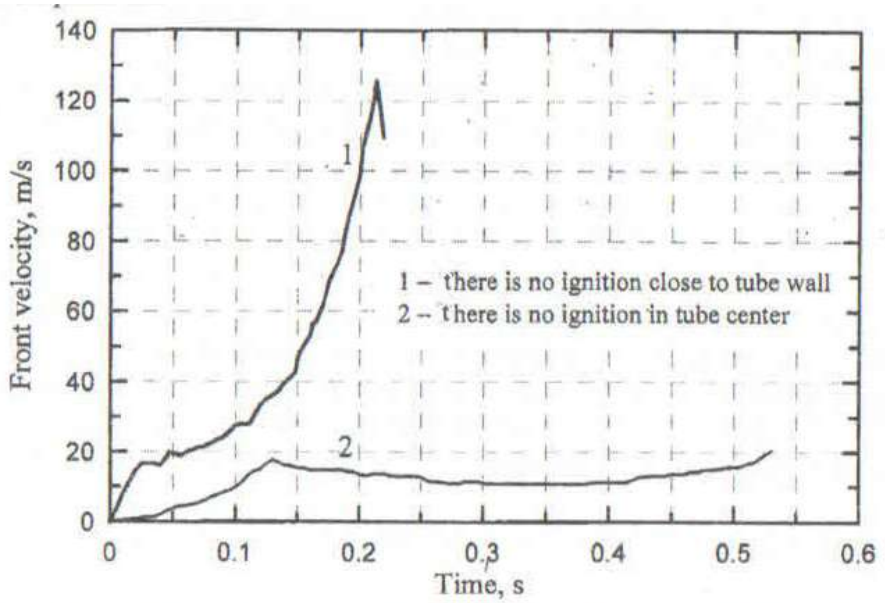

Fig. 2. Evolution of flame front velocity under different conditions of ignition

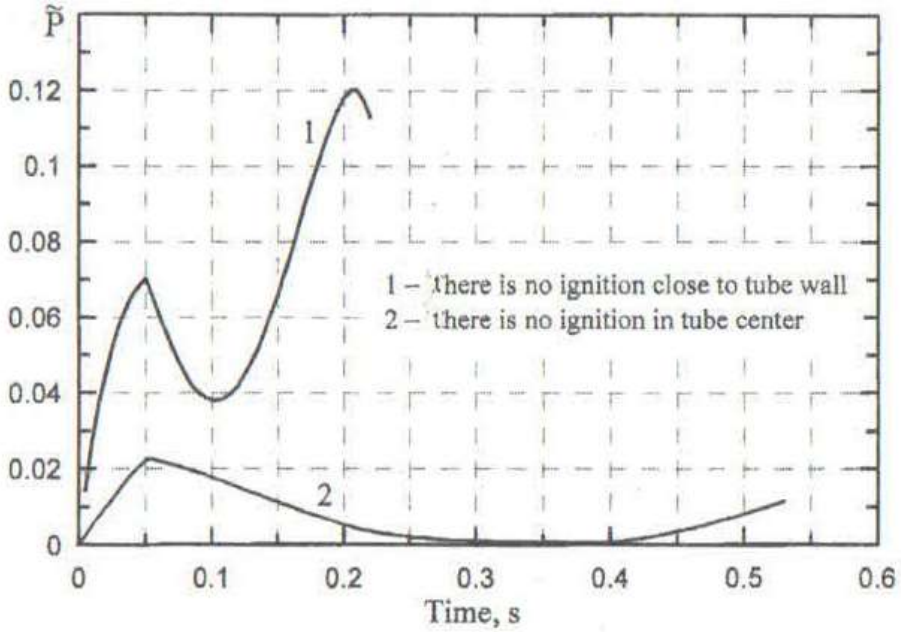

Fig. 3. Evolution of flame overpressure under different conditions of ignition

Conclusions

Usage of acceleration-relaxation models estimating overpressure has yielded reasonable results for rather simple geometry - tube without diaphragms. At the same time the further testing of such approach for more complex objects is necessary.

On the other hand, though the implementation of the algorithm based on ratio (1) does not take into account relaxation processes, but it is easier formalized in case of areas of complex shape. Numerical experiments on the further comparison of predictions of both techniques and experimental data can further stimulate the development of phenomenological description of deflagration explosions.

References

1. Shabunya S.I., Martynenko V.V. Phenomenological approach to simulation of deflagration explosions. Part 1. Basic model assumptions and governing equations // Intern. Workshop "Nonequilibrium processes in combustion and plasma based technologies". Minsk: НМЛ, 2006. Pp. 113-117.
2. Shabunya S.I., Martynenko V.V., Mikanovich A.S. Phenomenological description of Hume front propagation al deflagration explosions Heat and mass transfer 2007". Minsk, 2007. Pp. 149-157 *(in Russian).*
3. Shabunya S.I., Martynenko V.V., Mikanovich A.S. Phenomenological approach to simulation of deflagration explosions. Part 2. Explosion of hemispheric balloon filled by stoichiometric hydrogen/air mixture // Intern. Workshop "Nonequilibrium processes in combustion and plasma based technologies". Minsk: HMTI, 2006. Pp. 118-123.
4. Shabunya S.I., Martynenko V.V., Mikanovich A.S. Phenomenological simulation of slow deflagration explosions // Proc. of VI Minsk Intern. Heat and Mass Transfer Forum, Minsk, 19-23 May, 2008. Vol. 2. Pp. 404-405 *(in Russian).*
5. Sedov L.I. Metody podobyja I razmernosti v mekhanike. M.: Nauka, 1977. P. 438 *(in Russian).*
6. Moen I.O. and Lee J.H.S. // *Combustion and Flame.* 1982. Vol. 47. Pp. 31-52.

MODIFICATION OF A SINGLE VORTEX IN A MEDIUM WITH INTERNAL HEAT

N.A. VINNICHENKO, A.V. UVAROV, A.I. OSIPOV

Moscow State University, Physics Faculty, Moscow, Russia, nickvinn@yandex.ru

Introduction

The use of discharges of different kinds for aerodynamic control of an aircraft, drag reduction or enhancement of the burning inside the engines has been frequently proposed in last decades. Nevertheless, the interaction between vortical structures of the flow and non-equilibrium state of the medium remains an unresolved issue of modern physical hydrodynamics. Recently, we considered the influence of non-equilibrium state of medium upon a well-known vortical flow, von Karman vortex street [1, 2]. In this article, we consider some problems, associated with modification of parameters of a single round vortex in a non- equilibrium medium: i) interaction between the vortex and internal energy release and stability of the medium for different models of energy release, ii) influence of initial non- equilibrium state of

the medium on parameters of the vortex in axisymmetric and non- axisymmetric cases, iii) existence of integrals of motion for swirling flows with open boundaries and possible mass flow across the boundary. In particular, we are interested in the final state of a single vortex in stationary or initially non-equilibrium medium. Euler and Navier-Stok.es equations are solved. Non-equilibrium state of the medium is described by one relaxation equation or by the energy release depending on gas-dynamic parameters.

Interaction of vortex with stationary non-equilibrium medium

First, the problem of interaction of a single vortex with inviscid uniform stationary non-equilibrium medium is considered. The medium is described by temperature-dependent

$$Q(T) = \frac{\varepsilon - \varepsilon_{eq}(T)}{\tau(T)} - \frac{\varepsilon - \varepsilon_{eq}(T_0)}{\tau(T)} \qquad (1a)$$

or density-dependent

$$Q(\rho) = q\frac{\rho - \rho_0}{\rho} \qquad (1b)$$

energy release, which includes constant heat loss and vanishes in the absence of the vortex. The advantage of this problem formulation is that the medium is stationary in the absence of the vortex and the vortex is stationary in the absence of energy release, therefore we consider only the interaction between the vortex and energy release. Numerical simulations using Godunov method are performed and analytical solutions for energy release model (la) in two opposite limits of small and large relaxation time are constructed. Due to non-uniform profiles of temperature and density implied by the vortex, a non-zero energy release arises. The vortex is transformed into a new stationary state, either isothermal or isopycnic one, according to the type of energy release. A wave, propagating from the axis of the vortex, changes the parameters of the vortex: profiles of azimuthal velocity and density. The changes are small, since they are associated with the difference of the temperature (or density) profile in the initial vortex from T_o (ρ_o, accordingly). The issue of stability of the medium appears to be of crucial importance. In the case of temperature-dependent energy release (la), for sufficiently steep decrease of relaxation time τ with increase of the temperature both acoustic and thermal modes are amplified. For density-dependent model (lb) the medium appears to be unstable for any non-zero value of parameter q. In earlier studies [3], this instability was misinterpreted as quick dissipation of the vortex in non-equilibrium medium. We show, however, that this is instability of the medium with energy release (lb), which develops even in the absence of the vortex.

Influence of the initial non-equilibrium state of medium upon the vortex

Another, more realistic, problem formulation is to consider the evolution of a single round vortex due to initial perturbation of the energy of an internal degree of freedom. The non-equilibrium state of the medium is described in this case by one equation of relaxation. For axisymmetric initial perturbation the problem is analogous to the case of stationary non-equilibrium medium, except that the changes of parameters of the vortex may be large if the initial perturbation is large and that the final state is not isothermal. After the relaxation of internal degree of freedom, the wave is formed, propagating from the vortex axis and taking away some mass. The vortex still persists, with modified characteristics. Analytical solutions for the limits of small and large relaxation time are obtained and compared to the results of numerical simulations. As an example, an intermediate episode of vortex evolution for small relaxation time is shown in Fig. 1. Circles correspond to numerical simulation, solid line represents analytical solution. All values are non-dimensional, except for T and T_i, these are given in kelvins. One can see the compression wave with maximum at 6 radii of initial vortex, followed by a rarefaction wave. The process of relaxation is finished, the waves are formed and they propagate away from the axis, leaving behind a modified profile of azimuthal velocity.

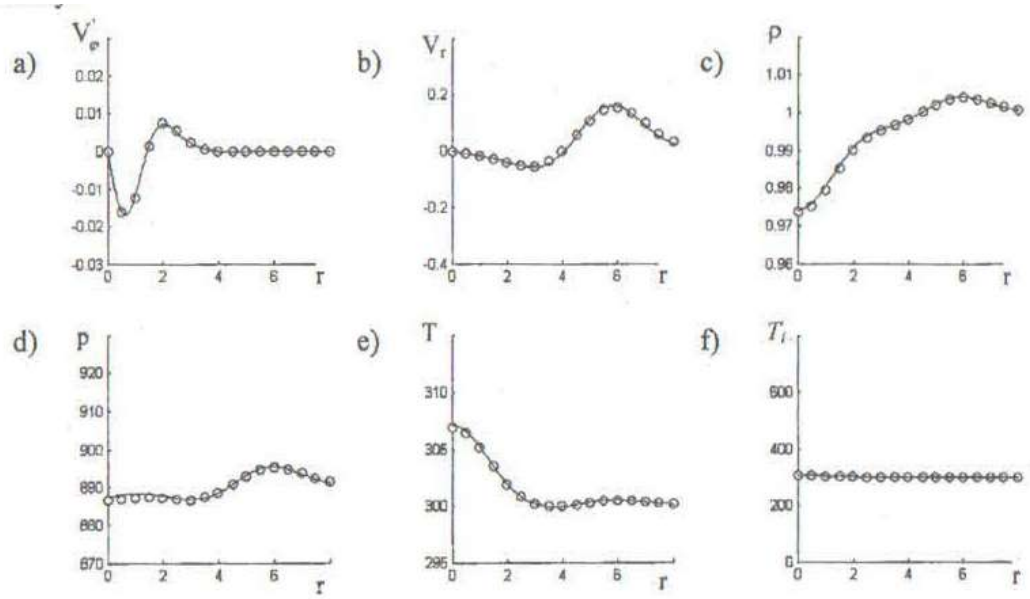

Fig. 1. Radial profiles of: a) change of azimuthal velocity, b) radial velocity, c) density, d) pressure, e) temperature, f) temperature of internal degree of freedom

For non-axisymmetric initial perturbation the process of vortex evolution can be divided into two stages. First, relaxation takes place, the wave is formed and propagates as in the axisymmetric case. At the end of this stage the velocity field of the vortex is somewhat modified in comparison with the initial vortex, but the main difference is a hot spot at the place of the initial perturbation and a corresponding decrease in density. Then the second, more slow, stage begins, including transformation of this hot spot into spiral because of vortex kinematics and falling of this spiral towards the centre of the vortex due to imbalance of centrifugal force and

the pressure gradient. Spiral shape also enhances mixing and possibly dissipation effects. The final state of the vortex is supposed to be axisymmetric.

Integrals of motion

Since the dynamics of vortex evolution is rather complicated in non-axisymmetric case, it is tempting to use some kind of conservation laws to obtain information about the final state. However, the existence of integrals of motion in swirling flows is challenging even for incompressible fluid because of the divergence of the integrals. There are methods to normalize the traditional integrals of motion to improve convergence. The situation is more complicated for compressible fluid, and almost nothing has been reported. Besides, there is a wave in our problem, which leaves the domain and takes away some mass. It is practically useless to extend the considered domain with time to account for the wave, so it is required that the conservation laws are not violated when the wave leaves the domain. Motivated by this requirement, we propose a criterion for $\iint A\,r\,dr\,d\varphi$ to be an integral of motion in an open system. It consists of three parts: first of all, A must satisfy the equation

$$\frac{dA}{dt} + A\,div\,\vec{v} = 0, \tag{2}$$

which is analogous to continuity equation, next, the flow across the boundary of the domain

$N(R) = R\int A\,v_r\,d\varphi$ must vanish with radius of the domain $R \to \infty$, and finally, the integral $\iint A\,r\,dr\,d\varphi$ must converge. Then it is possible to take the radius of the domain large enough, so that the flow across the boundary becomes negligible. For cylindrical waves $v_r \sim 1/\sqrt{R}$,

and the requirement of convergence of the integral appears to be more strict than that of decrease of the flow. Based on this criterion, a theorem is proved for axisymmetric case that for any

$$A = \rho F_1(\omega/\rho, v_\varphi r, s) + \omega F_2(\omega/\rho, v_\varphi r, s), \tag{3}$$

decreasing steeply enough to satisfy the conditions of vanishing flow and converging integral,

$\iint A\,r\,dr\,d\varphi$ is integral of motion. Here ω is vorticity, F_1 and F_2 are arbitrary functions, and the entropy s is their argument only for the equilibrium gas. In particular, this means that the total angular momentum $2\pi\int \rho\, v_\varphi r^2 dr$ is conserved even in relaxing non-equilibrium gas for all vortices with v_φ decreasing quicker than $1/r^3$, and the total circulation $2\pi\int \omega\, r\, dr$ is

conserved for all vortices with v_9 decreasing quicker than 1/r. For non-axisymmetric case, a non-zero right hand side arises in eq. (2), but it is proved that if the problem possesses a bilateral

symmetry, the integral of the right hand side is zero, and all integrals of motion of the class (3) remain. For the total angular momentum the condition of bilateral symmetry is unnecessary.

Acknowledgments

This work was supported (in part) by the Russian Foundation for Fundamental Research (Grants No. 05-08-49988a and No. 06-01-00203a).

References

1. Vinnichenko N.A., Nikitin N.V., Uvarov A.V. Karman vortex street in a vibrationally nonequilibrium gas *// Fluid Dynamics.* 2005. Vol. 40, No. 5. Pp. 762-768.
2. Osipov A.I., Uvarov A.V., Vinnichenko N.A. Influence of the initial nonequilibrium state of a medium on the structure of von Karman vortex street // *Phys. Fluids.* 2006. Vol. 18, No. 10. 105106.
3. Soukhomlinov V. S., Sheverev V. A., Ottigen M. V. Evolution of a vortex in glow discharge plasma *// Phys. Fluids.* 2005. Vol. 17, No. 5. 058102.

PECULIARITIES OF CHEMOIONIZED PLASMA FORMATION AT ISOCHORIC COMBUSTION OF PRECOMPRESSED GASOLINE-AIR MIXTURES

A.N. MIGOUN[1], E.A. MATVEICHIK[1], A.P. CHERNUKHO[1], A.M. STARIK[2], N.S. TITOVA[2], A. CENIAN[3]

[1]A.V. Luikov Heat and Mass Transfer Institute of NASB, Minsk, Belarus, migoun@itmo.by

[2]P.I. Baranov Central Institute of Aviation Motors, Moscow, Russia

[3]The Szewalski Institute of Fluid-Flow Machinery of PAS, Gdansk, Poland

Introduction

During last years we made a number of consequent efforts [1-3] to solve the inverse problem of reconstruction of initial fuel-air mixture composition before the ignition on the basis of an electric probe signal. This paper presents recent results of our numerical investigations of ion and electron formation during combustion of gasoline/air mixture in an adiabatic closed reactor that allowed us to formulate several preliminary criteria for identification of pre-ignition composition of a compressed gasoline/air mixture.

Kinetic model and numerical procedure

A gasoline fuel is assumed to be a mixture of the two individual hydrocarbons: n-heptane and i-octane. The mole fraction of the i-octane defines the octane number of the fuel. The PRF detailed reaction mechanism [4, 5] was used to take into account the complex kinetics of the gasoline combustion. This mechanism was supplemented by the kinetics of the N-containing species formation and kinetics of ion and electron origin in the course of cherno ionization reaction. The majority of nitrogen-related reactions were taken from [6]. The reaction mechanism involving the gaseous charged species was reported in [7]. The resulting kinetic mechanism comprises 4930 reactions between 1069 neutral and 46 charged species. The mechanism was verified and revised as described in [8].

It was assumed that initially a gasoline-air mixture was adiabatically compressed in a combustion chamber of a gasoline engine with the compression ratio equal to 10, i.e. initial gas temperature and pressure is about 600 K and 25 bar, respectively. We assume that there is no heat exchange with the chamber walls.

KinTool software [9] was used to simulate the isochoric combustion of gasoline/air mixture in a 0D adiabatic approximation.

Results and discussion

The numerical simulation was performed for several types of gasoline with octane number ranging from 0 to 100. It was established that the type of gasoline (with different octane number) does not affect noticeably the kinetics of ion formation. Below the results for the gasoline with octane number 92, which is the most widely used in Belarus, are presented.

In our analysis we assumed that the ignition is associated with the peak of CH radical concentration, which plays an important role in combustion development. The appearance of this peak is accompanied by rapid growth of gas temperature.

Fig. 1 shows the evolution of concentrations of main ions versus time for different fuel/air equivalence ratios for gasoline/air mixture. It is seen that the H_3O^+ ion prevails among positive ions in fuel lean and stoichiometric mixtures, while CH_3CO^+ and $C_3H_3^+$ ions become the most important just after ignition of fuel rich mixture. Soon after the ignition front the H_3O^+ ion regain its supremacy.

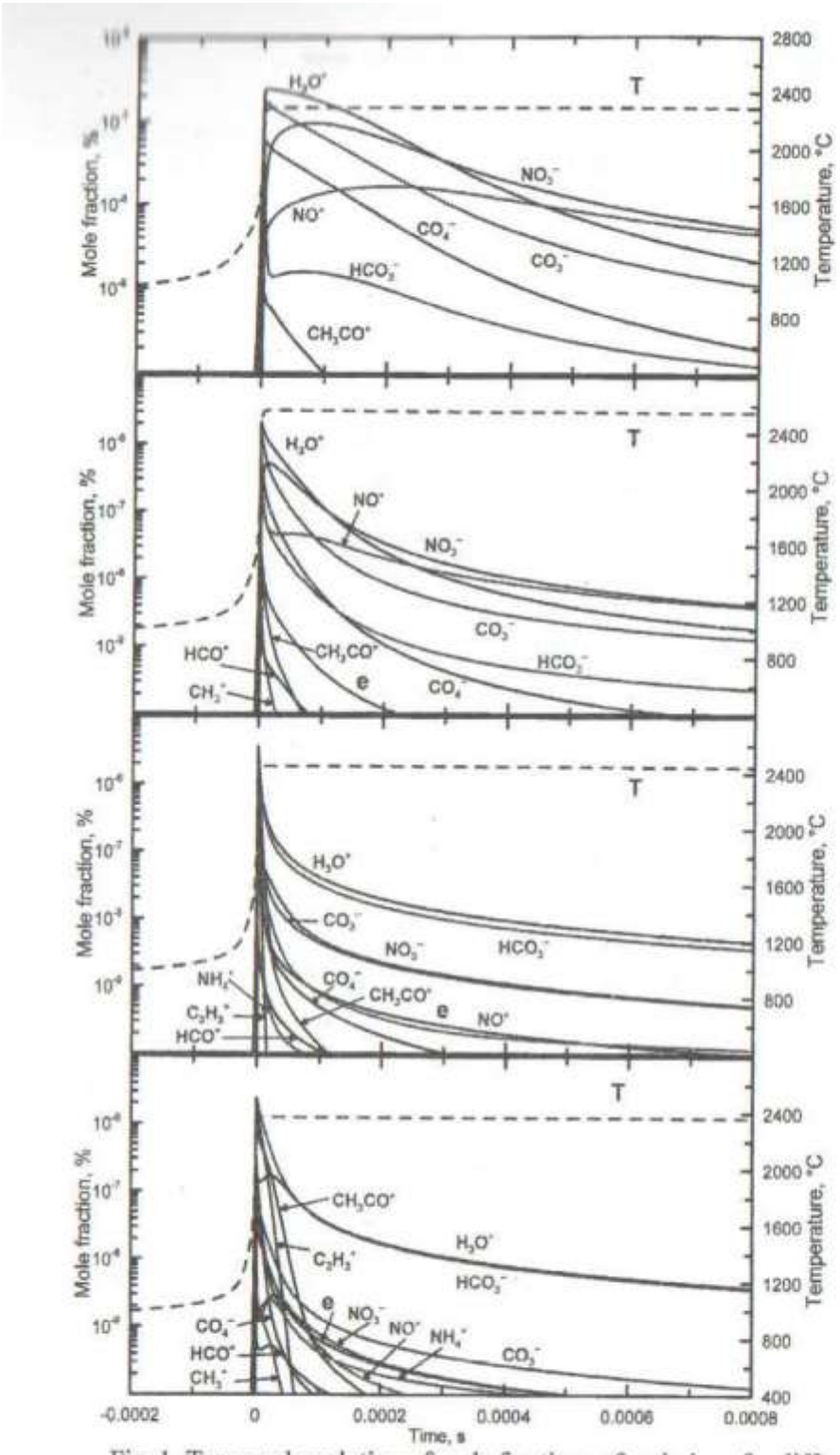

$\varphi = 0.8$

$\varphi = 1.0$

$\varphi = 1.2$

$\varphi = 1.4$

Fig. 1. Temporal evolution of mole fractions of main ions for different equivalence ratios of gasoline/air mixture

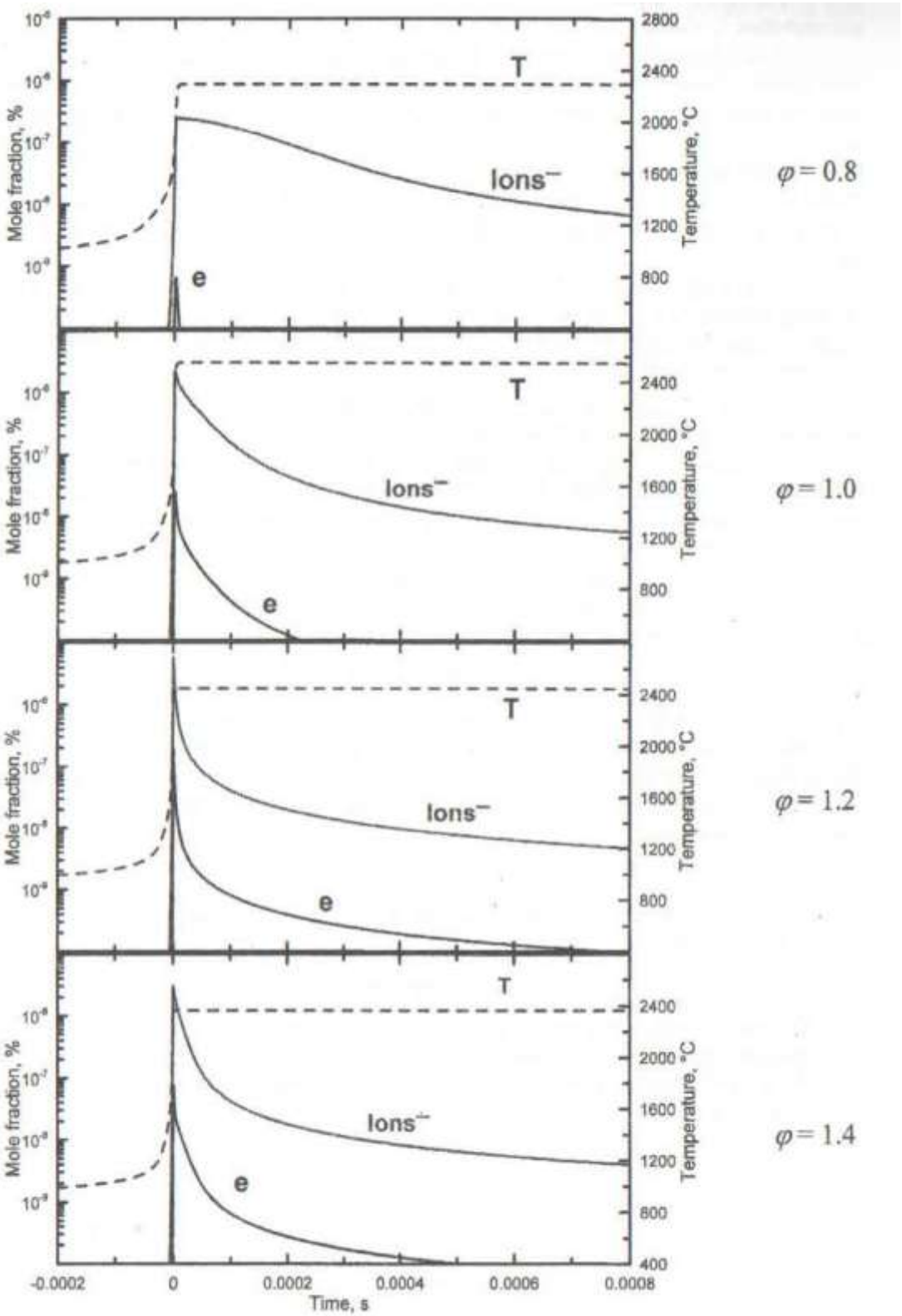

Fig. 2. Evolution of total ion concentration for different equivalence ratios of gasoline/air mixtures

The HCO_3^- ion dominates among negative ions. In the case of fuel reach mixtures, its concentration in the ignition front prevails that for H_3O^+ ion.

In fuel lean mixtures, the role of nitrogen containing ions, including the NO^+ and NO_3^- ions grows. Their formation starts several hundreds microseconds after ignition. Their concentrations reach corresponding maximum and begin to fall monotonically. Formation of these species starts intensively already in the ignition front in the case of fuel rich mixtures, however, the peaks of their concentrations are noticeably smaller than those in the fuel lean mixtures. Moreover, in contrast to fuel lean mixtures the fall of their concentrations is of the order of magnitude than those for other ionized species and they never prevail in fuel rich mixtures.

Fig. 2 shows the variation of the total negative ion and electron concentrations for different equivalence ratios of gasoline/air mixtures. Since the plasma was assumed to be charge neutral, the concentration of positive ions is a sum of two mentioned species. As follows from the plots in Fig.2 the maximal ion concentration is observed for fuel enriched mixture with φ = 1.2. In general, fuel enriched mixtures favor the formation of larger number of charged species than that for stoichiometric and fuel lean ones.

Flames in fuel lean mixtures are characterized by low number density of electrons, which may be used as criteria in probe diagnostics. The rate of the ion concentrations (for positive or negative ions) drops noticeably smaller for stoichiometric and fuel lean mixtures, and can be another criterion of fuel/air composition. The qualitative analysis of the chemoionized plasma composition at the later stages of the combustion, where dominate either nitrogen-oxide ions for lean mixtures or ions HCO_3^- and H_3O^+ for rich one, can also be an indication of the leaning or enrichment of the fuel mixture.

Conclusions

Kinetic mechanism that describes the formation of gaseous charged species during combustion of gasoline/air mixtures was developed. Complex modeling of the combustion of different gasoline/air mixtures have been performed. The possible criteria of the estimation of initial mixture composition prior to ignition on the basis of the known composition of burning plasma were formulated.

Acknowledgment

This work was supported in part by Russian Foundation for Basic Research (Grant 08-01-00808).

References

1. Chemukho A.P., Migoun A.N., Starik A.M., Titova N.S., Cenian A. Evolution of charges species in hydrocarbon/air flame: effects of diffusion *// Nonequilibrium Processes: Plasma, Combustion and Atmospheric Phenomena* / Eds. G.D. Roy, S.M. Frolov,

A.M. Starik (3rd Intern. Symp. NEPCAP'2007, Sochi, Russia, June 25-29, 2007). Moscow: Torus Press, 2007. P. 43.

2. Rodrigues J.M. Agneray A Jafftezic X Bellenoue M., Labuda S., Leys C., Chernukho A.P., Migoun A.N., Cenian A., Savel'ev A.M., Titova N.S., Starik A.M. Evolution of charged species in propane/air flames: mass-spectrometric analysis and modeling // *Plasma Sources Science and Technology.* 2006. Vol. 16. Pp. 161-172.
3. Cenian A., Chemukho A.P., Migoun A.N., Savel'ev A.M., Titova N.S., Starik A.M. Dependence of ion concentration on propane/air ratio in flames // Nonequilibrium processes in combustion and plasma based technologies. Contributed papers of the Second International Workshop, Minsk, August 26-31, 2006 / A.V. Luikov Heat and Mass Transfer Institute. Minsk, 2006. Pp. 56-59.
4. Curran H.J., Gaffuri P., Pitz W. J. and Westbrook C.K. A Comprehensive Modeling Study of iso-Octane Oxidation // *Combustion and Flame.* 2002. Vol. 129. Pp. 253-280.
5. Curran H.J., Gafluri P., Pitz W. J., and Westbrook C.K. A Comprehensive Modeling Study of n-Heptane Oxidation// *Combustion and Rome.* 1998. Vol. 114. Pp. 149-177.
6. Marinov N.M., Pitz W.J., Westbrook C.K., Hon M. and Matsunaga N. An Experimental and Kinetic Calculation of the Promotion Effect of Hydrocarbons on the NO-NO2 Conversion in a Flow Reactor // Proc. of the Combustion Institute. 1998. Vol. 27. Pp. 389-396. (UCRL-JC- 129372).
7. Starik A.M. and Titova N.S. Kinetics of ion formation in the volumetric reaction of methane with air// *Combustion, Explosion and Shock Waves.* 2002. Vol. 38, No. 3. Pp 253-268.
8. Chernukho A., Migun (Migoun) A., Zhdanok S., Rostaing J., Perrin J. Simulation of perfluoromethane decomposition in an atmospheric-pressure microwave discharge // *J. of Engineering Physics and Thermophysics.* 2005. Vol. 78, No. 2. Pp. 394—404.
9. Migoun A.N. PhD Thesis "Thermal physics and kinetics of hydrocarbons partial oxidation as applied to combustion processes in internal combustion engines" / A.V. Luikov Heat and Mass Transfer Institute. Minsk, 2006.

THE ALTERNATIVE BURNING OF HYDROCARBONS

H. STOLYARENKO, U. MARTSINYSHYN, V. VIAZOVIK, O. VODIANIK, S. HONCHAR

Cherkassy State Technological University, Cherkassy, Ukraine

The existent theory of geterogenious catalysis is based on notion "thermal energy of activating". This parameter for the flowline of concrete gas reaction represents the necessity of receipt by the system (Gas - Gas) energy for overcoming power barrier. Bringing in the area of the promoted temperature to the catalyst (Gas - Gas - Hard system) changes reactionary power of the system. It is necessary overcoming a few energies of activating the stages of catalysis, algebraic sum of which considerably (at the correct choice to the catalyst) below to energy of activating of gas reaction (Gas - Gas). Using the catalyst, thus, gives the possibility to intensify a process. But for flow lining the reaction in the system with a catalyst (for example, for the gas, exothermic, reverse reaction) necessary is rising of temperature to some one (enough high) level - "temperature of ignition " to the catalyst. In most cases rising of temperature is energetically unprofitably and economically not expediently. Practically, in all existent processes by achievement reactionable level a temperature is basic. Activating of chemical processes is possible also with the use of ultraviolet radiation, chemical processes in plasma and arc discharge in gases.

The fundamental scientific problem, which was put, is: to learn and develop the apparatus and technology of electro-catalysis as the method for declining the energy of activating on a catalyst due to bringing of him in the area of quiet electric discharge. In the processes of electro-catalysis of overcoming of energy of activating is carried out for the account of following acts: synthesis and extinguishing of oxygencontained radicals; reception of energoactive and reactionable atoms and molecules due to the stream of lone electrons; wave influence of discharge on the system in an area to the catalyst; ultraviolet irradiation; thermal influencing of quiet discharge.

Conduction of gas chemical reaction on a catalyst in the area of quiet discharge intensification of process is going in after a few directions:

- oxidizing power of the system changes because as an oxidant not only oxygen but also molecules of ozone (at low humidity) are used, and also (with the growth the water pressure part) oxygencontained radicals HO^*, HO_2^*, RO*, RO_2^*;
- molecules of reagent under action of high tension, stream of surplus electrons, ultraviolet irradiation, e.t.c., grow into the energetically-excited atoms, ions or ion- radicals;
- oxidation of such reagents by oxygen, ozone and radicals flow spontaneously or at the minimum of the energy charges;

- compensation of energetic thermal charges is possible due to the rise of temperature of the system in the area of discharge; it means using without bulky heat-exchange vehicles and caldrons;
- influencing of frequency of discharge, optimization of strimmers working, influence of temperature on a chemical reaction yield will be determined for every system experimentally.

During the electro-catalytic activating of the systems of burning (C_nH_m-Nr-O_2) the declining the energy of activating of the endothermic constituent on first stage of burning is achieved - hydrocarbons decomposition on carbohydrate radical and proton. The decline expenses of energy on the first stage of term destruction hydrocarbons of fuel leads to the increase the selection of heat on the main heat-havier, that, in the turn, results in the substantial economy of fuel (15-25 %).

Achievement of high indexes of electro-catalysis is related to the directed search of material of dielectric, laser treatment of surface of dielectric, by the artificial extinguishing the radical of oxygen by steam of water, studying of different constructions of ozonizers, as the reactors of quiet discharge, studying of terms of synthesis of high concentrations of oxygencontained radicals, prefiery preparations of fuel in fuel-air mixtures.

The process of burning of hard fuel from the difficult structure and composition of coal is very difficult and heterogeneous. At combustion of hydrogen, carbon and sulphur appeal accordingly aquatic steam, carbonic acid and oxides of sulphur. These chemical transformations are accomplished with a different speed and flowed not simultaneously. The rich in hydrogen organic volatile matters catch fire the first. In future, warmed-up by flame of volatile matters, hard mass catches fire - inert part of fuel - coke. Its burning divides into two stages. First around the particle of fuel from low maintenance of oxygen as the product of incomplete combustion appears oxide of carbon (II). Then this gas unites with oxygen of air and forms the product of complete combustion - oxide of carbon (IV). Burning of coke and burning of oxide of carbon (II) proceeds after burning down of volatile matters.

According to literary data, at all caldrons, burning is closed in lower part of heating chamber, and in the middle of heating volume in gases there is low concentration of particles unburning out. In overhead part of heating the slow burning conditioned by a presence in exhaust gases of some part of oxygen, and also that in this part of heating space the separate streams of gases are slowly mixed between itself.

It is necessary for more complete combustion of coal, that all components of fuel caught fire simultaneously and burned with identical speed. Attaining it is impossible, however, it is necessary for rapprochement of speeds, that round every hard particle there was the enough body

of oxygen, and oxidizing power of blowing was promoted due to the synthesis of oxygencontained radicals. If in the current air-fuel stream the simultaneous self- ignition of being found in different phases components of coal is not provided, oxygen of surrounding air will be used up on burning of those components of fuel, which have the lowered energies of activating. At the deficit of oxygen part of coal particles will not burn up even at heating to the ever-higher temperatures.

From here it follows that all components of fuel must catch fire in the comparatively narrow area of self-ignition. Loss from not accomplished burning the higher, than large stake of particles passes through this area not burning up. The presence of the radical blowing lowers the difference of energies of activating of primary endothermic processes, extends the area of self-ignition and levels speeds of burning of different components of hard fuel.

The major technical task of increase of degree and speed of incineration of hard fuel at the caldrons of large productivity is not decided.

From it follows coming all aforesaid, that the offered method of intensification of burning of hard fuel, essence of which consists in the use of ozone-radical catalytic processes, must result in more complete combustion of fuel during (possibly) minimization of coefficient of surplus of air. In the area of arc discharge the molecules of ozone which in 10^2 - a 10^3 time more active how an oxidant is on comparison with molecular oxygen appear on a catalyst, and also atoms and radicals O^*, HO_2^*, HO*, RO*, RO_2^*, activity of which in 10^3 - a 10^4 time higher, than at ozone. Such blowing in same queue are initiated by the additional chains of burning of fuel, that gives more complete burning down of coal.

Hard fuel burning. The experiments on optimization of hard fuel burning (anthracite coal) were conducted on setting which consists: from a combustion chamber with the are device; thermostat; source of energy and compressor. The arc device is the complete set of the reticulated electrodes with an inflicted on them catalyst. Electrodes are placed in the ceramic tube of combustion chamber. A combustion chamber is placed in an electro-thermostat which a coal inflames by. Air which before contiguity with a coal passed through electrodes was given from below in a combustion chamber.

Researches were conducted with a coal the particles which had a size about 0.25-2 to mm. In a combustion chamber loaded a 1 kg of coal which ignited by an electro-thermostat. After the self-ignition the igniter was disconnected. The output of heat was determined on heating of permanent quantity of water. Measuring of temperature of water produced in every 2 minutes, time of ending of coal burning was determined on $\Delta t = 0$. Adopted total time of getting up of water temperature in times of burning down of portion of coal maximal temperature to

which conducted heating there was 90 °C The process of the local boiling which takes large errors in determination of quantity of heat from the flowline of process of phase transition are possible and begin at more high temperatures. Time of burning down of coal for the hinge-plate 1 kg relies on the quantity of the given air and hesitates from 40 to 50 minutes.

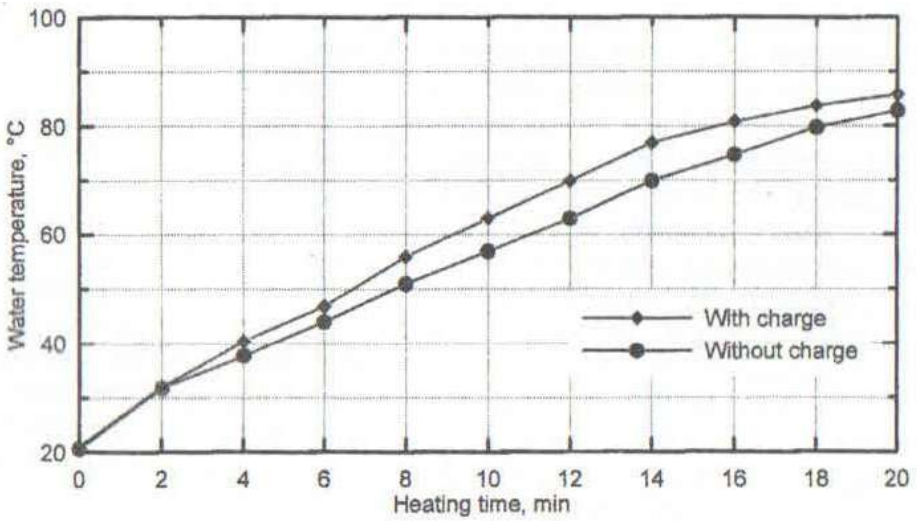

Fig. 1. Curves of dependence of water temperature change from time during conducting of zero experiment and experiment with a discharge

A coal was burned without the inclusion of arc device (single experience) and with the inclusion of arc device, to complete combustion of coal.

On the Fig. 1 dependences of water temperature change on time during carrying out single test and experiment with a discharge are presented. Two equal hinge-plates of coal took away by representative tests and burned at identical terms during one experiment.

Dependences of water temperature change and time of burning down of coal were marked.

As you can see from these dependences, at incineration of coal with a discharge there is the speed-up heating of water, that testifies to the selection of greater quantity of heat, than at single experience. On the resulted curves three regions are visible: region of establishment of even process of burning (beginning of curves from 0 to 2 min), region of the even burning of coal (rectilinearly area in sredine of curve from 2 to 16 min) and region of fading of process of burning (after a 16 min). For computation the power of coal combustion and efficiency in the described plant it was taken the area of the even burning.

Specific power of heat selection at single experience arrives at 2251.3 V., while at the use of arc arrives at 3076.84 V, that anymore on 26.8 % and in same queue lowers the expense of fuel on a the same part.

The degree of coal burning down during conducting of both experiments is definite. For this purpose was definite ashity of coal and degree of burning down of coal at burning without

arc and with arc. The degree of coal burning down at single experience makes approximately 72 % (that approximately corresponds to the caldrons having of heating with a whole grate); the degree of coal burning down at the using arc arrives at 89 %. The degree of increase of burning down made on the average 17.45 %.

Using this method of optimization of hard fuel burning process there is the declining of carbon oxide (II) in exhaust gases on 60-80 %, oxides of nitrogen to 40 %, aldehydes and benz(a)piren to 40-55 %, soot to 60 %. In connection with possibility to work at the coefficient of air surplus less than 1.17-1.19 the volume of outgoing gases goes down on 5-15%.

Thus, the offered method of intensification of burning process results in more complete burning down of hard fuel and rise of Output Input Ratio of caldron.

Optimization of process of burning of gaseous fuel. The experiments on optimization of burning process of gaseous fuel were conducted on stand and pilot options For prevention the declining of catalyst activity, a catalyst was shown out of area of burning.

The experiments were conducted, both with a clean gaseous fuel, and with addition in the gaseous fuel of different additives. As a fuel the methane and propane-butane mixture were used. A propane -butane mixture has the soft terms of electrocontacting comparatively.

Time of heating of definite volume of water was located from initial (the temperatures 8-20 °C) to 98 °C. The volumes of water made 1000 dm^3, tension in the area of radicals generation from 5 to 11 kV. Every experiment was repeated as minimally 3 times to reproduction of results. Researches were conducted at the expense of the gas 150, 200, 300, 400 dm^3/min (time of staying in the area of electrocatalysis accordingly 0.036, 0.027, 0.018, 0.014 s).

The most economy of fuel is achieved at the dosage in the gas stream of additives at tension 6-11 kV and arrived at approximately 12%. Consumable power at the electro- catalysis made on the average 3-5 % from the got power due to the economy of fuel. But consumable power here considerably higher. On the economy of fuel time of gas stream staying in the area of reaction does not mean.

At by the use as a fuel natural gas the electro-initiation of process of synthesis of radicals was carried out at tension of 10 kV and higher. There was the considerable economy of fuel (without addition of additives ~15 %, with addition of additives - 20 %).

The experiments on intensification of burning process of methane in the area of electro-catalysis in the conditions of turbines at the transportation of natural gas are conducted.

RANS MODELING OF TURBULENT CONFINED JET MIXING WITH NEUTRALIZATION REACTION

A.D. CHORNY

[1] A.V. Luikov Heat and Mass Transfer Institute of NAS of Belarus, Minsk, Belarus, anchor@hmti.ac.by

Introduction

Jet flows is one of the most widespread types of shear flows that are encountered in solving practical problems. The latter are concerned with technologies to be adopted for designing various sewage devices, burners, chemical reactors, heat exchanges, etc. In this case of much interest is the problem on turbulent jet mixing [1]. In turbulent flow studies, numerical simulation widely uses statistical models with closing of transfer equations for statistical moments (RANS modeling). Unlike Direct Numerical Simulation or Large Eddy Simulation (LES), such an approach requires smaller computational resources and allows obtaining the information on averaged characteristics of jet flow. However for chemical reacting flows the use of the statistical moment method yields in these equations the correlation terms, whose modeling invokes large volumes of the statistical information on the turbulence influence upon a rate of producing chemical products. A special difficulty arises in averaging the chemical source terms in the transfer equations for reagents. Usually, this causes the rate of the chemical reaction to strongly depend on thermophysical properties of a medium in the non-linear manner. That is why, when studying the processes with different physical and chemical actions the statistical moment method is applied together with the Probability Density Function (PDF) of various hydro- and thermodynamic parameters [2]. First of all, its advantage is in the exact representation of the chemical source influence on unknown quantities. The objective of the present work is to make RANS modeling of a turbulent axis-symmetrical jet with a co-flow of incompressible fluid (Schmidt number Sc ≈ 1000, constant density ρ) in the cylindrical channel with the chemical neutralization reaction for the large Damkohler number $Da \to \infty$ (infinite fast chemical reaction).

Model description

The simulation of flow hydrodynamics uses the RNG k-ε model and the standard turbulcnce k-ε model with the modified model constants (C_μ = 0.06 and C_{k2} = 1.87) in the corresponding transfer equations for a more exact forecast of a jet expansion radius and its decay. Analysis of turbulent mixing adopts the theory of conservative scalars and the concept of mixture fraction [2]. Computation of its averaged values and variance uses the mixing model at velocity-to-scalar-time-scale ratio R = 2 [2] and Multiple-Time-Scale (MTS) mixing model [3] allowing for the specific behavior of turbulent mixing of media with large Schmidt numbers. To close the chemical terms in the transfer reagent equations, one applied the Eddy- Dissipation Concept (EDC) model or the presumed p-PDF of mixture fraction [2].

Results and discussion

Numerical simulation of turbulent mixing with the chemical neutralization reaction was made by the above approaches for geometrical and hydrodynamic characteristics of the axis-symmetrical mixer used in experimental study [4]: d = 0.0052 m, D = 0.04 m, flowratc ratio Q = 56.2, Sc = 800 for three values of the Reynolds number Re_d= 13000, 20000, 25000.

As the acid-base neutralization reaction there proceeded the reaction of alkali and hydrochloric acid with the initial reagent concentrations Y_{NaOH} - Y_{HCl} = 0.9 kmol/m^3 in the jet and in the co-flow, respectively where K= 10^{11} m^3/(kmol s), that is, the infinite fast reaction can be assumed to occur. Unfortunately, in [4] the experiment was not described fully. Therefore, the jet turbulence intensity was prescribed by the relation Tu = 0.2 $Re_d^{-1/8}$.

In present calculation the reaction zone length L_R (95 % of *NaOH* conversion) at different Reynolds numbers Re_d was compared with that in experimental study [4] and at numerical simulation [5, 6] (Fig. 1).

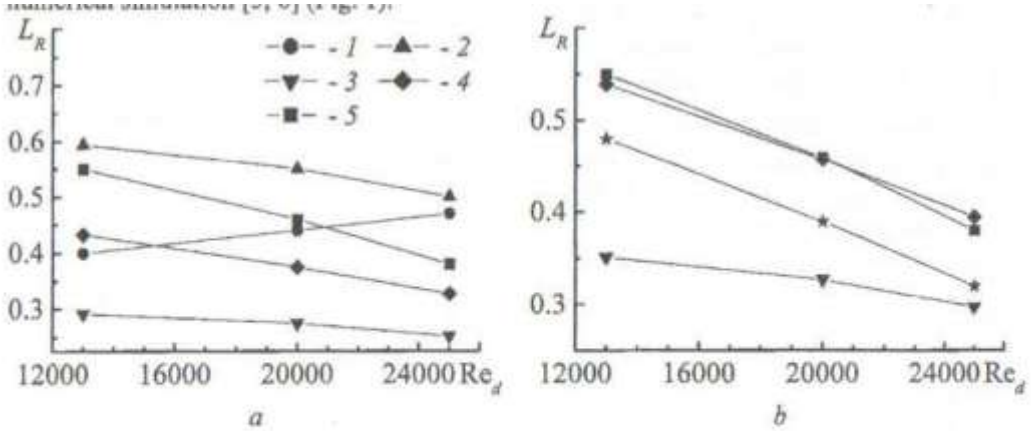

Fig. 1. Reaction zone length L_R vs. Reynolds number Re_d calculated using various models of turbulence and mixing: *a* – standard $k-\varepsilon$ модель, *b* – RNG $k-\varepsilon$ модель (*1* – calculation [5], *2* – EDC+MTS model, *3* – mixing model at R = 2 and β-PDF, *4* – MTS mixing model and β-PDF, *5* – experiment [4], ξ – calculation [6])

Fig. 1 shows that the calculation by the EDC+MTS model with invoking the standard k-ε model in [5] gives a wrong trend in changes of L_R with increasing the Reynolds number (Fig. 1 *a)* unlike our results. This is apparently connected with differences in the used models and with the different assignment of boundary conditions, first of all, for turbulent characteristics. In our approaches according to the used mixing models the reaction zone length decreases with increasing the Reynolds number (Fig. 1 *a, b).* The MTS model predicts L_R more close to the experimental and more extended one than following the mixing model at R = 2 for calculation of β-PDF. At die same time the RNG k-ε model (Fig. 1 *b)* gives a better agreement, as compared to

the standard k-ε model (Fig. 1 *a)*. Whereas the use of the RNG k-ε model and the MTS model with invoking β-PDF yields a rather exact coincidence of the predicted and experimental lengths.

Consider the influence of the ratio a = Y_{i0}/Y_{A0} of the initial concentration of reagents dissolved in the jet and in the co-flow of the chemical reacting at turbulent mixing in the axis-symmetrical mixer. The quantity a is connected with the chemical equivalence ratio $r_{eq} = n/a$. Use the data on the chemical neutralization reaction [7]:

$$NaOH + 0.5H_2SO_4 \xrightarrow{\omega_d} 0.5Na_2SO_4 + H_2O,$$

where K= 10^{11} m^3(kmol-s). Geometrical and hydrodynamic parameters of the mixer were as follows [7]: d-0.006m; D = 0.05 m; Sc=1000; flowrate ratio Q = 2.77; U_d= 10m/s; Tu = 4.5 %; Y_{NaOH} = 0.02 kmol/m^3. The reaction zone length L_R was determined through the alkali conversion up to the concentration $Y^{\infty}_{NaOH} = 10^{-8}$ kmol/m^3. Calculations were made for several values of the ratio $\alpha = Y_{H_2SO_4} / Y_{NaOH}$ using the above standard k-e модель and the power-law velocity profile at the jet issuing. In the mixing models the value of the turbulent Schmidt number Sc_1 was equal to 1.

Fig. 2 shows the comparison of the calculated L_R depending on the ratio α. As α is increased, the reaction zone length decreases. The chemical reacting proceeds at the stoichiometric ratio of reagent concentrations, that is, the equality $nY_{A0} - Y_{B0} = 0$ is satisfied. At α < n = 0.5 the chemical reacting occurs with an alkali excess while at α > n = 0.5 - with an acid excess. Thus, a sharp increase in L_R at α < 0.5 is attributed to an alkali excess in the mixture and the insufficient amount of acid for alkali to be converted to the concentration Y^{∞}_{NaOH}. At the same time, L_R decreases more uniformly at α > n = 0.5, that is, the acid-enriched mixture allows converting alkali up to the concentration Y^{∞}_{NaOH} at a relatively small distance from the turbulent jet issuing. Fig. 2 illustrates that at α > 1 the both mixing models provide the identical results coincident with the experimental data [7]. In its turn, at a < 1 these models underestimate the length L_R.

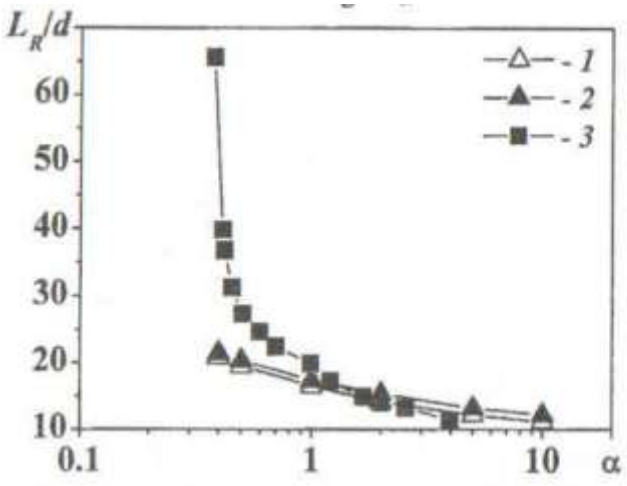

Fig. 2. Reaction zone length L_R vs. initial reagent concentration ratio α: *1* – mixing model at $R = 2$ and β – PDF; *2* – MTS model and β – PDF; *3* – experiment [7]

The theory of conservative scalers with the use of the mixture fraction concept and the PDF method enabled us to formulate a closed model for turbulent mixing with chemical reacting in the axis-symmetrical mixer. To do this, we used the RNG k-ε model and the standard k-ε model modifying of model constants in an effort to improve the accuracy of calculations of jet flows in the co-flow, as well as the mixing model at $R = 2$ and the MTS mixing model for Sc >> l. Numerical simulation showed that, as the Reynolds number or the initial reagent concentration ratio a was increased, the reaction zone length decreased, which is well supported by the comparison of the predicted results and the experimental data.

This work was sponsored by the Belarusian Republican Foundation of Fundamental Research (project T08R-101).

References

1. Abramovich G. N. Theory of Turbulent Jets. Moscow: Nauka, 1960.
2. Turbulent reacting flows / Eds. P.A. Libby and F.H. Williams. N.Y.: Acad. Press, 1994.
3. Baldyga J., Bourne J. R. Turbulent mixing and chemical reactions. NY: Wiley & Sons, 1999.
4. Pohorecki R., Baldyga J. New model of micromixing in Chemical reactors. 1. General development and application to a tubular reactor *// Ind. Eng. Chem. Fundam.* 1983. Vol. 22. Pp. 392-397.
5. Hjertager L.K., Osenbroch J, Hjertager B.H., Solberg T. Validation of the Eddy Dissipation Concept for fast chemical reactions in turbulent flows // Chem. Reaction Ing. VII: CFD, 6-11 August 2000, Quebec City, Canada. P. 9.
6. Hannon J., Hearn S., Marshall L., Zhou W. Assessment of CFD approaches to predicting fast chemical reactions // *FLUENT Technical notes.*No. 126. P. 15.

7. Tebel K.H., May H. O. Der Freistrahlrohrreaktor Ein effektives Reaktordesign zur Unterdrilckung von Selektivitatsverlusten durch schnelle, unerwiinschte Folgereaktionen // *Chem. Ing. Techn.* MS 1708/88. P. 28.

OPTIMIZATION AND TECHNICAL POTENTIAL OF FILTRATION COMBUSTION RECIPROCAL FLOW REACTORS

K.V. DOBREGO, I.A. KOZNACHEEV

A.V. Luikov Heat and Mass Transfer Institute of NAS of Belarus, Minsk, Belarus,

mabritch@hmti.ac.by

Introduction

The last decades the considerable experience is accumulated in investigation of filtration combustion (FC) and filtration combustion application (Heat and Mass Transfer Institute (Minsk) [1, 2], UIC (Chicago) [3,4], University of Erlangen-Nurnberg [5], Texas University (Austin) [6] and some other centres). The concept of the excess enthalpy combustion in porous media (the term "filtration combustion" is sometimes used) was developed in the works by F. Weiberg [7], Yu.S. Matros [8], G.A. Fateev [9] and evolved in [2, 10, 11] and others. Its essence is in the possibility of the thermal process intensification in the non-stationary thermal wave due to heat recuperation in a gas-porous medium system.

There are two main directions of application of FC - the thermal conversion of extra- rich fuel mixtures and oxidation of extra-lean fuel mixtures. The terms "extra-rich" and "extra-lean" mixtures mean fuel mixtures with concentrations laying outside of the normal flame combustibility limits. Historically the combustion of low calorific value (extra-lean) fuels was the first area of investigation. Due to various reasons for a long time there were no consistent investigations and understanding of the technical potential and limits of this technology, except of the notion that bigger scale reactors favors for extending the lean combustibility limit. More or less complete understanding of this problem was reached the last years due to systematic numerical investigations and parametric study. The main results regarding combustion in reciprocal flow reactors are discussed in the first part of this report.

The second part of the report is dedicated to superadiabatic FC application to thermal conversion of the extra-rich hydrocarbon mixtures. Particularly to the conversion of methane to hydrogen. The interest to this technology is due to the possibility of conversion of various hydrocarbons, including fluids. In spite of the attractive potential the practical implementation of this technology demands optimization of regimes and detailed investigations of the influence of the scale-up, geometrical and constructive factors, etc. The systematic investigations of the

mentioned factors was performed by the authors of this report for methane partial oxidation in the reciprocal flow filtration combustion reactor. The 2DBurner software was use for investigations [2]. The questions of optimization of this process are discussed in the second part of the report.

Low calorific fuels combustion limitations

In spite of rather long history of the investigations of extra-lean combustion in porous media the principal question of the best possible lean combustibility limit is not discussed consistently. Particularly, the U-shape of the lean combustibility limit (LCL) observed in experiments by Hoffman and Echigo [11] (Fig. 1) was not noted and discussed. Recently this principal peculiarity was analyzed [12]. An analytical model revealed the non-homogeneous character of the LCL as a function of the filtration velocity (or mass flow rate), Fig. 2.

Analysis shows that PM heat conductivity reduction as well as reactor length growth has strong potential for LCL improvement. Important result is non-monotonous behaviour of the LCL curve as function of gas flow rate (Fig. 2-4) and existence of optimum flow rate.

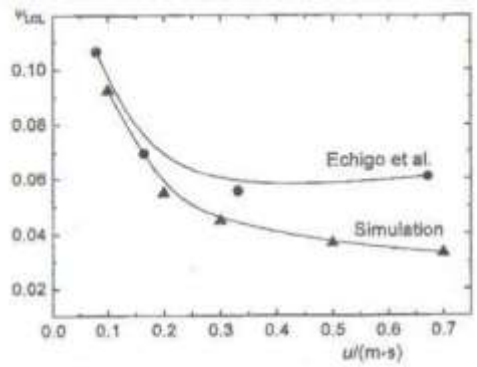

Fig. 1. Lean combustibility limit according to experiments [11] and corresponding simulation for sponge-type porous media [12]

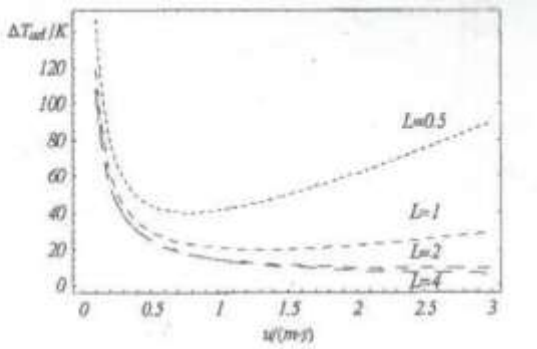

Fig. 2. Lean combustibility limit dependence on filtration velocity. Analytical model [12] Reactor length L = 0.5, 1.2 and 4 m as depicted on the graph

Systematic numerical study of LCL confirmed the mentioned peculiarity of the system and gave an important from practical viewpoint parametric dependencies, revealing potential of extra-lean combustion in Reverse Flow Reactors, Fig. 3, 4.

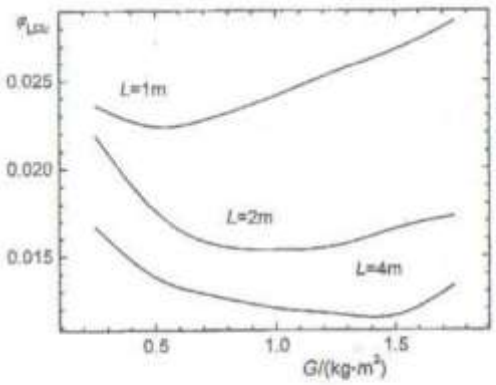

Fig. 3. Reciprocal flow reactor lean combustibility limit curves on the $\varphi - G$ plain. L values are on the graph

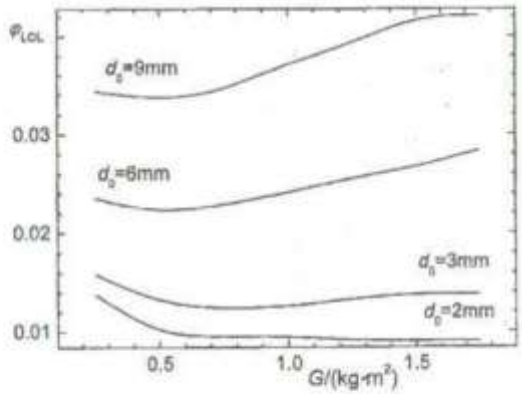

Fig. 4. Reciprocal flow reactor lean combustibility limit curves on the $\varphi - G$ plain. d_0 values are on the graph

Potential of the technology of the methane conversion to syngas

Among the numerous parameters that characterize partial oxidation of methane in a RFR, die specific mass flow rate G, fuel-to-oxidizer equivalence ratio Φ, and water concentration in the input mixture x_{H2O} are more suitable for variation and carrying out operative control over the process. These parameters are selected as basic variables for the parametric study, Fig. 5-8. The problems of scale up and corresponding parametric study was performed (the graphs are not presented because of lack of space).

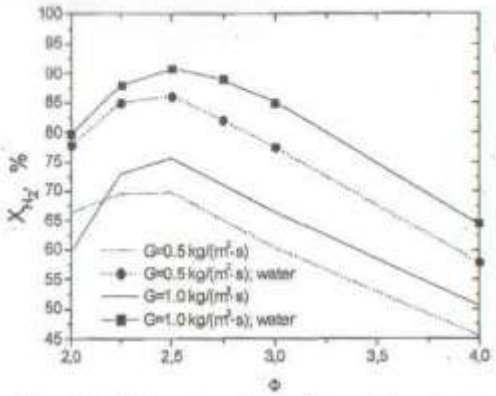

Fig. 5. Methane conversion ratio as a function of the equivalence ratio. Description is in the legend. Marked lines correspond to water admixing concentration maximizing conversion ratio; lines without marks – dry mixture

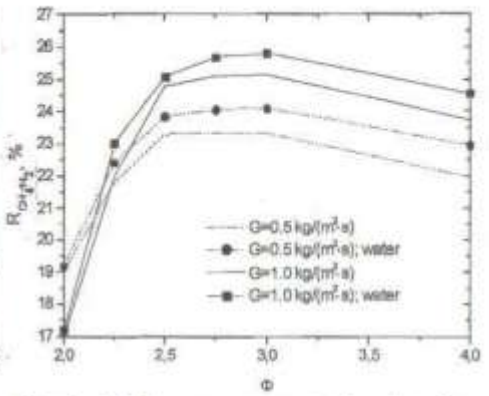

Fig. 6. Hydrogen concentration in the output gas as a function of the equivalence ratio. Description is in the legend. Marked lines correspond to water admixing concentration maximizing hydrogen concentration; lines without marks – dry mixture

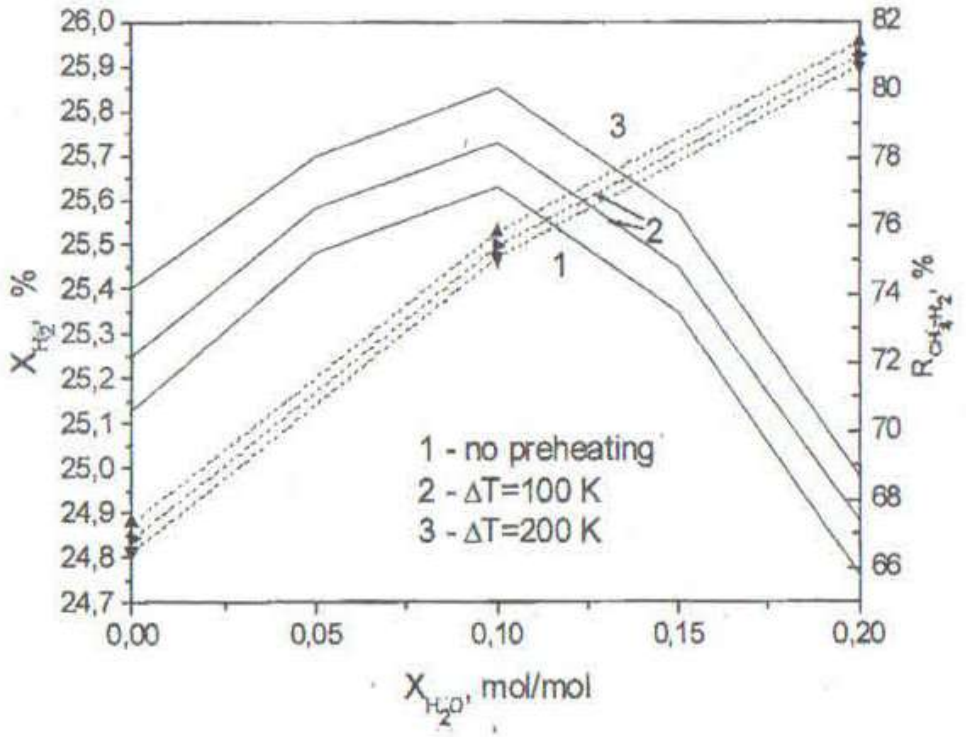

Fig. 7. Hydrogen output concentration (solid lines) and methane conversion ratio (marked dashed lines) as a function of water admixing concentration and input gas preheating, as indicated in the legend. The specific mass flow rate G = 1.0 kg/(m^2·s), Φ = 3.0, X_{H_2O} = 0.1. The parameters are from Table 1

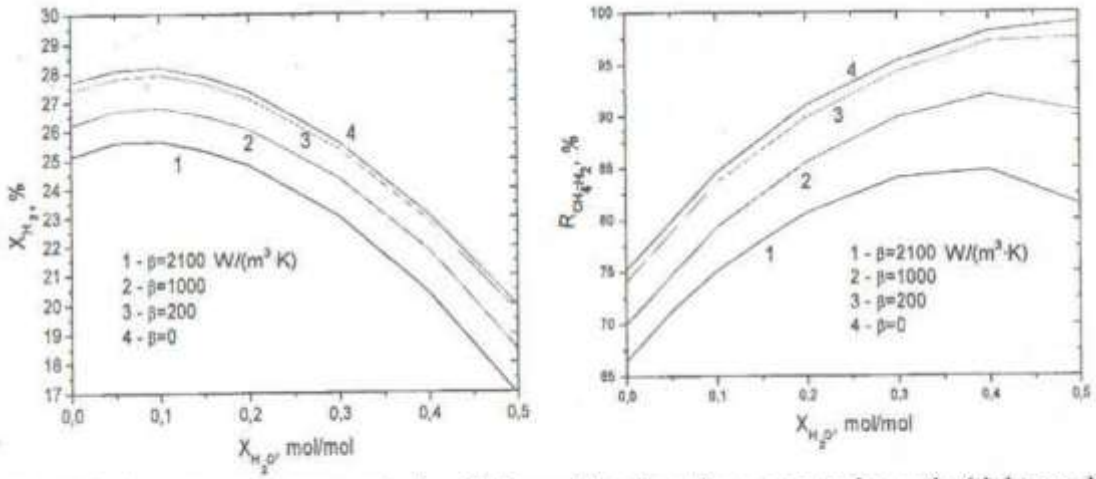

Fig. 8. Hydrogen output concentration (left graph) and methane conversion ratio (right graph) as a function of water admixing concentration and heat loss coefficient β, as indicated in the legend. The specific mass flow rate G = 1 kg/(m^2·s), Φ = 3, the parameters are from Table 1

Table 1. Parameters of the standard RFR for methane conversion. Packed bed - Al_2O_3 balls

Parameter	Dimension	Value	Parameter Description
G	Nm^3/h	4	gas flow rate
D_0	m	0.038	reactor chamber diameter
L	m	0.38	reactor length
d_0	m	$5 \cdot 10^{-3}$	packed bed particle diameter
L_{ist}	m	$9 \cdot 10^{-3}$	refractory layer width
β	$W/(m^3 \cdot K)$	2100	heat loss coefficient
T_0	K	300	initial temperature of the system
p_0	Pa	$1.013 \cdot 10^5$	pressure at exit of reactor
ε	-	0.6	emissivity of the packed bed particles
m	-	0.4	porosity
ρ_s	kg/m^3	2810	packed bed material density
c_s	$J/(kg \cdot K)$	794	packed bed material heat capacity
λ_s	$W/(m \cdot K)$	0.2	packed bed material thermal conductivity coefficient
λ_{ist}	$W/(m \cdot K)$	0.15	thermal conductivity of the refractory insulation layer
G_m	$kg/(m^2 \cdot s)$	1	mass flow rate density

Conclusions

The new investigations demonstrated the possibly attainable regimes of extra-lean mixtures oxidation and methane conversion to hydrogen and syngas. The non-homogeneous behavior of the lean limit curves is explained by the influence of temperature separation between the solid and gas phases. It is predicted that reasonable attainable lean limit may be 0.02 in dimensionless equivalence ratio (which correspond to adiabatic temperature -50 K), Fig. 3, 4.

The scale up parameters for reciprocal flow reactor for methane to hydrogen conversion are clarified. The reduced aspect ratio geometry is recommended. The influence of water addition on conversion efficiency is explored. The water admixing in the range of 5 to 40 molar percent may be recommended depending on the aim of optimization (hydrogen concentration or conversion ratio incensement).

References

1. Dmitrenko Yu.M., Zhdanok S.A., Klevan R.A., Minkina V.G. Methane-to-Hydrogen Conversion in the Filtration Combustion Wave of Rich Methane-Air Mixtures // *J. Eng. Physics and Thermophysics*. 2007. Vol. 80. Pp. 304-310.
2. Dobrego K.V., Zhdanok S.A. Physics of filtration combustion of gases. HMTI Publ. Minsk 2002.
3. Drayton M.K., SavelievA.V,, Kennedy L.A. et al. Superadiabatic partial oxidation of methane in reciprocal and counterflow porous burners, Proceedings of The 27-th Symp. Int. on Combust. Pittsburg. PA, 1998. P. 1361.

4. Bingue J.P., Saveliev A.V., Fridman A.A., Kennedy L.A. Hydrogen production in ultra-rich filtration combustion of methane and hydrogen sulfide // *Int. J. Hydrogen Energy* 2002. Vol. 27. P. 643.
5. Al-Hamamre Z., Trimis D., Wawrzinek K. Thermal partial oxidation of methane in porous burners for hydrogen production // Proc. 7th Int. Conf. on Technologies and Combustion for a Clean Environment. Lissabon, Portugal, July 2003.
6. Dhamrat R., Ellzey J. Numerical and experimental study of the conversion of methane to hydrogen in a porous media reactor // *Comb. Flame.* 2006. Vol. 144. P. 698.
7. Weinberg F.J. Combustion temperature - the future? // *Nature.* 1971. No. 233. P. 239.
8. Matros Yu. Sh. Unsteady processes in catalytic reactors // *Studies of Surface Science and Catalysis-Elsevier.* 1985. Vol. 22.
9. Fateev G.A. Heat Transfer in a Reacting Porous Body during Filtration of a Gas // Foreign Technology Div Wright-Patterson AFB Ohio. Accession Number AD0745460, 10 MAR 1972.
10. Babkin V.S. Filtration Combustion of Gases, Present State of Affairs and Prospects // *Pure Appl. Chemistry* 1993. Vol. 65. P. 335.
11. Hoffmann J.G., Echigo R., Yoshida H., Tada S. Experimental study on combustion in a porous media with a reciprocating flow system // *Comb. Flame.* 1997. Vol. 111. P. 32.
12. Dobrego K.V., Gnezdilov N.N., Lee S.H., Choi H.K. Lean combustdility limit of methane in reciprocal flow filtration combustion eractor // *Int. J. Heat and Mass Tr.* 2008. Vol. 51, No. 9. Pp. 2190-2198.

The Third International Workshop

HYDROGEN PRODUCTION IN REVERSIBLE FLOW FILTRATION COMBUSTION REACTOR

Yu.M. DMITRENKO, R.A. KLEVAN

A.V. Luikov's Heat and Mass Transfer Institute of NAS of Belarus, Minsk, Belarus

Introduction

Filtration combustion wave propagating in inert porous media can provide reasonably high conversion of rich air-methane mixture into hydrogen without external heating of reaction

zone. Such approach is based on "super adiabatic effect" of filtration combustion wave when combustion temperature can be much above the adiabatic temperature of fuel mixture [1]. The nature of this phenomenon is very intensive and internally self-organized process of heat recuperation between incoming fuel gas and solid porous media.

In the case of partial oxidation of methane the main conversion products are H_2, CO, CO_2, CH_4 and H_2O. Small amounts of some high molecular weight hydrocarbons are also present. The product composition is strongly dependent on process conditions, the temperature being the first. Though the process of partial oxidation of methane is exothermic, the thermal effect of reaction is insufficient for self-sustained non-catalytic process in adiabatic conditions.

In traditional industrial non-catalytic process of partial oxidation of methane the reaction temperature of about 1500 °C is attained by external heating of reaction zone. Two main drawbacks of such process are intensive soot formation and decrease of conversion efficiency at medium and low plant capacity. Advantages of alternative process based on super adiabatic combustion are simplicity and low cost due to the absence of catalyst.

Previous studies of superadiabatic filtration combustion [2-8] demonstrate a reasonably high efficiency of methane to hydrogen conversion (up to 63 %) at some conditions. The main factor governing the process is combustion temperature, which is a function of equivalence ratio y and specific flow rate of fuel mixture per unit of cross section area g. One can increase the combustion temperature either by increasing g, or decreasing γ.

For the practical usage of superadiabatic combustion for hydrocarbon conversion the filtration process should be made continuous. This can be done by periodically reversing of gas flow direction through a porous media. The first application of reversible flow filtration combustion reactor was related with development of the burner for an extra lean fuel mixture [9]. Reversible flow system can also be used as a non-catalytic reformer of methane to the hydrogen [10, 11].

Here the new results of an experimental study on methane-to-hydrogen conversion by its partial oxidation in reversible flow superadiabatic filtration combustion reactor are reported.

Experimental setup

The experimental setup consists of reversible flow porous media combustion reactor, reactor preheat unit, gas flow rate control equipment, temperature measurement system, gas chromatograph and data acquisition systems. A scheme of experimental setup is shown in Fig. 1.

The reactor case is a flanged stainless tube with 140 mm outer diameter and 6 mm wall thickness. The reaction zone is filled with randomly packed bed of alumina spheres 5-6 mm in diameter. The space around packed bed is filled with pressed Kaowool insulation. Gas filtration through insulation layer is negligible due to its extremely low permeability.

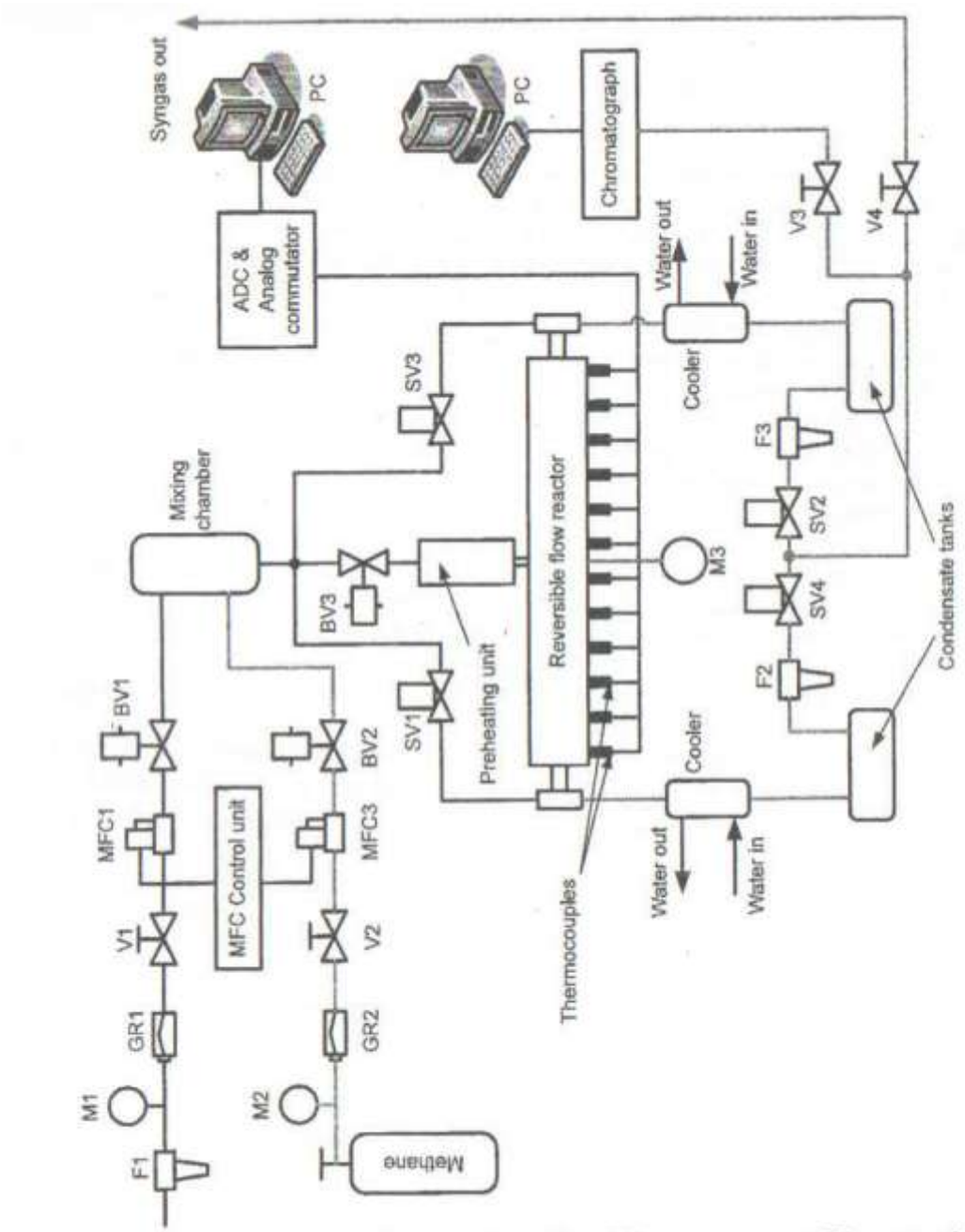

Fig. 1. Experimental setup: F1…F3 – gas filters; M1…M3 – manometers; GR – gas reducers; MFC1, MFC2 – mass flow controllers; V1…V3 – ball valves; SV1… SV4 – solenoid valves; V1…V4 – regulating valves

Preheat burner is used to preheat the porous medium prior to start the filtration combustion wave. It is a small porous media burner fueled by methane-air mixture and ignited by a spark plug.

The air is taken from the high-pressure line, while methane was taken from the standard 50-liter high-pressure cylinder. Flow rates of fuel components are controlled and measured by "Omega" mass flow controllers. Premixed gas reactants from mixing chamber are introduced into alternate ends of reversible flow porous media reactor. Periodically switching of the flow direction is provided by means of two pairs of "Omega" SV-351 solenoid valves. Reaction

products are cooled the room temperature by water coolers. Laboratory ventilation system is used to remove the exhaust gas out of the room.

The axial temperature distribution in the porous medium reactor is measured with an array of twelve S-type thermocouples (Pt—10 %Rh/Pt) in ceramic shell with exposed junction. A PC based data acquisition system was employed to read and record the temperatures with time resolution about 0.1 s.

Chemical composition of reaction products was measured using modified Chrom-4 Gas Chromatograph. Digital signal processing was performed with A/D Converter based on Analog Devices AD7289 chip. Component separation is achieved with 3 m long 3 mm in diameter column filled with molecular sieve CaA. Argon was used carrier gas.

Results

All experiments were made at minimal operating pressure in reactor p = 2.35 bar. Lower pressure limit is determined by hydraulic losses in valves, pipelines and reactor porous media. Half-cycle duration τ =120 s was held constant for all flow rates. This time is sufficient for full development of reaction zone after flow direction reversal. The efficiency of methane-to-hydrogen conversion in reversible flow superadiabatic combustion system is directly related with maximal reactor temperature T_m. The effect of specific flow rate g and equivalence ratio y of gas fuel mixture on T_m is given in Fig. 2. The tendency of T_m growth with g for all values of y completely agrees with experimental and numerical simulation results for a single filtration combustion wave [3]. The data on output concentrations of hydrogen arc given in Fig. 3. The increase of hydrogen yield with g can be explained by improvement of chemical reaction kinetics with combustion temperature growth. The most marked growth of hydrogen concentration is seen for g in the range of 0.4-1.2.

Concentration of residual methane in reaction products and methane-to-hydrogen conversion ratio are the most sensitive parameters of conversion efficiency. The later is a ratio of hydrogen yield of conversion process to the total hydrogen containing in input methane. This parameter can be estimated from input and output concentrations of N_2, H_2, and CH4:

$$\eta = \frac{C_{H_2}}{2C_{CH_4}^{in}} \frac{C_{N_2}^{in}}{C_{N_2}^{out}}.$$

The results on residual methane content in conversion products are given in Fig. 4. Output concentration of CH_4 decreases as g grows. The lowest values (about 2%) are found for lowest y. The methane-to-hydrogen conversion ratio η is given in Fig. 5.

The maximal value of conversion efficiency (η = 0.68) is attained for the lowest equivalence ratio (γ = 2.4) and highest specific flow rate (g = 1.8).

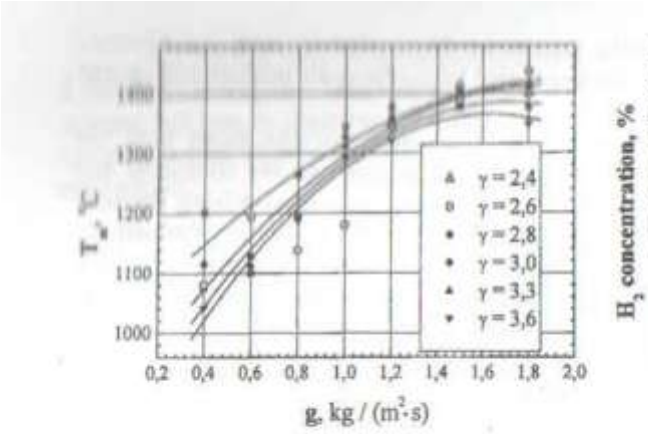

Fig. 2. The effect of g and γ on maximal reactor temperature

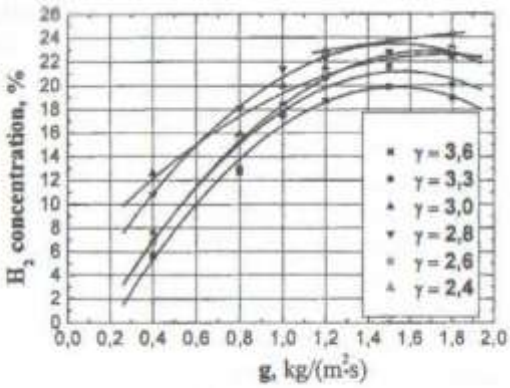

Fig. 3. The effect of g and γ on the hydrogen concentration

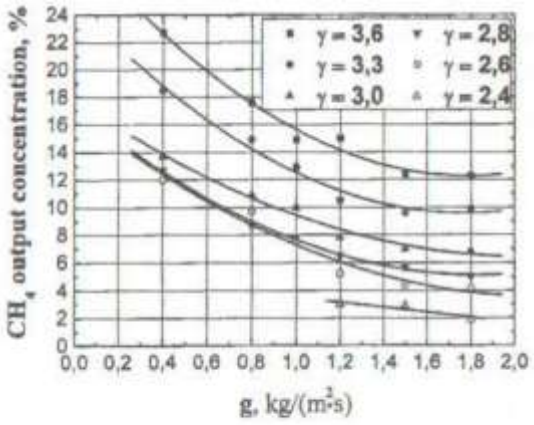

Fig. 4. The effect of g and γ on the output concentration of methane

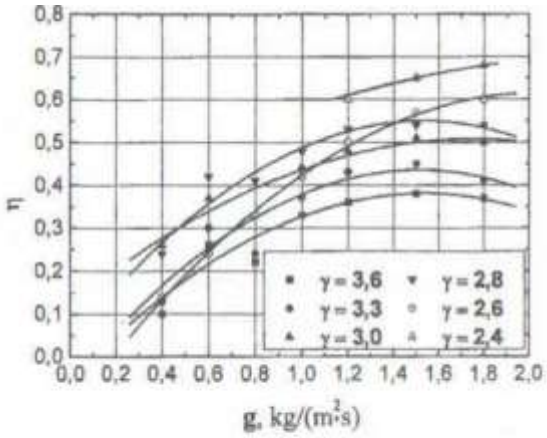

Fig. 5. The effect of g and γ on conversion ratio

Conclusion

Relatively high efficiency of non-catalytic process of methane-to-hydrogen conversion in reversible flow porous media combustion reactor is demonstrated. The conversion process seems to be most efficient for $\gamma \approx$ 2.6-2.4 and g = 1.6-1.8. At the lowest operating reactor pressure p = 2.35 bar no evidence of soot formation was observed. For further improvement of the process characteristics we plan to study the effect of properties of porous medium used (porosity and diameter) on the conversion efficiency.

References

1. Kennedy L. A., Fridman A. A. and Saveliev A. A. Superadiabatic combustion in porous media: wave propagation, instabilities, new type of chemical reactor *// Intern J. Fluid Mech. Res.* 1995. Vol. 22. Pp. 1-26.
2. Gavrilyuk V.V., Dmitrenko Yu.M., Zhdanok S.A., Minkina V.G., Shabunya S.I., Yadrevskaya N.L., Yakimovich A.D. A study of methane-to-hydrogen conversion process

in superadiabatic filtration combustion // *Theoretical fundamentals of chemical technology.* 2001. Vol. 35, No. 6. Pp. 627-635. (In Russian).

3. Gavrilyuk V.V., Dmitrenko Yu.M., Zhdanok S.A., Minkina V.G., Shebunye S I Yadrevskaya N.L., Yakimovich A.D. A study of methane-to-hydrogcn conversion process in a single filtration combustion wave // Proc. of IV Intern. Forum on I lent and Mass Transfer MIF-2000. Minsk. 2000. Vol. 4. Pp. 21-31.
4. Kennedy L.A., Bingue J.P., Saveliev A.V., Fridman A.A., Foutko S.. Chemical structures of methane-air filtration combustion waves for fuel-lean and fuel-rich conditions // *Proc. of Combust. Institute.* 2000. Vol. 28. Pp. 1431-1438.
5. Bingue J.P., Saveliev A.V., A.A. Fridman, L.A. Kennedy. Hydrogen production in ultra-rich filtration combustion of methane and hydrogen sulfide // *Intern. J. of Hydrogen Energy.* 2002. Vol. 27. Pp. 643-649.
6. Pedersen-Mjaanes H., Chan L. and Mastorakos E. Hydrogen production from rich combustion in porous media *И Intern. J. of Hydrogen Energy.* 2005, Vol. 30. Pp. 579-592.
7. Dhamrat R. S. and Ellzey J. L. Numerical and experimental study of the conversion of methane to hydrogen in a porous media reactor // *Combust.and Flame.* 2006. Vol. 144, No. 4. Pp. 698-709.
8. Dmitrenko Yu.M., Zhdanok S.A., Klevan R.A., Minkina V.G. Methane-to-hydrogen conversion in filtration combustion wave of rich air-methane mixtures // *J. of Engineering Physics.* 2007. Vol. 80, No. 2. Pp. 90-95. (In Russian).
9. Hoffman J. G., Echigo R., Yoshiba H. and Tada S. Experimental study on combustion in a porous media with a reciprocating flow system // *Combustion and Flame.* 1997. Vol. III, No. 1-2. Pp. 32-46.
10. Drayton M.K., Saveliev A.V., Kennedy L.A., Fridman A.A., Li Y. Syngas production using super adiabatic combustion of ultra-rich methane-air mixtures // Twenty-Seventh Symposium on Combustion/The Combustion Institute. 1998. Pp. 1361-1367.
11. Dmitrenko Yu.M., Gavrilyuk V.V., Minkina V.G., Shabunya S.I., Zhdanok S.A. Study of Methane-to-Hydrogen Conversion under Filtration Combustion//Nonequilibrium processes

and their Applications. Contributed papers of the IV Intern. School-Seminar. Minsk, 1998 / A.V. Luikov Heat and Mass Transfer Institute. Minsk, 1998. Pp. 170-173.

MACROKINETICS OF PEAT IGNITION WITH HOT SPOT

N.N. GNESDILOV, K.V. DOBREGO, I.M. KOZLOV

A.V. Luikov Heat and Mass Transfer Institute of NAS of Belarus, Minsk, Belarus

nick_gn@itmo.by

Introduction

Peat fires is a serious economic and ecological problem of Belarus and other countries that possess big amounts of drain peat bogs. Numerical simulation of peat fires not to be under investigation till recently. It can be explained by complexity of the problem.

In order to estimate tendency of a peat to be ignited by heat sources of different heat power it is necessary to have an appropriate physical and mathematical model. Such a model need to include a heat and mass transfer processes in peat layer, peat pyrolysis and organic component oxidation processes. To this end the set of 2D equations was proposed.

Model description

The system under investigation consists of peat cylindrical layer with porosity *m*. The upper border of layer is open in an atmosphere. The down and side borders are closed adiabatically. At initial time peat was preheated to temperature 1000 K in order to initiate pyrolysis and combustion (Fig. 1).

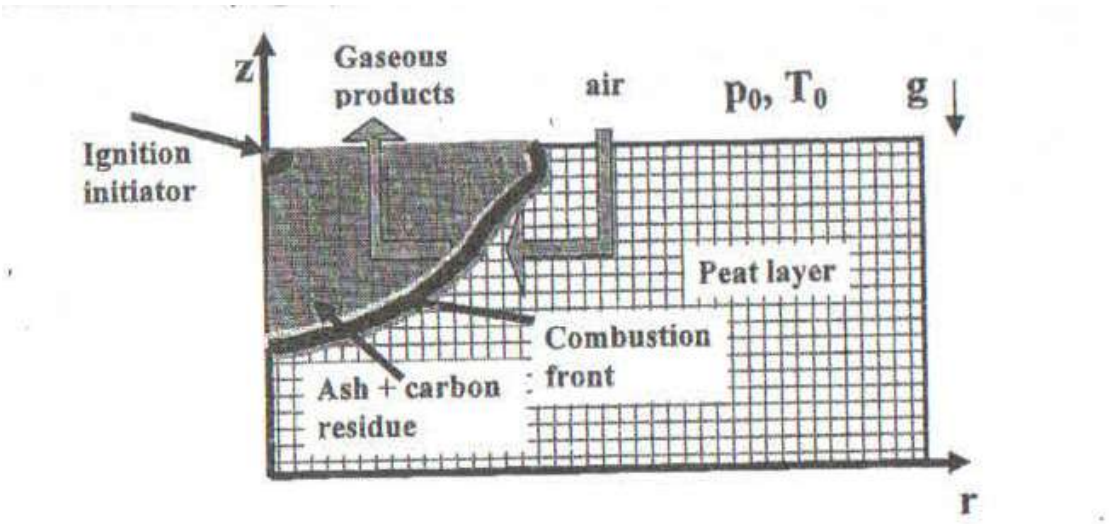

Fig. 1. Principal scheme of processes under modeling

Set of equations, what describes a system under investigation was based on the equations for filtration combustion [1].

Motion equation:

$$\frac{\partial m\rho \mathbf{v}}{\partial t} = -m\frac{\mu}{k}\mathbf{v} - m\nabla\tilde{p} + m(\rho - \rho_0)\mathbf{g}\,. \tag{1}$$

Gas chemical compounds conservation equation:

$$m\rho_g \frac{\partial Y_g^{\,l}}{\partial t} + m\rho_g \mathbf{u}\cdot\nabla Y_g^{\,l} + \nabla J_D^{\,l} = \dot{\rho}_{mg}^{\,l} - Y_g^{\,l}\dot{\rho}_{mg}\,. \tag{2}$$

Peat chemical compounds conservation equation:

$$(1-m)\rho_s \frac{\partial Y_s^{\,l}}{\partial t} = \dot{\rho}_{ms}^{\,l} - Y_s^{\,l}\dot{\rho}_{ms}\,. \tag{3}$$

Heat conductivity equation for a gas:

$$m\rho_g c_g \frac{\partial T_g}{\partial t} + m\rho_g c_g \mathbf{u}\cdot\nabla T_g = \nabla\cdot\left(m\Lambda\nabla T_g\right) + \alpha\left(T_s - T_g\right) + Q_g\,. \tag{4}$$

Heat conductivity equation for a peat:

$$\rho_s c_s \frac{\partial\left[(1-m)T_s\right]}{\partial t} = \nabla\cdot\left(\lambda\nabla T_s\right) + \alpha\left(T_g - T_s\right) + Q_s\,. \tag{5}$$

Ideal gas law:

$$\rho_g = \frac{pV}{\mu RT}\,. \tag{6}$$

Mass conservation equations for a peat (7) and a gas (8) arc sums of correspondent equations (2) and (3):

$$\rho_s \frac{\partial(1-m)}{\partial t} = \sum_i \dot{\rho}_{si}\,, \tag{7}$$

$$\frac{\partial\left(m\rho_g\right)}{\partial t} = -\nabla\cdot\left(m\rho_g\mathbf{u}\right) + m\sum_i R_i\,. \tag{8}$$

Heat release in a gas is defined as $Q_g = -\sum_j^{N\,gas.react.}\sum_i^{N\,comp.} h_{ij}\dot{\rho}_{ij}$, heat release in a peat is $Q_s = -\sum_j^{N\,gas.react.}\sum_i^{N\,comp.} h_{ij}\dot{\rho}_{ij}$, pressure was redefined $\tilde{p} = p - \left(p_0 + \rho_0 z\mathbf{g}\right)$, diffusivity flux is $J_D^{\,l} = -m\rho_g D\nabla Y_g^{\,l}$.

Elementary composition of organic part of peat is defined as PEAT(C:0:H=38:21:40 in molar fractions) [2]. In addition, peat consist of ash - Si, 10% to organic mass and water $H_2O(1)$ (10 % of mass). Mean physical properties of peat are taken from [2-5].

Set of chemical reaction defined in [6].

$PEAT \rightarrow 3.7C+0.1CO+2H_2O$ – peat pyrolysis to water, *CO* and carbon reminder.

$H_2O \rightarrow H_2O(l)$ – water condensation.

$H_2O(l) \rightarrow H_2O$ – water evaporation.

$2CO+O_2 \rightarrow 2CO_2$ – oxidation of CO to CO_2.

$2C+O_2 \rightarrow 2CO$ – oxidation of carbon reminder.

Results and discussion

The numerical code, based on the model equations (l)-(8) was developed. Numerical simulations gives propagation velocity of peat combustion is about 6 mm/h, what is in agreement with experimental data [7], where velocity is 7 mm/h. Using this code one can simulate numerically bog fire propagation at different ignition conditions and peat properties. Fig. 2 shows typical spatial distributions of peat temperature, peat mass fraction, porosity and velocity.

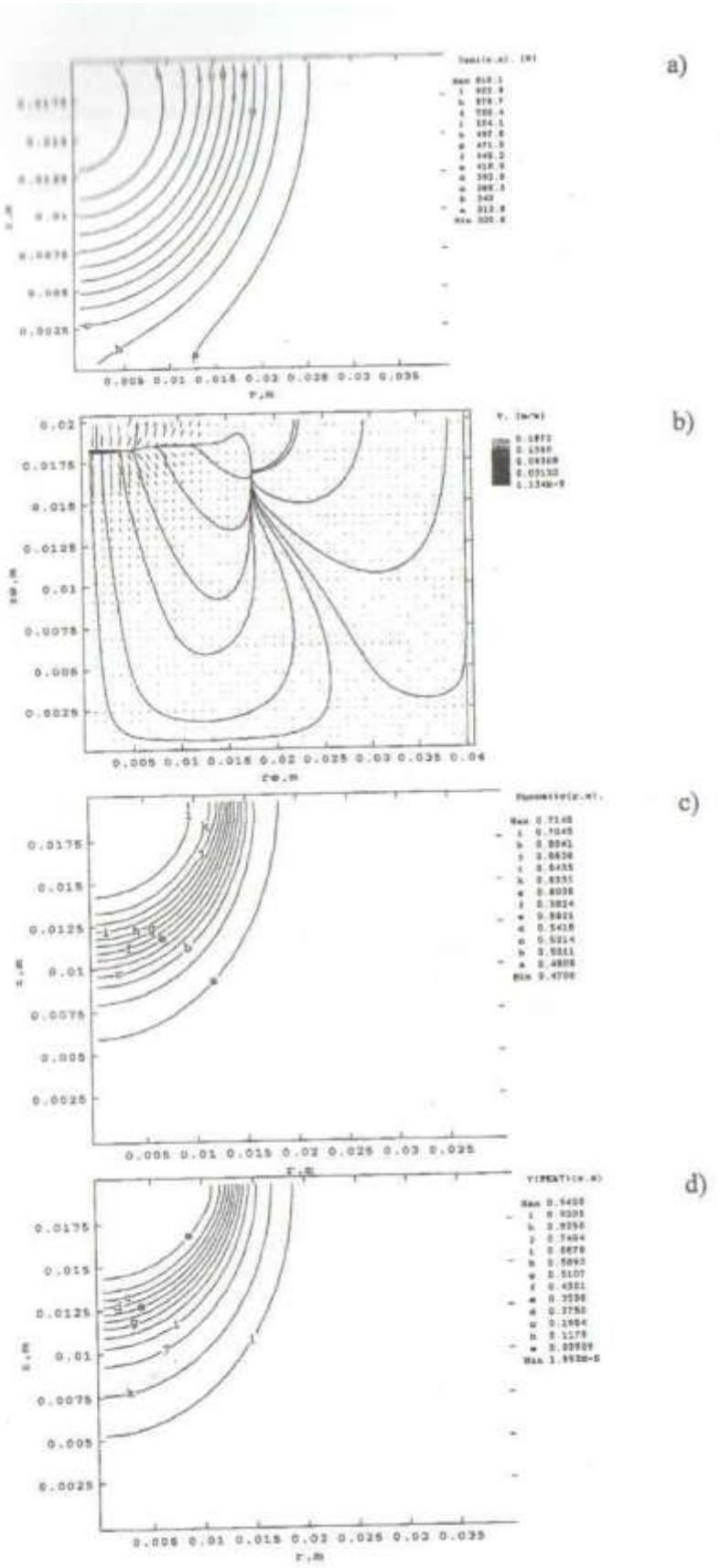

Fig. 2. Typical spatial distribution of: a) peat temperature, b) gas velocity, c) porosity of peat layer and d) mass fraction of PEAT. Initial porosity is 0.45, time 3500 s, peat density is 1500 kg/m^3

Conclusion

2D model of a peat pyrolysis and combustion was developed in order to simulate bog fires. Overall (brutto) chemical model was tested on experimental data [5, 7] and shows satisfactory agreement.

Nomenclature

c_p – gas specific heat, c_s – porous media specific heat, d_0 – diameter of packed bed particle, 0.1 mm, $\mathbf{D}$ – gas diffusivity tensor, include gas diffusivity and dispersion diffusivity, h_i – mass enthalpy of i^{-th} gas component, m –porosity, M –mean molar mass of gas mixture, PEAT – conventional chemical compound, defined as organic fraction of peat, p_0 – atmospheric pressure, R – universal gas constant, T_0 – initial temperature, T – temperature, $\mathbf{u}$ – gas filtration velocity, X_i –mole concentration of i^{th} component, Y_i – mass fraction of i^{-th} component, z – coordinate, α_{vol} – volumetric heat transfer coefficient, $\mathbf{\Lambda}$ – heat conductivity of gas tensor, $\mathbf{\Lambda} = c_p \rho_g \mathbf{D}$, λ – effective heat conduction coefficient of peat, μ – gas viscosity, ρ – density, $\dot{\rho}_i$ –i^{-th} component generation rate in all chemical reaction, $\dot{\rho}_{ij}$ – i^{-th} component generation rate in j^{-th} chemical reaction.

Subscripts: g – gas, s – peat, i – i^{-th} component of gas mixture or peat.

References

1. Dobrego K. V., Kozlov I. M., Gnesdilov N.N., Vasiliev V.V. 2DBurner - software package for gas filtration combustion systems simulation and gas non-steady flames simulation. Minsk. 2004 (Preprint / Heat and Mass Transfer Institute, No. 1.)
2. Lishtvan 1.1., Korol N. T. Main peat properties and methods for its determination. Science and technology. Minsk. 1975.
3. Kostiuk N. S. Physics of peat. Minsk. Science and technology. 1967.
4. Grishin A. M., Golovanov A. N. et al // *J. of Engineering Physics and Thermophysics.* 2006. Vol. 79, No. 3. Pp. 131-136.
5. Grishin A. M., Golovanov A. N. et al // *J. of Engineering Physics and Thermophysics.* 2006. Vol. 79, No. 3. Pp. 137-142.
6. Subbotin A. N. // *J. of Engineering Physics and Thermophysics.* 2003. Vol. 76, No. 5. Pp. 159-165.
7. Borisov A. A., Kiselev J. S., Udilov V. P. Thermophysics of forest fires. Novosibirsk. Science. 1984. Pp. 23-30.

AUTOIGNITION OF METHANE/ETHYLENE/AIR MIXTURES AT ELEVATED PRESSURES

E. BARANYSHIN[1], V. LESCHEVICH[1], O. PENYAZKOV[1], K. SEVROUK[1], V. TANGIRALA[2], N. JOSHI[2]

'A.V. Luikov Heat and Mass Transfer Institute of NAS of Belarus, Minsk, Belarus

[2]General Electric Global Research Center, Niskayuna, NY, USA

Introduction

Although methane and ethylene autoignitions at high temperatures have been well researched over the past decades, few experimental studies are available at the actual conditions of interest of detonation applications, gas turbines, engines and safety tasks, which require investigations for high-pressure fuel-air mixtures of different stoichiometrics. Previous works were mostly conducted under low-pressure (0.5-15 atm), high temperature (1200-2500 K), and for the mixtures with a high degree of argon dilutions (over 90 % Ar). Recent shock tube experiments [1,2] produced CH_4/O_2 ignition delay times for pressures up to 260 atm, temperatures as low as 1040 K, average diluent levels near 60 %, and equivalence ratios between 0.4-6.0. Few experimental data are available for the ignition delay time of methane/air mixtures under typical, engine relevant conditions, that is, for initial pressures above 16 atm, temperatures below 1400 K, and equivalence ratios ranged from 0.7 to 1.3 [3]. The same situation is for ethylene. Only two studies [4, 5] were devoted to auto-ignition properties of ethylene/air mixtures at low pressures. In general, the data are non-existent at detonation thermodynamic conditions.

Thus, there is an obvious lack in experimental data concerning the combustion and auto-ignition of methane/ethylene/air mixtures at high pressures and temperatures. This work presents systematic experimental investigations of ignition times, auto-ignition modes and detonability limits of methane/ethylene/air mixtures for a wide range of temperatures, pressures, and equivalence ratios.

Experiment

A stainless steel shock tube of 76 mm in diameter and 8.5 m long was used for reflected shock wave studies. The runs were performed in stoichiometric ($\phi = 1$), lean ($\phi = 0.5$), and rich ($\phi = 2$) methane/air mixtures at pressures of 5-22 atm. Mixtures were prepared by the method of partial pressures from commercially grade methane and ethylene of 99.92 % purity (contents: nitrogen-oxygen 0.03 %; ethane-propane 0.02 % and water 0.02 %), nitrogen and oxygen of 99.995 % purities. Five high-frequency pressure sensors monitored pressures along the tube with a rise time less than 1.5 and a 1.5 mm spatial resolution (Fig. 1). The end wall tourmaline pressure sensor measured the reflection time and pressure history behind reflected shock waves. To detect arrival times of reaction front six ion current sensors were installed along the tube.

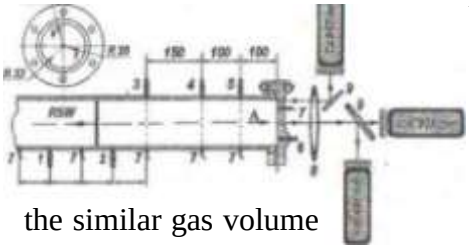

To monitor reaction progress along the tube two ∅ 8 mm quartz rods were mounted into the end wall (Fig. 1). The first rod ensured emission measurements from the 0 5 mm gas column along the centerline of the tube, the second-from along the tube wall in the boundary layer. Luminosities of the similar gas volume OH (308.5 nm, $\Delta\lambda$ = 1.4 nm) and CH (430.8 nm, $\Delta\lambda$ = 2.6 nm) molecules were implemented to measure auto-ignitions along the centerline of the tube. The emission of C_2 radicals (516.3 nm, $\Delta\lambda$ = 4.6 nm) was detected to identify the auto-ignition in the boundary layer. Shock-tube series were performed at constant density of the gas behind reflected shock waves. In that way fuel, oxygen, and nitrogen concentrations were kept constant within a studied temperature range.

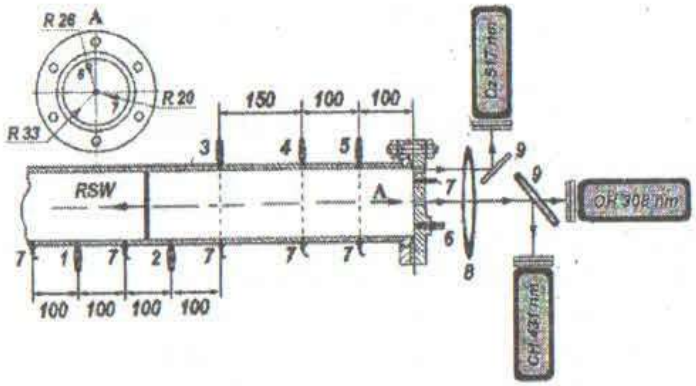

Fig. 1. Schematic of the test section for auto-ignition studies in methane/ethylene/air mixtures in a 76 mm shock tube: 1–4 – high-frequency pressure transducers; 5 – ion current sensors; 6 – lens; 7 – beam splitters; 8 – double narrow-band filters with aperture diaphragms; 9 – photomultipliers

Reflected shock wave (RSW) velocity measurements [7,8] in a frame of reference attached to gas flow behind incident shock wave (ISW) and pressures identified the auto- ignition modes of the mixture (strong, transient and weak) [9]. Fig. 2 illustrates typical experimental dependence of RSW velocity on the post- shock temperature for low- density stoichiometric methane/air mixtures. On the basis of pressure and emission observations the inflection point of velocity curve at low temperatures for distances of 100 mm (Fig. 2) was used for determining positions of the strong explosion limits.

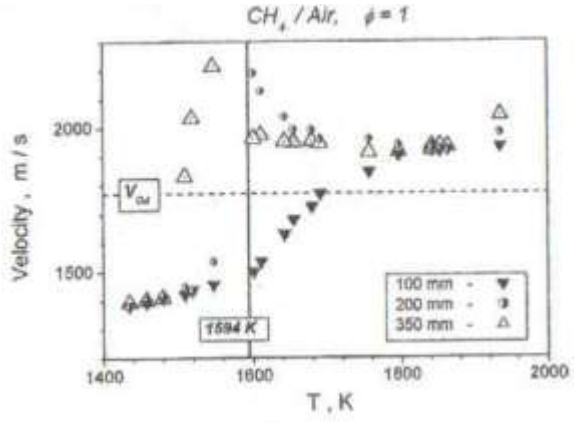

Fig. 2. Velocities of reflected shock wave at 100, 200 and 350 mm from reflecting wall vs. post-shock temperature in low-density stoichiometric methane/air mixture $\rho = 2.0 \pm 0.06$ kg/m^3

Results

For stoichiometric methane/ and ethylene/air mixtures, the results of induction time measurements are plotted in Fig. 3. Simultaneously, low-temperature ignition limits were established in the course of experimental series. Positions of the limits are plotted on the graphs by dashed vertical lines. As is seen on the Fig. 3 a, for stoichiometric methane/ air mixtures the global activation energy is within the range of 51.3-55.8 kcal/mole. It is consistent with previous results of. Induction curves exhibit clear linear Arrhenius behavior within studied temperature range. Plots 3a illustrate correlations of our results with existing literature data of Huang et al. [3] recorded at equivalent post-shock conditions. The data [3] is based on pressure measurements of the induction time behind reflected shock waves and shows considerably shorter ignition delays within studied range of conditions. This evidences on an insuffielent flow control facilitating auto-ignitions of methane/air mixtures during these experiments in a tailored sock tube (3).

For ethylene measurements show a significant decreasing in global activation energy of ethylene at high temperatures T> 1300 K (Fig. 3 b). Approximations of different parts of induction time curve give activation energies of 33.73 kcal/mole at high temperatures T>1300 K, and 52 kal/mole at low temperatures T<1300 K . At high pressures this tendency is not и clearly pronounced. Obviously, that such nonlinear behavior has underlying kinetic reasons, which are supported by predictions of detailed reaction mechanisms of ethylene oxidation [10]. Fig. 3 b illustrates correlations of current measurements with literature data |4, 5J at similar post-shock conditions and mixture compositions. At high temperatures, the best agreement is observed with low-pressure measurements of Brown & Thomas [5] in stoichiometric ethylene/air mixture. In spite of a two times lower density of the mixture the data [5] considerably under-predict the current results at temperatures T<1300 K. A possible explanation of such discrepancy is the influence of a buffer gas section, used for separation of the driver and driven gas mixtures in experiments [5], which can affect on uniformity of the flow behind ISW. The analysis of pressure traces presented in [5] shows the evident pressure variations behind ISW. The imposed flow perturbations may induce the local temperature increasing, enhance the ignition and, consequently, reduce the induction times. For ethylene/oxygen mixture with 70 % of Ar dilutions, the low-pressure data of Suzuki et al. [4] (Fig. 3b) demonstrate shorter ignition times within the studied range of post-shock conditions.

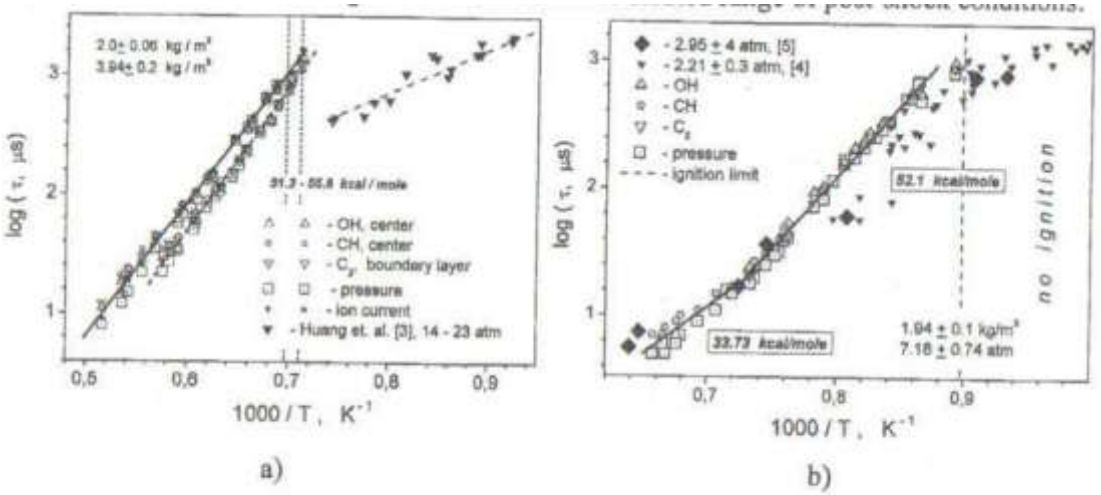

Fig. 3. Ignition delay time vs. reciprocal temperature in stoichiometric methane (a) and ethylene (b) /air mixtures

Correlation equations for methane and ethylene ignition times

For methane the experimental data within the temperature range of 1340-2090 K, pressures 7.0-22 atm, and stoichiometrics ϕ = 0.5-2 were approximated by correlation equations (see Fig. 4 a):

$$\tau(\mu s) = 1.377 \cdot 10^{-8} \cdot \exp\left(\frac{26090}{T}\right) \cdot [O_2]^{-0.8084} \cdot [CH_4]^{0.1798}, \quad (1)$$

where, t is the ignition time in (μs) , T is the post-shock temperature in (K), $[CH_4]$ is the methane concentration in (mole/cm^3), and $[O_2]$ is the oxygen concentration in (mole/cm^3).

Because the plots of induction time exhibit a large changing in activation energy тми» the stoichiometry of the mixture several equations for ethylene/air ignition time have been derived from experimental data:

for lean mixtures ϕ =0.5-1.0,

$$\tau(\mu s) = 5.764 \cdot 10^{-10} \cdot \exp\left(\frac{26930}{T}\right) \cdot [O_2]^{-0.3855} \cdot [C_2H_4]^{0.041} \quad (2)$$

for stoichiometries ϕ-0.5-2.0 (Fig. 4 b)

$$\tau(\mu s) = 2.127 \cdot 10^{-8} \cdot \exp\left(\frac{22410}{T}\right) \cdot [O_2]^{-0.1074} \cdot [C_2H_4]^{-0.2773}. \quad (3)$$

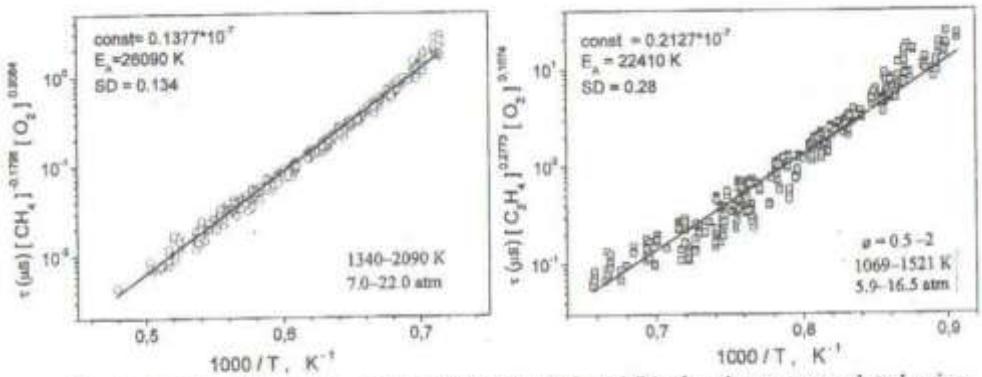

Fig. 4. Ignition delays for methane/ (a) and ethylene/ (b) air mixtures correlated using equations (1) (a) and (3) (b) vs. reciprocal post-shock temperature

Conclusions

Ignition times and auto-ignition modes for Ethylene/Methane/Air mixtures have been investigated behind reflected shock waves in a shock tube of 76 mm in diameter. Experiments were performed within the temperature range of 1060-2090 K, pressures of 5.9-22 atm, and stoichiometrics of ϕ = 0.5, 1.0, and 2.0. Emissions of OH (308.9 nm), CH (431.5 nm) and C_2 (516.5 nm) radicals, pressures and ion current observations were implemented to measure ignition and reaction times of the mixture along the centerline of the tube and in the boundary layer. Empirical correlations for Ethylene and Methane ignition times have been deduced from the experimental data. Auto-ignition modes and ignition limits of the mixtures (strong, transient

and weak) were identified comparing velocities of reflected shock wave at different locations from reflecting wall. Extensive database for validations of high-temperature Ethylene and Methane reaction mechanisms and numerical simulations has been obtained from experimental observations.

Acknowledgements

These works were sponsored by GE Global Research, and Research Program "Hydrogen" (Belarus).

References

1. Petersen E.L., Davidson D.F., Hanson R.K. // *J. Prop. Power.* 1999. Vol. 15, No. 1. Pp. 82-91.
2. Petersen E.L., Davidson D.F., Hanson R.K. // *Combust. Flame.* 1999. Vol. 117. Pp. 272-290.
3. Huang J., Hill P.G., Bushe W.K., Munshi S.R. // *Combustion and Flame.* 2004. Vol. 136. Pp. 25-42.
4. Suzuki M., Moriwaki T., Okuda T., Tanzawa T. *II Astronautica Acta.* 1973. Vol. 18, No. 5 Pp. 359-365.
5. Brown C.J., Thomas G.O. // *Combust. Flame.* 1999. Vol. 117, No. 4. Pp. 861-870.
6. Colket M.B., Spadaccini L.J. // *J. of Propulsion and Power.* 2001. Vol. 17, No. 2. Pp. 315-323.
7. Pcnyazkov O.G., Ragotner K., Dean A.J., Varatharajan B. *II Proc. Combust. Inst.* 2005. Vol.30. Pp. 1941-1947.
8. Dean A.J., Penyazkov O.G., Sevruk K.L., Varatharajan B. *II Proc. Combust. Inst.* 2007. Vol. 31. Pp. 2481-2488.
9. Saytzev S.G., Soloukhin R.I. // *Proc. Combust. Inst.* 1962. Vol. 8. Pp. 344-347.
10. Varatharajan B., Williams F.A. // *J. of Propulsion and Power.* 2002. Vol. 18, No. 2. Pp. 352-362.

KARHUNEN-LOEVE ANALYSIS OF SPATIOTEMPORAL PHENOMENA (INCLUDING FLAME PATTERNS)

M.U. KARELIN

A.V. Lykov Heat and Mass Transfer Institute of NAS of Belarus, Minsk, Belarus,
nkarelin@yahoo.co.uk

Introduction

Karhunen-Loeve (KL) decomposition is a valuable method of analysis of complex spatiotemporal phenomena [1]. It is based on bi-orthogonal representation of the data under study and is used for extraction of underlining dynamics in quite different areas, including aero- and hydrodynamics, optics, control theory, chemistry, and so on. Depending on the application area, this method (and its generalizations) is known under different names, such as proper orthogonal decomposition, empirical eigenfunctions method, factor analysis, Schmidt decomposition, coherent-mode approach and so on. In applied mathematics, this method is usually referred to as singular value decomposition; appropriate subroutine (svd) is available in most of current numerical analysis software.

It is necessary to note, that KL decomposition is widely used in analysis of flame dynamics [2] and combustion processes [3], where it provides significant inside of underlying processes and may provide a way of simplified characterization of the spatiotemporal process.

The aim of the present paper is to present an introductory review of the KL method and some examples of its use.

Decomposition and its properties

The formalism of KL decomposition is rather straightforward, see [1-4] and references therein: having some results of experiment or simulations, $A(x, t)$, one wants to find its representation if a form

$$A(x,t)=\sum_k \sqrt{\lambda_k}\, B_k(x)\,\alpha_k(t), \qquad (1)$$

where basic functions form orthogonal sets both in time and space

$$\int B_m(x)\, B_n^*(x)\, dx = \delta_{m,n},$$

$$\int \alpha_m(x)\, \alpha_n^*(x)\, dx = \delta_{m,n}$$

and the representation (1) provides a minimal r.m.s. approximation of the analyzed process

$$\int dt \int dx \left| A(x,t) - \sum_k \sqrt{\lambda_k}\, B_k(x)\,\alpha_k(t) \right|^2 = \min .$$

Rigorous mathematical theory states, that the above formulated requirements are fulfilled, if the basic functions are solutions of two integral equations (relative strengths of the decomposition terms are eigenvectors of these equations):

$$\lambda_n B_n(x) = \int \Gamma_S(x,x') B_n(x')\, dx',$$
$$\lambda_n \alpha_n(t) = \int \Gamma_T(t,t') \alpha_n(t')\, dt'$$

(or similar matrix equations for the "real", sampled data). Kernels of the equations are spatial and temporal cross-correlation functions of the analysed process:

$$\Gamma_S(x,x') = \int A(x,t)\, A^*(x',t)\, dt,$$
$$\Gamma_T(t,t') = \int A(x,t)\, A^*(x,t')\, dx.$$

Definition of KL representation determines its rather unique properties:

1. The truncated representation of form (1) with bi-orthogonality conditions has minimal r.m.s. error for the given number of terms in series.
2. For the "physical" process with finite norm $\int dx \int dt\, |A(x,t)|^2 < \infty,$ the number of terms in decomposition (1) is countable, and, moreover, effectively finite: only a number of coefficients λ_n has significant value, while all other are just noise.
3. The representation (1) describes the spatiotemporal structure of analyzed process as a whole. In particular, complexity of the spatiotemporal dynamics can be characterized by effective number of terms in decomposition (1), defined as

$$N_{eff} = \left(\sum_n \lambda_n\right)^2 / \sum_n \lambda_n^2,$$

or by Shannon entropy

$$S = -\sum_n \frac{\lambda_n}{\sum_n \lambda_n} \ln \frac{\lambda_n}{\sum_n \lambda_n}.$$

The properties 1) and 2) mean, that use of KL method enables to select from given data $A(x, t)$ only the part that contain significant dynamics, or in other words, perform "numerical filtering". The KL decomposition, in particular, was used to estimate the parameters of numerical model that are best approximation of experimental data [4].

On the other hand, optimal nature of the KL method is related to eigenproblem of integral equations. It means, that the decomposition (1) can be calculated analytically only in some very specific cases, even for precisely known functional dependence $A(x, t)$. Practically, one need to use numerical techniques, which poses requirements on effectiveness of the used algorithms, especially for large sets of experimental data.

Application example

To illustrate the use of KL formalism, it is proposed to consider the case of "optical turbulence": complex spatiotemporal oscillatory pattern originated from simulation of nonlinear optical system with delayed feedback [5] (see also results in [6]). While this example is not

concerning the combustion dynamics, it worth to mention, that such systems are described by the system of equations that is very similar to that describing flame dynamics [2].

The analyzed process (establishing of oscillations) is presented in Fig. 1, and results of KL analysis are shown in Fig. 2 and Fig. 3. Reconstruction of the process using four most significant terms leads to visually the same picture as presented in Fig. 1.

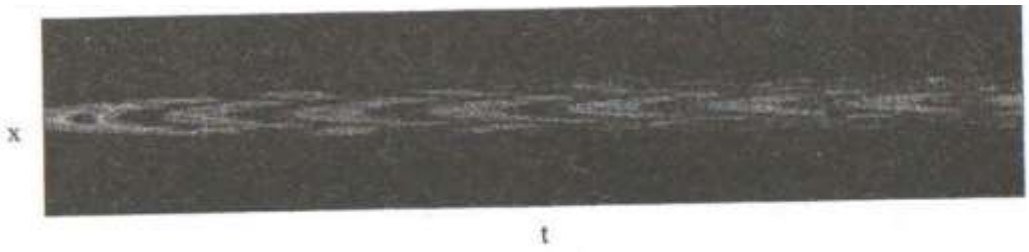

Fig. 1. Example of complex spatiotemporal process [5] ("optical turbulence")

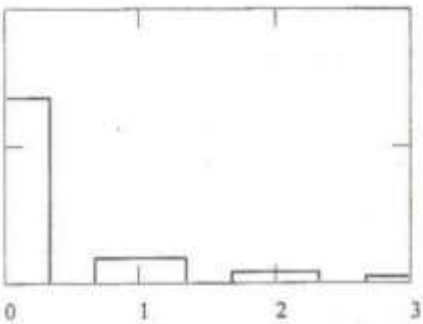

Fig. 2. Relative strengths of most significant terms in KL expansion of the process in Fig. 1

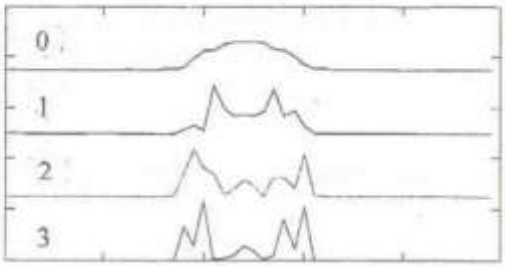

Fig. 3. Spatial profiles of first four terms in decomposition for the process in Fig. 1

References

1. Holmes P., Lumley J. L., Berkooz G. Turbulence, coherent structures, dynamical systems, *and symmetry.* Cambrige: Cambrige University Press, *1996. P. 420.*
2. Palacios A., Gunaratne G. H., Gorman M., Robbins K. A. Karhunen-Lo£ve analysis of spatiotemporal flame patterns // *Phys. Rev. E.* 1998. Vol. 57. Pp. 5858-5971.
3. Fogleman M., Lumley J., Rempfer D., Haworth D. Application of the proper orthogonal decomposition to datasets of internal combustion engine flows // *J. Turbulence.* 2004. Vol. 5, No. 23. Pp. 1-18.
4. Ravoux J. F., Gal P. L. Biorthogonal decomposition analysis and reconstruction of spatiotemporal chaos generated by coupled wakes// *Phys. Rev. E.* 1998. Vol. 58, No. 5. Pp. R5233-R5236.
5. Karelin N. V., Romanov O. G. Analysis of complex field dynamics in nonlinear Fabry-Perot interferometer by Karhunen-Lo6ve decomposition // Intern, conference of young

scientists and specialists "Optics-99". Book of abstracts, S.-Petersburg, 1999. P. 75 (in Russian).

6. Karelin M. U., Babushkin I. V., Paulau P. P. Karhunen-Loeve analysis of complex spatio-temporal dynamics of thin-films optical system // e-print arXiv.org:physics/0410069, 2004.

4. PLASMA AND COMBUSTION ASSISTED TECHNOLOGIES APPLICATIONS

NANOMATERIALS: NON-EQUILIBRIUM, BALLISTIC HEAT TRANSFER

A. CENIAN

The Szewalski Institute of Fluid-flow Machinery, Polish Academy of Sciences, 80-952 Gdansk, Fiszera 14; Poland, cenian@imp.gda.pl

Introduction

There is a growing interest in micro- and nanotechnologics, related e.g. to nanotubes, nanolayers, micro-heat-pipes or nanolasers. It is well known that heat transfer in nano-systems, especially under condition of high excitation, proceeds with strong ballistic component - which could not be described by the Fourier law [1, 2]. The possible necessary conditions for establishing the normal (Fourier) type thermal conductivity, i.e. structural and isotopic disorders, nonlinearity, system dimensionality and external on-site potentials, were extensively studied - see [3-6] and references there. It is well known that linear and integrable systems do not support normal (Fourier) heat conductivity, mainly due to zero temperature gradients in these systems. Moreover, nonlinearity and disorder are not sufficient conditions for establishing the normal heat conductivity - see e.g. [5]. Lippi et al. [5] have also shown that the thermal conductivity constant $\kappa \sim N^{2/5}$ in a ID non-linear chain (where N - number of atoms in the chain) and $\kappa \sim \ln(N)$ in a 2D non-linear lattice. It looks like that the role of on-site potentials, which impose the normal heat conductivity even in the case of ID chains [7], is related to the near neighbour interactions in a real 3D crystal. These interactions enhance the energy dissipation of soliton-like structures propagating in crystals (see e.g. ref. [1] and [8], and so, dump the ballistic part of a heat flow [9].

It has been shown [1] that after a local kinetic excitation of an atom in the 3D crystal the soliton-like energy-structure propagates in the direction of closest neighbour - see Fig. 1. This soliton-like structures are related to the Toda solitons [2, 10]. They propagate with a velocity larger than the sound velocity in the crystal and the velocity grows linearly with the square root of an atom initial excitation-energy - i.e. it satisfies the Hugoniot relation for shock waves. It was proven that the soliton-like structures preserve their shape after collision - see Fig. 2.

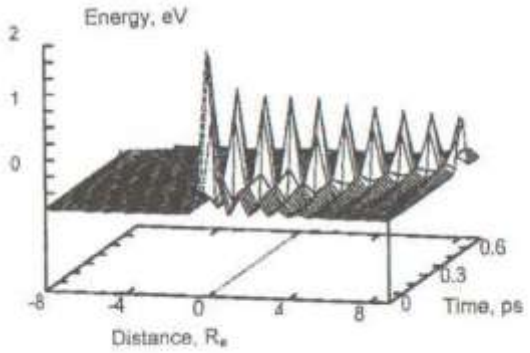

Fig. 1. A soliton-like energy structure after a local kinetic excitation (2 eV) of an single atom propagates through the crystal with the closest neighbour distance R_e

Furthermore, we have studied an energy equilibration process as a function of time and the crystal temperature. To this end, we have investigated the time evolution of the energy partition function [9]

$$P(t) = <\varepsilon_j(t)>^2 / <\varepsilon_j(t)^2>,$$

where ε_j is the kinetic energy of the j-th atom and < ... > denotes an ensemble average. P(t) is equal to 1, if the energy is equally distributed among all atoms, and takes the value 1/N, if it is localized at one atom. For a Maxweliian distribution it approaches the value 0.6.

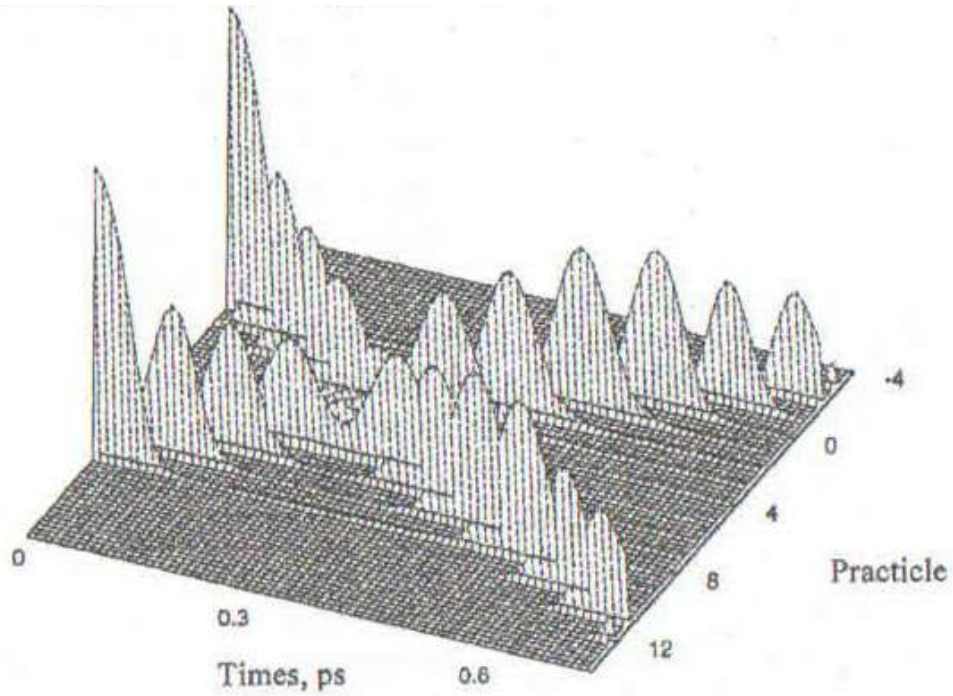

Fig. 2. Collision of solitary pulses; initial energies 2 eV

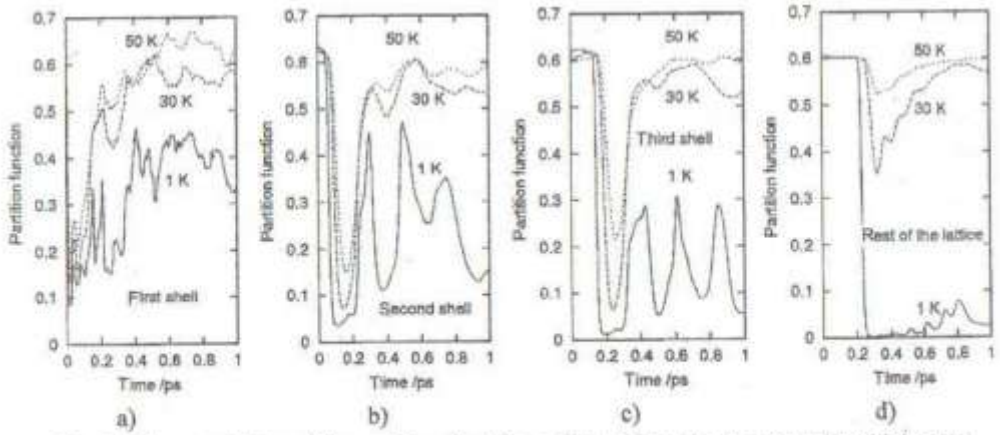

Fig. 3. Time evolution of the partition function calculated for the first 3 shells and the rest of the lattice; $E_0 = 2$ eV, excitation direction [110]

The temperature-dependent partition functions for different subsystems (shells - ordered by the distance from initial excitation) are depicted in Fig. 3, from which a few conclusions can be drawn:

- P(t) is a rather smooth function for an ensemble consisting of a large number of atoms (~ 2800 in Fig. 3d), but shows a very erratic behaviour for the first shell (12 atoms in Fig. 3a). The number of atoms increases to 42 (122) in the second (third) shell turning P(t) into gradually smoother curves - see Fig. 3.
- By decreasing the lattice temperature, the equilibrium-recovery time increases from about 0.8 ps for 50 K and the minima of P(t) drop to lower values, since the thermal energies of the atoms contribute to it as well. At lower temperatures (30 and 1 K), the ballistic contribution to heat transfer is significant even 1 ps after the excitation event (P(t) significantly less than 0.6).
- P(t) provides information on the shell-to-shell propagation of the shock pulse. For example, at a time slightly larger than 0.2 ps, the first pulse leaves the third shell - see Fig. 3c.

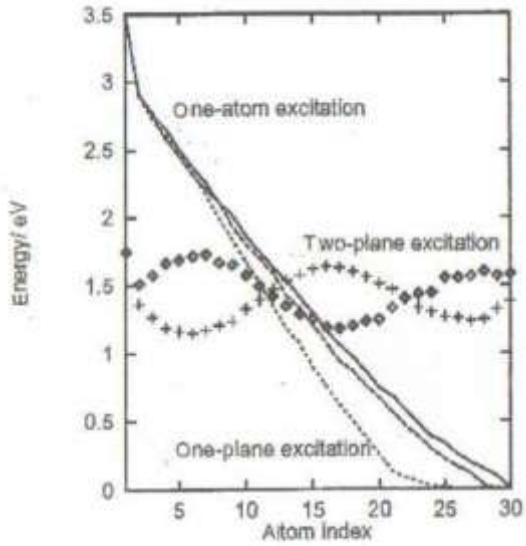

Fig. 4. A comparison of energy dissipation after the various local excitations: an one-atom, one-plane and two-plane excitation in direction [110] of fcc crystal

These soliton-like structures slowly dissipate energy through interactions with the closest neighbouring atoms lying along the direction of their propagation. The relation between a coherent excitation of various groups of atoms and their energy dissipation was studied in [2]. It was found that an excitation of few atoms lying on the same plane (perpendicular to the soliton propagation) does not change the dissipation

process significantly. Even, the coherent excitation of a whole plane of atoms docs not lead to the suppressing of energy dissipation (at least in the fee crystal) - see Fig. 4. Some kind of a co-operative motion (and a dissipation suppression) was observed when the coherent excitation of atoms lying in the two following planes of atoms (perpendicular to propagation direction) was initiated (see points in Fig. 4). However, a coherent excitation of more than two planes does not add any further to a suppression of dissipation [11].

The situation can radically change when considering non-coherent excitation, e.g. during a laser-ablation process i.e. when a short laser-pulse interacts with a matter. Here we report results of an introductory investigation of the heat transfer in nanolayers after a short laser excitation. The studies were performed using the MD algorithm presented in [2].

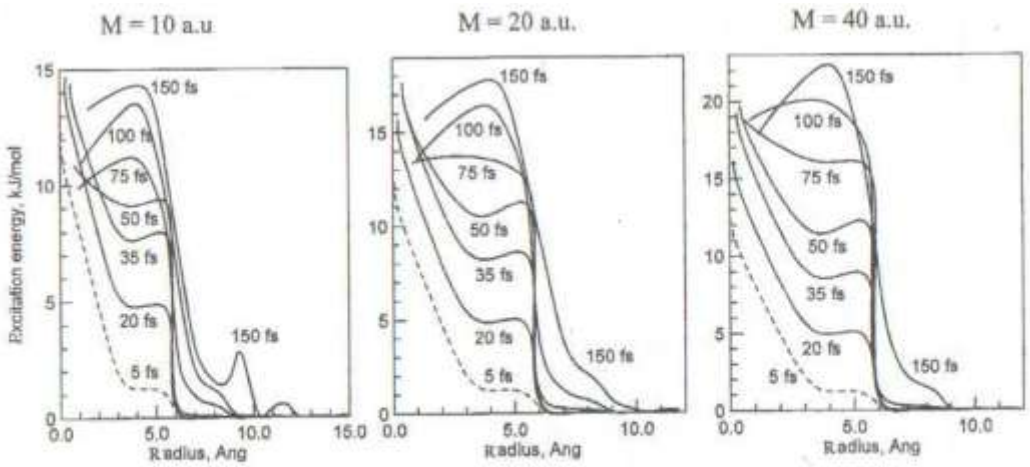

Fig. 5. Time evolution of energy profiles in ~2 nm thin layer during the first 150 fs after an excitation in the crystals with atomic masses 10, 20 and 40 a.u.

Model description

The atoms of the modelled thin films in the fee structure (2.5 nm in thickness) have atomic masses (m_i = 2.5, 10, 20 or 40). The Ar potential [12] was used to model the interactions between atoms. The matrices are kept at low temperature To = 1 K.

The heat transfer from a region excited by the 300 fs laser-pulse was studied. It is assumed that the radiation is absorbed only by the atoms of an excitation region, which comprises 14 atoms in the hemisphere of 0.52 nm in radius (the first atom absorbing radiation is chosen as lying in its centre). An averaged power density of 10.6 pm radiation was equal to 10^{13} W/m^2. The energy of radiation is absorbed by the atoms gradually, an quantum after an quantum, with the rate determined by the assumed power density. An index of absorbing-atom and the time instance of absorption are determined by a random number generator in accord with the Monte-Carlo method. The presented results are averaged over 30 different initial configurations.

Figs. 5 and 6 present the time evolution of energy profiles in ~2 nm thin layer during the first 500 fs after an excitation in die crystals with atomic masses 10, 20 and 40 a.u. The energy

transfer is far from equilibrated Fourier type, characterized by non-locality and anisotropy, i.e. some atomic layers are excited preferentially - see the small maxima at 0.95, 1.2, 1.5 and 1.7 nm. A significant growth in the maximum energy can be observed as the atomic mass increases. At the same time the energy is comprised in a thinner sheath. Fig. 6 shows a decreasing time shift for excitation of these maxima as we proceed with observation of matrices from lower to higher atomic masses.

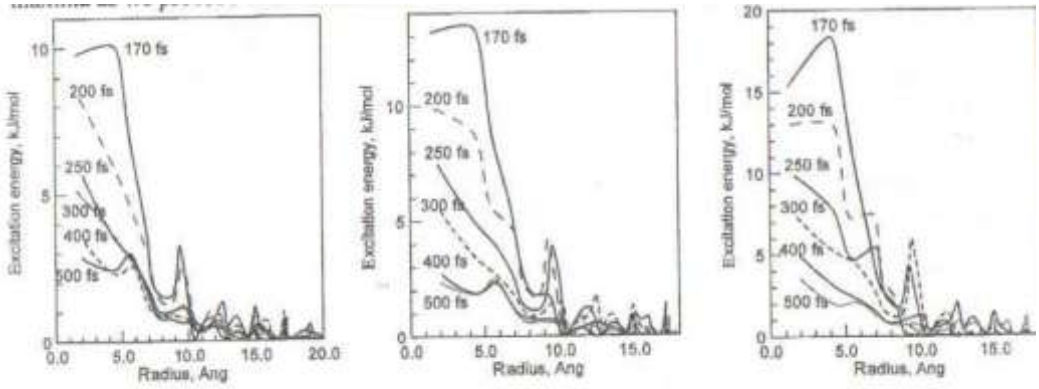

Fig. 6. Time evolution of energy profiles in ~2 nm thin layer 170 – 500 fs after an excitation in the crystals with atomic masses 10, 20 and 40 a.u.

References

1. Cenian A., Hennig S., Gabriel H. *И J. Chem. Phys.* 1995. Vol. 102. P. 9276.
2. Cenian A. and Gabriel H. *II J. Phys.: Condens. Matter.* 2001. Vol. 13. P. 4323.
3. Li B., Zhao H. and Ни B. // *Phys.Rev.Lett.* 2001. Vol. 86. P. 63.
4. Tsironis G.P., Bishop A.R., et al. // *Phys.Rev.E.* 1999. Vol. 60. P. 6610.
5. Lippi A. and Livi R. *II J. Stat. Phys.* 2000. Vol. 100. P. 1147.
6. Prosen T. and Robnik M. *II J. Phys. A.* 1992. Vol. 25. P. 3449.
7. Ни B., Li B. and Zhao H. // *Phys. Rev.* 2000 .Vol. 6Г P.3828.
8. Zhang F., Isbister D. J. and Evans D. J. // *Phys. Rev.* 2000. Vol. 61. P.3541.
9. Ohtsubo Y., Nishiguchi N. and Sakuma T. *II J. Phys..Condens. Matter.* 1994. Vol. 6. P. 3013.
10. Toda M. *II Physica Scripta.* 1979. Vol. 20. P. 424.
11. Cenian A., Third International Symposium on Non-equilibrium Processes, Plasma, Combustion and Atmoshepric Phenomena //NEPCAP'2007, Sochi, Russia, submitted to Proceedings.

12. Aziz R.A. and Slaman M.J. // *Mol. Phys.* 1986. Vol. 58. P. 679.

HYDROGEN ENERGY FOR BELARUS: STATE OF ART AND TRENDS

S.A. FILATOV, S.A. ZHDANOK

A.V. Luikov Heat and Mass Transfer Institute of NAS of Belarus, Minsk, Belarus,

fil@hmti.ac.by

Introduction

The development of new energy sources and the partial changeover of energy supply infrastructure is one of the greatest challenges of the 21st century. Unique solution for this problem - is novel hydrogen technology, based on hydrogen as energy carrier with zero carbon content. Different energy resources, such as biomass, wind and solar energy, clean fossil fuels and nuclear energy can be use for hydrogen production. Cost-effective in the long term hydrogen technology can improves national economy security due to the decoupling of demand and resources. Hydrogen can be storage for long period and than converted to power and heat with high efficiency and zero emissions by fuel cells (PEMFC, SOFC, MCFC etc.).

Transfer to hydrogen economy requires a well-coordinated international strategy which ranges from short-term measures to a fundamental investigation of alternative energy sources and an adapted energy infrastructure.

Model description

Hydrogen is a clean and storable energy vector that can be produced from a variety of primary energy sources (including fossil, renewable and nuclear). It can be converted into electrical and mechanical power and heat using both conventional combustion energy converters, or by the so called "fuel cell energy converters". Hydrogen fuelled fuel cells are intrinsically clean, very efficient, electro-chemical energy converters that can be adapted to a wide range of applications such as stationary combined heat and power generation, vehicle propulsion and portable and micro-power devices (e.g. laptops). Hydrogen and fuel cells together offer great potential to address the problems of energy supply security and mitigating the effects of climate change caused by greenhouse gas emissions from burning fossil fuels.

Today Belarus had no special policy document on hydrogen economy. First research of hydrogen technology in Belarus headed by academician A. Krasin in 1971-1977 concentrated near hydrogen production by nuclear energy and electrochemical cycles. Applied research of this period also include study of electrode materials for fuel cells. Since 2002 year all research in hydrogen technology in Belarus provided under domestic scientific program "Hydrogen", headed by academician S. Zhadanok.. Heat and Mass Transfer Institute play role of leader organization and concentrated more than half of whole research projects. Current research include

investigation in area hydrogen generation from different sources, storage and utilization of hydrogen by fuel cells (PEM FC and SOFC). Applied research also include study of new hydrogen reach fuel, gasification of biomass, microbiology production of hydrogen, development of novel hydrogen electrolysertechnology, technology of fuel cells, novel nanocatalysts for fuel cells, storage technology.

The existing power supply system in industry actuates electrical power supply, the gas supply, liquid fuel supply for engines and cars and solid fuel also. Usage of a nuclear energy provides at the conventional approaches only electrical and particularly - heat power systems, but other energy needs remain dependent from natural hydrocarbon raw material or products of its processing. Hydrogen or artificial fuel on its basis are invoked to substitute these power supplies inhydrogenous power engineering systems.

In domestic economy the main branches, consuming hydrogen, are petrochemical (for example, Grodno's "Azot" plant, where on hydrogen obtaining from natural gas during its subsequent usage at ammonia, methanol and other chemical goods synthesis - about 10 % of all natural gas, consumed by our country), food (margarine plants, where hydrogen used for hydrolysis), mechanical engineering (treatment of machines parts with the purpose of surface hardening in hydrogen atmosphere) and many other. One of the most perspective directions of hydrogen usage is its application in fuel grade of in chemical current sources for needs of a small and mean power engineering as soon as possible

Among perspective problems of a power engineering the relevant place is taken with problems of direct conversion of chemical energy of the natural and synthesized fuels in electrical energy. The urgency of this problem is obvious, because now 90 % of all useful power receives at a burning of natural fuel, and the mean conversion coefficient in traditional units does not exceed 25 %, while the efficiency of direct conversion of chemical energy in electrical in modern chemical current sources in 2-3 times is more. The special variety of chemical current sources are the fuel cells, in which one should continuously use fuel and oxidant and to be retracted reaction products and warmly [1, 2].

Obtaining cheap hydrogen and hydrogenous fuel can be supplied by using of high-performance hydrogen conversion systems for hydrocarbon fuel based on non-equilibrium plasma and superadiabatic filtration combustion in porous mediums, hyperthermal thermolysis of water in specialized new generation of nuclear reactors, in high-performance electrolytic baths with proton-exchange membranes, or by usage of renewable energy, biogas etc. The technologies of fuel cells are the most critical component of a hydrogenous power engineering with direct conversion of chemical energy in electrical - in fuel cells, including proton-exchange membranes (PEM FC) and in fuel cells with direct conversion of a methanol (DMFC), high

temperature solid oxide fuel cells(SOFC), alkaline fuel cells (AFC) and molten carbonate fuel cells (MCFC). The intensity of global scientific researches in PEM fuel cells area allows to forecast a fast decrease of the cost of propulsive plants on their basis and increase of efficiency and power of the single installations (up to 65 ... 85 % and 50-100 dollars per kW at power up to 100-300 kW with predictable resource till 40000 hours). In SOFC the expensive catalysts will not be used and power ofstand aloneinstallations look up to 1 MW with electrical efficiency up to 60 % and 80-90 % at a heat recovery with resource activity above 20 thousand hour. The hydrogenous technologies for a power engineering include independent power units up to 1 MW with systems of hydrogenous accumulation of the electric power, hybrid propulsive plants can use internal-combustion engines, microturbines and fuel cells, installations with steam-electric cycle with hydrogenous steam generators, also as systems on the basis of restored power resources with production of hydrogen by an electrolysis of water and total power consumption up to several megawatts. The development of non-polluting transport depend from operating hydrogenous fuel envisions creation for hybrid and hydrogenous cars and methanol cars, infrastructure of filling stations. The storage of hydrogen is supposed in cryogenic and metalhydride systems, in high- pressure bottles from composite materials, in systems of bound storage of hydrogen on the basis of carbon nanomaterials. In many respects the development of a hydrogenous power engineering is determined by formation of the international and national ecological programs for environmental protection and tendency of carrying on countries for the power safety in conditions of hydrocarbon fuels expense.

Now researches in the field of a hydrogenous power engineering in Belarus run in framework of the State Program "Hydrogen". Aim of this program is the organization of wide area fundamental and applied research in the field of a hydrogen power engineering oriented on maintenance of a leading position of our country in this area; association of efforts and available resources for obtaining new scientific outcomes and creation of the scientific fundamentals of operational use of hydrogen; designing both production of the prototypes and prototypes of propulsive plants appropriate to a world level. Current research include:

- Physical, chemical and biological methods of obtaining of hydrogen;
- Hydrogen transport and storage of hydrogen;
- Development and production of fuel cells;
- Technology solution for hydrogen production hydrogen from renewable and traditional source;
- Synthesis of high purity hydrogen;
- Development of new composite materials and alloys for hydrogen technology;
- Design of new fuels and hybrid engine;

- Creation of certification infrastructure for hydrogen power and research.

Results and discussion

The transition to a hydrogen economy will not happen simultaneously. For this reason, technology specific policy support is needed as well as general long-term stimulating policies focussing on sustainability. Today we can say that we need establish Belarus domestic Roadmap to hydrogen economy.

Belarus hydrogen roadmap will identify critical factors for the industry and market and also provide strategic planning tools for academia, education and governments. We needidentify gaps between the current capabilities and future requirements in hydrogen market.

For research organizations and educational institutions, this Roadmap will provide guidance for structuring future programs. For governments, this Roadmap provides a strategic direction for industrial development activities.

Bio-based hydrogen. Hydrogen fuel cell technology will be dominate in nearest future Bio-based products such as bio ethanol will open new areas for research. State of art hydrogen fuel cells reduce environment by carbon dioxide. However the state of art methods of producing hydrogen from hydrocarbons, though economical, creates pollutants at the manufacturing site. Research need be devoted to ethanol since it is environmentally friendly and based on renewable resources. Conversion of biomass materials such as ethanol into hydrogen is a more cost-efficient method to power fuel cells.

One of key point of future technology - using ofinter-metallic compounds in fuel cell electrodes for oxidize ethanol. These materials are not alloys but have ordered structures wherein atoms are very specifically arranged.

Electrolysis of water using hydroelectric or nuclear, wind, or solar power also produces hydrogen. However, in the present economic condition, these methods may not prove to be cost effective. Current production processes, such as partial combustion of natural gas or electrolysis of water require cheap fossil fuels or electrical power.

We need find new process for use of enzyme systems present in photosynthetic bacteria, cyanobacteria, and green algae such as Chlamydomonas reinhardt - we need to detect microorganisms that are immune to oxygen and that would prove to be good alternatives to produce hydrogen commercially.

Nanocatalyst for hydrogen. Today in hydrogen research we use platinum catalyst as the most efficient electrocatalyst for accelerating chemical reactions in fuel cells. However, in reactions during the stop-and-go driving of a fuel-cell-powered electric car, the platinum dissolves. In novel accelerated tests, as much as 45 percent of the catalyst can be lost during one

week. State of art solution - is combination of platinum nanocatalystand gold clusters to a new electrocatalyst. State of art research of Brookhaven researchers show that if weplace gold on carbon-supported platinum nanoparticles by displacing a single layer of copper and subject it to several sweeps of voltage (the copper is needed to reduce the charged gold particles to neutral atoms; it then conveniently forms a monolayer of platinum by an adsorption process, the binding of molecules or particles to a surface). As predicted, during laboratory testing, the platinum electrocatalyst remains stable for many decades.

Another application of nanocatalysts - are synthesis of hydrogen peroxide (H2O2) from hydrogen and oxygen. H_2O_2 is a clean, environmentally friendly oxidant that can substitute for environmentally harmful chlorinated oxidants in many manufacturing operations. However, the current H_2O_2 manufacturing process is complex, high cost, and energy-intensive. This process uses several toxic and hazardous chemicals, which cause environmental pollution when disposed. We need development a nanocatalyst technology that enables the synthesis of H_2O_2 from hydrogen and oxygen. This breakthrough technology eliminates all the hazardous chemicals of the existing process, along with its undesirable byproducts. It can produces H_2O_2 more efficiently, cutting both energy use and costs, and generates no toxic-waste.

Today the catalysts on which more than 20 percent of world industrial production is based including the expensive platinum employed to scrub clean the exhausts of millions of vehicles and the molecules pharmaceutical giants use to manufacture drugs - soon could be replaced in large part by more effective nanotechnology upgrades. Reducing catalytic substances to nanometers in size greatly increases the surface area available per gram, which in turn boosts the level of catalytic activity.

The global market for nanocatalysts is projected to approach $5.0 billion dollars in 2009, at an average annual growth rate (AAGR) of 6.3 %; Commercially well-established nanocatalysts such as industrial enzymes, zeolites and transition metal nanocatalysts accounted for about 98 % of global sales in 2008; Newer types, such as transition metal oxide, metallocene, asymmetric, carbon nanotube and others, are expected to more than triple their combined market share by 2009, to 6.8 %.

For example, contrary to the current understanding of Pt-Ru electrocatalyzed oxidation of methanol, the bimetallic alloy is not the most desired form of the catalyst. In the nanoscale Pt-Ru blacks used to electrooxidize methanol in direct methanol fuel cells, Pt-Ru has orders of magnitude less activity for methanol oxidation than does a mixed-phase electrocatalyst containing Pt metal and hydrous ruthenium oxides (RuO_xH_y). Bulk, rather than near-surface, quantities of electron-proton conducting RuO_xH_y are required to achieve high activity for methanol oxidation.

Hydrogen storage. One of necessary part of futurehydrogen economy is safe, efficient and viable storage of hydrogen. More efficient is solid-state hydrogen storage. Key element for future solution is new materials design for solid-state hydrogen storage. One of possible solution is lithium Bbrohydride, or $LiBR_4$, and it contains 18 % hydrogen by weight. Presently, it's created under enormous pressure, but is showing extreme promise as a new- candidate for permanent hydrogen storage through future chemical refinement and a lower pressure system. Unfortunately, the extensive work in the area of conventional metal and intermetallic hydrides did not result in materials suitable for on-board hydrogen storage. Carbon nanotube technology represents a new direction for solid-state hydrogen storage, especially if these materials can be altered to store large amounts of hydrogen at room temperature. State of art research is focused on modifying carbon nanotube systems in an attempt to enhance and tune the hydrogen storage capabilities of the nanotubes. The objective of this research has been to introduce transition metals and hydrogen bonding clusters into the nanotubes. The success of making doped carbon nanotubes with transition metals and alloys can allow for a weak covalent bond similar to cases of dihydrogen bond that is not restricted to pure physisorption or chemisorption bond. Controlling the type and size of tubes and dopant is expected to tune the product for hydrogen sorption to occur at desired temperature and pressure.

Nonequilibrum for hydrogen. Nonequlibrum and plasma technology is effective way for future hydrogen processes. Steam reforming of methane, propane, hexane, cyclohexane, methanol, and ethanol using a nonequilibrium pulsed discharge can be realized under atmospheric pressure and low temperature (393 K) without the use of catalyst. In each case, steam reforming proceeded efficiently and selectively and hydrogen was formed as a main product. As compared with the conventional catalytic steam reforming process, this method has some advantages such as fast start-up, quick response, and miniaturization and simplification of a hydrogen production system.

Another possible application of plasma technology - treatment of wastes containing hydrogen sulfide to recover not only sulfur, but also hydrogen in closed-loop process in which hydrogen sulfide (H2S) is dissociated in a high-temperature thermoelectric reactor with high energy efficiency.

Hydrogen production from methanol by plasma treatment is an interesting and promising option for the energy supply of fuel cells and other applications. Compared to the developed hydrogen storage technologies, the use of methanol as an effective storage of hydrogen is much safer and cheaper. The developed hydrogen production technologies from methanol include steam reforming, partial oxidation, oxidative steam reforming and decomposition. The decomposition of methanol provides a better alternative for the hydrogen production.

State of art research include investigation ofplasma reformer for the chemical reforming of gaseous mixtures of water and hydrocarbon fuels for producing hydrogen. This type ofreformer contains a reaction chamber with outer lateral walls containing emitter electrodes and inner lateral walls containing collector electrodes. The emitter electrodes and collector electrodes form an electric circuit. There are a multiplicity of thin needle-like extrusions on the emitter electrode from which a profusion of high energy electrons are emitted. These high-energy electrons dissociate the hydrocarbon fuel through absorption and ionization emitting low energy electrons in the process. These low energy electrons cause dissociation of water. Thus, dissociation of hydrocarbon fuel acts to initiate dissociation of water. The molar ratio of water to hydrocarbon fuel in the input mixture for reactions, and therefor the production of hydrogen from water, increases with carbon number of the hydrocarbon fuel.

Nuclear hydrogen. Today, when we look forward for solution of climate change problem and energy security, we look forhydrogen as an energy carrier. Since the natural sources of pure hydrogen are extremely limited, it is necessary to develop technologies to economically produce large quantities of hydrogen. The presently-dominant technology to produce hydrogen is based on the reforming of fossil fuels, with the subsequent release of greenhouse gases. Hydrogen could be produced by water cracking, using heat and surplus electricity from nuclear power plants. State of art nuclear to hydrogen research include the sulphur-iodine thermo-electrochemical cycle, alternative thermo-electrochemical cycles and high-temperature electrolysis, standardization of materials and chemical property measurement and verification, materials development, including structural materials, membranes, and catalysts. High-temperature heat from an advanced nuclear system could be supplied to a hydrogen-producing thermochemical or high-temperature electrolysis plant through an intermediate heat exchanger. Such an arrangement could provide high efficiency and avoid the use of carbon fuels. Significant research and development will be required in order to complete a commercial-scale demonstration. The hydrogen production system and heat transfer components, such as intermediate heat exchangers, will require the evaluation and development of high-temperature, corrosion-resistant materials.

Solar hydrogen. Solar hydrogen for residential and industrial energy use would be technically easy to arrange. When the United States rolled out its hydrogen vision in 2002 and its strategy in 2003, the source of the hydrogen was perceived primarily to be natural gas an approach that hardly ignited the renewable community. Nuclear, wind, bio energy, and solar have positioned themselves to serve as the energy re-sources to produce the required hydrogen. Among these resources, solar possesses some special attributes that may make it the power of choice in the future. If one looks at the more than 14 TW total primary energy equivalent

required currently worldwide or the 26-30 TW predicted to be consumed at the coming half-century point, only solar of the renewable resources could actually meet this total and only nuclear from the nonrenewables. Future energy can include photo-voltaic (PV) and hydrogen. The concept of the zero-energy building can be envisioned to expand to the "energy-plus home" that produces more energy (electricity for the residence, hydrogen for night-time power). Key topics of state of art research include: identification of potential solar- hydrogen systems, definitions of key technologies for given markets/applications, identification of technological barriers and challengesand critical R&D pathways.Solution include direct photo electrochemical production of hydrogen, low temperature and high- temperature electrolysis solutions.

Alternative Motor Fuels. The European Commission has set ambitious targets for the development of cleaner and more energy efficient transportation fuels, consistent with its emissions reduction commitments under the Kyoto Protocol and its broader commitment to sustainable development. The Commission has set an EU-wide target of 20 % substitution of alternative fuels in the transportation sector by 2020 and aims to meet this objective by focusing its R&D resources on three fuels that could play key roles: natural gas, hydrogen, and biofuels.

Short- to medium-term research projects focus on actions to identify and assess technical and institutional barriers to the wider adoption of alternative transportation fuel technologies. Since urban areas present some of the most pressing transportation challenges, the program focuses on new and alternative fuel distribution and refueling infrastructure, particularly for fleet vehicles in cities.

International worldwide cooperation. Today EU sponsored renewable energy research focuses on bringing the next generation of more cost-effective renewable energy technologies to market, with emphasis on European markets. Sponsored projects are expected to yield technologies that are capable of competing in the liberalized market place with little or no government subsidy. Primarily, renewable energy research seeks to reduce the costs associated with renewably-generated energy in the form of green electricity, heating and cooling, and liquid and gaseous biofuels [1-3].

The European Commission believes that hydrogen and electricity, together with fuel ceils, have great potential as interlinked energy carriers for a more environmentally sustainable and secure energy future. The transition to sustainable energy systems demands the widespread diffusion of both renewable and hydrogen-based energy technologies for the large scale adoption of distributed energy production.

The integrated research and deployment strategy developed by the European Hydrogen and Fuel Cell Technology Platform (HFP) provides the basis for a strategic, integrated programm for transport, stationary and portable applications, aimed at providing a strong

technological foundation for building a competitive European Union fuel cell and hydrogen supply and equipment industry. The programm will comprise: fundamental and applied research and technological development; demonstration projects at an appropriate scale to validate research results and provide feedback for further research; cross-cutting and socio-economic research activities including infrastructure issues to underpin sound transition strategies and provide a rational basis for policy decisions and market framework development. The industrial applied research, demonstration and cross-cutting activities of the program could be implemented through the Joint Technology Initiative (JTI). This strategically managed, goal oriented action will be complemented and closely coordinated with more upstream collaborative research effort aimed at achieving breakthrough on critical materials, processes and emerging technologies.

This activity will address topics for research that will not be addressed by the JTI, taking into consideration the input received from the HFP strategic documents, in particular the Implementation Plan. It will cover basic oriented research on novel materials, process engineering, components and sub-systems, as well as cross-cutting issues, aimed at achieving significant performance and durability improvements and cost reductions in order to meet the relevant targets specified in the HFP Implementation Plan.

Conclusions

Hydrogen is an option that offers a high potential with respect to emission reduction, improvement of security of supply and energy conservation. The transition to hydrogen offers an economic opportunity to strengthen Europe's position in car and energy equipment manufacturing. The introduction of hydrogen in road transport contributes to a noticeable improvement of air quality in the short to medium term. This holds specifically for the most polluted areas such as city centres where the sense of urgency is greatest.

In the first place, costs of hydrogen end-use application must be substantially reduced through up-scaling of production and increasing R&D. Secondly, the required infrastructure for hydrogen must be set up simultaneously. The analysis shows that under favourable conditions the break-even point, the point when hydrogen can compete with traditional fossil fuels like petrol and diesel, can be reached between 2025 and 2035. In the early commercialisation phase, technology-specific deployment support and R&D must go hand-in- hand. A European public-private partnership between industry and the EC, such as a Joint Technology Initiative (JTI), is the most suitable framework to meet these conditions.

References

1. National hydrogen energy roadmap // National hydrogen energy roadmap workshop. Washington, DC April 2-3, 2002. United States Department of Energy, November 2002. 58 p.
2. Hydrogen posture plan: plan an integrated research, development, and demonstration plan United States department of energy february 2004. 54 p.
3. Altmann M. Towards a european hydrogen roadmap/ (www.lbst.de) hydrogen in europe - towards a consistent policy framework for sustainable energy and mobility 23-24 june 2004. College of Europe, Bruges, Belgium. 2004. 36 p.

DIFFERENTIAL METHODS FOR EXPERIMENTAL STUDY OF SODIUM BOROHYDRIDE KINETICALLY

S.I. SHABUNYA, V.V. MARTYNENKO, V.I. KALININ, V.G. MINKINA, A.A. NESTERUK

A.V. Luikov Heat and Mass Transfer Institute of NAS of Belarus, Minsk, Belarus

For the recent decade an interest in alkali metals borohydrides hydrolysis kinetics was revived. A vast majority of published works deal with sodium borohydride hydrolysis as the most promising substance for hydrogen storage. The first wave of interest in this substance arose in latest 60^{th} - early 70^{th} [1-8], and by 90^{th} activity of publishing on this topic decreased significantly. Research field of the second (present) wave deals mainly with applied problems of hydrogen storage and production, while during the first period applied purposes were not emphasized and publications were mostly general scientific. It was 60-70 years, when step- by-step kinetic hydrolysis procedures still being the last results of this kind were developed and published. Present experimental studies deal mostly with water-alkali borohydride solutions stable storage and with catalytic hydrolysis processes in these solutions. Kinetic hydrolysis procedures of the first wave works [9-16] were not checked for the new data, and we have not seen new published works on development of step-by-step kinetics. At the same time kinetic coefficients and even schemes introduced in [10, 11] have significant variances. Adjustment and testing of these procedures was performed within relatively limited range of temperatures and water-alkali sodium borohydride solutions. The range of solution parameters used in present applied tasks is significantly larger than that in 60-80*\ Hence there is a necessity to analyze sodium borohydride solutions hydrolysis kinetics using broadened parameters range.

Analysis of four most developed procedures [10-13] performed by us and submitted for publishing [17] has showed:

Only in two models an effort was made to simulate step-by-step mechanism of alkali metals borohydrides hydrolysis, the rest of the works are gross process approximation;

The models introduced are not universal, i.e. suitable only for limited range of the parameters (pH and T);

Only solutions with low borohydride concentration were considered.

Therefore to improve kinetic description of sodium borohydride water-alkali solutions hydrolysis processes a sequence of experimental tasks and theoretical calculations to be performed within the study was listed. Since the set of published data is absolutely insufficient for solution parameters selected, the main goal of the first stage is creation of experimental bench and development of data collection methods appropriate for this range of parameters. Experimental methods applied and two modifications of method used for study of solutions at small hydrolysis rates are discussed in the present work.

There are two ways to determine $NaBH_4$ conversion during hydrolysis. These are an iodometry and two modifications of hydrogenometry. The former one is based on oxidation of fixed hydrogen by iodine (hydrogen is determined by quantity of iodine reacted), and two latter ones measure produced hydrogen: according to one of them hydrogen volume is measured (typically at atmospheric pressure), according to the other pressure is measured (hydrolysis in closed vessel). Although it is often believed that iodometry determines ion BH_4, concentration, it is not likely to be correct. The main process of the method is oxidation of hydrogen by reaction:

$$BH_4^- + 4I_2 + 4H_2O \rightarrow B(OH)_4^- + 8I^- + 8H^+ .$$

If there were intermediates in initial solution, i.e. BH_3OH^-, $BH_2(OH)_2^-$, $BH(OH)_3^-$ ions, then all of them would be converted into $B(OH)_4$ in the same manner:

$$BH_3OH^- + 3I_2 + 3H_2O \rightarrow B(OH)_4^- + 6I^- + 6H^+ ,$$
$$BH_2(OH)_2^- + 2I_2 + 2H_2O \rightarrow B(OH)_4^- + 4I^- + 4H^+ ,$$
$$BH(OH)_3^- + I_2 + H_2O \rightarrow B(OH)_4^- + 2I^- + 2H^+ .$$

In this ease iodometry will determine total amount of all four ions, or in other words all the fixed hydrogen. This point is very important, because if iodometry determines all the fixed hydrogen and hydrogenometry - all the produced hydrogen, then combined application of the two methods will not give any additional information. If iodometry had measured only BH< ion concentration, then combination of the two methods would have given information on intermediates content in solution.

Since as a source of information neither iodometry, nor hydrogenometry have any advantages, one should compare these methods by laboriousness and precision in various ranges

of test parameters (concentration and temperature). Iodometry is undoubtedly more labor-consuming and requires a large amount of manual operations, while both ways of hydrogenometry are easily automatized. Iodometry is almost unacceptable in case of fast processes, i.e. its range is slow and very slow processes. Method of these experiments seems to be simple enough, but requires much time. It is necessary to prepare a number of different test solutions, place them into thermostats (according to experimental schedule) and keep them for a long time taking samples for iodometry through periods of time. These experiments may last for several months, but besides patience and care two more criteria must be complied with: constant temperature in thermostats and sealability of test mixtures to prevent water evaporation (or absorption) and absorption of atmospheric CO_2. As it can be seen from evaluation by kinetic constants [10] for solutions with high alkali content two degrees temperature difference can significantly change process rate. That is why error for continuous (during several months) tests at "room" temperature is difficult to evaluate. Even if it could be possible to arrange uninterrupted functioning of thermostats during several months, then investigation procedure, when the result is expected during such a long time, appears to be outdated, at least in the field of chemical kinetics studies.

Use of hydrogenometry during several months is connected with even greater problems as it requires either very large volumes of test solutions (when volume of hydrogen produced is measured), or solution of very difficult task of prevention of leakage off the reactor (for experiments in closed vessel). For these types of experiments all the problems connected with long-termed thermostating of solutions in these methods are also present.

To conduct investigations at reasonable dynamic mode it is necessary to develop and use accelerated methods considering modem facilities of experiment automatization and data processing. Hydrogenometry seems to be a better controlled experimental method.

The first way to accelerate method was to cancel measurements of all borohydride conversion curve $\eta(t)$. Instead of this measurements of hydrolysis rate in several solutions with different conversion values η_i, i.e. $\eta_i|_{\eta=\eta_i}$, are offered. With this set of data it is possible to plot approximation function $F(\eta)$, such that $F(\eta_i) \approx \eta_i|_{\eta=\eta_i}$ and $F(1) = 0$. Further solving ordinary differential equation:

$$\frac{d\eta}{dt} = F(\eta), \qquad (1)$$

using initial condition $\eta(0) = 0$, function $\bar{\eta}(t)$ can be computed. Applicability of such method is illustrated by Fig. 1, 2. After 45 days of continuous experiment for water solution

6,93% $NaBH_4$, 3% NaOH a "standard" curve $\eta(t)$ was obtained. Then four relatively short experiments were performed for solutions: initial one and with conversion 25, 50 and 80 %.

The results of these experiments are performed in Table 1, and function $F(\eta_1)$ plotted by the data of this table is performed in Fig. 1. After integration the function $\bar{\eta}(t)$ was obtained, and it is depicted in the Fig. 2 together with function $\eta(t)$ marked with numbers 1 and 3 respectively.

Curves $\bar{\eta}(t)$ and $\eta(t)$ differs at high values of conversion, but it is difficult to evaluate which one is more precise. Hydrogenometry precision decreases at low consumption, and for differential approach this part of the process is determined from asymptotic level - hydrolysis rate is equal to zero at conversion 100%.

Table 1

$N_{solution}$	c_{NaBH_4}, %	c_{NaOH}, %	c_{NaBO_2}, %	Conversion, %	Rate, % $NaBH_4$/hr
1	6.93	3	0	0	0.477
2	5.197	3	3.0	25	0.31
3	3.465	3	6.0	50	0.178
4	1.348	3	9.72	80	0.0684

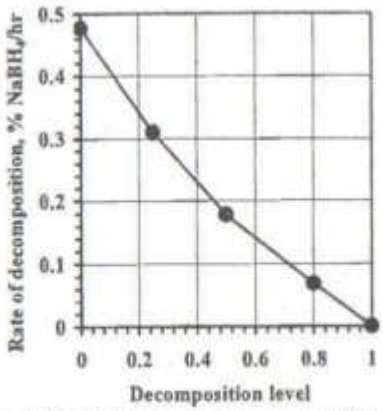

Fig. 1. Hydrolysis rate vs. conversion

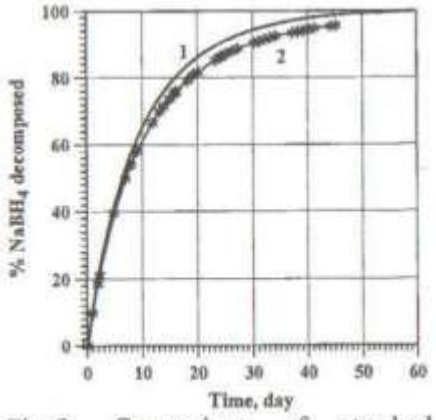

Fig. 2. Comparison of standard method and differential one

Though the example given demonstrates sufficient effectiveness of the accelerated method, some critical notes are necessary. Implicit condition of this method applicability is an assumption that at any conversion there are only two substances in solution, connected with hydrolysis: initial borohydride - $NaBH_4$, and finished product - metaborate $NaBO_2$. If significant quantities of intermediate ions BH_3OH^-, $BH_2(OH)_2^-$, $BH(OH)_3^-$ (at least one of them) are formed in chemical process, then solutions composed of $NaBH_4$ and $NaBO_2$ will not correspond to any actual composition of initial solution "natural" hydrolysis. After some time the prepared solution will reach "natural" state, but it will happen at another (greater) conversion value, than

calculated one for solution of $NaBH_4$ and $NaBO_2$. Relaxation time is hard to predict as it depends on kinetic constants ratio, that is not well-known. It is their determination that is the purpose of kinetics study.

Evaluation of relaxation time in case of prepared solution till "natural" hydrolysis state can be demonstrated for situation with two main ions suggested in [12]. In this approach hydrolysis of ions BH_3OH^- and $BH(OH)_3^-$ is much faster than that of the two remaining ones; after fast reaching of quasistationary mode of inner reactions two simple equations describe hydrolysis process:

$$\frac{d\left[BH_4^-\right]}{dt} = -k_1\left[BH_4^-\right]\left[H^+\right], \qquad (2)$$
$$\frac{d\left[BH_2(OH)_2^-\right]}{dt} = k_1\left[BH_4^-\right]\left[H^+\right] - k_3\left[BH_2(OH)_2^-\right]\left[H^+\right].$$

If produced metaborate will not significantly change solution pH, then $[H^+]$ cation concentration will be constant, and system (2) will be linear with solution:

$$\left[BH_4^-\right] = \left[BH_4^-\right]_0 \exp\left\{-K_1 t\right\},$$
$$\left[BH_2(OH)_2^-\right] = \left[BH_4^-\right]_0 K_1 \frac{\exp\left\{-K_1 t\right\} - \exp\left\{-K_3 t\right\}}{K_3 - K_1}, \qquad (3)$$
$$K_1 = k_1\left[H^+\right], \qquad K_3 = k_3\left[H^+\right]$$

that is depicted in the Fig. 3. As it can be seen, at the beginning ion $BH_2(OH)_2$ concentration increases, then it decreases in concordance with that of ion BH_4^-. It is evident that relaxation time is somewhat greater than period when ion $BH_2(OH)_2^-$ concentration reaches the maximum value τ_{max}. For the case under consideration τ_{max} is simply calculated:

$$\tau_{max} = \frac{1}{K_1 - K_3} \ln\left[\frac{K_1\left(2K_3 - K_1\right)}{K_3^2}\right].$$

In the Fig. 4 two plots of hydrolysis rate vs. conversion (i.e. function $F(\eta)$) are showed: 1 corresponds to "natural" process, while 2 relates to solution 75 % $NaBH_4$ and 25 % $NaBO_2$. Vertical dashed line shows time interval 2 τ_{max} from the start of hydrolysis. For calculations constants K_1 and K_1 from [12] were used.

At slow processes the value of w is also very large (about 5 days! for the example given in the Fig. 4, 5), and the gain of the suggested differential method is not very significant. Due to this fact method modification was considered where the process acceleration was achieved by heating instead of intermediate solutions preparation. Main idea of the method is performed in the Fig. 5. Conversion curve (measurement result) consists of sites of slow increase (low

temperature is a purpose of conducted experiment) and sites of fast increase obtained by thermostat heating. To plot function $F(\eta)$ derivatives measured on the slow sites are used. Relaxation time is less by this method (about $\tau_{max} \approx K_3^{-1}$), but the problem is not solved fundamentally.

That is why at present time method for "global" tuning of kinetic coefficients is considered. All the previous methods considered measurement of kinetic curves for a set of fixed temperatures. This traditional parameters search is not suitable for solutions with a wide variety of inhibiting component (alkali). Since elemental hydrolysis chemical processes procedure is determined to some extent, we can test processes with controlled temperature change instead of isothermal experiments. To set optimal kinetic constants of the model data at constant temperature are not necessary. Required criterion is not constant temperature vs. time, but hydrogen rate measurement supplied with solution parameters: temperature, and molar alkali, borohydride and water content per liter of solution. It is evident that these parameters must be uniform throughout the solution.

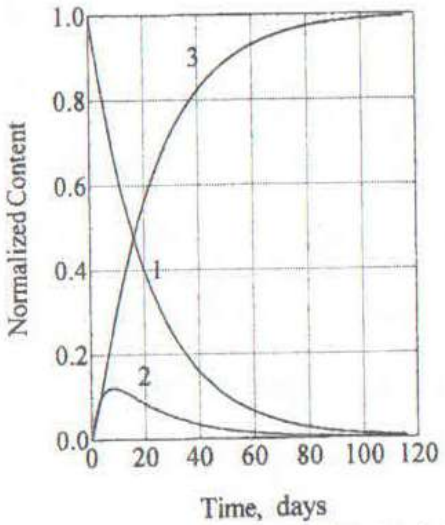

Fig. 3. Normalized parameters of hydrolysis: $1 - BH_4^-$, $2 - BH_2(OH)_2^-$, $3 - H_2$

In other words temperature variation in thermostat and reactor must be gradual, so that their difference would be small, say, wouldn't be greater than 1 degree. Another important issue of method for "global" tuning of kinetic coefficients is a choice of variation method of concentrations and temperatures. Response ranges of model parameters must be studied and compared to ranges of acceptable precision at experimental measurements. Appropriate experimental schedule can substantially reduce a number of experiments with the same informativity.

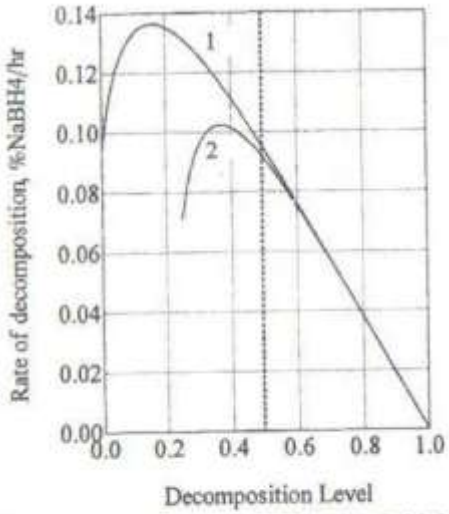

Fig. 4. Hydrolysis rates for the initial solution and «solution with 25 % conversion»

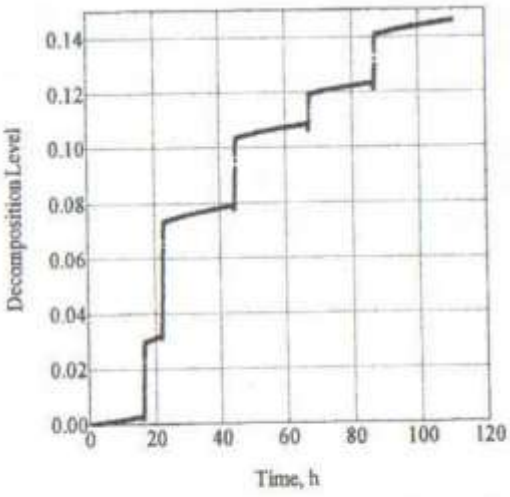

Fig. 5. Periodical acceleration of hydrolysis by heating of the solution

References

1. Jensen E.H. A study on sodium borohydride. Copenhagen. 1954. 219 p.
2. Lyttle D.A., Jensen E.H., Struck W.A. A simple volumetric assay for sodium borohydride *// Anal. Chem.* 1952. Vol. 24. Pp. 1843-1844.
3. Knechtel J.R., Fraser J.L. Preparation of a Stable Borohydride Solution for Use in Atomic-absorption Studies *// Analyst.* 1978. Vol. 103. Pp. 104-105.
4. Davis R.E., Bromels E., Kibby C.L. Boron hydrides. III. Hydrolysis of sodium borohydride in aqueous solution *// J. Amer. Chem. Soc.* 1962. Vol. 84. Pp. 885-892.
5. Davis R.E. Boron Hydrides. IV. Concerning the Geometry of the Activated Complex in the Hydrolysis of Borohydride Ion by Trimethylammonium Ion // *J. Amer. Chem. Soc.* 1962. Vol. 84. Pp. 892-894.
6. Pecsok R.L. Polarographic studies on the oxidation and hydrolysis of sodium borohydride *// J. Amer. Chem. Soc.* 1953. Vol. 75. Pp. 2862-2864.
7. Davis R.E., Kibby C.L., Swein C.C. An inverse hydrogen isotope effect in the hydrolysis of sodium borohydride *// J. Amer. Chem. Soc.* 1960. Vol. 82. Pp. 5950-5951.
8. Davis R.E., Swein C.C. General acid catalysis of the hydrolysis of sodium borohydride // *J. Amer. Chem. Soc.* 1960. Vol. 82. Pp. 5949-5950.
9. Kreevoy M.M., Hutchins J.E.C. H2BH3 as an intermediate in tetrahydridoborate hydrolysis *// J. Amer. Chem. Soc.* 1972. Vol. 94, No. 18. Pp. 6371 -6376.

10. Kreevoy M.M., Jacobson R.W. The rate of decomposition of NaBI-L» in basic aqueous solutions // *Ventron Alembic.* 1979. Vol. 15. Pp. 2-3.
11. Mesmer R.E., Jolly W.L. The hydrolysis of aqueous hydroborate *// Inorganic Chemistry.* 1962. Vol. 1, No. 3. Pp. 608-612.
12. Mochalov K.N., Shifrin Kh.V., Bogonostsev A.S. Sodium borohydride hydrolysis // *J. of Physical Chemistry.* 1963. No. 11. Pp. 2404-2407.
13. Khain V.S., Volkov A.A. On stability of water solutions of sodium and potassium tetraborohydrides *// J. of Applied Chemistry.* 1980. Vol. 53, No. 11. Pp. 2404-2406.
14. Mochalov K.N., Shifrin Kh.V., Bogonostsev A.S. Kinetics of hydrolysis of potassium borohydride // *Kinetics and Catalysis.* 1964. Vol. 5, No. 1. Pp. 174-177.
15. Mochalov K.N., Khain B.S., Gil'manshin G.G. Overall procedure of borohydride-ion and diborane hydrolysis // *Transactions of Academy of Science of the USSR.* 1965. Vol. 162, No. 3. Pp. 613-616.
16. Mochalov K.N., Khain V.S., Gil'manshin G.G. Kinetic study of intermediate stages of ion BELf hydrolysis *// Kinetics and Catalysis.* 1965. Vol. 6, issue 3. Pp. 541-543.
17. Shabunya S.I., Martynenko V.V. Kinetic schemes of sodium borohydride hydrolysis // *Theoretical basis of inorganic chemistry* (in press).

MICROFLUIDIC COMBUSTION DIAGNOSTICS WITH SUPER RESOLUTION CROSS CORRELATION ANALYSIS OF SPECKLE PHOTOGRAPHY DATA

N. BEILLANT[1], N. BAZYLEV[2], N. FOMIN[2], S. MARTEMIANOV[1]

'ESIP, University of Poitiers, France, beilIant@univ-poitiers.fr [2]A,V. Luikov Heat and Mass Transfer Institute of NAS of Belarus, Minsk, Belarus, fomin@hmti.ac.by

Introduction

Heat and mass transfer processes determine the efficiency of modern Fuel Cells (FCs), which convert the energy of the electrochemical combustion (EC) into the electric one. Among the FCs under development, the polymer electrolyte membrane fuel cells (PEMFCs) are demonstrating high performances and have advantages due to its zero noise and pollutions, low-temperature operation, high power density, and robustness. The transport of both the EC reactants and the products is accomplished by a forced convection mechanism, therefore the flow

structure is vitally important for heat and mass transfer processes in the PEMFCs . Quantitative diagnostics of flow parameters in microchannels of the PEMFCs is rather complicated problem because of the complex flow geometries of microfluidic combustion, absence of the optical access, and the needs of very high spatial resolution.

One major problem in upgrading the efficiency of modern fuel cells is the provision of optimal conditions for feeding components and distributing them over the surface of the polymer electrolyte membrane (PEM) under the conditions of conversion of released energy of electrochemical reactions to useful electric energy (sec Fig. 1) [1, 2]. It is transparent for protons and opaque for electrons, thus providing an electron flow in the external circuit, as shown in Fig. 1. The acronym PEM is also used for as Proton Exchange Membrane. Improvements of PEMFC performances can be reached by optimisation of catalysts and the functional parameters (cell temperature, humidification, pressure) which govern heat and water regimes in fuel cell.

Quantitative visualization of flows needed for such optimization is difficult in investigating processes under the conditions of internal microchannels with characteristic dimensions of 1 mm and less. One of the most developed methods of quantitative anemometry of flows is the so-called speckle photography (SP) or PIV method (particle image velocimetry — anemometry by analyzing images of visualizing particles) based on the statistical analysis of images of speckles or particles added to the flow [3]. The switch to digital laser technologies of direct input of high-resolution images into a personal computer (PC) and the possibility of their real-time analysis eliminated this disadvantage and considerably widened the possibilities of this technique [4, 5].

FC model with optical access

The traditional difficulties of microflow diagnostics, which also remain in using the new methods of digital laser anemometry called DPIV (Digital PIV — digital (laser) anemometry by analyzing images of visualizing particles), are organization of optical access to the channel, formation of laser illumination, and selection of visualizing particles in investigating flows in microchannels (μ-PIV). To solve these problems, a number of experimental models of fuel elements providing optical measurements on both cold and hot models have been developed. This paper presents the results of the quantitative anemometry of the flow in microchannels of the cold model of a fuel cell (see Fig. 1). The data have been obtained by the single-exposure PIV method developed by the authors which is based on autocorrelation analysis of the speckle fields generated under probing laser radiation scattering by the microspheres visualizing the flow.

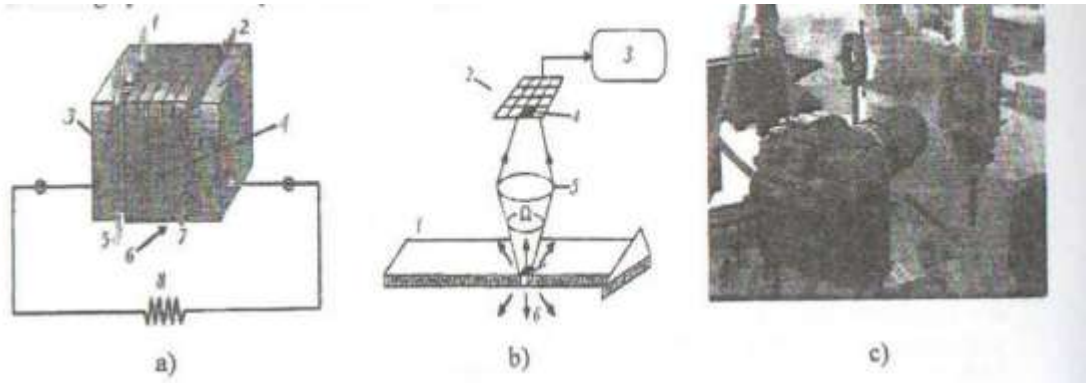

Fig. 1. a) geometry of the PEM fuel element cells in the assemblage: 1 – fuel (hydrogen) supply; 2 – oxidizer (air or oxygen) supply; 3 – anode with a platinum catalyzer causing decomposition of hydrogen into positively charged ions (protons) and electrons; 4 – PEM membrane passing only positively charged ions; 5 – water formed on the cathode as a result of the recombination of charged reaction products; 6 – cathode; 7 – outlet of unused oxidizer; 8 – useful load. b) digital speckle field recorder: 1 – "laser plane" for illumination; 2 – CCD matrix element; 3 – personal computer; 4 – working cell (pixel); 5 – focusing optics; 6 – scattering volume. c) photograph of the recorder. The camera is focused on a semi-transparent model of the fuel cell

Experiments

The laser speckle anemometry used in the present work is based on statistical analysis of displacements of images of particles visualizing the flow being investigated in a finite time interval with digital recording of these particles in a selected plane by means of a CCD camera, as shown in Fig. 1. Statistical averaging is made over a small zone of the CCD matrix containing a sufficient number of recording working cells (pixels), and in each chamber pixel the image is formed as a result of the total scattering in the volume given in Fig. lb by the particles visualizing the flow into the solid angle Ω.

It is usually impossible to organize laser illumination in microchannels exactly as shown in Fig. 1 because of the smallness of the channels and their complex configuration. In the present work, the microchannels were illuminated by collimated laser radiation just as in the case of anemometry in the near-surface blood flow in biotissue microcapillaries. In so doing, as in biotissues, the influence of the multiple scattering effects leading to a faster transition from images of visualizing particles to speckle fields increases, and averaging of the information obtained over the channel depth (z-axis) occurs.

The speckle technologies are based on the cross-correlation analyses of flow images, obtained using coherent (laser) probing of the flow pattern. Statistical information about flow studied is extracted as well, and maps of the local velocities and vorticity are quantitatively determined by using obtained digital image records. The turbulent flows arc the very complicated case for such reconstruction of local parameters, and only statistical description of the flow field is available for this case. Turbulence affects the propagation of a laser beam through the medium under investigation by way of variations in the refractive index. These variations in different heat and mass transfer processes can be caused by concentration

fluctuations in a mixing zone of components with different refractive indexes. For one-component flows the refractive index variations are caused by density fluctuations, or, in the case when the pressure variations are small (e**.g.,** in open flames), by temperature fluctuations.

Image analysis

The conventional algorithm of processing successive images with intensity distributions Ii, h in their digital recording is described below. In double exposure mode, (DEM), the sought shift of particles in each averaging window is determined by calculating the two-dimensional cross-correlation function of these images, also called specklegrams. For DEM, the data treatment is based on cross-correlation analysis, like for the well-known PIV technique. The image is interrogated with small windows called interrogation zones, and then a correlation coefficient between the corresponding windows of two subsequent frames is calculated. Taking into account experimental noise at each specklegram interrogation zone $(m,n),\ \tilde{\sigma}(m,n),$ the cross-correlation function of the two images is the product of spatial convolution of .the images:

$$R_{1,2}(m,n) = I_1(m,n) \otimes I_2(m,n) + \tilde{\sigma}(m,n). \quad (1)$$

Corresponding Fourier spectra are:

$$\mathbb{F}\{R_{1,2}\}(u,v) = \mathbb{F}\{I_1\}(u,v) \bullet \mathbb{F}\{I_2\}(u,v) + \sigma(u,v), \quad (2)$$

with $\sigma(u,v)$- corresponding noise in the Fourier spectrum. The estimate of the sought cross- correlation function is\

$$\tilde{R}_{1,2}(m,n) = \mathbb{F}^{-1}\left\{\mathbb{F}\{\tilde{I}_1\}(u,v) \bullet \mathbb{F}\{\tilde{I}_2\}(u,v)\right\}, \quad (3)$$

with $\tilde{I}_1$, $\tilde{I}_2$ – filtered images.

For single exposure mode, (SEM), the digital data treatment is based on the autocorrelation analysis of the specklegram obtained. The auto-correlation function is

$$\Im_{1,1}(m,n) = I_1(m,n) \otimes I_1(m,n) + \tilde{\sigma}(m,n) \quad (4)$$

and the Fourier spectrums are:

$$\mathbb{F}\{\Im_{1,1}\}(u,v) = \mathbb{F}\{I_1\}(u,v) \bullet \mathbb{F}\{I_1\}(u,v) + \sigma(u,v), \quad (5)$$

and the estimate of the sought function $\tilde{\Im}_{1,1}$ is :

$$\tilde{\Im}_{1,1}(m,n) = \mathbb{F}^{-1}\left\{\mathbb{F}\left\{\tilde{I}_1\right\}(u,v) \bullet \mathbb{F}\left\{\tilde{I}_1\right\}(u,v)\right\}. \quad (6)$$

Results

Fig. 2 shows fragments of the velocity field in a microchannel of the fuel element model obtained in autocorrelation processing of single-exposure specklograms. The exposure time was adapted to the velocity so that at a maximum velocity in the channel of 5 cm/s the particle or speckle image had a relative extension of about 5, which corresponds to the linear region of the calibration curve obtained. The size of the analyzed region was 20x30 mm. In the centered region of the singled-out fragment of size 2jc2 mm, about 50 velocity vectors with a data density over 10 vectors per 1 mm^2 were obtained. In the flow field on the matrix used at such a data density up to 50,000 velocity vectors can be obtained, which makes it possible to determine with a high accuracy the spatial moments of flow, beginning with vorticity to high-order moments. Figure 4 shows the vorticity field in the singled-out fragment of the flow calculated by the given data. Analysis shows that vorticity is generated mainly in wall-adjacent flows. Despite the fact that in general the vorticity integral throughout the field is small, the intensity of positive vortices in the singled-out fragment is much higher. The evolution of this quantity in the flow is a convenient parameter characterizing the flow structure and permitting detailed comparison with the results of the numerical simulation of the operating conditions in the PEM fuel element. Thus, despite the noise organically inherent in them speckle fields are a convenient carrier of useful information extracted from a noisy signal by the methods of statistical processing of two-dimensional arrays. The main sources of speckle noise in the given measuring circuit can be considered to be speckle fields generated by the stationary channel walls and the noises of the CCD structures. These noises soften the initial contrast of the speckle fields and lower the accuracy of anemometry. Additional errors can be introduced by the multiple scattering effects in the presence of a three-dimensional structure of velocity in the microchannel and a high degree of loading of the flow with visualizing particles. One way of controlling the statistics of speckle fields under their filtering is the analysis of the probability density of intensity distribution in the speckle field being filtered proposed in [4, 5]. Taking into account that the probability density in a perfect speckle field is described by a negative exponential dependence on the intensity, in filtering the speckle field its pedestal was subtracted so that the relation held.

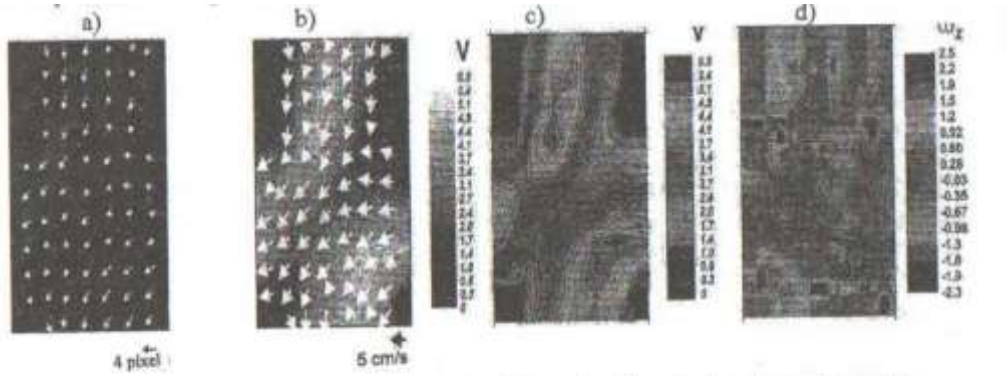

Fig. 2. Specklogram and fragments of the microflow in the fuel cell model reconstructed as a result of digitization of the single-exposure specklogram (a); velocity isolines in the singled-out fragment in a black-and-white representation (b) and in quasi-color (c); field of vorticity z-components (d) calculated in a 20x30 mm flow fragment by the data presented in (c). V, cm/s

Conclusions

It has been shown that quantitative diagnostics of microflows with the use of digital dynamic speckle photography is possible. The proposed software makes it possible to recover up to 250,000 velocity vectors in a two-dimensional flow region of size 20x30 mm in photography with an optical magnification M = 1. The experiments were performed on a cold model of a fuel cell. Future tests on a hot model will permit real-time optimization of the flow. Investigation of regions of smaller (by a factor of 10-100) sizes is possible with optical magnification by means of adequate microoptics. In the configuration presented, the spatial resolution in the measuring plane is about 100 pm. On the coordinate along the optical beam averaging over the flow depth occurs -— in the given case it is 1 mm. The use of tomographic techniques for reconstructing such complex flows proposed in [6] with the aim of obtaining three-dimensional fields is the task of future studies.

Acknowledgements

The authors wish to thank Drs. S. A. Filatov and E.I. Lavisnkaya helping to perform experiments and develop programs for mathematical treatment of images, Professors J.-B. Saulnier (CNRS, France), W. Merzkirch (Essen Univ., Germany) and C.A. Greated (The Univ. of Edinburgh, UK) for valuable discussion, recommendation, and leadership in a number of international projects, as well as the INTAS, Belarus National Academy of Science, Belorussian Foundation for Basic Research and CNRS, France, for partial financial support of the work with grants and projects INTAS No 05-1000007-425, T07-070, T07Ф- 005, T07M-112, and "Vodorod-19".

References

1. Kadjo J.-J., Brault P., Caillard A. et al. Improvement of proton exchange membrane fuel cell electrical performance by optimization of operating parameters and electrodes preparation *// J. of Power Sources.* 2007. Vol. 172. Pp. 613-622.
2. Grigoriev S.A., Lyutikova E.K., Martemianov S., Fatcev V.N. On the possibility of replacement of Pt by Pd in a hydrogen electrode of PEM fuel cells // *Int. J. of Hydrogen Energy.* 2007. Vol. 32. Pp. 4438-4442.
3. Fomin N. Speckle Photography for Fluid Mechanics Measurements, Springer Verlag, Berlin, 1998.
4. Campbell M., Cosgrove J., Fomin N. et al. Quantitative measurements of acoustical field by digital particle image velocimetry and speckle photography // Intern. Workshop "Nonequiiibrium processes in combustion and plasma based technologies". Minsk, HMTI, 2004. Pp. 173-4176.
5. Azharonok V.V., Filatova I.I., Bazylev N.B. et al. Low current pulse discharge tissue treatment and monitoring by digital laser speckle technology // Intern. Workshop "Nonequiiibrium processes in combustion and plasma based technologies". Minsk, HMTI, 2006. Pp. 63-67.
6. Lavinskaya E.I., Martem'yanov S., Saulnier J.-B., Fpmin N.A. Limited-projection laser tomography of complex gas-dynamic flows // *J. of Engineering Physics and Thermophysics.* 2004. Vol. *11,* No. 4. Pp. 94-104.

MODELING OF ACETYLENE CYLINDER CHARGING/DISCHARGING PROCESS

A.P. CHERNUKHO[1], A.N. MIGOUN[1], E. BAUNE[2], G. CANNET[2]

[1]A.V. Luikov Heat and Mass Transfer Institute of NAS of Belarus, Minsk, Belarus,

chern@itmo.by

[2]Air Liquide - C.T.A.S., France

Acetylene is a simplest member of unsaturated hydrocarbons called alkynes or acetylenes. The hydrocarbon class of alkynes includes those with carbon-carbon triple bonds. Such molecules are very unstable, thus few naturally occurring alkynes exist outside the laboratory. The smallest of the alkynes, acetylene, is primarily used as a raw material in the production of chemicals such as acetaldehyde, acetic acid, acrylonitrile, perchloroethylene, vinyl chloride and trichloroethylene [1]. Also used for oxyacetylene welding, cutting and heat-treating.

Small amounts used for lighting purposes in buoys and beacons, and as a fuel in atomic absorption instruments.

Acetylene can explode with extreme violence if the pressure of the gas exceeds about 200 kPa as a gas or when in liquid or solid form, so it is shipped and stored dissolved in acetone in a cylinder packed with a porous mass material. Thus, main attention was previously paid to safety of acetylene shipping and storage. However, recently attention is attended to increase performance characteristics of acetylene cylinders.

Fig. 1 shows the typical structure of the acetylene cylinder. It is seen that almost whole volume of the cylinder is filled by a porous media. Previously packed beds were usually used, and now main producers use monolith fillers that are baked inside the cylinder in a hydrothermal process. Fig. 2 presents the typical microstructure of the currently used fillers. It has rather high porosity (ε ~ 85-92 %) and small characteristic size of pores (mean pore diameter d_{por} ~ 0.3-0.7 pm). Pore diameter distribution function usually has a bimodal character (see Fig. 3). Characteristic value of the permeability of the empty filler may significantly vary not only for different manufacturers, but also for different series from the same producer. This is connected with peculiarities of the hydrothermal synthesis and baking procedure and therefore filler composition or microstructure variations, as a rule it is in the range $3*10^{-15}<K<8*10^{-14}$ m^2. Under filling of the cylinder with acetone and later with acetylene the system porosity falls down to ε ~ 20-25%. This leads to a certain decrease of the system permeability, however, not as high as the Kozeny-Carman law based on $(K \sim \varepsilon^3/(1-\varepsilon)^2)$. Indeed, calculation shows that the permeability can drop by three orders of magnitude in this case. In actuality the mentioned drop is not so dramatic because of capillary forces that make the acetone-acetylene solution to reside in the smallest pores under filling of the filler; i.e. the left wing of the pore diameter distribution function (PDDF) is filled (see Fig. 3). At that the largest pores remain empty and serve as transport channels for filtration of acetylene through the porous medium.

In [2] we have presented the 2D nonsteady model of acetylene cylinder. It includes three second order differential equations that describe laws of the energy conservation, gas filtration and kinetics of acetylene condensation and dissolving, as well as the set of algebraic equations, which define the state of a real gas, the solubility of acetylene in acetone, the dependence of the solution volume on the temperature and concentration of acetylene and other. Results presented in this article are obtained by making use of the mentioned model and the software that were developed on its base.

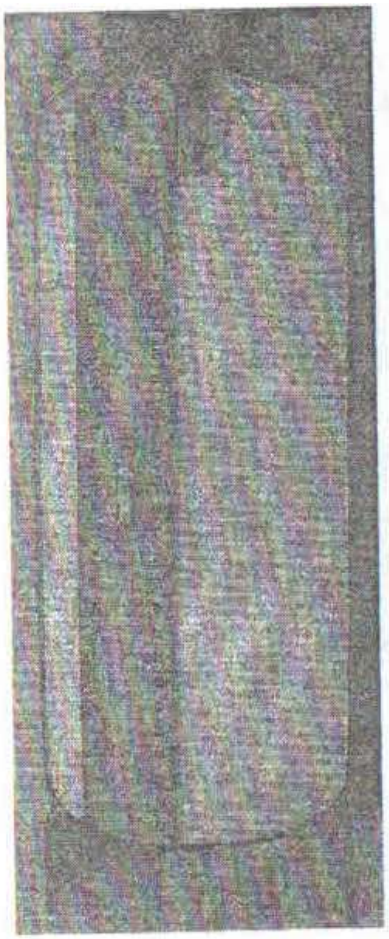

Fig. 1. Structure of 3.35 l acetylene cylinder

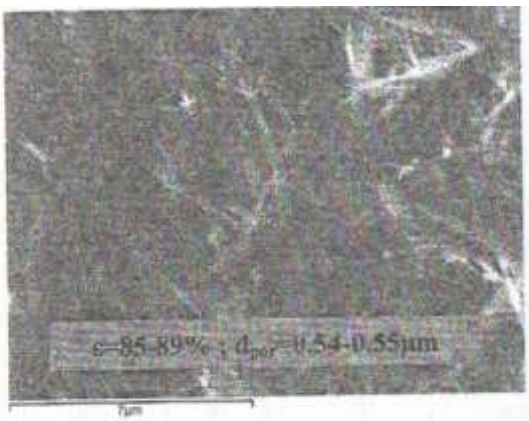

Fig. 2. Typical microscope view of the filler microstructure

Table 1. Configuration and performance characteristics of the model 7.7 l acetylene cylinder used in calculations (see Fig. 4)

	Configuration	t_{restit}, min	RD,%
a	$K= 1 \cdot 10^{-14}$ m^2, axial filtration	53.8	47.5
b	$K= 5 \cdot 10^{-14}$ m^2, axial filtration	78.5	68.2
c	$K= 1 \cdot 10^{-14}$ m^2, radial filtration	88.6	77.0

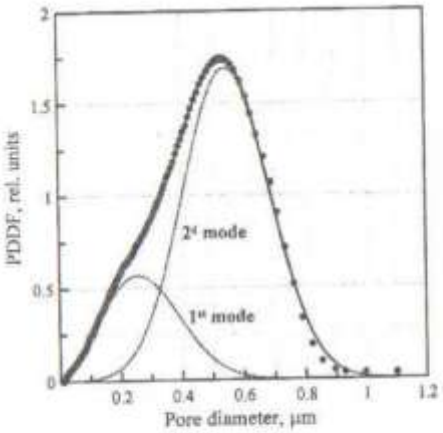

Fig. 3. Pore diameter distribution function of the filler: points – experiment (measured by mercury porosimeter), solid line – approximation by bimodal normal distribution function

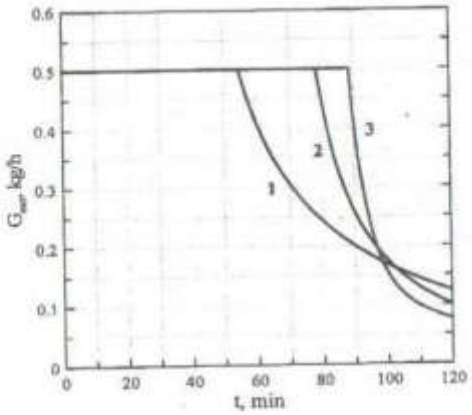

Fig. 4. Dynamics of discharging of the standard 7.7 l acetylene cylinder under the constant extraction flow rate G_{ext}=0.5 kg/h: 1, 2 – axial filtration, 3 – radial filtration; 1, 3 – K= $1 \cdot 10^{-14}$ m^2, 2 – K= $5 \cdot 10^{-14}$ m^2

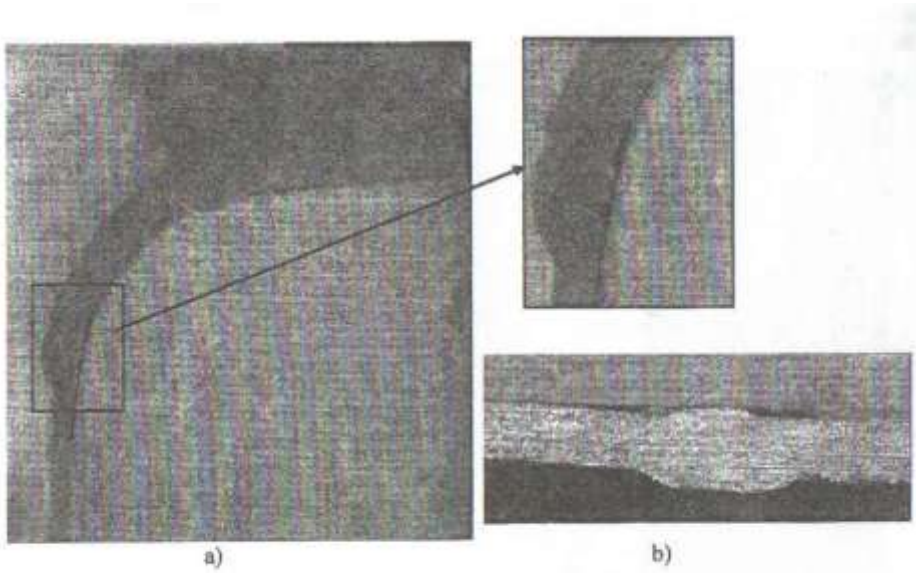

Fig. 5. Through (a) and local (b) parietal side clearance (cylinder cut view)

Discharging of a cylinder usually occurs under constant rate, which does not depend in the cylinder's size and amounts to 400 Nl/h (~0.5 kg/h). Fig. 4 shows the dynamics of acetylene discharging for different cylinders' configurations. It is seen that the acetylene flow rate stars to vanish after a certain time. This is mainly caused by two reasons. The first is connected with the overall drop of acetylene pressure under its discharging, which hamper the filtration though a porous medium. The second is related with the fact that the acetylene gasification process is endothermic (~600 kJ/kg) and leads to significant decrease of the system temperature, which may amount to several tens of degrees. That, in turn, results in the reduction of the acetylene vapor saturation pressure (that is the pressure in the cylinder) and, in the final analysis, also hampers the gas filtration. When the pressure becomes too low to maintain the required acetylene flow rate the discharge rate begins to fall. In real conditions the discharge process is

brought to a stop at this particular mentioned moment, which is called the restitution time. The percentage of released acetylene freed during restitution time is called the restitution degree (RD). RD is therefore an individual property of a cylinder, which may vary from 20 to 80 % and depends on the heat transfer regime and peculiarities of the cylinder configuration: permeability K of the porous medium, construction of the cylinder throat part (see Fig. 1) and the presence of a parietal side clearance (see Fig. 5). The latter can be formed under the shrinkage of the filler at the baking procedure and has a strong influence on the performance ability only in the case when it is not local but through. In this case the character and characteristic length of the filtration can change - it transforms from axial to radial one (see Fig. 6), which facilitates the filtration and can lead to dramatic advance of performance characteristics. Indeed, the presence of parietal side clearance results in a stronger effect than the increase of the permeability of the filler in 5 times (see Fig. 4 and Table 1). Moreover even a small value of the side clearance can have a significant effect. Fig. 7 presents the calculated data on the time of the free evacuation of the one-half of nitrogen charged at 10 atm into an acetylene cylinder. It is seen that even several tenths of millimeter are enough to change the character of filtration from axial to radial one and to improve filtrational characteristics. Note that this test (N_2 extraction on full cylinder) is the prompt and convenient way of classification of either new or used cylinders by their filtrational ability, which is an indirect indicator of their performance ability. Fig. 8 present numerical data on the correlation of N_2 extraction and performance characteristics for 7.7 I acetylene cylinder. The data were calculated for three different permeabilities of filler and various depths of parietal side clearance (the extent of the side clearance from cylinder's throat towards the bottom).

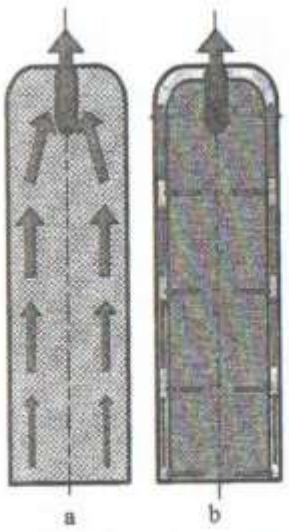

Fig. 6. Direction of gas filtration under discharging of acetylene cylinder without (a – axial filtration case) and with (b – radial filtration case) parietal side clearance

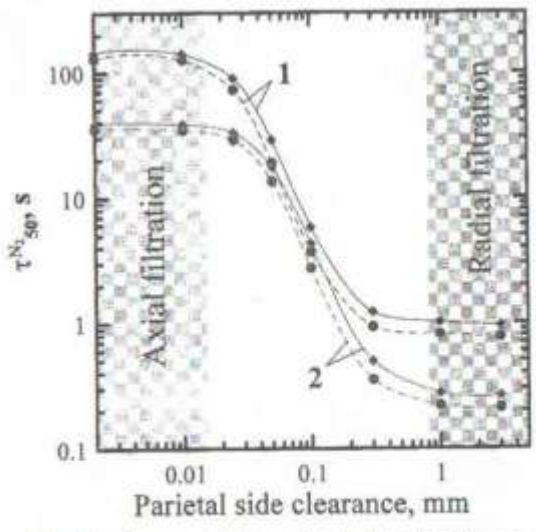

Fig. 7. Influence of the parietal side clearance on characteristic N_2 extraction time for cylinders 5.8 l (solid lines) and 3.35 l (dashed lines) with different filler permeability: 1 – K=0.8·10^{-14} m^2; 2 – 10^{-14}

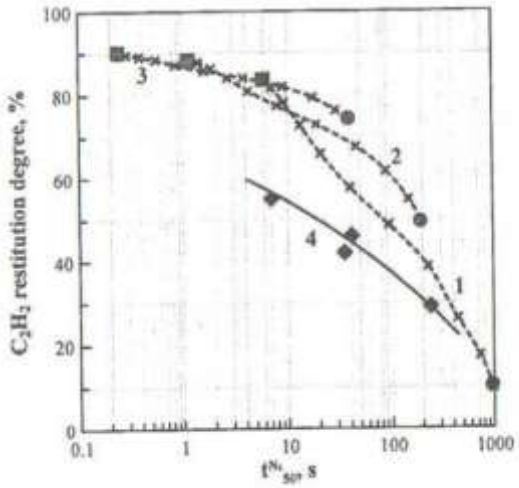

Fig. 8. Correlation between the characteristic N_2 extraction time and performance characteristics of acetylene cylinder: rhombuses and solid curve 4 – experimental data for V=5.9 l; dashed lines – theoretical data for model cylinder of V=7.7 l with different filler permeability K and different side clearance surface: 1 – $K=2\cdot10^{-15}$ m^2, 2 – $1\cdot10^{-14}$, 3 – $5\cdot10^{-14}$; circles correspond to axial filtration case (zero side clearance surface), squares – to radial filtration case (maximal side clearance surface)

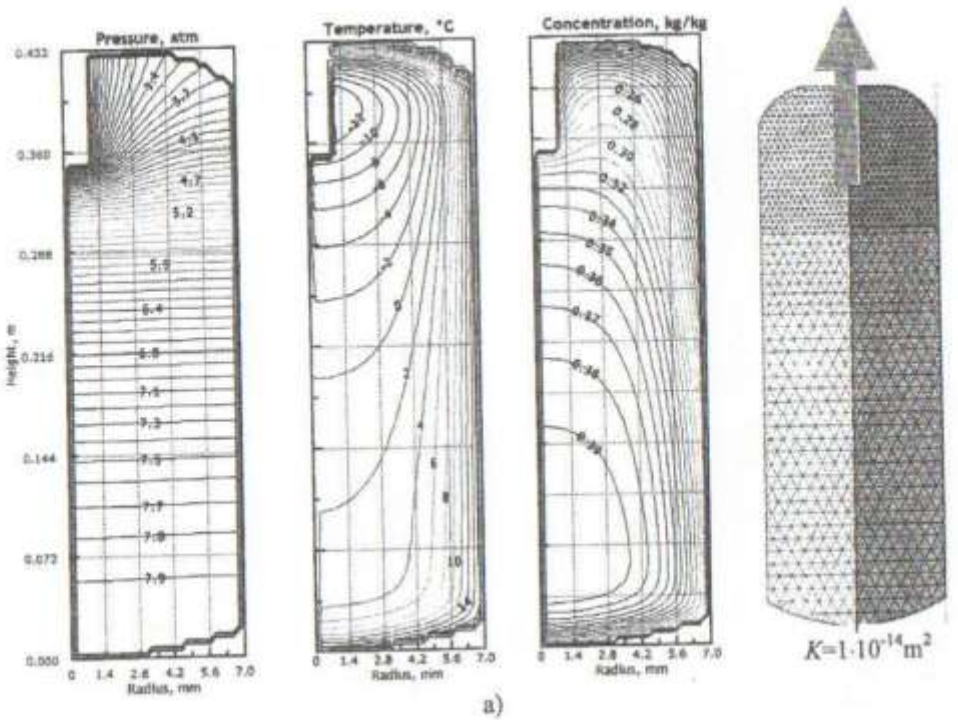
Pressure, atm
Temperature, °C
Concentration, kg/kg
Height, m
Radius, mm
K=1·10^{-14}m^2

a)

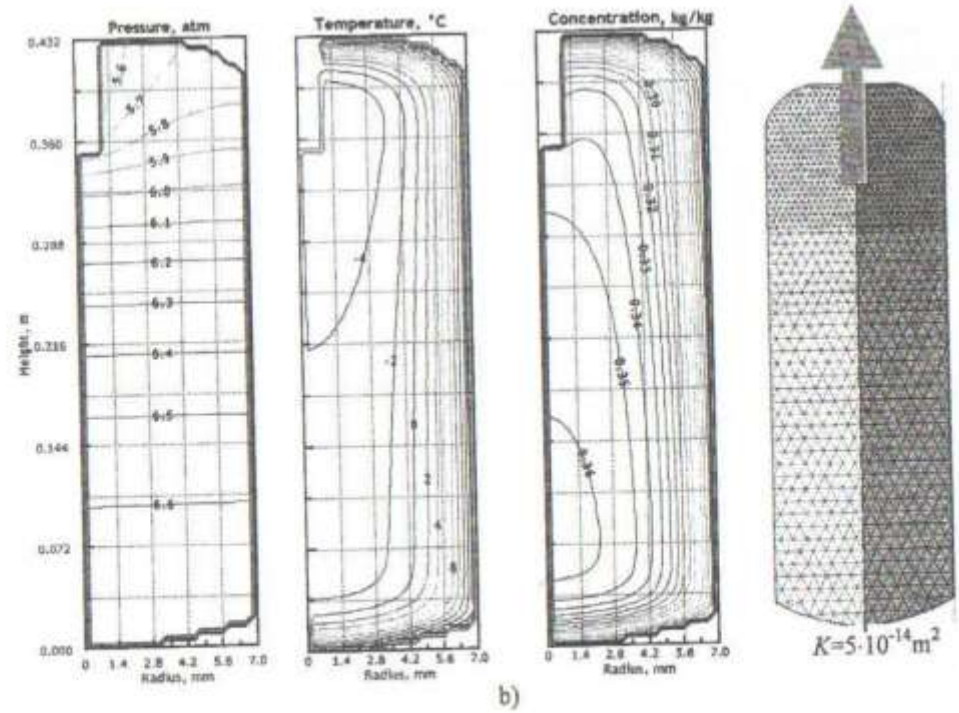
Pressure, atm
Temperature, °C
Concentration, kg/kg
Height, m
Radius, mm
K=5·10^{-14}m^2

b)

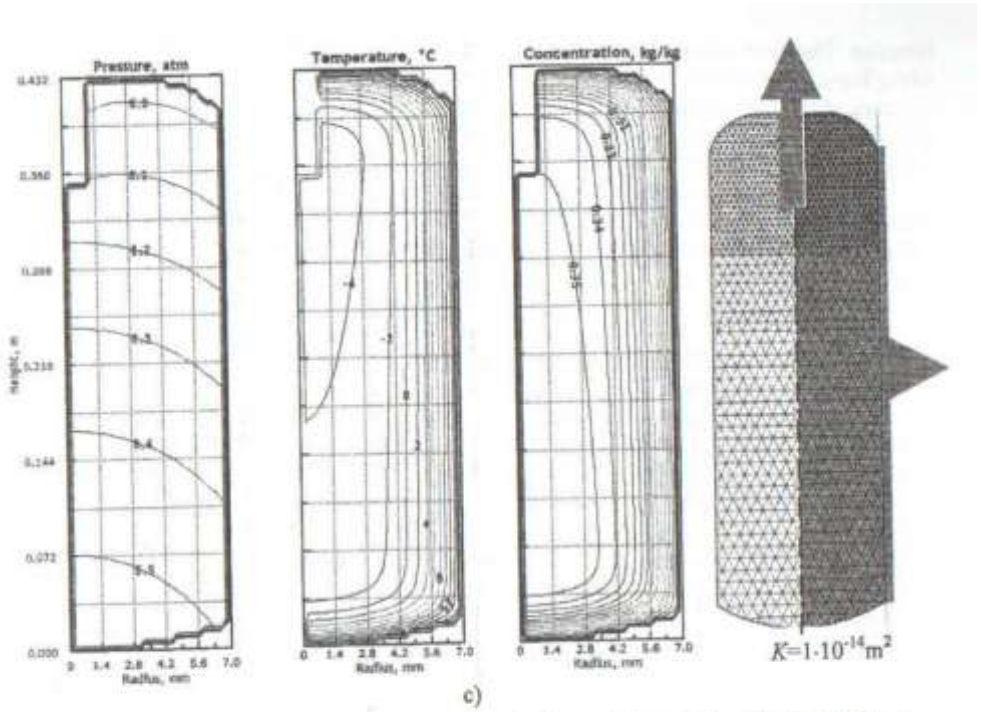

Fig. 9. Distribution of main parameters within the model acetylene 7.7 l cylinder at t = 53.8 min: G_{ext} = 0.5 kg/h; a, c – K = 1·10^{-14}m^2; b – K = 5·10^{-14}m^2; c – configuration with developed parietal side clearance

It is seen that there is rather clear correlation between the shown characteristics, although there is certain dispersion: decrease of characteristic N2 extraction time leads, as a rule, to the increase of acetylene restitution degree. The same figure depicts experimental data for slightly smaller cylinders. It is clear that the theoretical curves lie somewhat higher than the experimental ones. That is caused by the fact that the calculations were performed for cylinders of ideal regular shape (cylinder) and constant temperature of cylinders' surface (forced heat exchange). Nevertheless, the shape of the curves is absolutely identical.

Fig. 9 shows the spatial distribution of main parameters over the cylinder's volume: pressure, temperature and concentration of acetylene in acetone. The data is shown for three configurations presented in Fig. 4 and Table 1 at the end of restitution time for 1" basic regime (tram - 53.8 min). The beginning of the flow rate fall corresponds for that moment for the first regime. It is seen that at that moment the pressure at the cylinder's exit drops to the atmospheric one. The filtration runs strictly along the axis (see Fig. 9 a) and only in the throat part turns following the cylinder's curvature. The same is in the second calculation performed for the increased permeability of the filler. In the presence of a parietal side clearance the filtration turns in a radial direction. One can see that the value of heat conductivity of the system of porous medium partially filled with a solution ($Я$ ~ 0.2 W/(m K)) is not enough to compensate by the heat exchange with environment the heat effect of acetylene gasification, which leads to a large spatial inhomogeneity of temperature field. In all three cases the maximum freezing occurs in a throat part of a cylinder. The field of concentrations is defined mainly by the thermal picture of

the discharge process and only in part by the direction of gas filtration. The most efficient discharging occurs in hot parietal regions, which is the evidence of the importance of heat transfer processes. Increase of the filtrational ability of a cylinder by increase of the permeability of a filler (Fig. 9 b) or due to the presence of a side clearance (Fig. 9 c) makes all main parameters more homogeneous that has a positive effect on the performance ability of cylinder.

Note that the presented calculations were performed for the uniform initial distribution of acetone within a cylinder. Under real conditions that is not always the case and as a rule has negative influence on cylinder's characteristics, these latter effects are however out of the scope of the present article.

References

1. Miller S.A. Acetylene: its properties, manufacture and uses, Volume I.Ernest Benn Limited, London, 1965.
2. Chernukho A.P., Migoun A.N., Baune E., Cannet G. 2D multiphase model of acetylene cylinder charging/discharging process // 2nd Intern. Workshop "Nonequilibrium Processes in Combustion and Plasma Based Technologies", Minsk, Belarus, 2006, Contributed Papers Pp. 102-106.

SYNTHESIS AND CHARACTERIZATION OF CARBON NANOMATERIALN

S.A. FILATOV, G.S. KUCHINSKY, M.N. DOLGIKH, E.V. BYKOVA, O.S. FILATOV A, A.A. GUNKEVICH

A.V. Luikov Heat and Mass Transfer Institute of NAS of Belarus, Minsk, Belarus,

fil@hmti.ac.by

Introduction

Today carbon nanoparticles and carbon nanotubes are one of more interesting novel materials. Carbon nanotubes have unique physical properties that could impact broad areas of science and technology.

Mechanical measurements have recently demonstrated that carbon nanotubes have the largest Young's modulus of any known materials. Direct measurements of the full stress- strain behavior of individual nanotubes have also shown that nanotubes undergo a striking elastic buckling deformation, and are exceedingly tough materials. It is, however, the remarkable electronic properties of carbon nanotubes that have elicited the greatest interest. For single wall carbon nanotubes (SWNT's), which consist of a single graphene sheet rolled into a seamless tube, theoretical calculations predict that both metallic and semiconducting nanotubes are possible depending only on the diameter and the helicity of the nanotubc. The ability to display

fundamentally distinct electronic properties without changing the local bonding sets nanotubes apart from other nanowire materials [1, 2].

Model description

For optimization of CVD reactor 3D simulation was used. For hydrodanmics description we use Navies-Stocks equation with in next form [3]:

$$\frac{\partial \rho}{\partial t}+\frac{\partial}{\partial x_i}(\rho u_i)=0,\ i=1,2,3, \tag{1}$$

$$\frac{\partial}{\partial t}(\rho u_i)+\frac{\partial}{\partial x_j}(\rho u_i u_j)=-\frac{\partial p}{\partial x_i}+\frac{\partial}{\partial x_j}\left[\mu\left(\frac{\partial u_i}{\partial x_j}+\frac{\partial u_j}{\partial x_i}-\frac{2}{3}\delta_{ij}\frac{\partial u_l}{\partial x_l}\right)\right]+\frac{\partial}{\partial x_j}\left(-\rho\overline{u_i' u_j'}\right) \tag{2}$$

for last member of equation (2) we use Bussinek theory:

$$-\rho\overline{u_i' u_j'}=\mu_t\left(\frac{\partial u_i}{\partial x_j}+\frac{\partial u_j}{\partial x_i}\right)-\frac{2}{3}\left(\rho k+\mu_t\frac{\partial u_i}{\partial x_i}\right)\delta_{ij}. \tag{3}$$

Under use of spart-almaras and k-epsilon model v is identical to turbulent viscosity. Equation for $\tilde{\nu}$ look like:

$$\frac{\partial}{\partial t}(\rho\tilde{\nu})+\frac{\partial}{\partial x_j}(\rho\tilde{\nu}u_i)=G_\nu+\frac{1}{\sigma_{\tilde{\nu}}}\left[\frac{\partial}{\partial x_j}\left\{(\mu+\rho\tilde{\nu})\frac{\partial\tilde{\nu}}{\partial x_j}\right\}+C_{b2}\rho\left(\frac{\partial\tilde{\nu}}{\partial x_j}\right)^2\right]-Y_\nu+S_{\tilde{\nu}}, \qquad (4)$$

where G_ν - turbulent viscosity; Y_ν- influence of turbulent viscosity near wall; $\sigma_{\tilde{\nu}}$ and C_{b2}– constants; ν-molecular viscosity; S_ν - source part. Turbulent viscosityμ_1 given from:

$$\mu_t=\rho\tilde{\nu}f_{\nu1}, \qquad (5)$$

where $f_{\nu1}$:

$$f_{\nu1}=\frac{\chi^3}{\chi^3+C_{\nu1}^3}, \text{ where } \chi\equiv\frac{\tilde{\nu}}{\nu}. \qquad (6)$$

Than

$$G_\nu=C_{b1}\rho\tilde{S}\tilde{\nu} \text{ , where } \tilde{S}\equiv S+\frac{\tilde{\nu}}{k^2d^2}f_{\nu2} \text{ and } f_{\nu2}=1-\frac{\chi}{1+\chi f_{\nu1}}. \qquad (7)$$

C_{bi} and k - constant; d - distance to wall; S-deformation scalar.

$$S\equiv\sqrt{2\Omega_{ij}\Omega_{ij}}, \qquad (8)$$

where Ω_{ij} :

$$\Omega_{ij}=\frac{1}{2}\left(\frac{\partial u_i}{\partial x_j}-\frac{\partial u_j}{\partial x_i}\right). \qquad (9)$$

$$Y_\nu=C_{w1}\rho f_w\left(\frac{\tilde{\nu}}{d}\right)^2, \text{ где } f_w=g\left[\frac{1+C_{w3}^6}{g^6+C_{w3}^6}\right]^{\frac{1}{6}}, \qquad (10)$$

$$g=r+C_{w2}\left(r^6-r\right), \qquad (11)$$

$$r\equiv\frac{\tilde{\nu}}{\tilde{S}k^2d^2}., \quad C_{w1},C_{w2},C_{w3}-\text{ constant:} \qquad (12)$$

$$C_{b1}=0.1355;\ C_{b2}=0.622;\ \sigma_{\tilde{\nu}}=\frac{2}{3};\ k=0.4187;\ C_{\nu1}=7.1;$$

$$C_{w1}=\frac{C_{b1}}{k^2}+\frac{(1+C_{b2})}{\sigma_{\tilde{\nu}}};\ C_{w2}=0.3;\ C_{w3}=2.0\ .\tilde{\nu}=0. \qquad (13)$$

Turbulence heat transfer:

$$\frac{\partial}{\partial t}(\rho E)+\frac{\partial}{\partial x_i}\left[u_i(\rho E+p)\right]=\frac{\partial}{\partial x_j}\left[\left(\lambda+\frac{c_p\mu_t}{\Pr_t}\right)\frac{\partial T}{\partial x_j}+u_i(\tau_{ij})_{eff}\right]+S_h, \qquad (14)$$

where λ – heat conductivity; E –energy.

$$(\tau_{ij})_{eff}=\mu_{eff}\left(\frac{\partial u_j}{\partial x_i}+\frac{\partial u_i}{\partial x_j}\right)-\frac{2}{3}\mu_{eff}\frac{\partial u_i}{\partial x_i}\delta_{ij}. \qquad (15)$$

Numerical solution of (1)—(15) give possibility study 3D heat and concentration distribution in CVD reactor with axial symmetry, Figs. 1, 2.

We also use 2D solution from QuickField 5.0 for verification of 3D solutions [4, 5].

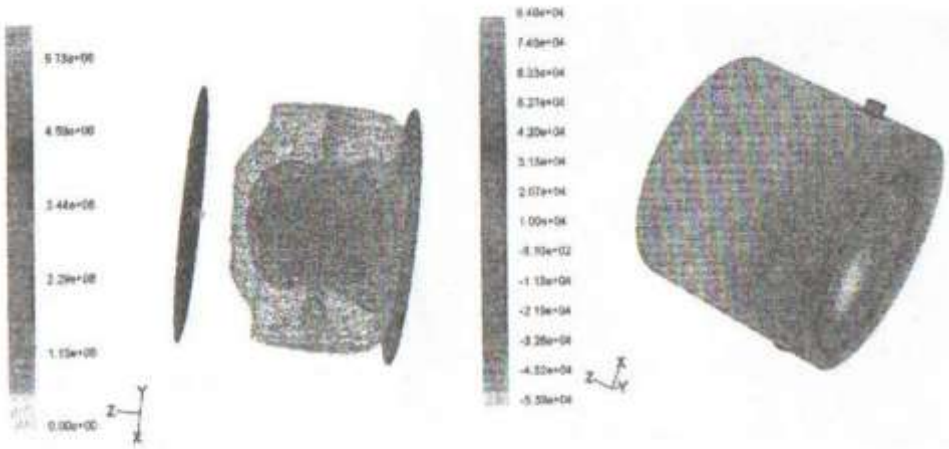

Fig. 1. Computer simulation of C-C concentration in CVD reactor during carbon nanotubes growth

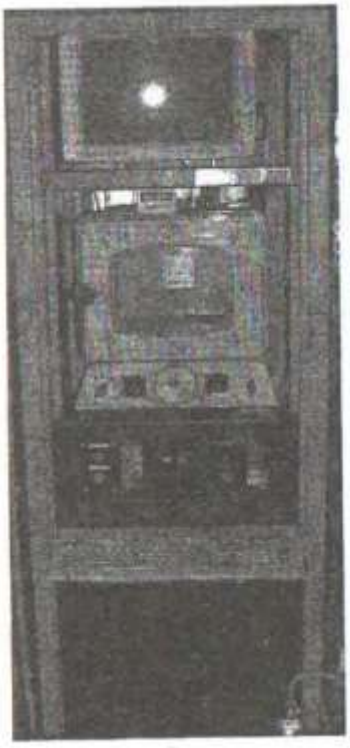

Fabrication method	CVD
Vacuum chamber	12 dm^3
Pressure	10–4…10–1 bar
Temperature	600…9000 °C
Carrier gas	Ar
Fluid	C_2H_6
Catalyst	$Fe(C_5)_2$
Substrate diameter	100 mm
Substrate thickness	1…3 mm
Time	20…120 min
Regulator	PID
Channel number	4

Fig. 2. Common view of CVD (PECVD) reactor

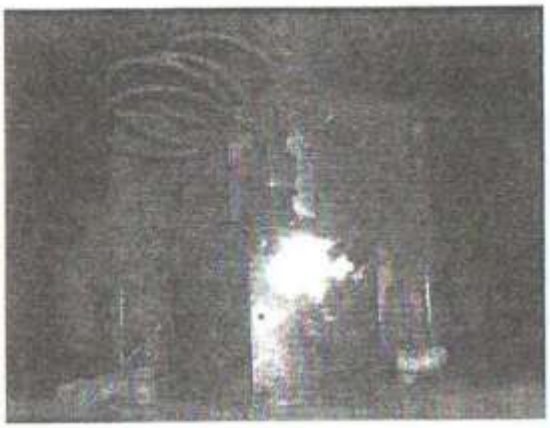

Fig. 3. CVD reactor with thermal catalyst hydrocarbons cracker

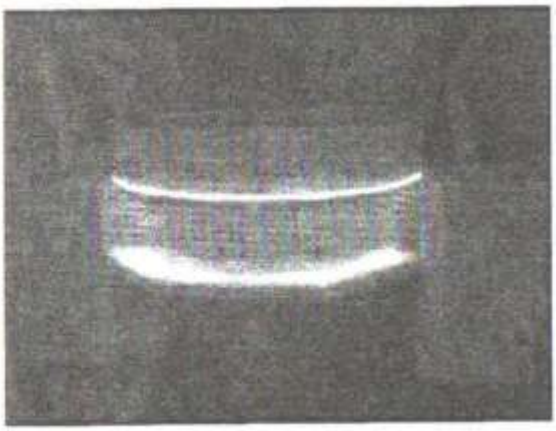

Fig. 4. Reactor modification with glow discharge for hydrocarbons cracking

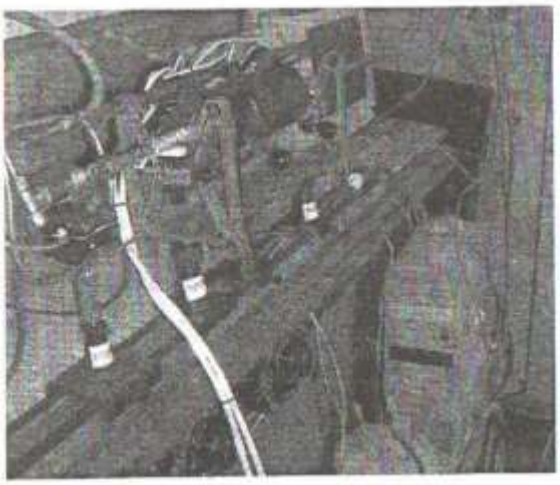

Fig. 5. Semi industrial CVD reactor with soluble carrier for carbon nanotubes growth

Results and discussion

By using of chemical vapor deposition (CVD) and plasma enhanced (PECVD) methods different forms aligned and nonaligned CNT can be fabricated and tested by flaman spectroscopy, SEM and TEM microscopy, thermal, electric and magnet methods. By CVD technology we can obtain more chemical stable CNT coating from oriented or random CNT with excellent heat contact with "hot" surface. That can improve heat dissipation in 10 or (in special cases) 70-80 times for example after CVD deposition of CNT on silicon surface. CVD technology also provides a possibility to obtain coating in complicate surface. But CVD process for CNT coating has very big potential and give excellent possibility - by using of PECVD

(plasma enhanced CVD) we can obtain DLC (diamond like coating) with unique heat conductivity of surface and than obtain CNT "radiator" for improve conductive and radiation heat transfer of surfaces as we need (Figs. 3-5).

On next pictures, Figs. 6-8 we can sec typical surfaces that we can obtain by CVD process in our equipment [4, 5].

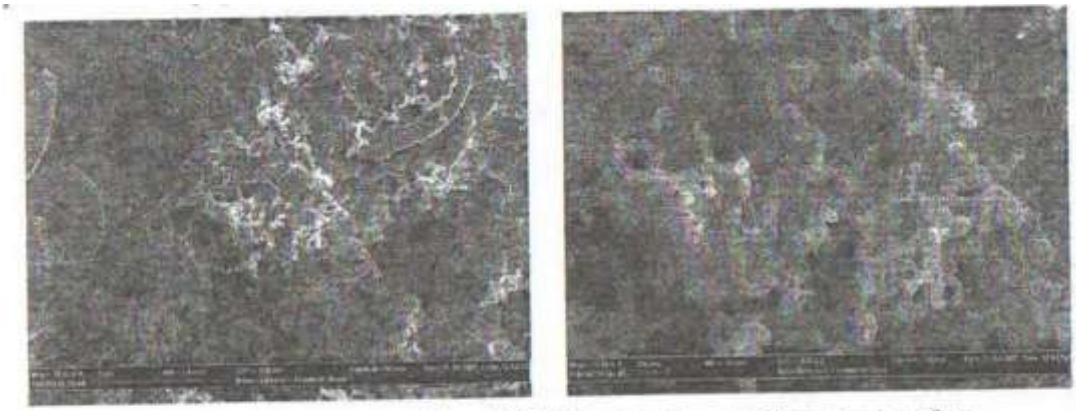

Fig. 6. Homogenous multiwall CNT (random) on stainless steel surface

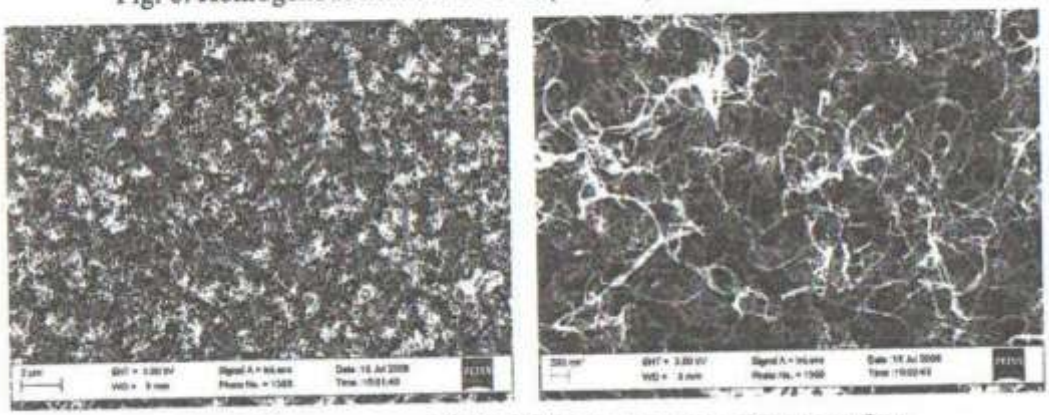

Fig. 7. Homogeneous SWNT CNT (random) on silicon surface

Different type of CVD coating (Figs. 1-3) demonstrate good thermal properties and can be extremely useful for different application. It also possible improve heat dissipation by applied electrical field to this surface (nanoscale "electrical" wind) for conductive heat fluxes or by using of evaporation of distilled water from such surfaces. Another possibility under design is internal coating of heat pipes and study of nanoscale heat transfer on superconductive CNT or research of hydrophilic properties of CNT and CNT coating. Separate question is possibility use CNT as part of thermoelectric cooler for microscale devices (we provide some experiments in this area now).

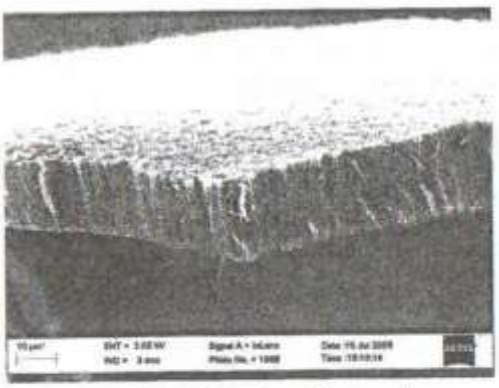

Fig. 8. SWNT CNT on silicon surface

Experimental research include CNT coating on Si and stainless steel samples preparation and their study by electron microscopy and Raman spectroscopy for testing and characterization of CNT type (SWNT, MWNT, alignment etc.) and also a design of special test unit for study of heat

flow rate from CNT enhanced surface. Key laboratory equipment include equipment for carbon nanotubes growth (CVD and PECVD - our own design), Raman spectrometer Nexus 550 Fig (Thermo Nicolet), scanning electron microscopy Supra 55 (Carl Zeiss) with microanalysis system INCA 350 (Oxford Instruments), transparent microscopy unit EMV- 100, VIS fiber optic and IR Fourier spectrometers (Ocean Optics, Thermo, etc.), systems for thermal analysis and TGA, thermograph unit IR SnapShot 310.

Conclusions

CVD technology with thermal cracking of hydrocarbon gas with precursors-is most attractive technology for carbon nanotubes growth. Different type of CNT can be obtain by CVD technology by modification of reactor and selection of growth condition. The choice of support and catalyst materials has been proved to be critical to scalable chemical vapor deposition synthesis of carbon nanotubes. The effects of reaction conditions such as temperature, flow rate of the gas and the types of catalysts and supports on the properties of CNT were investigated and characterized by Raman spectroscopy, TEM and SEM microscopy and thermogravimetry (TG) techniques.

References

1. Dresselhaus, M.S. Science of Fullerences and Carbon Nanotubes. San Diago: Academic Press, 1996.
2. Xie S., Li W., Pan Z., Chang B., Sun L. Mechanical and Physical properties of Carbon Nanotubes. *// J. of Physics Hinze J. O. Turbulence.* New York: McGraw-Hill Publishing Co., 1975.
3. Spalart P., Allmaras S. A one-equation turbulence model for aerodynamic flows. Technical Report AIAA-92-0439, American Institute of Aeronautics and Astronautics, 1992.
4. Filatov S., Kuchinski G., Dolgikh M., Baturev E. Carbon nanomaterials plasma synthesis study by Raman and IR spectroscopy // Nonequilibrium Proc. in combustion and Plasma Based Technologies. International Workshop. Minsk, 21-26 august 2004. Pp. 192-195.
5. Filatov S.A., Dolgikh M.N., Kuchinskii G.S., Akhremkova G.S., Gunkevich A.A., Kumeisha N.A. Thermal Methods for Analyzing Carbon Nanomaterials // Abstracts of papers and communications submitted to the VI Minsk International Heat and Mass Transfer Forum, May 19-33. 2008. P. 92.

NANOSCALE DIAMOND LIKE COATING OF SURFACES BY PLASMA ENHANCED CVD

S.A. FILATOV, G.S. KUCHINSKY, E.V. BATYREV, M.N. DOLGIKH

A.V. Luikov Heat and Mass Transfer Institute of NAS of Belarus, Minsk, Belarus,
fil@hmti.ac.by

Introduction

Diamond-like carbon (DLC) is one of forms of amorphous carbon materials that display some of the unique properties of natural diamond and usually applied as coatings to other materials that could benefit from some of those properties. By mixing carbon atoms arranged in a cubic lattice and in hexagonal lattice in various ways at the nanoscale level of structure, DLC coatings can be made that at the same time are amorphous, flexible, and yet purely sp^3-type bonded "diamond". The hardest and strongest and robust in such type mixture, known as tetrahedral amorphous carbon, or *ta-C,* since it consists only of sp^3 bonded carbon atoms. Diamond-like carbon (DLC) coatings have very special physical and chemical properties such as high wear resistance, very low friction coefficient and high corrosion resistance. There are several methods available to deposit DLC or other coatings at the outer surface of components; such as chemical vapor deposition (CVD), physical vapor deposition (PVD), electroplating, flame spray and sol-gel. CVD techniques are limited in this application as well, due to the need to supply heat for the chemical reaction, which damages heat sensitive substrates.

Model description

PECVD (plasma enhanced chemical vapor deposition) can be used to lower the temperature required for reaction, but then there is difficulty in maintaining a uniform plasma near sample surface in vacuum chamber. In the case of very low-pressure techniques such as PVD, where the pressure is below or near the molecular flow region, coating internal surfaces has been limited to tubing with large diameters and short lengths, due to line of sight deposition [1-6].

DLC fabrication method	Main advanced
PECVD (DC, HF, RF.ECR, pulsed DC)	Low Hardness & Thermal Stability, Non Uniform in Complicated Shape
Sputtering: ion beam	Low Adhesion, Poor Film Quality
Laser Ablation	High Adhesion & Hardness, Low Productivity
PSII	High Adhesion but Arcing, Low Hardness & Thermal Stability
Filtered Vacuum Arc	High Adhesion , High Hardness & Thermal Stability High Residual Stress

In our experiments we successfully obtain diamond-like carbon (DLC) films on silicon (100) and stainless steel substrates by plasma enhanced chemical vapor deposition (PECVD) from isobutene. We use thermal catalyst cracker technology with thermal heating of isobutene to 480-650 °C with pulse AC discharge (25-30 kV and 35 kHz). Different deposition parameters such as AC voltage, plasma source power, gas flow and pressure was studied. It was found that barrier discharge scheme also can be successfully realized for PECVD growth on different type substrates.

Results and discussion

Today, deposition of DLC films by PECVD is usually performed in RF plasma, but AC plasmas have also been used for PECVD of DLC films. Typically AC deposition of DLC has been performed in PECVD systems with an additional screen in front of the sample electrode or by using a triode configuration. In experiments also been shown that highly insulating DLC films can be deposited on electrically conductive substrates using a AC- powered diode-type parallel-plate reactor, Fig. 1. The deposition is possible at sufficiently high bias because the resistivity of the DLC films is not constant and drops several orders of magnitude at high electric fields, enabling bias transfer to their surface. DLC films several micrometers thick have been grown by AC PECVD at high rates using low power densities (0.25-1.0 W/cm^2).

Catalyst: $Fe(C_5)_2$
Sample diameter – up to 100 mm

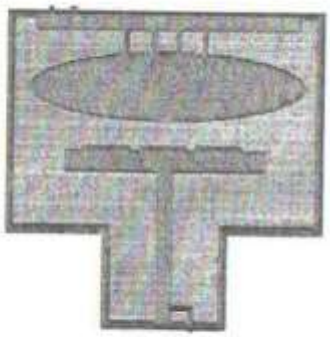

PECVD reactor parameters:
Working volume – 12 l
Working pressure – 10^{-4}–10^{-1} bar
Temperature of surface 560–900 °C
Gases: Ar, C_2H_6, N_2

Fig. 1. Experimental PECVD reactor during DLC on Si plate growth and scheme for standard diode-type parallel-plate reactor

In our experiments we use PECVD reactor with barrier discharge and additional Ar gas carrier improvement of discharge capability on different pressure.

It was possible obtain modified DLC films in our PECVD reactor by addition by precursors of the modifying elements to the main gas feed. For example N-DLC films can be prepared from isobutene : nitrogen (1:10) mixtures.

The structures of the DLC were characterized by Fourier transform infrared (FTIR) spectroscopy and Raman spectroscopy, Figs. 3-6 and also by scan electron microscopy (SEM) by Carl Zeiss Supra 55 with microanalysis system FNCA 350, Figs. 7, 8. The surface morphology of the films also was characterized by atomic force microscope (AFM).

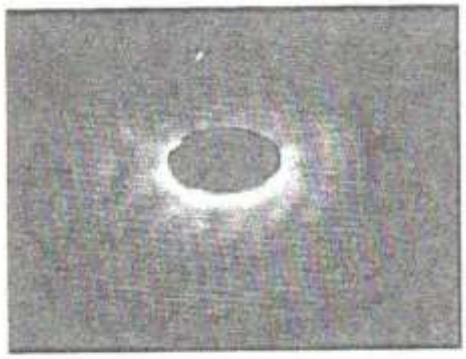

Fig. 2. PECVD barrier discharge reactor for DLC coating growth

It was found that highest plasma density and the suitable deposition environment of hydrocarbon radicals to atomic or ionic hydrogen are important for depositing hard and high quality DLC films. The high frequency glow discharge or barrier discharge PECVD deposition technique allows low process temperatures, between 50 °C and 200 °C, and compatible with a large variety of substrates in this temperature region. PECVD system can process substrates as large as 10 cm by 10 cm now, but can be exchanged to 30x30 cm in new installation. Amorphous nanosize carbon coating, give us a new class of multi-functional electronic materials, coatings, with conductivity that can be varied from dielectric to metallic, by change of doped gas. The standard PECVD produced film is an amorphous dielectric with a composition consisting of a substantially sp^3-bonded carbon network that also contains silicon oxygen [7, 8].

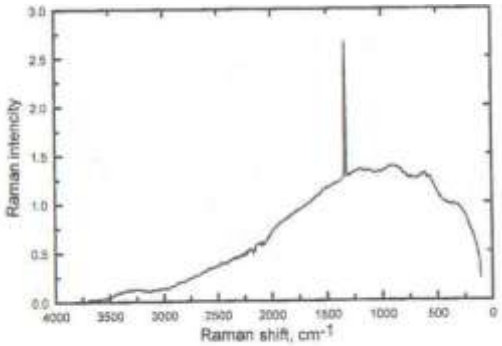

Fig. 3. Raman spectra of diamond

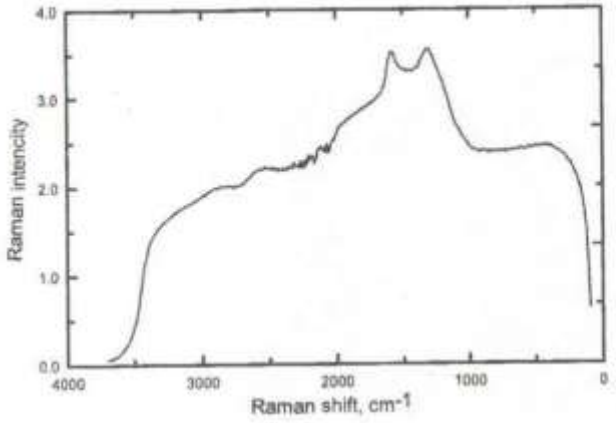

Fig. 4. Raman spectra of DLC film

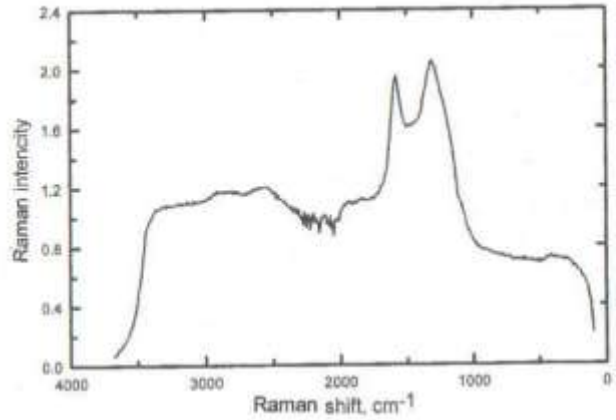

Fig. 5. Raman spectra of barrier discharge DLC system

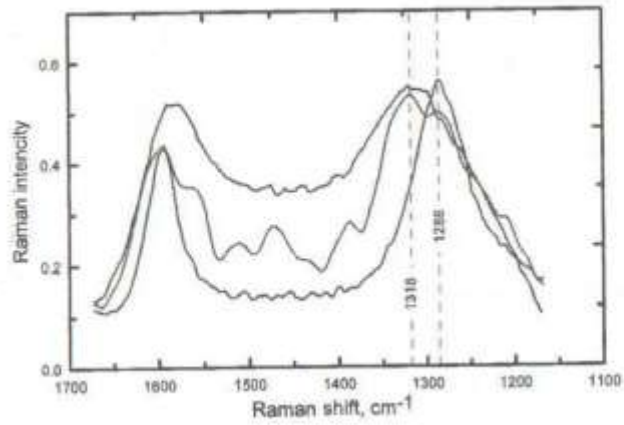

Fig. 6. Comparison of multiwall CNT (D-mode peak – 1286 cm^{-1}) and DLC films

Raman spectra shows that the films have typical DLC characteristics with a D line peak at ~1318 cm^{-1} and a G line peak at ~1544 cm^{-1}, and the low intensity ratio of I_D/I_G indicate that the DLC films have a high ratio of sp^3 to sp^2 bonding, which is also in accordance with the results of FTIR spectra.

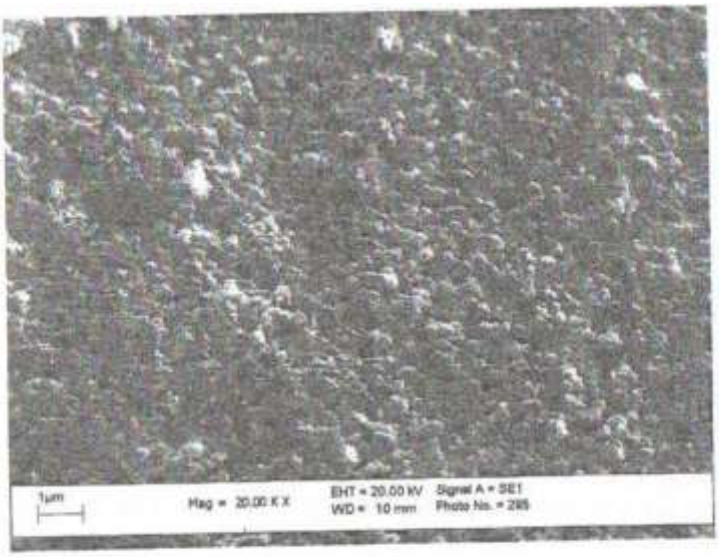

Fig. 7. DLC films (x 20.000)

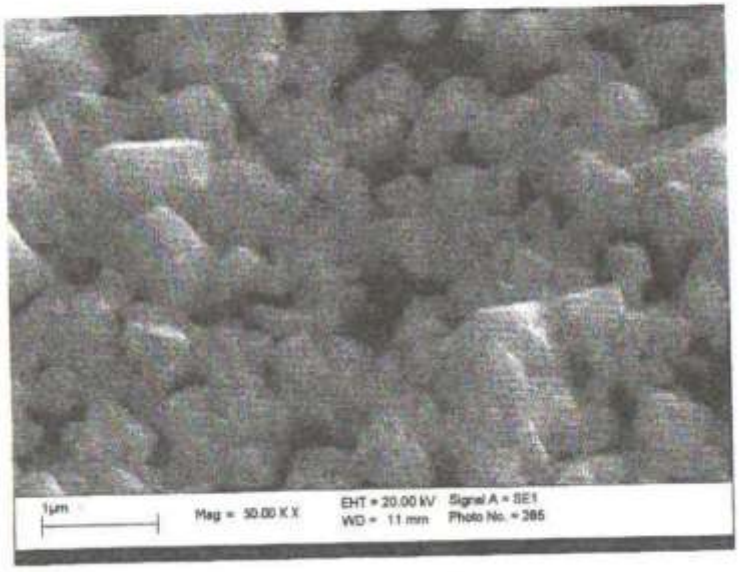

Fig. 8. DLC films (x 50.000)

Conclusions

DLC coating formed by barrier discharge PECVD demonstrate good adhesion on Si and stainless steel, good uniformity per sample square, high electrical breakdown field, possibility to doping with nitrogen, thermal conductivity variable, up to 700 W/(m-K) and also micro hardness approximately 40 GPa. This parameters can be extremely useful for technical application of DLC for microelectronics, chemical engineering and optical application.

References

1. Mcletis E.I., Erdemir A. and Fenske G.R. Tribological characteristics of DLC films and duplex plasma nitriding/DLC coating treatments // *Surface and Coatings Technology.* 1995. Vol. 73. Pp. 39-45.

2. Voevodin A.A., Donley M.S., Zabinski J.S. Pulsed Laser deposition of diamond-like carbon wear protective coatings: a review // *Surface and Coatings Technology.* 1997. Vol. 92. Pp. 42-49.
3. Erdemir A., Fenske G.R., Terry J., Wilbur P. Effect of source gas and deposition method on friction and wear performance of diamondlike carbon films // *Surface and Coatings Technology.* 1997. Vol. 94-95. Pp. 525-530.
4. Akkerman Z.L., Efstathiadis H., Smith F.W. Thermal Stability of diamondlike carbon films *// J. of Applied Physics.* 1996. Vol. 80. Pp. 3068-3075.
5. Deshpandey C.V., Bunshah R.F. Diamond and diamondlike films: Deposition and properties // *J. of Vacuum Science & Technology A.* 1989. Vol. 7. Pp. 2294-2302.
6. Wei Q., Narayan J. Superhard, Diamond-like carbon: preparation, theory, and properties // *Intern. Materials Review,* 2000. Vol. 45. Pp. 133-164.
7. Dischler B., Wild C. (Eds). Low-Pressure Synthetic Diamond: Manufacturing and Applications. Springer, Berlin, 1998.
8. Hayashi K. et al. Study of the effect of hydrogen on transport properties in chemical vapor deposited diamond films by Hall measurements // *Appl. Phys. Lett.* 1996. Vol. 68. P. 376.

HIGH EFFICIENCY RADIOFREQUENCY FEED SYSTEM OF ARC/SPARKLE GASEOUS DISCHARGE

S.V. GORBATOV, P.A. DAVIDOVICH, I.V. KURNOSAU, F.V. PLIAVAKA, Y.M. PRYKHODZKA

A.V. Luikov Heat and Mass Transfer Institute of NAS of Belarus, Minsk, Belarus,

psdesign@itmo.by

Introduction

The arc/sparkle gas discharges at atmospheric pressure are well-known for a long time and have wide application range in researches and technology. However the feeding of such type discharges with high efficiency stills actual problem up to now. High-usage fluorescent lamp power supplies so-called "electronic ballast" circuits have good efficiency, auto-firing feature and small dimensions. But it is difficult to use such devices to excite atmospheric pressure discharges - they have not enough firing voltage, relative low conversion frequency and quite

inertial. Sometimes [1, 2] the high-speed dynamic control in multichannel plasma system is interesting too. Discussed arc/spark generator has next distinctive features:

- high firing voltage - up to 20-25 kV;
- good efficiency - 70-80 % and more;
- high conversion frequency - 1 MHz;
- short response time - few microseconds to fire discharge;
- multi-channel possibility.

Principle of operation

Discharge feed system works in two main, automatically switching modes: *fire*, with high output voltage and *limit,* during discharge burning, with limited output power. It can include a lot of independently controlled channels with parallel feed. Single channel block diagram is presented on Fig. 1.

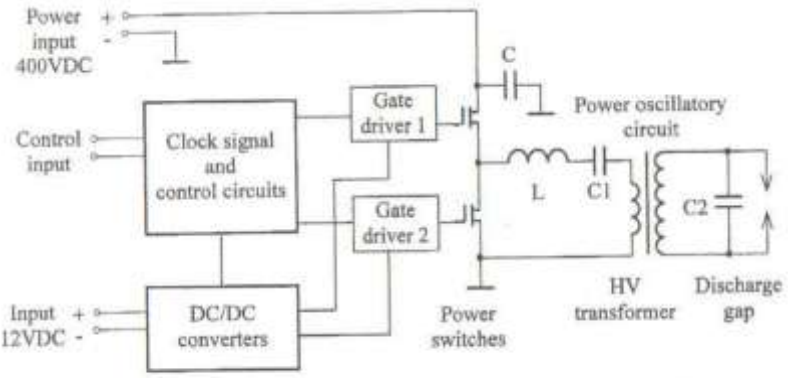

Fig. 1. Block diagram of high-voltage arc-discharge power supply

Clock signal generator, protect and control circuits are realized by using programmable logic device (PLD). Thus chip configuration(and generation parameters) could be changed in-system by special JTAG (Joint Test Action Group)-programmer.

Control signal are boosted by gate drivers and gone to the power switch gates. The converter is designed as half-bridge circuit using MOSFET(Metal-Oxide-Semiconductor Field Effect Transistor) or IGBT(Insulated Gate Bipolar Transistor) switches and fed of external voltage 400 VDC.

Power oscillatory circuit, included elements L, CI, C2 and high voltage step-up transformer, forms output voltage. In fire mode this circuit part can be modeled as two coupled oscillators; one of them consists of L and C2 and has resonance frequency about 1 MHz. As a result, output voltage will increase fast and reach breakdown level.

After discharge gap breakdown, in limit mode, capacitor C2 is shunted by small arc impedance and we can ignore its influence on power oscillation. Resonance of power oscillatory

circuit in this mode will be defined by elements L and CI and resonance frequency value will be less significantly than clock signal frequency(l MHz). Output voltage will decrease a lot and power supply passes to limit mode.

Control circuit is fed by galvanic isolated DC/DC converters from auxiliary voltage 12VDC. External control signal has standard TTL (Transistor-Transistor Logic) levels and transferred by optocouplers.

Results and discussion

Modeling results are shown on the Fig. 2. Rectangular wave generation imitates power switches output signal, sinusoidal-like curve is the calculated voltage on the discharge gap. We can see this voltage reach breakdown level, -17 kV here, during -2.5 ps after start of generation.

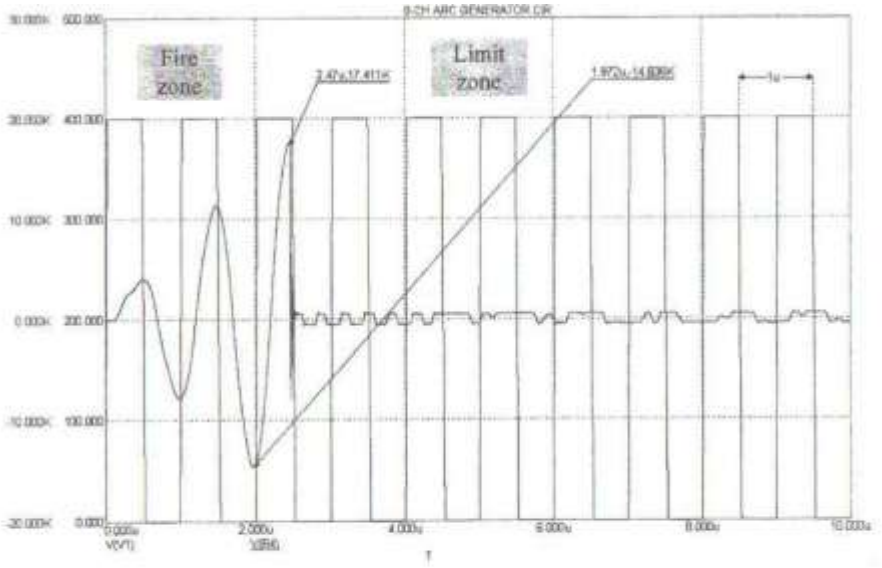

Fig. 2. Simulation results

Experimental waveforms of the same signal are cited on Fig. 3. Notable output voltage at *fire* zone practically coincides with model, but at *limit* zone the curves are not the same. Probably it is a result of using classical("hot") arc voltage-current characteristic [3] for simulation whereas real discharge (5 mm gap at atmospheric pressure) can have big enough active part of impedance like e.g. "atmospheric pressure high-voltage plasma" [4].

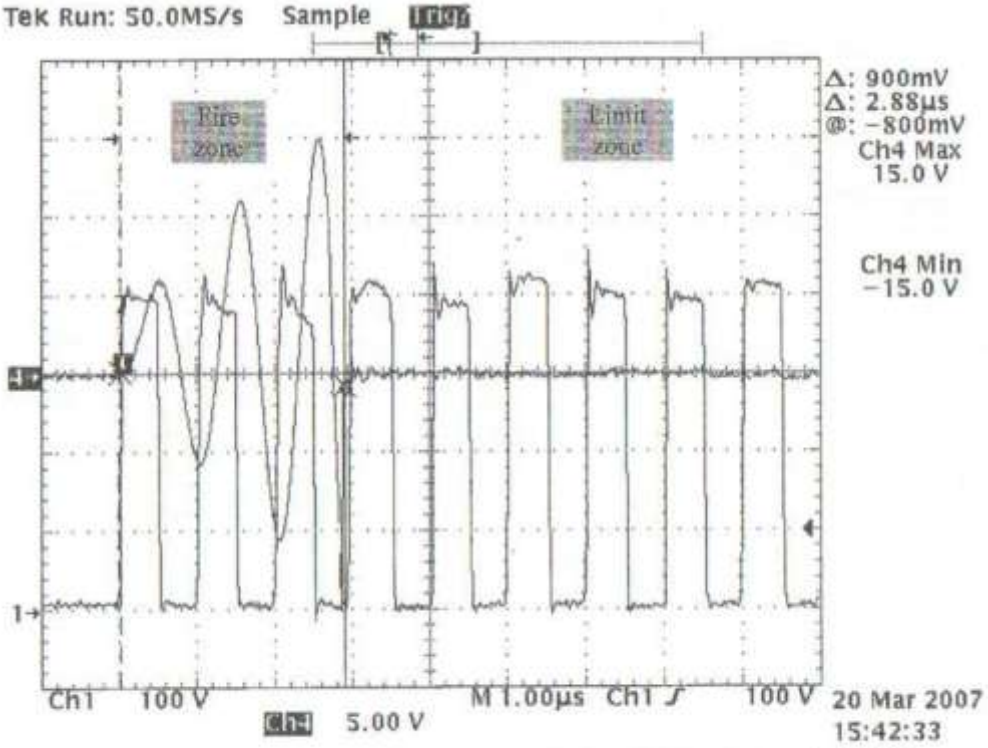

Fig. 3. Real oscillogramms. CH_4 –voltage at the load, divider 1:1000 (5 kV/div)

The Table 1 gives efficiency measurements results for different type of power switches. Maximal values -83 % and -94 % were achieved for *fire* and *limit* modes correspondingly.

Table 1. Efficiency calculation

Power switch type	Efficiency (fire mode)	Efficiency (limit mode)	Comments
1RFP27N60	0.750	0.925	MOSFET
FCH20N60	0.460	0.943	MOSFET
FGAF40N60	0.830	0.778	IGBT
SPP24N60C3	-	0.928	MOSFET
STGP19NC60WD	0.785	0.680	IGBT

Conclusions

Designed and developed radiofrequency feed system has good enough electrical features to use it for dynamic exiting of arc/spark discharges at atmospheric pressure. The compact multichannel generators design is possible as a result of using high conversion frequency and simple control of each channel. It permits to recommend such power supplies for using in gas flow control, firing fuel gas mixture and other fields of scientific and technology application.

References

1. Yurii G. Utkin, Saurabh Keshav, Jin-Hwa Kim, Jeff Kastner, Igor V. Adamovich and Mo Samimy. Development and use of localized arc filament plasma actuators for high-speed

flow control *// J. Phys. D: Appl. Phys.* 2007. Vol. 40. Pp. 685-694. Online at stacks.iop.org/JPhysD/40/685.

2. Corke T.C. and Matlis E. Phased plasma arrays for unsteady flow control // *AIAA Fluids* 2000 Conf. (Denver, CO, 19-22 June 2000) AIAA Paper 2000-2323.
3. Yuri P. Raizer. Gas discharge physics // *Springer-Verlag,* 1991.
4. BuyakovI.F., Volzhankin V.M., Krauklis A.V.,' Samtsov P.P., Solntsev AP. Formation of Carbon Nanomaterials Under the Conditions Formed by Atmospheric Pressure High-Voltage Plasma *// Minsk Intern. Colloquium on Physics of Shock Waves, Combustion, Detonation and Non-Equilibrium Processes, MIC 2005,* Minsk, 14-19 Nov., 2005.

MAGNETIC PROPERTIES MEASUREMENT TEST BENCH OF FERROMAGNETS AT HIGH AMPLITUDE PULSE MAGNETIC FIELD

P.A. DAVIDOVICH, S.V. GORBATOV, Y.M. PRYKHODZKA, I.V. KURNOSAU, F.V. PLLAVAKA

A.V. Luikov Heat and Mass Transfer Institute of NAS of Belarus, Minsk, Belarus

Introduction

The generators of high-voltage pulses are designed and assembled in department. Magnetic compression lines are used in their construction [1]. In order to increase the accuracy of calculation of magnetic compression line it is important to use measured parameters of the corc. To increase the precise of calculation we use the measured values because the datasheets give us the range of possible values or upper or lower threshold these parameters. System for measurements of dynamic magnetic properties of ferromagnets [2] is used. Measured data are the following: saturation induction (Bs), coercive force (He), residual induction (Br), area of magnetic hysteresis loop (magnetic looses per cycle), initial magnetic permeability (|i) and the main curve of magnetization. Magnetic materials in devices we design works on high frequency. We cannot measure the magnetic parameters at high frequency on the measurement system [2] and the extrapolation the values in high frequency range cannot have proper precision. The pulse test bench measures magnetic parameters on frequency near 1 MHz. It is the frequency on which the first compression circuit works.

Test bench description

The flow diagram of test bench is shown in Fig. 1. C2 is charged through switch Q1

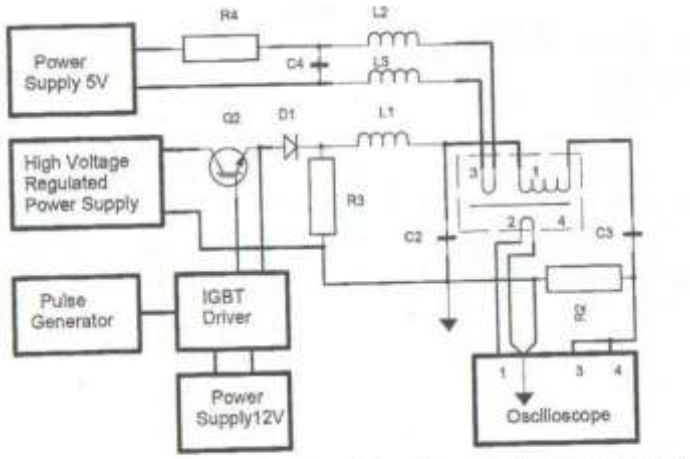

Fig. 1. The flow diagram of test bench for pulse magnetic measurements: 1 – magnetizing toroidal coil, 2 – measuring turn, 3 – premagnetizing turn, 4 – toroud ferromagnet specimen

and choke L1. The time of charging is calculated the same as the volt-second rating [3] of ferromagnet 4 and coil 1. The measuring process takes place when C3 charges from C2 through coil 1. Signals on turn 2 and resistor R2 are written in memory of oscilloscope TDS 644A (signal on R2 go on two channels with different gains). The data from oscilloscope convert in Excel format. The magnetic parameters are calculated by Excel tools.

Features of pulse measurements

The measurements in saturation state have some features in comparison with the ones in small magnetic field. They are: the symmetrical configuration of magnetizing coil, the necessity to compensate additional magnetic flow through measuring turn, parallel current measuring on two channels with different gains to obtain wide dinamic range. All these features were investigated while the test bench assembling and setting. The parts of hysteresis loop are shown on Fig. 2 a, b.

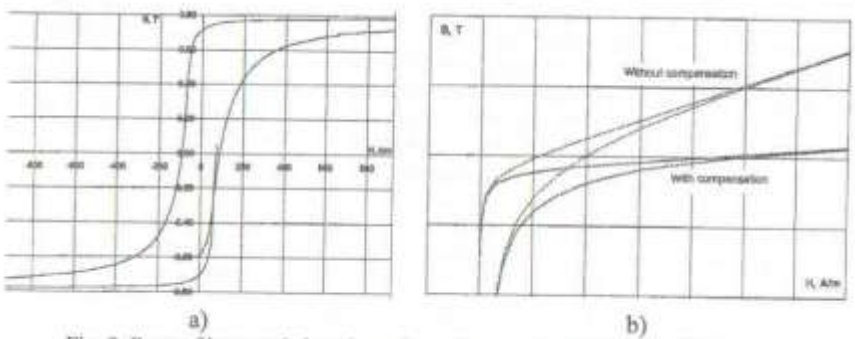

a) b)

Fig. 2. Parts of hysteresis loop in regions of magnetic field: a) small b) high

Conclusions

The test bench for pulse magnetic measurements has been built. It gives the opportunity to measure magnetic properties of magnet materials in saturation mode and to design magnetic compression circuits more precisely.

References

1. Harbatau (Gorbatov) S.V., Davidovich P.A., Kurnosau I.V., Pliavaka F.V., Prykhodzka Y.M. 1 kW 100 kHz high voltage pulse generator to excite nonequiiibrium gaseous plasma // Contributed papers of Intern. Workshop "Nonequiiibrium processes in combustion and plasma based technologies", August 21-26, Minsk, 2004. Pp.177-180.
2. Davidovich P.A., Harbatau (Gorbatov) S.V., Kurnosau I.V., Pliavaka F.V., Prykhodzka Y.M., S.A. Zhdanok System for measurements of dynamic magnetic properties of ferromagnets for magnetic compression circuits // Contributed papers of VI Intern. School-seminar "Nonequiiibrium processes and their applications", Minsk, 2002. Pp.130-132.
3. Philip T. Krein Elements of power electronics. Oxford University Press, 1998. Pp. 427-430.

METHOD OF PROCESSING OF CARBON NANOMATERIAL **PRODUCED IN THE LOW-TEMPERATURE PLASMA GENERATOR-EQUIPPED SET-UP**

I.F. BOUYAKOV, A.V. KRAUKLIS, I.S. KRYLOV

A.V. Luikov Heat and Mass Transfer Institute of NAS of Belarus, Minsk, Belarus,

krauklis@itmo.by

Introduction

Experience in producing carbon nanomaterial in amount suitable for industrial or half-industrial applications shows that morphologically its composition is most often complex and represents a mixture of different carbon structurized forms: nanotubes, nanofibers, amorphous carbon, graphite-like particles, etc. The percent content of each of the components depends on a method of producing material and on particular parameters of the process. This hampers the development of reliable reproducible technologies of using carbon nanometerial in composite materials of different type.

The present work is aimed at describing a method of processing carbon nanomaterial produced on the low-temperature plasma generator-equipped set-up with objectives to diminish its polydispersity.

Experimental

An initial carbon nanomaterial (hereinafter CNM) (Fig. 1) was produced on an experimental set-up detailed in [1]. It is a low-temperature plasma generator, to whose outlet a mixture of gaseous carbon (natural gas or propane-butane) and air was supplied. A collected

deposit was processed in salt acid, annealed in the air at a temperature of 450 °C, and ground in a ball mill. After such processing the material contained 40-50 % of carbon nanotubes, 20-30 % of carbon nanofibers, and about 30% of amorphous carbon with graphite-like particles.

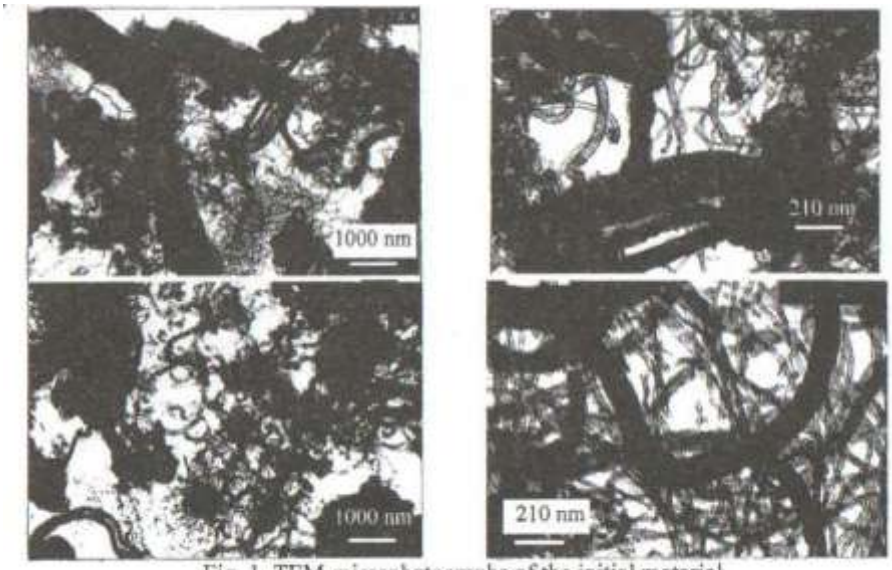

Fig. 1. TEM-microphotographs of the initial material

CNM was processed with the use of the following methods. 100 mg of CNM is poured into a glass with a volume of 250 ml and 150 ml of distilled waster is added. A mixture of water and CMN is being processed in an ultrasound bath for 25 min. In doing so, a stable suspension is formed, whereas a film (Fig. 2) is formed at the water surface and is then transferred to the water surface in a Petri dish (Fig. 3).

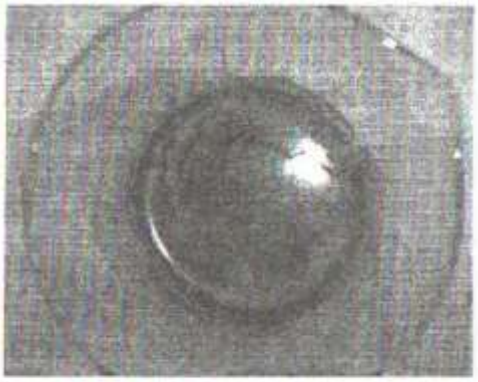

Fig. 2. Formed film

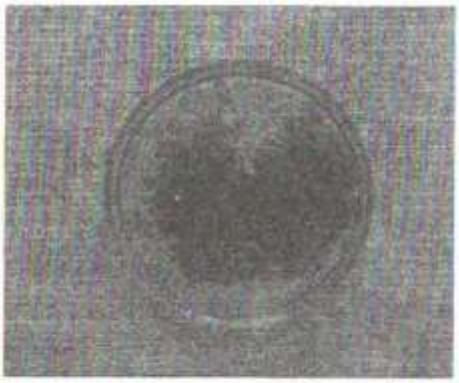

Fig. 3. Film at the water surface in a Petri dish

Distilled water is vaporized, a film is collected from the glass surface, and weighed on the analytical balance. Then the ultrasonic processing and all remaining operations are repeated. The obtained results are tabulated.

Table 1

Experiment No.	1	2	3	4	5	6	7	8	9	10	11	12
Film mass, mg	2	2	2.5	5	5	4	4	2	2.5	4.5	3	2.5

Total mass of film, mg	2	4	6.5	11.5	16.5	20.5	24.5	26.5	29	33.5	36.5	39
Experiment No.	13	14	15	16	17	18	19	20	21	22	23	
Film mass, mg	2.5	2.5	2	1.5	2	1.5	2	0.6	1	0.4	1	
Film total mass, mg	41.5	44	46	47.5	49.5	51	53	53.6	54.6	55	56	

After experiment No. 23 the rest of the suspension is poured into an evaporating dish and is evaporated. The remaining residue is weighed on the analytical balance and its mass is equal to 35 mg.

Results and discussion

The sampling was made after experiment No. 23. The obtained samples were analyzed on an TEM - photography. According to the second law of thermodynamics, in closed systems with T = const and V = const there will proceed spontaneously such processes that are accompanied by free energy loss. A dispersed carbon-distilled water system is in stable equilibrium when its free energy has a smaller value as possible under given conditions. Total energy at the carbon-distilled water W_{sw} at the interface is determined as [2]:

$$W_{sw} = \sigma_{sw} * S_{sw}, \quad (1)$$

where σ_{sw} is the specific free energy at the carbon-distilled water interface, erg/cm^2, S_{sw} is the total interface, cm^2.

Following the principle of minimum of free energy the quantity W_{5w} will tend to minimum. Expression 1 shows that this may be attained in two ways: decreasing the interface and diminishing the free energy at carbon-distilled water interface.

A tendency in decreasing the value of the interface manifests itself in the process of self-coarsening of colloidal particles: small particles merge into larger ones. The number of particles becomes smaller and their total surface decreases. In reality such a process easily arises in the colloidal systems and is called coagulation.

In the colloidal system opposite tendencies: self-coarsening and stabilization are seen. A large total value of the surface of the carbon phase sharply improves its adsorptivity. Carbon particles adsorb substances that diminish free energy at the interface, and the stability of the carbon-distilled water system is enhanced.

A stable carbon-distilled water system will tend to elevate its adsorptivity by removing particles with less adsorptivity from the dispersed system. In this ease such particles are relatively coarse particles of graphite and amorphous carbon, relatively coarse braids of tubes and fibers. The suspension mainly contains separate carbon nanotubes, which is supported by electron microscopy (Figs. 4, 5).

The formation of a film is connected with the fact that carbon particles penetrating into the surface layer diminish the surface tension at the water-air interface, which favors the carbon particle accumulation in the surface layer. As a result, the carbon concentration in the suspension is displaced in one direction: a concentration difference appears between the surface layer and the remaining volume of the suspension. In turn, this enhances the osmotic forces that tend to level the concentration over the entire suspension volume. Thus, there proceed simultaneously two mutually opposite processes:

1. Adsorption that provides the carbon particle accumulation in the surface layer according to the principle of minimum of free energy.
2. Desorption caused by levelling the carbon concentration over the entire suspension volume.

As a result, the adsorption equilibrium is established, which is characterized by a definite distribution of carbon particles between the surface layer and the suspension volume.

To confirm the theory for film formation, let us mix 250 ml of 200 mg of CNM and 150 ml of distilled water in a glass and add a surfactant with a concentration of 10 mmol/1 in the aqueous solution, which diminishes the water surface tension. It is known that a surfactant - sodium dodecylsulfate $C_{12}H_{25}OSO_3Na$ - already with a concentration of 10 mmol/1 in the aqueous solution at 20 °C diminishes the water surface tension at the water-air interface from 72.8 to 30 erg/cm^2 [3]. Let us process a mixture of water, CNM and sodium dodecylsulfate in the ultrasonic bath for 25 min. In this situation, a stable suspension is formed, and a film at the water surface is not practically formed.

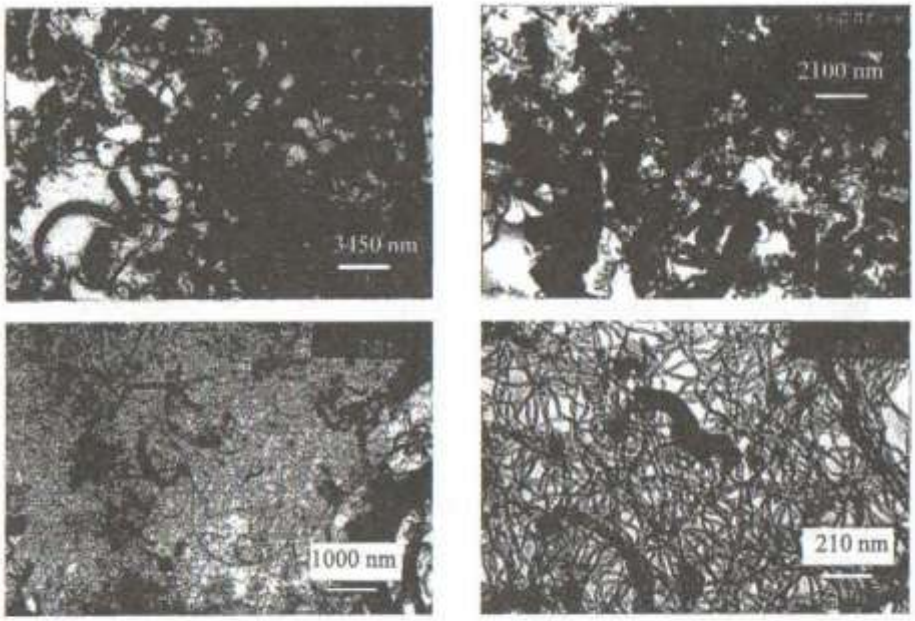

Fig. 4. TEM - microphotographs of a film

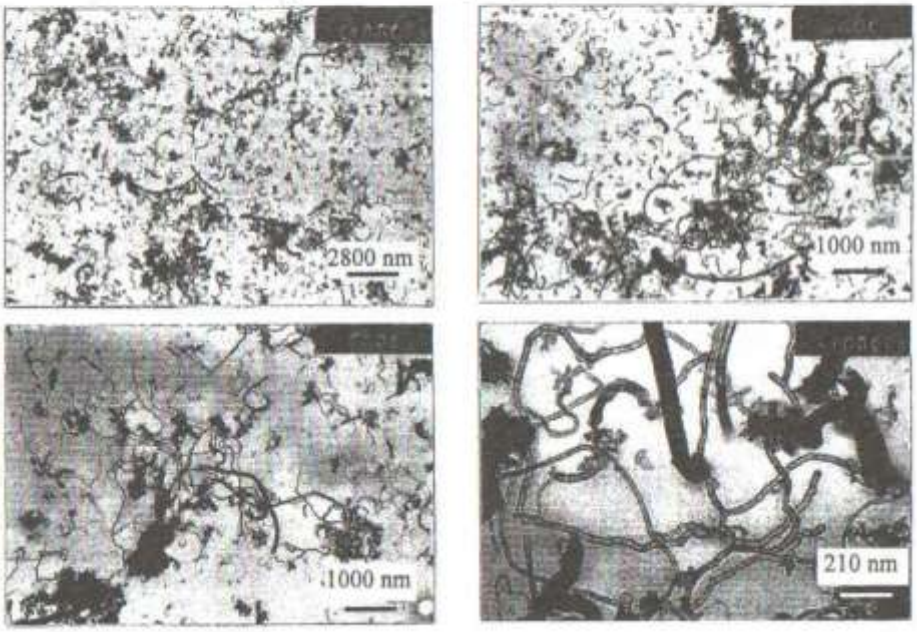

Fig. 5. X-ray electron microphotographs of the residue

Conclusions

Processing a carbon nanomaterial produced on the low-temperature plasma generator-equipped set-up in the ultrasound bath followed by removing a film results in diminishing polydispersity of a residue.

Braids of carbon nanotubes cannot be considered as nanoobjects since during the processing in the ultrasonic bath these formations do not decay into separate nanotubes (Fig. 4).

References

1. J. Zhdanok S.A., Krauklis A. V., Buyakov I. F. et al. Formation of Carbon Nanomaterials Under the Conditions Formed by Atmospheric Pressure High-Voltage Plasma // Minsk

Intern. Colloquium on Physics of Shock Waves, Combustion, Detonation and Non-Equilibrium Processes, MIC 2005. Minsk: HMTI, 2005. Pp. 142-146.
2. Koulman A.G. Physical and colloid chemistry. Moscow, 1963.
3. Shinoda K., Nakagawa T., Tamamushi B., Isemura T. Colloidal Surfactants. Some physicochemical properties. NewYork and London, 1963.

GASIFICATION OF A POROUS CARBON PARTICLE BY STEAM

V.M. GREMYACHKIN, E.P. MAZANCHENKO

Institute for Problems in Mechanics RAS, Moscow, Russia, grema@ipmnet.ru

Introduction

Gasification of carbon is a prospective process for generation of hydrogen, gaseous fuels for power and chemical industries. During combustion and gasification, porous carbon particles interact not only with oxygen [1, 2], but also with steam and carbon dioxide. During gasification, reactions of carbon with steam and carbon dioxide are the main ones, because in this case useful products, e.g. hydrogen and carbon monoxide, are generated. However, the carbon gasification models have not been developed now adequately because the mechanism of the process and the basic laws remain unknown. This article is a continuation of previous researches and basically concentrates on the development of the diffusive-kinetic model of porous carbon particle gasification and on the determination of the basic process characteristics, such as the gasification rate and composition of the gasification products, as well as the relation between these characteristics and oxidizing environment composition, pressure, furnace temperature, particle size and, most importantly, its internal surface area.

Model description

The mathematical model applied in this study was described in general in [1]. The diffusive-kinetic model considers the processes of heat and mass transfer inside the porous particle and in the gas phase above it. Heat losses by radiation from the particle to furnace wall are taken into account. In the model the heterogeneous reactions of carbon with steam and carbon dioxide and homogeneous reaction of carbon monoxide with steam are considered. The pressure variation inside the particle caused with the gas release is also taken into consideration.

Results and discussion

In the process of carbon particle gasification, is it possible that the chemical reactions run both in the gas phase above the particle surface and inside the porous particle. At the same time, the gasification rate is determines by the rates of heterogeneous reactions in the particle and the composition of gasification products depends to a large extent on the homogeneous reactions in the gas phase.

To determine the characteristics of gasification, it is required to consider the processes both in the gas phase and into the porous particle.

Inside the particle and at the particle surface carbon monoxide and carbon dioxide generation are possible as well as hydrogen generation. Fig. 1 shows a domain in which the solution exists. Calculations were carried out for a furnace temperature of 1400 K and the carbon particle size in the range of 100-200 pm.

Fig. 1 implies that the real dependence of gasification rate on the surface temperature must belong to the narrow domain between curves 2 and 3, where the carbon dioxide and carbon monoxide concentrations are positive.

The homogeneous reaction $CO + H_20 = C0_2 + H_2$ is supposed to be in equilibrium. Considering the rate of heterogeneous reactions $Wc = 760 \exp(-30205/T) [C0_2]$ as known [3], the equations of the model may be solved. The analysis of the model inside the porous particle made it possible to determine the correlation between the reaction rate of carbon with steam and the reaction rate of carbon with carbon dioxide. As a result, the rate of the reaction of carbon with steam is supposed to be $W_h = 3.79\ 10^4 z_3\ \rho \exp(-30205/T)$ [4].

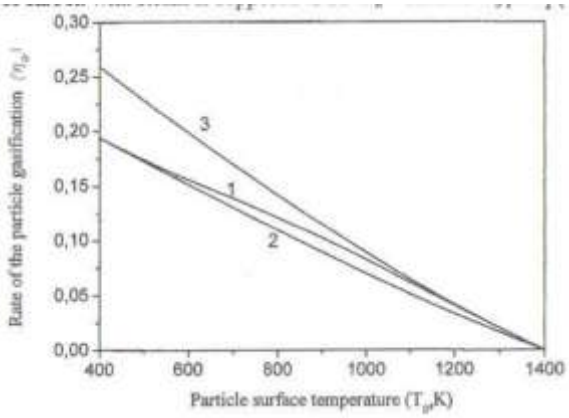

Fig. 1. Dependence of dimensionless gasification rate of the porous carbon particle on its surface temperature, under the assumption of homogeneous reaction equilibrium and for $[CO_2] = 0$ and $[CO] = 0$

Then, the dependences of the particle gasification rate and composition of the gasification products vs. composition, pressure and temperature of ambient gas and the internal surface of the porous particle are determined.

Figs. 2-4 show the dependences of the dimensionless gasification rate on the particic size, furnace temperature, and pressure. It was observed that with the increase in pressure, furnace temperature and particle size, the gasification rate grows. But as a result of endothermic reactions, the particle temperature decreases with the increase in the gasification rate, therefore it turns out of that the gasification rate grows only weekly, especially for small internal surface areas.

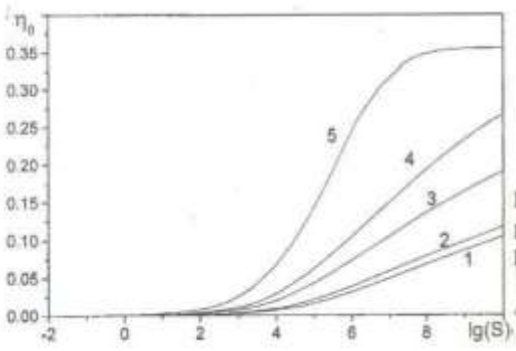

Fig. 2. Dependence of dimensionless gasification rate on dimensionless particle size:
1 – A =0, 5; 2 – A = 1; 3 – A = 5; 4 – A = 10; 5 – A = 50

Subject to various conditions, two domains where

solution exists may be determined. In the first one, the reaction takes place throughout all the particle volume. With the increase in the carbon dioxide concentration in the ambient gas and, accordingly, with the decrease in the steam concentration, carbon dioxide consumption zone shifts towards the particle and the reaction of carbon with steam takes place in a layer at the particle surface.

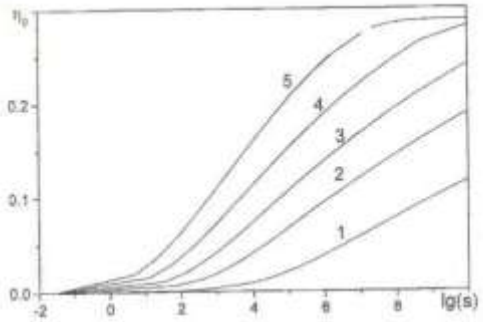

Fig. 3. Dependence of dimensionless gasification rate on furnace temperature: 1 – 1500 K, 2 – 1800 K, 3 – 2000 K, 4 – 2200 K, 5 – 2400 K

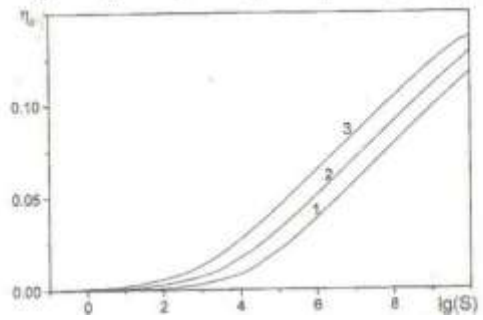

Fig. 4. Dependence of dimensionless gasification rate on pressure: 1 – 1 atm, 2 – 5 atm, 3 – 10 atm

Conclusions

The diffusion-controlled combustion regime of a porous particle was analyzed, and the principal characteristics of the process were determined.

In case of large internal particle surface areas, steam becomes the main oxidizer in the steam-carbon dioxide mixture. In case of small internal surface areas these oxidizers are virtually equivalent.

To provide generation of carbon monoxide as the primary gasification product, one must maintain the particle temperature high enough. In this case, it is necessary to have high heat fluxes to particle surface. It may be achieved either by increasing the furnace temperature or by increasing the particle size and, therefore, external particle surface.

References

1. Gremyachkin V.M., Fortsch D., Schnell U., Hein K.R.G. *// Comb, and Flame.* 2002. Vol. 130. P. 161.
2. Grenyachkin V.M. //Proceedings of the European Combustion Meeting. Brussels, 2005.
3. Lee S., Angus J.C., Edwards R.V., Gardrer N.C. *// A.I.Ch.E. J.* 1981. Vol. 30. P. 583.
4. Gremyachkin V.M. *// Chemical physics.* 2007. Vol. 26, No. 5. P. 26.

PLASMA-CHEMICAL DEPOSITION OF THE NANOCATALYST ON A METAL SURFACE AND ITS INFLUENCE ON CNT GROWTH

S.V. SHUSHKOU, S.V. GORBATOV, E.A. BYKOVA, I.S. KRYLOV, A.A. MIKHAILAU, Y.M. PRYKHODZKA, K.F. PLIAVAKA, F.V. PLIAVAKA, S.A. ZHDANOK

A.V. Luikov Heat and Mass Transfer Institute of NAS of Belarus, Minsk, Belarus

Introduction

To growing of carbon nanotubes (CNT) from plasma are used substrates from metals of a subgroup of iron [1]. Efficiency of CNT growth can be increased by special treatment of a surface, for example, thin mechanical polishing [2], etc. However the most effective method is preliminary creation of nanosize catalytic particles on a surface [3].

The aim of work was formation of catalytic nanoparticles at the surface of metal substrates using of barrier discharge plasma at atmospheric pressure, and research of influence of the received nanocatalyst on efficiency of CNT growth.

Experimental condition

The reactor of the barrier discharge (DBD) at atmospheric pressure with flat geometry of electrodes (Fig. 1) was used for the treatment of substrates.

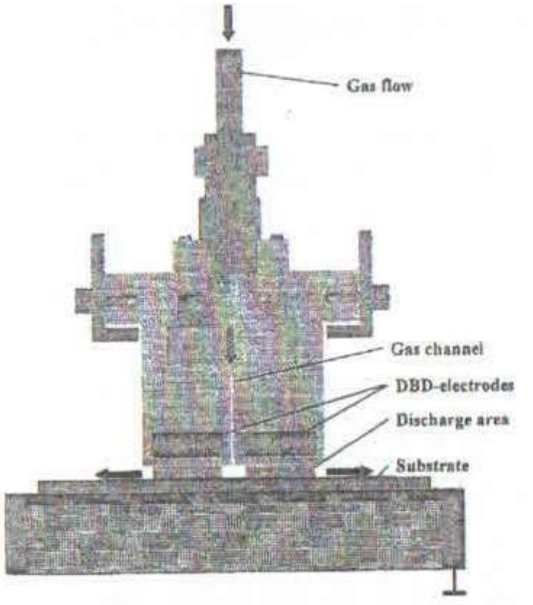

Fig. 1. The scheme of the nanocatalyst deposition on a substrate in the barrier discharge at atmospheric pressure

Substrates from nickel Ni, nickel - chromium alloy (55-78 % Ni, 15-23 % Cr, 1.5 % Mn, the rest - Fe), permalloy 79NM (80 % Ni, 4% Mo, 15 % Fe), copper Cu, aluminum Al were applied.

As an initial substances for a catalytic nanoparticles formation were used ferrocene $Fe(C_5H_5)_2$ and cobalt sorbate $Co(C_6H_7O_2)_2$. The ferrocene was sublimated by heating up to 150-170 °C and it was mixed to carrying gas - nitrogen N_2. Ferrocene was carried out due to a fast stream, and time of delivery to the substrate was ~ 0.2 s. Simultaneously the substrate was treated by the barrier discharge.

The cobalt sorbate was deposited on a surface of a substrate from alcohol solution, and Fig. 1. The scheme of the nanocatalyst after drying the substrate also was treated by deposition on a substrate in the barrier discharge.

DBD plasma treatment was made in two stages on both sides of samples. The flow of nitrogen made 2 nl/min. Energy input at a frequency of 10 kHz was estimated up to 10 W. The area of electrodes was 40x15 mm (2 pcs). The treated substrates were investigated on scanning electronic (SEM) and on atomic - force (AFM) microscopes.

Then samples were passed to the stand of the high-voltage arc where the deposition of CNT-containing carbon materials from a mixture of methane CH_4: air (γ- 4) was made.

CNT-growing were carried out under various conditions. First the plasma torch with the cathode from Invar (36 % Ni, 64 % Fe) was applied, the anode and a wall of a reactor was made of stainless steel. Further all the details of copper have been installed in the plasma torch. Then the cathode from graphite has been installed, the anode and a wall of a reactor have been kept copper.

After treatment the samples were weighed and amount of the formed material were calculated. The analysis of taken samples on transmission and scanning electronic microscopes with the definition of a share of contained CNT in the deposit was carried out.

Experimental results

It is possible to observe nanoscaled structures on a surface of substrates after the deposition of products of decomposed ferrocene from DBD- plasma (Fig. 2). The nanosized particles are formed after cobalt sorbate decomposition also (Fig. 3).

Fig. 2. The SEM - image of the DBD-treated surface of the Ni- substrate when inflow ferrocene $Fe(C_5H_5)_2$

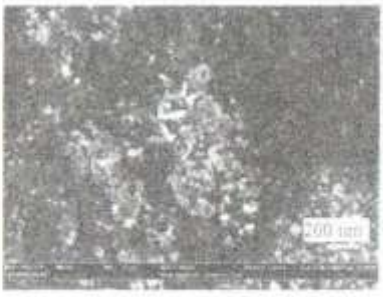

Fig. 3. The SEM - image of the DBD-treated surface of the Ni-substrate after cobalt sorbate $Co(C_6H_7O_2)_2$ deposition

AFM-scanning shows a characteristic picture with nanoscaled structure (Fig. 4). A linear scanning has shown a significant number of roughnesses which can serve as points of CNT-initiation.

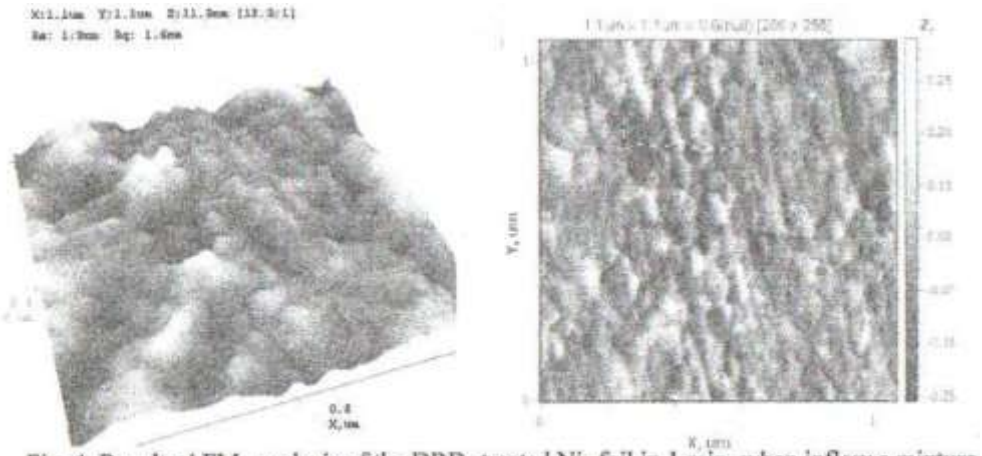

Fig. 4. Results AFM- analysis of the DBD- treated Ni- foil in 1 min, when inflow a mixture of nitrogen and ferrocene

In experiments with invar cathode the formation of a carbon deposit on various samples was observed (for example, on nickel up to $4.5\text{-}10^{-5}$ g/(hour mm^2)), but a significant influence from the prior deposition catalyst to the substrate has not been made. On a wall of a reactor from a stainless steel the deposit has made $-16*10^{-5}$ g/(hour*mm^2).

Fig. 5. The CNT- deposit grown on a Ni- foil with the ferrocene catalytic precursor

Fig. 6. The CNT- deposit grown on a copper wall of the reactor

To analyze of the cathode sputtering effect, the cathode from copper was installed, the anode and a wall of a reactor as copper have been executed also. The effect from preliminary DBD- treatment with the ferrocene was essential, for example, on nickel the CNT-deposit has grown in 1.4 times. The amount of the deposit reaches up to $20\text{-}10^{-5}$ g/(hourmm^2), and at contents CNT 50 % (Fig. 5). On a copper wall the deposit was insignificant, ~ $0.7*10^{-5}$ g/(hour mm^2), however formed CNT had the rectilinear form and have been combined into bunches (Fig. 6).

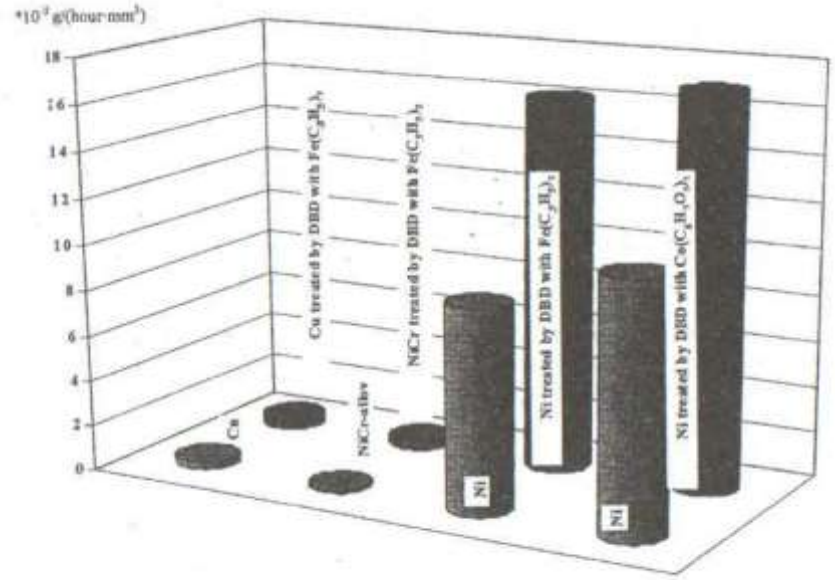

Fig. 7. CNT- deposit on initial substrates and on substrates with the catalyst

In a series with the graphite cathode the CNT-deposit on the nickel without treatment has made 8.8-10^{-5} g/(hour*mm^2), while on nickel treated with the ferrocene the output has increased in 1.8 times (16.2*10^{-5} g/(hour*mm^2)) (Fig. 7).

Conclusion

The nanocatalytic structure on a surface of metal substrates is formed with the help of DBD- plasma in a mix of nitrogen with an ferrocene $Fe(C_5H_5)_2$ impurity, and also as result of the decomposition of cobalt sorbate $Co(C_6H_7O_2)_2$.

The ferrocene used as the catalytic precursor on a Ni -foil allows to increase the output of CNT- deposit up to 85 %.

The cobalt sorbate used as the catalytic precursor on a Ni- foil allows to increase the output of CNT- deposit up to 60 %.

The greatest specific quantity of the CNT- containing material 20*10^{-5} g/(hour*mm^2) was formed on a nickel foil with the catalytic particles from a cobalt sorbate.

Authors thank T.A. Kuznetsova for carrying out of AFM- researches of samples.

References

1. Zhdanok S.A., Gorbatov S.V., Mikhailau A.A., Pliavaka F.V., Pliavaka K.V., Shushkou S.V., Savenko V.P., Belanovich A.L., Shchukin G.L., Sviridov D.V. Catalytic synthesis of carbon nanotubes in plasma of the pulse barrier discharge *// J. of Engineering Physics and Thermophysics.* 2007. Vol. 80, No. 6. Pp. 44-48.
2. Kukovitskii E.F., L'vov S.G., Sainov N.A., Chemozatonskii L.A. Correlation between metal catalyst particle size and carbon nanotube growth *// Chem. Phys. Lett.* 2002.

3. Rakov E.G. Nanotubes and fullerenes. Moscow: Logos, 2006.

INVESTIGATIONS OF NOVEL PLASMA CHEMICAL REACTORS FOR CNT SYNTHESIS FROM ALCANES USING MAGNETIC FIELD ASSISTANCE

A.F. BUBLIEVSKY, L.I. CHARAK.HOVSKY, D.S. SKOMOROHOV, A.N. NIKONCHUK, A.V. GORBUNOV, G.V. DOLGOLENKO, V.A. KOVAL, S.A. ZHDANOK

A.V. Luikov Heat and Mass Transfer Institute of NAS, Minsk, Belarus

skomorohovdm@mail.by

Introduction

Plasma chemical synthesis (PCS) of carbon nanotubes (CNTs) in stationary and dynamic electromagnetic fields is developed as evolution of traditional area of CNTs' arc synthesis [1-4]. Promising researches were carried out in this area. Specifically soot with 97 % multiwall CNTs was produced using plasma reactors with magnetic field assistance [1-3]. Data on magnetic field influence on CNTs growth in arc reactors with hydrocarbon plasmas has been presented [3].

For investigations in this area few novel plasma chemical reactors were designed in I-IMTI to study CNTs formation under partial oxidation and related modes with various magnetic fields influence.

Experimental and discussion

Using four special designed installations the investigation of CNTs based soot plasma synthesis with stationary and dynamic magnetic fields was carried out. Installation types being used during experiments were as follows:

i. installation based on plasma arc low pressure (0.03-0.04 MPa) reactor operated with stationary or dynamic magnetic field with induction of 0.1 T1 (related of Kratchmer's reactor),
ii. installation based on atmospheric pressure high-voltage discharge reactor (AHVD) with stationary or dynamic fields with induction up to 0.1 Tl,
iii. installation based on coaxial plasma arc reactor with magnetic annular arc (MAA) operated at atmospheric pressure of alcanes-air mixture and induction up to 1.1 Tl, arc power level of 50-100 kW.

Analysis of carbon products and catalytic reactor surfaces was carried out using transmission electron microscopy, thermal gravimetric method and XRD.

Operating conditions of the first of our installations based on DC arc discharge between ablating graphite electrodes in rare gas atmosphere with stationary and dynamic magnetic fields. Experiments were carried out with main parameters as follows: pressure of argon (with propane admixture) 0.03-0.06 MPa, arc current of 100 A, voltage level up to 40 V. Stabilization influence

of magnetic field with induction 0.02-0.1 Tl on arc discharge and high temperature area near electrodes were shown. In this experiments more higher yield of CNTs and more homogeneous distribution of nanostructures were achieved.

Operating conditions of the second of our installations based on AHVD with voltage of 1-4 kV and current of 100-300 mA, which realized in quartz tube reactor in zone between electrodes, which were made from catalytic iron group materials in propane-air mixture. Cycle of research work allowed to design improving type of high-voltage discharge reactor (AHVD) with magnetic system (Fig. 1), which formed stationary or dynamic magnetic field. [4] We carried out number of experiments on this reactor, we investigated synthesis processes of original and unoriginal CNTs from propane-butane mixture with magnetic field. Main parameters of experiments are current I = 87+240 mA, voltage - U = 0.55+3.6 kV, flow of air- G_B 0.24+0.65 g/s, flow of propane-butane - G_{Pb} = 0.04+0.275 g/s, induction of rotation magnetic field - B = 30 mTl. We determined that yield of CNTs increase if we are using adjacent magnetic field. It's 10-30 %. With rotation magnetic field influence with induction up to 0.032 T1 zone of discharge is increase in radial direction with increasing voltage and power about 1.4-1.5 are shown. Yield of CNTs increase too, and it 70 % mass, in better operating conditions. Achieving efficiency is about (10—20)-!0"^{5} g/(h mm^2). In the issue rotation magnetic field may be recommend for application in this type reactor for more higher cast of multiwall CNTs. Example of orientate CNTs, which synthesized on AHVD with $\gamma > 6$ is demonstrate at Fig. 2.

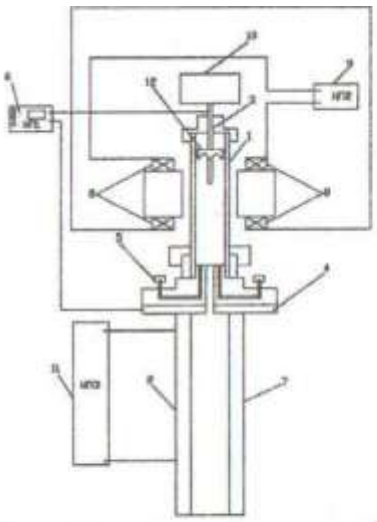

Fig. 1. Atmospheric pressure high – voltage discharge reactor (AHVD): 1 – quartz tube, 2 – chamber of soot deposition, 3 – cathode, 4 – anode, 5 – gas supply system, 6 – power supply, 7 – thermal couple, 8 – magnetic system, 9 – power supply for magnetic system, 10 – cathode moving mechanism, 11 – heating system, 12 – deflector

Fig. 2. TEM image of soot with CNTs synthesized with AHVD

Operating conditions of the third of our installations based on arc discharge (MAA type) between coaxial electrodes in magnetic field with propane-air mixture with argon admixture. During experimental work with stationary magnetic field we synthesized soot with 10 % content of CNTs and content of CNTs increase with increasing magnetic field at that.

After the comparison of results obtained using our installations with magnetic systems it's evidently that plasma parameters of low current discharges and high current ones as well as CNTs' produced yield can be influenced by rotating field even under its low induction' level (up to 0.03 TI).

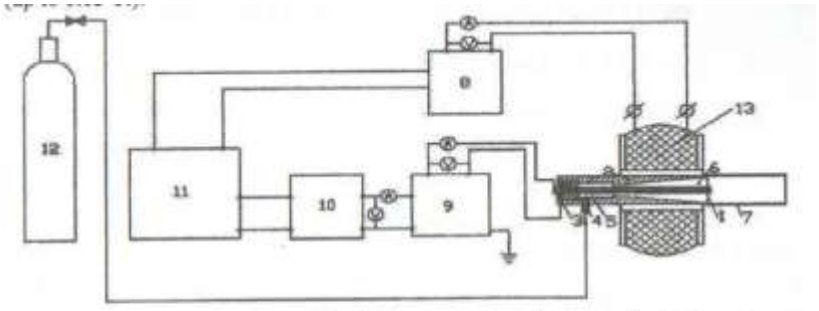

Fig. 3. Gliding arc tip plasma chemical reactor: 1 – tube electrode of plasmatron, 2 – external electrode, 3 – insulator trube, 4 – gas inlet, 5 – plasma gas vortex chamber, 6 – discharge zone of plasmatron, 7 – chamber of soot deposition, 8 – power supply for magnetic system, 9 – HV transformer, 10 – AC voltage regulator, 11 – 220 V line, 12 – gas system, 13 – magnetic system for stationary field generation

The fourth gliding arc tip plasma chemical reactor was also researched by us (Fig. 3). During our experiments, which carried out with magnetic field and metallic catalyst we detected that dominating factors as follows: 1) catalyst influence of the wall of the reactor, which was provided by cementite Fe_3C with volume of low-level cell V = 0.1564 nm^3 and intermetallic phases of Fe-Cr and Fe-Ti in working conditions with equivalence factor of propane-air mixture more then y = 4 and when y was low then 3 it was provided by oxygen phases Fe_2O_3 and Fe_3O_4 and austenite phase of steel; 2) component plasma composition before exit of reaction canal and conditions of plasma arc.

For realizing mechanism of this processes based on GA we designed a new simple plasma installation (Fig. 3) of alternating current for synthesis of nanomaterials (soot with 15- 20 % multiwall CNTs), which is protected by Belarus Patent [6].

References

1. Anazawa K., Shimotani K., Manabc C., Watanabe H., Shimitzu M. High-purity carbon nanotube synthesis method by an arc discharging in magnetic field *// Appl. Phys. Lett.* 2002. Vol.81.
2. Lee S.J., Baik H.K., Yoo J., Han H.J. Large scale synthesis of carbon nanotubes by plasma rotating arc discharge technique // *Diamond and related materials.* 2002. Vol. 11. Iss. 3-6. Pp. 914-917.
3. YarbecD., Meunier J-L., Guo L., GauvinR., MallahN. Carbon nanotubrs from the dissociation of C2CI4 using a dc thermal plasma torch // *J. Phys. D: Appl. Phys.* 2004. Vol. 37. Pp. 2121-2126.
4. Belarus Patent 4190 (2008 yr.).
5. Charakhovski L., Gorbunov A., Zhdanok S. et al. On the electric characteristics of a plasma reactor with magnetic annular arc // Proc. of 17th Intern. Symp. on Plasma Chemistry. Toronto, Canada, 2005. 5 p.
6. Belarus Patent 4519 (2008 yr.).

PRODUCTION OF CARBON NANOSTRUCTURES BY DECOMPOSITION OF HYDROCARBONS IN LOW-TEMPERATURE PLASMA

I.F. BUYAKOV, A.V. KRAUKLIS, K.O. BOR1SEVICH

A.V. Luikov Heat and Mass Transfer Institute ofNAS of Belarus, Minsk, Belarus,

borisevich-kir@yandex.ru

Introduction

Different carbon nanomaterials were discovered not a long time ago but well-known because of their peculiar properties [1]. Nowadays the task of production of gram amounts of such structures is not so relevant as five years ago, and prime cost of nanotubes and nanofibres is still pretty high. In addition, the demands of buyers of such materials grows greatly owing to expansion their potential fields of use. Solution of such problems could be found by means of high-volume nanomaterials manufacture organization. There are some methods of nanotube and nanofibres production: in arc discharge [2], at laser ablation of graphite [3], in CVD (carbon vapor deposition) processes [4, 5] etc. Most of the methods of carbon nanomaterials production have low productivity (up to 10 g/h), and require developing of special conditions in synthesis area (low pressure, use of promoter or catalyst, high temperature etc.) that leads to increasing of power inputs and decreasing of process efficiency.

This investigations were directed to familiarization a new plasma-chemical process of carbon nanomaterials manufacturing at decomposition of hydrocarbons in low-temperature plasma. Coming results could help in decreasing of prime cost of nanostructures and increasing of productivity of the process.

Experimental setup

Experimental setup was developed on the base of low-temperature plasma generator (plasmatrone). In such construction the energy of discharge is used for heating of gas mixture containing hydrocarbons and initiation the reactions of thermal decomposition and partial oxidation. Scheme of the setup representing on the Fig. 1 includes follow main systems:

- plasma-chemical reactor (PCR);
- power system with low-temperature plasma generator and two clectrodes in the upper part of reactor;
- cooling system 1 for electrodes and other parts of setup under intensive heating;
- cooling system 2 for gaseous products of reactions;
- feed system of gas mixture and plasma gas (air);
- control system;

PCR was a steel funnel with follow parameters: length 1200 mm, outer diameter 220 mm, inner diameter 210 mm. In funnel was placed the removable cylindrical insertion (filler plate). Carbon nanostructures arc grown on the inner side of this cylinder. There are heat-insulating layer between funnel and insertion with thickness in the range of 5-10 mm. Plasmatron was established on the cooling cover of the PCR, and consists of cathode realized as copper con and anode - as hollow copper cylinder, including two parts: inlet part (diameter ~ 18 mm, length ~ 103.5 mm) and outlet part (diameter ~ 22 mm, length - 60 mm). Current and voltage were

changed in the range 140-190 A и 160-200 V respectively. Air was used as plasma gas. Feed system of plasma gas allows variation of flow rate over the range 2-8 m^3/h.

Gas mixture of air and hydrocarbon was fed in the plasma flow after anode with following flow rates: 2-6 and 0.5-1.5 m^3/h respectively. Gas mixture and plasma gas were injected tangential, that favor to forming of vortex flow.

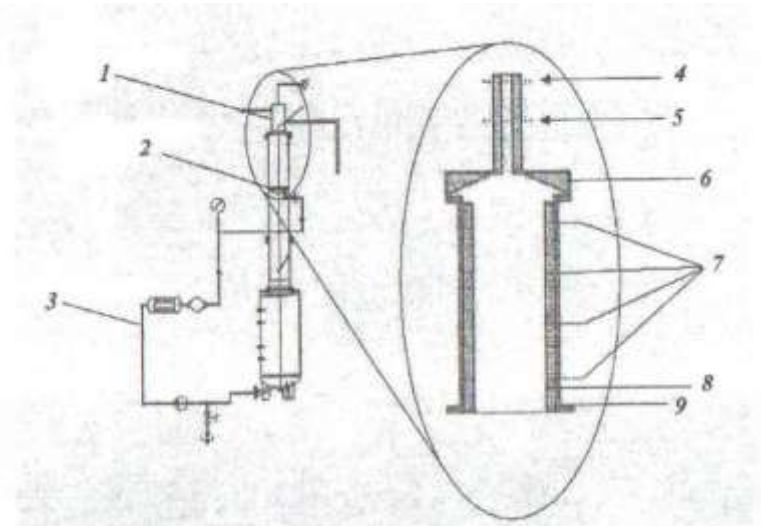

Fig. 1. Experimental setup: 1 – power system and cooling system 1; 2 – plasma-chemical reactor; 3 – cooling system 2; 4 – plasma gas feeding; 5 – gas mixture feeding; 6 – cooling cover; 7 – thermocouples; 8 – inner steel cylinder of plasma-chemical reactor; 9 – heat-insulating layer

Cooling system 1 serves for chilling inner parts of plasmatron exposed by effect of high temperatures. Cooling system 2 serves for quenching products of reactions in the PCR. This system consists of following elements: block of jets in the bottom of PCR, water tank, heat exchanger, water pump and water pipe system with hydraulic filter. Water circulates from the bottom of the water tank through the hydraulic filter and heat exchanger. Al the end of experiment water containing carbon particles pumped out in the special separating tanks. In the water tank metallic net was placed for precipitation of the dense part of the suspension. In that way, collection of the carbon material is carried out from three different zones: from the walls of the PCR, from the net in the water tank and from suspension in separation tanks.

Control system consisted of flow and pressure sensors at the feed lines of gaseous mixture and plasma gas; set of thermocouples placed in PCR; ADC and computer.

Results and discussion

Experiments were carried out at atmosphere pressure. The power of discharge was varied in the range of 25-35 kW. Air was used as a plasma gas, and the mixture of hydrocarbons including propane, butane, propylene, butane as a raw material. During experiment following parameters were registered: temperatures in different parts of PCR; inlet gaseous pressures and flow rates; current and voltage of discharge, and relative ratio amounts of reagent and oxidizer, called equivalent ratio.

Gas mixture supplied in the plasma flow after anode. Because of high temperature and presence of oxygen in gas mixture in reactor could be initiated reactions of incomplete combustion and thermal decomposition at the same time. Products of reactions were exposed to cooling and filtering. Average temperatures of the process was varied from 800 to 900 °C. At the end of every experiment carbon materials were collected, purified and analyzed by means of transmission and scanning electron microscopy (TEM and SEM respectively).

As pointed above, collection of the carbon materials carried out from three zones. Pumped out from the separating tank suspension, and part of the deposit on the net in the water tank were undergone by drying. Resulting product constituted black-and-gray powder with average packed density about 0.22 g/cm^3. Carbon nanotubes and nanofibers content in obtaining products were determined by TEM and SEM. Fig. 2 represents observations of the carbon materials from different zones. Analysis of numerous micrographs showed that dry carbon material from suspension and deposit on the net in the water tank had similar composition and consisted mainly of amorphous carbon particles with various dimensions. Content of carbon structures in the deposit collected in the PCR reached 40-50 %, amorphous up to 30 %. The rest of the products included graphite (~15 %) and metal particles or oxides (~5 %). Material containing carbon nanostructures subjected to the special acid and thermal treating for purification from amorphous and graphitized carbon and metal particles. After purification content of carbon structures achieved 70-80 %.

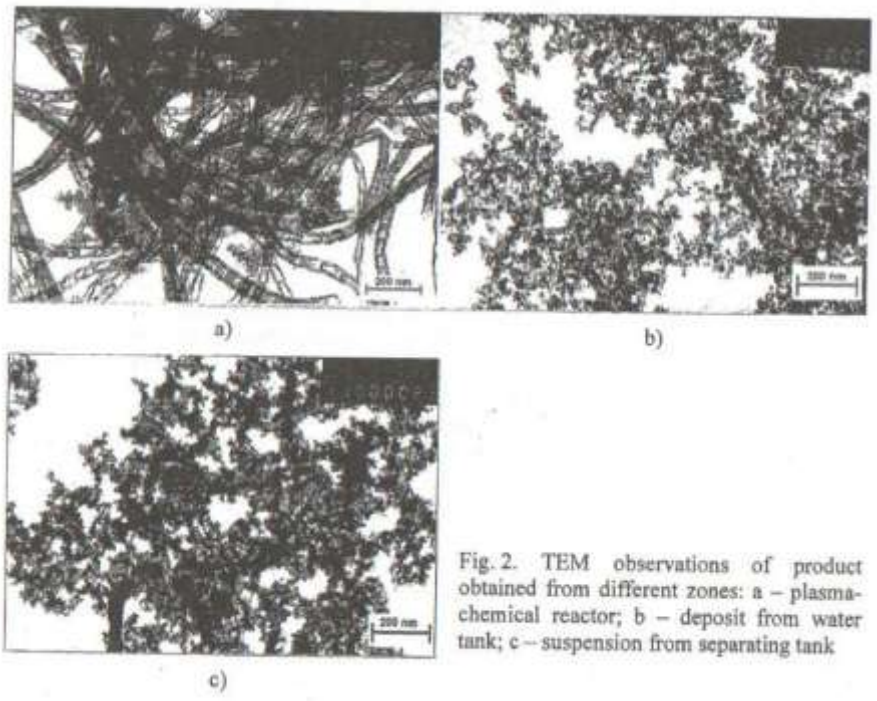

Fig. 2. TEM observations of product obtained from different zones: a – plasma-chemical reactor; b – deposit from water tank; c – suspension from separating tank

In that way it is possible to conclude, that organized carbon structures formation occurs on the surface of the steel containing iron and nickel, that is in agreement with "carbide cycle" hypothesis [6]. Fig. 3 shows TEM and SEM photos of carbon nanomaterial obtaining in the

PCR. It is clear that some structures represent nanofibers with typical diameters about 300 nm and different lengths and shapes. At the same time products contains structures with smaller diameters 50-70 nm and length about 1 pm, which could be considered as a multiwall carbon nanotubes.

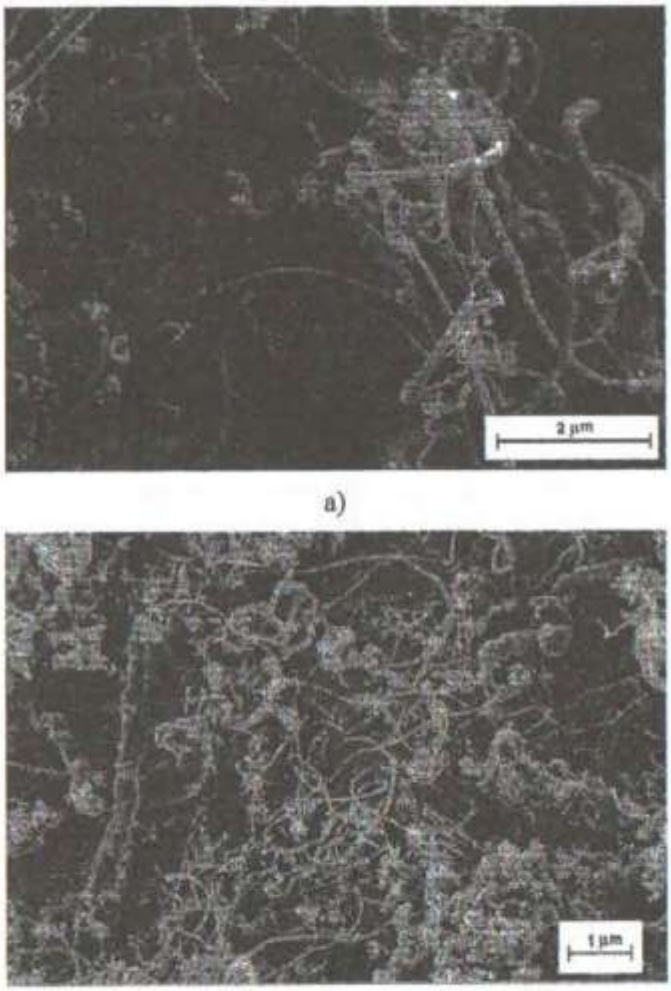

Fig. 3. SEM observations of carbon nanostructers: a – with bigger diameters; b – with smaller diameters

Conclusions

So, as a result of researches carried out the method of carbon nanostructures production at the hydrocarbon decomposition in low-temperature plasma was worked out. It is established that carbon nanostructures formation occurs on the metal surface of the PCR from the iron and nickel particles as precursors. The productivity of that process is about 100 gram per hour, content of carbon nanostructures achieved up to 50 %.

References

1. Rodriguez N.M. A review of catalytically grown carbon nanofibers *// J. Mater. Res.* 1993. Vol.8, No. 12. Pp. 3233-3249.
2. Cadek M., Murphy R., McCarthy B., Drury A., Lahr B., Barklie R.C. Optimisation of the *are*-discharge production of multi-walled carbon nanotubes // *Carbon.* 2002, Vol.40. Pp. 923-928.

3. Arepalli S., Nikolaev P., Holmes W., Bradley S. Files, Production and measurements of individual single-wall nanotubes and small ropes of carbon // *Applied Physics Letters.* 2001. Vol. 78, No. 10. Pp. 1-3.
4. Chen P., Wu X., Lin J., Li H., Tan K.L. Comparative studies on the structure and electronic properties of carbon nanotubes prepared by the catalytic pyrolysis of CH4 and disproportionation of CO *// Carbon.* 2000. Vol. 38. Pp. 139-143.
5. Kiseiev N.A., Hutchison J.L., Moravsky A.P., Rakova E.V., Dreval E.V., Hetherington C.J.D., Zakharov D.N., Sloan J., Loutfy R.O. Carbon micro- and nanotubes synthesized by PE-CVD technique: tube structure and catalytic particles crystallography // *Carbon.* 2004. Vol. 42. Pp. 149-161.
6. Sinnott S.B. ct. al. Model of carbon nanotube growth through chemical vapor deposition // *Chem. Phys. Let.* 1999. Vol. 315. Pp. 25-30.

PLASMA TREATMENT OF DIESEL EXHAUST GASES

S.A. FILATOV, G.S. KUCHINSKY, E.V. BATYREV, N.A. KUMEYSHA
A.V. Luikov Heat and Mass Transfer Institute of NAS of Belarus, Minsk, Belarus,
fil@hmti.ac.by

Introduction

Diesel exhaust emissions contain carcinogenic and toxic particles and chemical species. Correction of diesel engine exhaust is a societal obligation. New diesel engines do not emit the black soot of former times and give the false impression that they are clean - but they are not clean of this most serious component. Fortunately, retrofitting diesel engines with highly efficient diesel particle filters (DPF) successfully remove 99 % of the solid nanoparticles. The diesel oxidation catalysts that have been applied to older diesel engines since the late 1960s do little good, and there is a growing interest in retrofitting diesel particle filters (DPF) to in-use diesel engines. By different companies several diesel particle filter (DPF) designs are fully developed and have proved to be an effective, reliable and durable method to filter and collect solid particles from diesel exhaust. Each PFS requires a highly efficient DPF to collect all solid particles and a filter cleaning process (regeneration) where collected particles are removed. The regeneration process Can be accomplished by one of several combustion techniques that convert the collected soot by oxidation (combustion) to gaseous CO_2 which exits the tailpipe, returning the DPF to its original clean state. Many types of commercially available PFS have been

developed and proven effective, reliable and durable. A PFS incorporating a high efficiency DPF will also filter inorganic solids originating from engine wear, toxic lubrication oil ash compounds, and certain PFS types remove gaseous toxic hydrocarbons and carbon monoxide. The most efficient DPF designs have been found to be 99.9% efficient for filtration of nanometer sized lung alveoli penetrating particles in the size range of 10 to 500 nm in diameter. Primary nanometer sized solid carbon particles are formed along with basic chemical structures of typical diesel engine hydrocarbon species as peak temperatures continue to fall. The primary solid soot particles grow in diameter and then agglomerate into long chains and branches of particles. There are an enormous number (ten to hundreds of millions of solid particles per cubic centimeter) of agglomerated solid particles in the size range of 10 to 500 nanometers in diameter. The number of diesel exhaust particles in the nanometer sized solid particle range is very large compared to the number of larger particles. Nanometer sized particles are invisible while the smaller number of larger particles is seen as typical diesel black smoke. Almost the entire total solid surface area is due to the surface area of nanometer sized particles, but this fraction contributes almost none of the total particle mass in terms of (g/cm^3 or g/(bhp-h)) of diesel exhaust. The larger particles formed in the range of 1 micrometer (1,000 nm) to 10 micrometers constitute almost all of the total particle mass of diesel exhaust but comparatively few of the total particle number and less than 1 to 2 % of particle surface area. In the past decade, diesel engine technology has stepwise greatly reduced total particle mass emissions from about 1 to 0.02 g/(kW-h) [1-3].

Model description

The primary objective of the DPF (Diesel Particle Filter) is health protection. The DPF shall minimize the number of solid particles in the alveoli-intruding size range 20-500 nm.

Typical parameter of DPF can be:

- Filtration efficiency > 99 % for particles in the size range 10-500 nm at all steady state and transient operating conditions, also during the regeneration: Full load exhaust-gas temperatures till 750 °C;
- Temperature spikes till 1400 °C, during external regeneration;
- High thermo-mechanical stresses during temperature transients;
- Material compatibility with oil ash, lubrication oils and fuel additives; High retention capacity for soot and ash;
- Very low pressure loss to prevent engine harm;
- Low thermal inertia (rapid response);
- Robust against vehicle vibrations, particularly when located in engine proximity;
- Rugged immunity to damage during ash cleansing;

- Low costs (< 20 6/kW); Small size for easy placement;
- Durability matching the engine life and retrofit capability.

State of art filter medium must have a fine porous microstructure, which is within a surface-rich macrostructure. The pore size or fiber diameter determines filtration, and must be about 10 μm or smaller. The macrostructure surface must be so large that the flow velocity through the filter medium is in the range of a few cm/s. The only suitable structures arc heat resistant materials like monolithic porous ceramic cellular formats (wall flow) or foams, highly alloyed porous metal sinters and metal foams. Also suitable are fiber structures, or structure from textiles (knitted or woven) using ceramic and metallic fibers. A pulsed corona surface discharge (PCSD) system was selected for particulate matter (PM) and NO_x removals from a diesel engine. Figs. 1-3. The PCSD was carried out with a dielectric barrier discharge (DBD) reactor and a pulse power supply at atmospheric pressure and room temperature. The DBD reactor consisted mainly of an alumina (Al_2O_3) tube and a stainless steel rod (cathode) inserted in the alumina tube, and an aluminum coil (anode) wound on the outside surface of the Al_2O_3 tube.

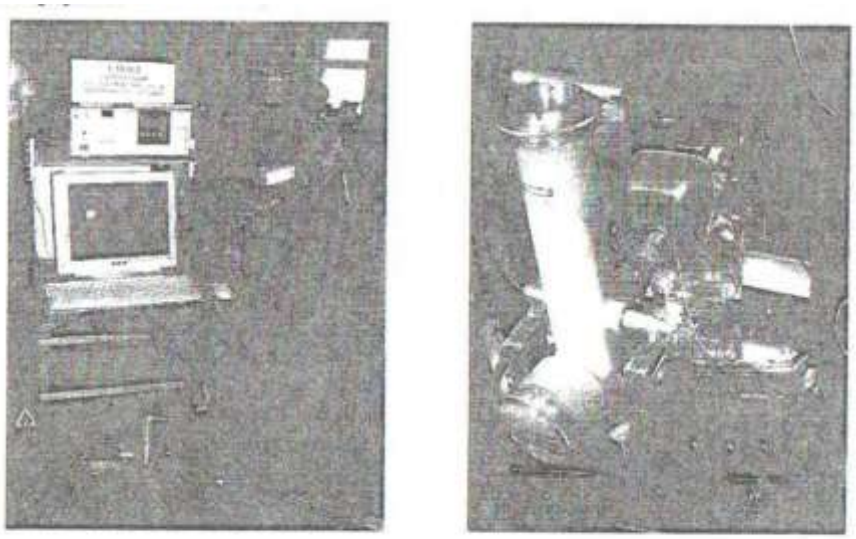

Fig. 1. Common view of test equipment: engine gas generator (left) and DPM filter (right)

Results and discussion

Pulse voltage was applied to the outside Al coil and stainless steel rod. PM was removed at a rate of 89 % at maximum with 40 % NO_x removal. Relations of pulse voltage and frequency to PM and NO_x removals were investigated. PM was oxidized by NO_2 and other kinds of active oxygen species, such as O and O_3 from plasma discharges.

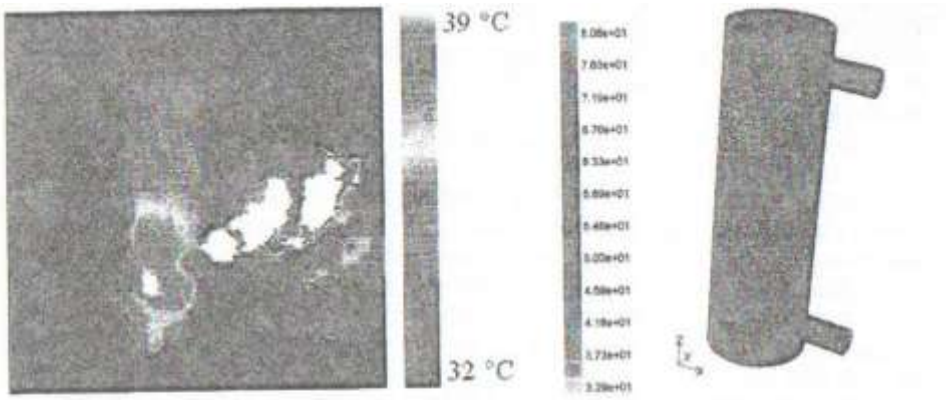

Fig. 2. IR thermography image of DPF (left) and 3D model of temperature distribution (right) on DPF with barrier discharge

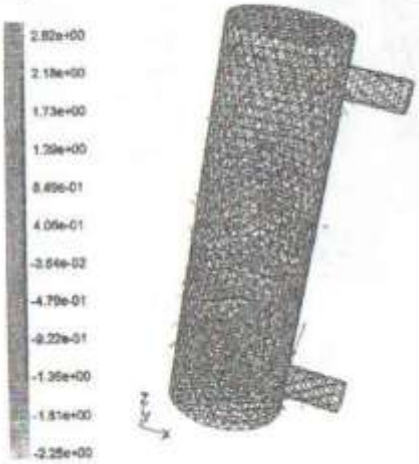

Fig. 3. 3D simulation model of flows in barrier discharge DPF

State of art filter medium must have a fine porous microstructure, which is within a surface-rich macrostructure. The pore size or fiber diameter determines filtration, and must be about 10 pm or smaller. The macrostructure surface must be so large that the flow velocity through the filter medium is in the range of a few cm/s. The only suitable structures are heat resistant materials like monolithic porous ceramic cellular formats (wall flow) or foams, highly alloyed porous metal sinters and metal foams. Also suitable are fiber structures, or structure from textiles (knitted or woven) using ceramic and metallic fibers. A pulsed corona surface discharge (PCSD) system was established for particulate matter (PM) and NO_x removals from a diesel engine. This system was carried out with a dielectric barrier discharge (DBD) reactor and a pulse power supply at atmospheric pressure and room temperature. The DBD reactor consisted mainly of an alumina (Al_2O_3) tube and a stainless steel rod (cathode) inserted in the alumina tube, and an aluminum coil (anode) wound on the outside surface of the Al_2O_3 tube. Pulse voltage was applied to the outside coil and stainless steel rod. PM was removed at a rate of 89 % at maximum with 40 % NO_x removal. Relations of pulse voltage and frequency to PM and NO_x removals were investigated. In experiments can be shown that PM was oxidized by NO2 and other kinds of active oxygen species, such as O and O_3 from plasma discharges [4].

Removal of NO_x from diesel exhaust has been a challenge to researchers as many conventional techniques such as catalysis, exhaust gas recirculation and other engine design modifications have failed to bring down the level of NO_x to mandatory limits. In this context, electrical discharge plasma technique appears to be very promising. However, it has been established that electric discharge plasma alone cannot remove NO_x from diesel exhaust [1-4]. This demands electric discharge plasma technique to be combined with other aftertreating techniques. At present, electric discharge plasma combined with heterogeneous catalysis is being studied extensively by many researchers. There have been many published papers in this research area showing NO_x removal efficiencies somewhere in the range of 60-90 %N. Another typical catalyst is V_2O_5/TiO_2. Ammonia also was used as reducing agent for the catalysis process.

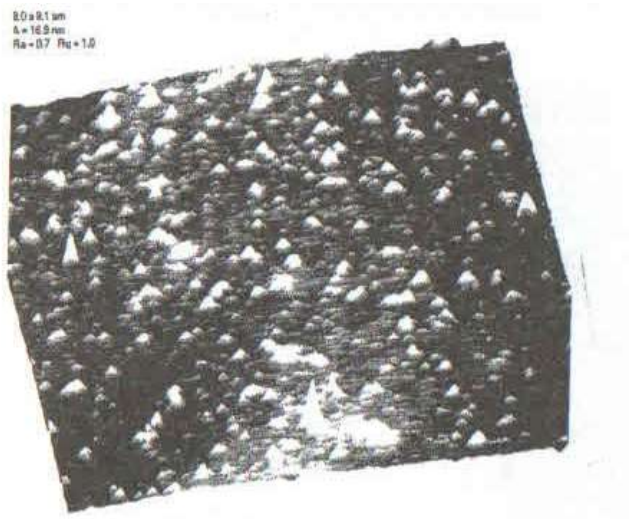

Fig. 4. Typical view of particles before DPF (full size 8x8 μm)

For fraction analysis of dust particle we use atomic force microscopy (AFM). Sample (clean glass plate) for short time (2 second) placed in exhaust system before and after particle filter for comparison, Fig. 4.

A dielectric barrier discharge reactor (referred to as plasma reactor) was employed in the present studies. The plasma reactor was a cylindrical glass tube (inner diameter: 15 mm and outer diameter: 17 mm) consisting of a stainless steel rod 1 mm thick as the inner electrode and an foil wrapped over the glass tube as the outer electrode, Fig. 5.

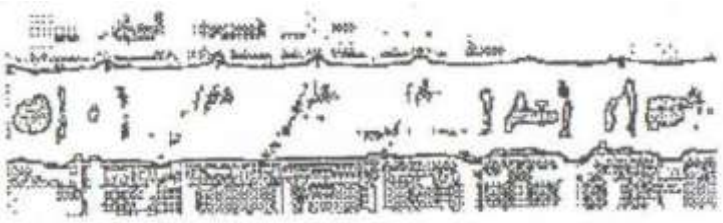

Fig.5. Typical view of atmosphere pressure DBD in DPF

We also use gas analysis for study DPF by measurement of IR spectra of exhaust gases from different parts of exhaust pass, Fig. 6. Technique include cleaning procedure of hot by dry nitrogen and analysis of differential spectra.

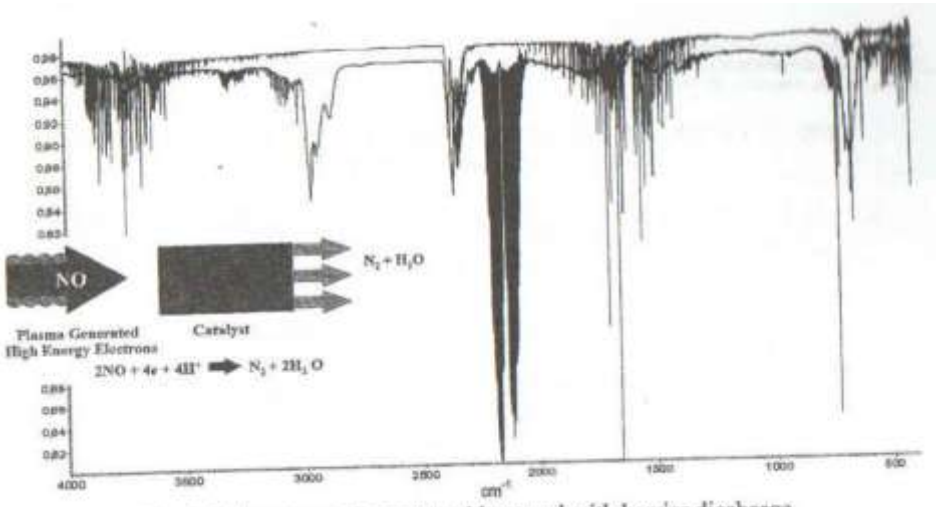

Fig. 6. Exhaust gas IR spectra without and with barrier discharge

Conclusions

In our experiments was shown that the increase in energy input the NO removal increases at all temperatures. The NO removal at room temperature by DBD was high than 90 % at an energy density of 96 J/l. The water in exhaust gas are dissociated into H and OH radicals in presence of electrical discharge plasma. The OH radicals enhance the oxidation of NO to NO_2. The hydrocarbons present in the diesel exhaust initially are reacted with O, OH and O_3 radicals released during electrical discharge to produce hydrocarbon "fragments" enhance the oxidation of NO to NO_2. It was found that the NO removal efficiency decreased with the increase in exhaust temperature. The NO_x removal mainly takes place by the reactions involving various hydrocarbons present in the diesel exhaust as follows. In DBD with catalyst layer like V_2O_5/TiO_2 (plasma assisted catalytic reactor - PACR) can be use a SCR catalyst and ammonia as its reducing agent at near room temperature.

References

1. *Hackam R, Akiyama H. //* IEEE Transactions on Dielectrics and Electrical Insulation. *2000. Vol. 7. P. 654.*
2. Penetrante B. M., Brusasco R. M., Merritt B. T. et al. // Pure and Applied Chemistry. 1999. Vol. 71. P. 1829.
3. Kim H. H., Takashima K., Katsura S., et al. // *J. of Physics D: Applied Physics.* 2001. Vol. 34.
4. Rajanikanth B. S., Ravi V. $DeNO_x$ Study in Diesel Engine Exhaust Using Barrier Discharge Corona Assisted by V_2O_5/TiO_2 Catalyst // *Plasma Science & Technology.* 2004. Vol. 6. No. 4.

EFFECT OF SINGLET OXYGEN PRODUCED BY CROSS DISCHARGE ON METHANE COMBUSTION

K. PLIAVAKA[1], A. BOURIG[2], K. ZAHRINGER[2], D. THEVENIN[2], J.-P. MARTIN[3], V. LAGO[3], E. BARBOSA[3], F. PLIAVAKA[1], S. GORBATOV[1], S. SHUSHKOU[1], E. PRIHODZKA[1]

[1]A.V. Luikov Heat and Mass Transfer Institute of NAS of Belarus, Minsk, Belarus, kirillp@tut.by

[2]University of Magdeburg "Otto von Guericke", Laboratory of Fluid Dynamics, Magdeburg, Germany

[3]ICARE, CNRS, Organs, France

Introduction

Work objective is the development of a method for assisted combustion and efficiency increasing of gaseous fuel burning. One of the most perspective ways of achievement of work objectives is the method based on acceleration of chain reactions, underlying ignition and burning of the majority hydrocarbon fuel, hydrogen and other combustible substances, by excitation of internal (vibrational and electronic) degrees of freedom of reacting molecules [1-5]. The scientific idea consists in the realization of the most effective and energetically favorable methods of vibrational and electronic states excitation of reacting atoms and molecules, influencing on gas by volumetric electric discharge, in which electrons energy corresponds to a maximum of dependence of excitation cross-sections of single vibrational or electronic states of molecules on energy [6]. The opportunity of effective influence on combustion process by various type electric discharges is discussed in the scientific literature for quite a long time and by now became a subject of intensive research. Depending on type and parameters of the discharge it is possible to allocate three basic mechanisms of influence of the discharge in a gas mixture on combustion and ignition processes: 1) strong temperature and pressure increase in a zone of influence (arc, spark, surface, etc. discharges) which can be accompanied even by generation of a shock wave and results to mixture firing, as well as usual torch ignition (initiation of the chain mechanism occurs as a result of thermal dissociation of molecules and to formation of free radicals); 2) molecules dissociation by electronic impact and formation of active atoms and radicals initiating chain reactions (the barrier or decaying self-sustained discharge at big values of the reduced electric field, $E/N > 1.5\text{-}10^{-16}$ V-cm^2, subnanosecond discharge with a wave of ionization, etc.); 3) excitation of vibrational and electronic states of molecules by electronic impact (non-self-sustained and self-sustained discharges of various type with $E/N > 1.5\text{-}10^{-16}$ V-cm^2), and chemical reactions proceeding with participation of excited molecules (they react 100-

1000 times faster, than non excited molecules) results in formation of active atoms and radicals - carriers of the chain mechanism of combustion.

Plasma composition and consequently discharge parameters should be optimized on the basis of the joint analysis of processes in the electric discharge and processes of combustion/ignition of the mixture. In this work subsonic burner with crossed discharge chamber for singlet oxygen (SO) producing was realized. Presence of SO on this stage of investigations was registered with intensified CCD digital camera of visible spectral band. Intermediate experimental results have shown an increasing of a flame front. Stabilization of the flame was observed when crossed discharge switched on. Experiments are in progress new experimental results will be performed on the presentation.

Experimental setup

In order to optimize the singlet oxygen yield in the plasma, the discharge should operate at E/N values where the energy input into the exited states is maximal. For exiled molecules generating we used crossed discharge reactor (CDR). In the crossed discharge short high voltage DBD pulses produce ionization while a comparatively low electric DC field supports the electric current between ionizing pulses. This allows adjusting of the reduced electric field close to the optimum for excitation of singlet oxygen molecules to increase the production yield.

As it can be observed on the Fig. 1 a premixed CH_4/O_2/He mixture is injected in the slot nearby the plasma crossed discharge reactor slot, the latest being supplied by a binary mixture O_2/He. Helium is connected to a divider allowing the initial helium flow to be divided into three ways: one way is sent to the first mixer that constitutes a premixed mixture (with CH_4 and O_2). This premixed mixture is then sent to a burner slot. The second way is sent to the second mixer to form a binary mixture with oxygen. The binary mixture supplies to the crossed discharge plasma slot of the hybrid burner. Finally, the third way is splitted into two lines that feed two outer-part slots of the burner (which constitute a helium shield).

Flow control is performed by electronic mass flow meters, piloted by computer. Flow meters are calibrated for each gas individually in 7 calibration points within the total range of operation (0 to 2 m7h). This calibration is performed in tenth of percent resolution. Thanks to that high resolution, the output flow can be adjusted with a precision higher than 1 %.

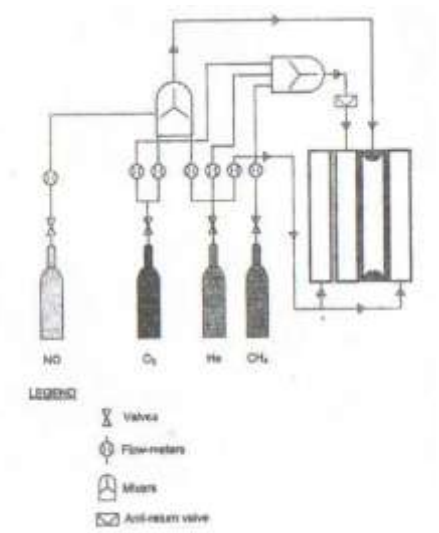

Fig. 1. Gas feeding for premixed and partially premixed flame

Experimentally, the excited oxygen produced in the former generator will interact with premixed flame. But, as the gas mixture contains a maximum of 6 % of O2 in He, we use the premixed flame to ensure

combustion. Experimental flow conditions are summarized in the following Table 1. This corresponds to flame equivalence ratio varying from 0.9 to 1.

Table 1. Experimental flow conditions

	Premixed slot	Discharge slot
CH_4 (m^3/h)	0.045	-
O_2 (m^3/h)	0.085	0.02–0.04
He (m^3/h)	0.25	0.25–0.65
NO (ppm)	-	250

Table 2. Camera settings that were set in order to avoid signal saturation (saturation reached at 4095 counts)

Resolution	190 – 900 nm
Gate	50 μs ± 10
Burst count	13
Gain	65

Nitric oxide was adding for atomic oxygen removal that quenches singlet oxygen [7]. The mixture ignited by an arc discharge at 500 torr, and then the pressure reduced to 200 torr. The experimental conditions of the crossed discharge were: $\mathbf{U}_{DC}$ = up to **1.4** kV, frequency was up to 25 kHz. These conditions are optimal for exciting the singlet oxygen. The Fig. 2 shows the design of CDR.

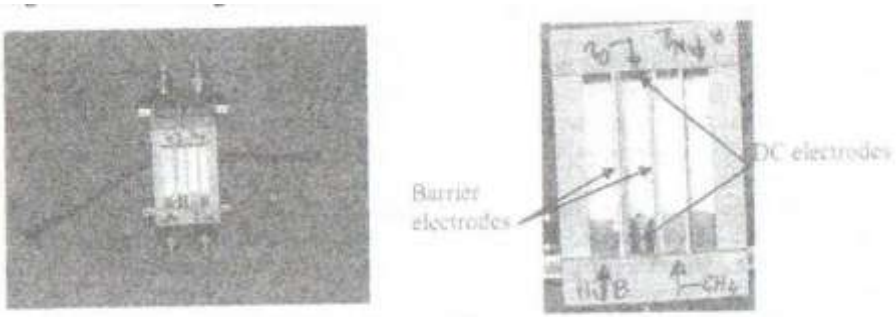

Fig. 2. Crossed discharge reactor (48 mm gap DC electrodes, 6.5 mm gap between barrier electrodes)

Optical measurements were conducted with optical digital spectral camera LAVISION. Camera settings are presented on Table 2.

Results and discussions

The Fig. 3 shows a stabilized partially premixed flame at P = 200 torr. The flow was stabilized by adding small glass balls into the two channels allowing the gas input.

Fig. 3. View of the stabilized partially premixed flame at P = 200 torr

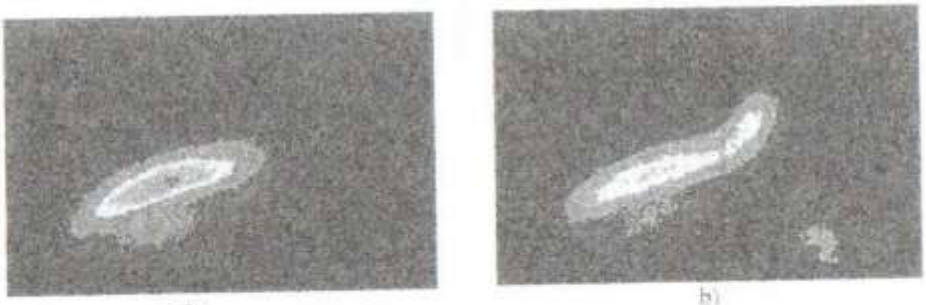

a) b)

Fig. 4. Pictures of a flame without (a) and with (b) plasma obtained with optical spectral digital camera

In the Fig. 4 one can observe an extension of the flame due to the presence of exited molecules produced by the plasma discharge.

Conclusions

Increasing of the flame front and the flame stabilization were observed when the crossed discharge is applied.

Acknowledgements

This work was supported by BRFFR T07Φ-003, INTAS 06-1000014-5675.

References

1. Naumov V.V., Chernukho A.P., Starik A.M., Titova N.S. Modeling of plasma-chemical initiation of detonation in a supersonic flow of combustible mixtures // *Combust, and Atmospheric Pollution. Moscow. Torus Press Ltd.* / Ed. by G.D. Roy, S.M. Frolov, A.M. Starik. 2003. Pp. 312-317.
2. Starik A.M., Titova N.S. Possibility of initiation of combustion of CH4-O2 (Air) mixtures with laser-induced excitation of molecules *И Combust. Explosion and Shock Waves.* Vol. 40. Pp. 499-510.
3. Kof L.M., Starikovskaya S.M., Starikovskii A.Yu. // *12th Intern. Conf on Gas Discharge and Their Applications.* Greifswaild. 1997. Vol. 1. P. 380.

4. Packan D., Messina D., Bonnet J., Vervisch P., Grisch F. and Attial Tretout B. Study of plasma-assisted combustion using optical diagnostics // *Combust, and Pollution: Environment Impact. Moscow Torus Press* / Ed. by G.D. Roy, S.M. Frolov, A.M. Starik. Pp. 79-86.
5. Magre P., Sabel'nikov V., Teixeira D., Vincent-Randonnier A. Effect of a dielectric barrier discharge on the stabilization of a methane-air diffusion flame // ISABE-2005- 1147.
6. Pliavaka K.F., Gorbatov S.V., Shushkou S.V., Pliavaka F.V., Chernukho A.P., Zhdanok S.A., Naumov V.V., Starik A.M., Bourig A., Martin J.-P. Singlet oxygen production in electrical non-self-sustained HV pulsed+DC cross discharge at atmospheric pressure with application to plasma assisted combustion technologies // *Intern. Scientific Workshop "Nonequiiibrium processes in combustion and plasma based technologies"* Minsk. Belarus. August 26-31. 2006. Pp. 186-191.
7. Hicks A., Bruzzese J., Lempert W.R., Rich J.W., Adamovich I.V. Effect of nitric oxide on gain and output power of a non-self-sustained electric discharge pumped oxygen-iodine laser // Department of Mechanical Engineering. The Ohio State University, Columbus, OH.